

Air Force Institute of Technology

AFIT Scholar

Theses and Dissertations

Student Graduate Works

6-2005

High-Temperature Ferromagnetism in Transition Metal Implanted Wide-Bandgap Semiconductors

Jeremy A. Raley

Follow this and additional works at: <https://scholar.afit.edu/etd>



Part of the [Electronic Devices and Semiconductor Manufacturing Commons](#)

Recommended Citation

Raley, Jeremy A., "High-Temperature Ferromagnetism in Transition Metal Implanted Wide-Bandgap Semiconductors" (2005). *Theses and Dissertations*. 3640.

<https://scholar.afit.edu/etd/3640>

This Dissertation is brought to you for free and open access by the Student Graduate Works at AFIT Scholar. It has been accepted for inclusion in Theses and Dissertations by an authorized administrator of AFIT Scholar. For more information, please contact AFIT.ENWL.Repository@us.af.mil.



**HIGH-TEMPERATURE FERROMAGNETISM IN
TRANSITION METAL IMPLANTED WIDE-BANDGAP
SEMICONDUCTORS**

DISSERTATION

Jeremy A. Raley, Captain, USAF

AFIT/DS/ENP/05-04

**DEPARTMENT OF THE AIR FORCE
AIR UNIVERSITY**

AIR FORCE INSTITUTE OF TECHNOLOGY

Wright-Patterson Air Force Base, Ohio

APPROVED FOR PUBLIC RELEASE; DISTRIBUTION UNLIMITED

The views expressed in this dissertation are those of the author and do not reflect the official policy or position of the United States Air Force, Department of Defense, or the United States Government.

AFIT/DS/ENP/05-04

HIGH-TEMPERATURE FERROMAGNETISM IN
TRANSITION METAL IMPLANTED WIDE-BANDGAP
SEMICONDUCTORS

DISSERTATION

Presented to the Faculty
Graduate School of Engineering and Management
Air Force Institute of Technology
Air University
Air Education and Training Command
in Partial Fulfillment of the Requirements for the
Degree of Doctor of Philosophy

Jeremy A. Raley, B.S.E.E., M.S.E.E.
Captain, USAF

July 2005

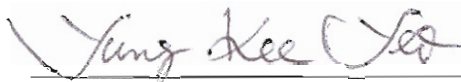
APPROVED FOR PUBLIC RELEASE; DISTRIBUTION UNLIMITED

HIGH-TEMPERATURE FERROMAGNETISM IN
TRANSITION METAL IMPLANTED WIDE-BANDGAP
SEMICONDUCTORS

Jeremy A. Raley, B.S.E.E., M.S.E.E.
Captain, USAF

Approved:

Date



Yung Kee Yeo (Chairman)

9 June '05



William P. Baker (Dean's Representative)

9 Jun 05



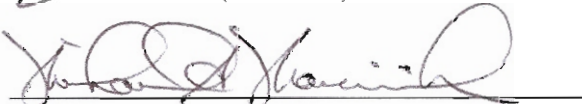
Robert L. Hengehold (Member)

9 Jun 05



James A. Lott (Member)

09 JUN 05



Michael A. Marciniak (Member)

9 JUN 05



Todd D. Steiner (Member)

9 June 05

Accepted:

Robert A. Calico, Jr.

Dean, Graduate School of Engineering and Management

Date

Abstract

The field of spin transport electronics (spintronics), where carrier spin is used in addition to charge to convey information, is becoming a viable candidate for advancing computing and communication technologies. Material with both semiconductor and magnetic properties, which is commonly called a dilute magnetic semiconductor (DMS) is proving most useful in the fabrication of spintronic devices. In order to produce a dilute ferromagnetic wide-bandgap semiconductor at above room temperature, a transition metal (TM) such as Mn, Cr, Ni, or Fe is implanted into host semiconductors of p -GaN, $\text{Al}_{0.35}\text{Ga}_{0.65}\text{N}$, or ZnO. Through magnetic hysteresis measurements using superconducting quantum interference device (SQUID) magnetometry, it is found that some of the material combinations clearly show strong ferromagnetism above room temperature, others show marginal evidence of ferromagnetism, and several do not demonstrate ferromagnetism, rather they are superparamagnetic or diamagnetic. Among the various measured samples, the most promising materials for creating spintronic devices using ion implantation are Mn-implanted p -GaN, Cr-implanted $\text{Al}_{0.35}\text{Ga}_{0.65}\text{N}$, and Fe-implanted ZnO nanotips grown on sapphire.

In p -GaN implanted with Mn at 200 keV with a dose of $5 \times 10^{16} \frac{\text{ions}}{\text{cm}^2}$ and annealed at 725 °C for 5 minutes, ferromagnetism persists to room temperature with a coercive field (H_c) value of 186 Oe and a remanent field (B_R) value of 11% of the saturation magnetization (M_S) of 3.2×10^{-5} emu. The Curie temperature (T_C) is estimated to be above 350 K.

In Cr-implanted $\text{Al}_{0.35}\text{Ga}_{0.65}\text{N}$, a room-temperature coercive field of 249 Oe is obtained for a sample implanted with $5 \times 10^{16} \frac{\text{ions}}{\text{cm}^2}$ at 200 keV and annealed at 775 °C. The remanent field also remains greater than 20% of the 6×10^{-5} emu M_S observed at 300 K in this sample. T_C for this sample is estimated to be around 350 K.

Fe-implanted ZnO nanotips grown on *c*-Al₂O₃ show a coercive field width of 209 Oe at 300 K for the sample implanted at 200 keV to a dose of $5 \times 10^{16} \frac{\text{ions}}{\text{cm}^2}$ and annealed at 700 °C for 20 minutes. A B_R of 12% of M_S (2.3×10^{-5} emu) is also present at room temperature. T_C in this material appears to be well above 350 K.

In each of these samples, the ferromagnetic dilute magnetic semiconductor behavior is confirmed by temperature-dependent field-cooled and zero-field-cooled magnetization measurements. The optimum anneal temperatures found in these samples are also confirmed by photoluminescence or cathodoluminescence measurements.

As progress is made toward realizing practical spintronic devices, the work reported here will be useful for determining material combinations and implantation conditions to yield the needed DMS materials.

Acknowledgements

I would like to thank the sovereign Creator of the universe for allowing me insight into a small piece of His creation and for providing the opportunity to study His handiwork. More so, I thank God for providing peace during the Ph.D. experience by providing for a relationship with Him through His Son, Jesus Christ.

Without the support of my wife, I never would have even applied to stay at AFIT and attempt this work. She knew what would be involved and gave her support anyway. She has helped me to balance this work with my responsibilities to my sons and has taken up the slack when I failed to balance correctly. This is the sort of selflessness that makes her so special to me. She truly is a Proverbs 31 woman.

My parents, siblings, and in-laws have also been instrumental in the production of this work because of their great support and encouragement. This support structure was vital and I thank all of you for your support and your understanding even when my actions may have sent the message that I was too busy to stay in touch.

Dr. Yeo told me when I first signed on that “family is the most important thing,” so I hope he doesn’t mind being mentioned after them. Obviously, this project could not have happened without his inspiration, guidance, and correction throughout my research effort. I also have to thank him for watching out for my future while I was short-sighted and more focused on immediate goals.

This research was made possible by funding from AFOSR/NE and AFRL/SNDD. Their monetary support is gratefully acknowledged.

Finally, I must thank Virginia Commonwealth University for allowing me to use their SQUID system while waiting for delivery of AFIT’s system.

Jeremy A. Raley

Table of Contents

	Page
Abstract	iv
Acknowledgements	vi
List of Figures	xii
List of Tables	xxiv
List of Symbols	xxv
List of Abbreviations	xxvii
I. Introduction	1-1
1.1 Motivation	1-1
1.2 Brief Background	1-2
1.2.1 Challenges	1-2
1.2.2 Current State of Research	1-2
1.3 Problem Statement	1-3
1.4 Results of This Research	1-4
II. Background	2-1
2.1 Terminology	2-1
2.2 Spintronics Challenges	2-5
2.2.1 Spin Injection	2-5
2.2.2 Spin Transport	2-7
2.2.3 Spin Manipulation	2-7
2.2.4 Spin Detection	2-8
2.2.5 Relevant Factors for Spintronic Device Fabrication	2-8
2.3 Promising Materials	2-9
2.4 Prior Art	2-10

	Page	
2.4.1	Relevant Experiments Involving ZnO	2-10
2.4.2	Relevant Experiments Involving GaN	2-11
2.4.3	Relevant Experiments Involving Al _{0.35} Ga _{0.65} N	2-13
2.5	Theory of Dilute Magnetic Semiconductors	2-13
2.6	Conclusion	2-15
III.	Experimental Methods	3-1
3.1	Ion-Implantation	3-1
3.2	Thermal Annealing	3-2
3.2.1	Annealing of <i>p</i> -GaN and Al _{0.35} Ga _{0.65} N	3-2
3.2.2	Annealing of ZnO	3-2
3.3	Superconducting Quantum Interference Device (SQUID) Magnetometry	3-3
3.4	Optical Characterization	3-6
3.4.1	Cathodoluminescence	3-6
3.4.2	Photoluminescence	3-7
3.5	X-Ray Diffraction	3-9
IV.	Characteristics of Transition Metal Implanted p-type Gallium Nitride	4-1
4.1	Manganese-implanted Gallium Nitride	4-1
4.1.1	Magnetic Hysteresis Measurements	4-1
4.1.2	Temperature-Dependent Magnetization	4-6
4.1.3	Optical Measurements	4-8
4.2	Chromium-implanted Gallium Nitride	4-11
4.2.1	Magnetic Hysteresis Measurements	4-11
4.2.2	Temperature-Dependent Magnetization	4-15
4.2.3	Optical Measurements	4-19
4.3	Nickel-implanted Gallium Nitride	4-21

	Page
4.3.1	Magnetic Hysteresis Measurements 4-21
4.3.2	Temperature-Dependent Magnetization 4-26
4.3.3	Optical Measurements 4-28
4.4	Conclusions 4-30
V.	Characteristics of Transition Metal Implanted
	Aluminum Gallium Nitride 5-1
5.1	Manganese-implanted Aluminum Gallium Nitride 5-1
5.1.1	Magnetic Hysteresis Measurements 5-1
5.1.2	Temperature-Dependent Magnetization 5-7
5.1.3	Optical Measurements 5-8
5.2	Chromium-implanted Aluminum Gallium Nitride 5-10
5.2.1	Magnetic Hysteresis Measurements 5-11
5.2.2	Temperature-dependent Magnetization 5-15
5.2.3	Optical Measurements 5-18
5.3	Nickel-doped Aluminum Gallium Nitride 5-20
5.3.1	Magnetic Hysteresis Measurements 5-21
5.3.2	Temperature-Dependent Magnetization 5-26
5.3.3	Optical Measurements 5-28
5.4	Conclusions 5-30
VI.	Characteristics of Transition Metal Implanted
	Epitaxial Zinc Oxide 6-1
6.1	Manganese-Implanted Zinc Oxide (First Run) 6-1
6.1.1	Magnetic Hysteresis Measurements 6-1
6.1.2	Temperature-Dependent Magnetization 6-6
6.1.3	Optical Measurements 6-6
6.2	Manganese-Implanted Zinc Oxide (Second Run) 6-9
6.2.1	Magnetic Hysteresis Measurements 6-9

	Page	
6.2.2	Temperature-Dependent Magnetization	6-15
6.2.3	Optical Measurements	6-15
6.3	Chromium-Implanted Zinc Oxide	6-18
6.3.1	Magnetic Hysteresis Measurements	6-18
6.3.2	Temperature-Dependent Magnetization	6-23
6.3.3	Optical Measurements	6-25
6.4	Nickel-Implanted Zinc Oxide	6-27
6.4.1	Magnetic Hysteresis Measurements	6-27
6.4.2	Temperature-Dependent Magnetization	6-32
6.4.3	Optical Measurements	6-34
6.5	Iron-Implanted Zinc Oxide	6-36
6.5.1	Magnetic Hysteresis Measurements	6-37
6.5.2	Temperature-Dependent Magnetization	6-41
6.5.3	Optical Measurements	6-44
6.6	Conclusions	6-46
VII. Characteristics of Transition Metal Implanted		
	Zinc Oxide Nanotips Grown on Various Substrates	7-1
7.1	Zinc Oxide Nanotips on Quartz	7-2
7.1.1	Manganese-Implanted ZnO Nanotips on Quartz	7-3
7.1.2	Iron-Implanted ZnO Nanotips on Quartz	7-10
7.2	Zinc Oxide Nanotips on <i>c</i> -Plane Sapphire	7-20
7.2.1	Manganese-Implanted ZnO Nanotips on <i>c</i> -Al ₂ O ₃	7-21
7.2.2	Iron-Implanted ZnO Nanotips on <i>c</i> -Al ₂ O ₃	7-30
7.3	Iron-Implanted Zinc Oxide Nanotips on Glass	7-39
7.3.1	Magnetic Hysteresis Measurements	7-40
7.3.2	Temperature-Dependent Magnetization	7-46
7.3.3	Optical Measurements	7-47
7.4	Conclusions	7-49

	Page	
7.4.1	General Conclusions	7-49
7.4.2	Specific Findings	7-50
VIII.	Conclusions	8-1
8.1	Summary of Results	8-1
8.2	Future Work	8-7
8.2.1	Devices	8-7
8.2.2	Further Characterization	8-9
8.2.3	Dopant Distribution Uniformity in Nanotips	8-12
8.2.4	Materials Warranting Further Investigation	8-13
8.3	Finale	8-14
Appendix A.	Prior Experimental and Theoretical Results for GaN and ZnO Doped with Transition Metals	A-1
A.1	Theoretical Calculations	A-2
A.1.1	Zinc Oxide Theoretical Calculations	A-2
A.2	Summary of Experimental Results	A-5
A.2.1	Zinc Oxide Experimental Results	A-5
A.2.2	Gallium Nitride Experimental Results	A-11
Appendix B.	Secondary Phase Concerns in Transition-Metal-Implanted ZnO, GaN, and AlGaN	B-1
Appendix C.	Detailed Summary of Magnetic Behavior	C-1
	Bibliography	Bib-1
	Vita	VITA-1

List of Figures

Figure		Page
2.1.	Illustration of the magnetic response of a superparamagnetic material while the applied magnetic field is varied. This is a theoretical illustration modelled after Bean [12].	2-2
2.2.	Local ordering of magnetic moments in (a) a ferromagnet, (b) an antiferromagnet, and (c) a ferrimagnet. After O'Reilly [80].	2-2
2.3.	A magnetic hysteresis loop with the coercive (H_c) and remanent (B_R) fields and saturation magnetization (M_S) labelled for reference purposes. This magnetization-versus-applied-field measurement was taken from an epitaxial ZnO sample implanted with Fe and annealed at 625 °C for 10 minutes. The contribution of background diamagnetism was removed from this data.	2-4
2.4.	Configurations for semiconductor-based electrical spin injectors, (a) using a ferromagnetic DMS layer [79], and (b) leveraging giant Zeeman splitting [104].	2-6
2.5.	Computed values of the Curie temperature (T_C) for various p-type semiconductors containing 5% Mn and $3.5 \times 10^{20} \frac{\text{holes}}{\text{cm}^3}$ [30].	2-9
2.6.	Illustration of the two most prevalent explanations for ferromagnetism in transition metal implanted semiconductors: (a) the mean-field theory; (b) the bound magnetic polaron theory [89].	2-14
3.1.	(a) Simple schematic of a SQUID pick-up loop used for detecting weak magnetic fields and small changes in magnetic fields. After Turton [127]. (b) A second-order gradiometer made of superconducting wire [70]. This is the configuration used in Quantum Design's Magnetic Property Measurement System, which is the system used to make the magnetic measurements reported in this research.	3-4
3.2.	Schematic diagram of the cathodoluminescence measurement apparatus used to collect optical data.	3-7
3.3.	Schematic diagram of the photoluminescence measurement apparatus used to collect optical data.	3-8

Figure		Page
3.4.	Configuration for XRD measurements on a single crystal thin film when: (a) the reciprocal lattice vectors of the reflecting planes are parallel to the surface normal; and (b) the asymmetrical case where reciprocal lattice vectors are aligned at an angle α to the sample surface normal (after Hammond [41, Fig. 9.16]).	3-10
4.1.	Raw magnetic hysteresis data from SQUID measurements of Mn-implanted <i>p</i> -GaN annealed as indicated for 5 minutes in N ₂ flowing at $2 \frac{L}{\text{min}}$.	4-2
4.2.	Magnetic hysteresis data for <i>p</i> -GaN implanted with Mn: as-implanted and annealed as indicated. Linear diamagnetic influences have been removed from this data.	4-4
4.3.	Coercive field strengths at 5 and 300 K for various annealing conditions of Mn-implanted <i>p</i> -GaN.	4-5
4.4.	Remanent field strengths at 5 and 300 K for various annealing conditions of Mn-implanted <i>p</i> -GaN.	4-6
4.5.	Temperature-dependent magnetization for <i>p</i> -GaN implanted with Mn and annealed as indicated for 5 minutes in N ₂ flowing at $2 \frac{L}{\text{min}}$. Note that the <i>y</i> axis spans the same range of magnetic moment despite the fact that background offset causes a difference in absolute values.	4-7
4.6.	Cathodoluminescence and photoluminescence spectra of <i>p</i> -GaN implanted with Mn and annealed as indicated for 5 minutes in N ₂ flowing at $2 \frac{L}{\text{min}}$. Note that the as-grown and as-implanted samples are PL spectra and are not to scale with the annealed samples for which CL spectra were collected. The PL and CL spectra were collected from samples cooled to ~ 10 and ~ 5 K, respectively.	4-9
4.7.	Raw data from magnetic hysteresis SQUID measurements of Cr-implanted <i>p</i> -GaN as-implanted and annealed as indicated for 5 minutes in N ₂ flowing at $2 \frac{L}{\text{min}}$.	4-12
4.8.	Magnetic hysteresis data for <i>p</i> -GaN implanted with Cr and annealed as indicated. Linear diamagnetic influences have been removed from this data.	4-14

Figure	Page
4.9. Coercive field strengths at 5 and 300 K for various annealing conditions of Cr-implanted <i>p</i> -GaN.	4-15
4.10. Remanent field strength as a function of saturation magnetization at 5 and 300 K for various annealing conditions of Cr-implanted <i>p</i> -GaN.	4-16
4.11. Temperature-dependent magnetization for <i>p</i> -GaN implanted with Cr and annealed as indicated. Note that the <i>y</i> axis spans the same range of magnetic moment despite the fact that background offset causes a difference in absolute values.	4-17
4.12. Cathodoluminescence spectra, collected from samples cooled to approximately 5 K, of <i>p</i> -GaN implanted with Cr and annealed as indicated in a $2 \frac{\text{L}}{\text{min}}$ flow of N ₂ for 5 minutes.	4-20
4.13. Raw data from magnetic hysteresis SQUID measurements of Ni-implanted <i>p</i> -GaN annealed as indicated for 5 minutes in N ₂ flowing at $2 \frac{\text{L}}{\text{min}}$	4-22
4.14. Magnetic hysteresis data for <i>p</i> -GaN implanted with Ni and annealed as indicated. Linear magnetic influences have been removed from this data. Note that the horizontal scale is doubled for the samples annealed at 700 and 725 °C as well as the as-implanted sample.	4-24
4.15. Coercive field strengths at 5 and 300 K for various annealing conditions of Ni-implanted <i>p</i> -GaN. The data for the sample annealed at 675 °C is obscured because of an artifact of the diamagnetism correction algorithm.	4-25
4.16. Remanent field strengths at 5 and 300 K for various annealing conditions of Ni-implanted <i>p</i> -GaN.	4-26
4.17. Temperature-dependent magnetization for <i>p</i> -GaN implanted with Ni and annealed as indicated for 5 minutes. Note that the <i>y</i> axis spans the same range of magnetic moment despite the fact that background offset causes a difference in absolute values.	4-27
4.18. Cathodoluminescence spectra of <i>p</i> -GaN implanted with Ni and annealed as indicated for 5 minutes in N ₂ flowing at $2 \frac{\text{L}}{\text{min}}$. These measurements were taken at approximately 5 K.	4-29

Figure		Page
5.1.	Raw data from magnetic hysteresis SQUID measurements of Mn-implanted $\text{Al}_{0.35}\text{Ga}_{0.65}\text{N}$ annealed as indicated in N_2 flowing at $2 \frac{\text{L}}{\text{min}}$	5-2
5.2.	Magnetic hysteresis data for $\text{Al}_{0.35}\text{Ga}_{0.65}\text{N}$ implanted with Mn and annealed as indicated. Linear diamagnetic influences have been removed from this data.	5-4
5.3.	Coercive field strengths at 5 and 300 K for various annealing conditions of Mn-implanted $\text{Al}_{0.35}\text{Ga}_{0.65}\text{N}$. The data that have been skewed by the background subtraction process are obscured in this figure.	5-5
5.4.	Remanent field strength differences at 5 and 300 K for various annealing conditions of Mn-implanted p -GaN. Note that this data is presented as magnetization values in emu, not as a percentage of saturation magnetization as in the other figures reporting B_R	5-6
5.5.	Temperature-dependent magnetization for $\text{Al}_{0.35}\text{Ga}_{0.65}\text{N}$ implanted with Mn and annealed as indicated for 5 minutes in N_2 flowing at $2 \frac{\text{L}}{\text{min}}$. Note that the y axis spans the same range of magnetic moment despite the fact that background offset causes a difference in absolute values.	5-7
5.6.	Cathodoluminescence spectra, collected from samples cooled to ~ 5 K, of $\text{Al}_{0.35}\text{Ga}_{0.65}\text{N}$ implanted with Mn and annealed at the indicated temperatures for 5 minutes in N_2 flowing at $2 \frac{\text{L}}{\text{min}}$	5-9
5.7.	Raw data from magnetic hysteresis SQUID measurements of Cr-implanted $\text{Al}_{0.35}\text{Ga}_{0.65}\text{N}$ annealed as indicated for 5 minutes in N_2 flowing at $2 \frac{\text{L}}{\text{min}}$	5-12
5.8.	Magnetic hysteresis data for $\text{Al}_{0.35}\text{Ga}_{0.65}\text{N}$ implanted with Cr and annealed as indicated in N_2 flowing at $2 \frac{\text{L}}{\text{min}}$ for 5 minutes. Linear diamagnetic influences have been removed from this data.	5-13
5.9.	Coercive field strengths at 5 and 300 K for various annealing conditions of Cr-implanted $\text{Al}_{0.35}\text{Ga}_{0.65}\text{N}$	5-14
5.10.	Remanent field magnetization values at 5 and 300 K for various annealing conditions of Cr-implanted $\text{Al}_{0.35}\text{Ga}_{0.65}\text{N}$. Note that this is raw data and not presented as a function of saturation magnetization.	5-15

Figure		Page
5.11.	Remanent field strengths as a function of M_S at 5 and 300 K for various annealing conditions of Cr-implanted $\text{Al}_{0.35}\text{Ga}_{0.65}\text{N}$. . .	5-16
5.12.	Temperature-dependent magnetization for $\text{Al}_{0.35}\text{Ga}_{0.65}\text{N}$ implanted with Cr. Samples were annealed in N_2 flowing at $2 \frac{\text{L}}{\text{min}}$ at the temperatures indicated for 5 minutes. Note that the y axis spans the same range of magnetic moment despite the fact that background offset causes a difference in absolute values.	5-17
5.13.	Cathodoluminescence spectra of $\text{Al}_{0.35}\text{Ga}_{0.65}\text{N}$ implanted with Cr and annealed as indicated for 5 minutes in N_2 flowing at $2 \frac{\text{L}}{\text{min}}$. CL measurements were taken at approximately 5 K.	5-19
5.14.	Raw data from magnetic hysteresis SQUID measurements of Ni-implanted $\text{Al}_{0.35}\text{Ga}_{0.65}\text{N}$ annealed as indicated in N_2 flowing at $2 \frac{\text{L}}{\text{min}}$ for 5 minutes.	5-22
5.15.	Magnetic hysteresis data for $\text{Al}_{0.35}\text{Ga}_{0.65}\text{N}$ implanted with Ni and annealed as indicated for 5 minutes in a $2 \frac{\text{L}}{\text{min}}$ flow of N_2 . Linear diamagnetic influences have been removed from this data. . . .	5-23
5.16.	Coercive field strengths at 5 and 300 K for various annealing conditions of Ni-implanted $\text{Al}_{0.35}\text{Ga}_{0.65}\text{N}$	5-24
5.17.	Remanent field strengths at 5 and 300 K for various annealing conditions of Ni-implanted $\text{Al}_{0.35}\text{Ga}_{0.65}\text{N}$	5-25
5.18.	Temperature-dependent magnetization for $\text{Al}_{0.35}\text{Ga}_{0.65}\text{N}$ implanted with Ni. Samples are annealed as indicated in the figure for 5 minutes in N_2 flowing at $2 \frac{\text{L}}{\text{min}}$. Note that the y axis spans the same range of magnetic moment despite the fact that background offset causes a difference in absolute values.	5-27
5.19.	Cathodoluminescence spectra collected at ~ 5 K for $\text{Al}_{0.35}\text{Ga}_{0.65}\text{N}$ implanted with Ni and annealed as indicated for 5 minutes in N_2 flowing at $2 \frac{\text{L}}{\text{min}}$	5-29
6.1.	Raw data from magnetic hysteresis measurements of Mn-implanted ZnO annealed as indicated in O_2 flowing at 25 sccm.	6-2
6.2.	Magnetic hysteresis data for ZnO implanted with Mn and annealed in O_2 flowing at 25 sccm as indicated in the figure. Linear diamagnetic influences have been removed from this data. . .	6-3

Figure	Page
6.3. Coercive field strengths at 5 and 300 K for various annealing conditions of Mn-implanted ZnO.	6-4
6.4. Remanent field strengths at 5 and 300 K for various annealing conditions of Mn-implanted ZnO.	6-5
6.5. Temperature-dependent magnetization for ZnO implanted with Mn and annealed as indicated in the figure in O ₂ flowing at 25 sccm. Note that the <i>y</i> axis spans the same range of magnetic moment despite the fact that background offset causes a difference in absolute values.	6-7
6.6. Photoluminescence spectra of ZnO implanted with Mn and annealed as indicated in the figure in O ₂ flowing at 25 sccm for 10 minutes. The spectra are collected at a temperature of approximately 10 K.	6-8
6.7. Raw data from magnetic hysteresis SQUID measurements of Mn-implanted ZnO annealed as indicated for 10 minutes in a 25 sccm flow of O ₂	6-10
6.8. Magnetic hysteresis data for epitaxial ZnO implanted with Mn and annealed as for 10 minutes in O ₂ flowing at 25 sccm. Linear diamagnetic influences have been removed from this data. . .	6-12
6.9. Coercive field strengths at 5 and 300 K for various annealing conditions of Mn-implanted ZnO. The values that are suspect due to artifacts from the background correction algorithm are obscured.	6-13
6.10. Remanent field strengths at 5 and 300 K for various annealing conditions of Mn-implanted ZnO. The data for the sample annealed at 725 °C is obscured because it is erroneously large due to the high sensitivity of M_S to the background subtraction process compared to B_R	6-14
6.11. Temperature-dependent magnetization for ZnO implanted with Mn and annealed as indicated in the figure for 10 minutes in O ₂ flowing at 25 sccm. Note that the <i>y</i> axis spans the same range of magnetic moment despite the fact that background offset causes a difference in absolute values.	6-16

Figure		Page
6.12.	Cathodoluminescence spectra of ZnO implanted with Mn and annealed as indicated in a 25 sccm flow of O ₂ for 10 minutes. The spectra were collected from samples cooled to approximately 10 K.	6-17
6.13.	Raw data from magnetic hysteresis SQUID measurements of Cr-implanted ZnO annealed as indicated for 10 minutes in O ₂ flowing at 25 sccm.	6-19
6.14.	Magnetic hysteresis data for epitaxial ZnO implanted with Cr and annealed as indicated for 10 minutes in O ₂ flowing at 25 sccm. Linear magnetic influences have been removed from this data.	6-21
6.15.	Coercive field strengths at 5 and 300 K for various annealing conditions of Cr-implanted ZnO.	6-22
6.16.	Remanent field strengths at 5 and 300 K for various annealing conditions of Cr-implanted ZnO. Note that these are raw sample magnetization values and not presented as a percentage of M _S	6-23
6.17.	Temperature-dependent magnetization for ZnO implanted with Cr and annealed as indicated for 10 minutes in O ₂ flowing at 10 sccm. Note that the <i>y</i> axis spans the same range of magnetic moment despite the fact that background offset causes a difference in absolute values.	6-24
6.18.	Cathodoluminescence spectra of ZnO implanted with Cr and annealed as indicated in O ₂ flowing at 25 sccm for 10 minutes. CL measurements were taken at a temperature of approximately 5 K.	6-26
6.19.	Raw data from magnetic hysteresis SQUID measurements of Ni-implanted ZnO annealed as indicated in the figure for 10 minutes in O ₂ flowing at 25 sccm.	6-28
6.20.	Magnetic hysteresis data for epitaxial ZnO implanted with Ni and annealed as indicated in O ₂ flowing at 25 sccm for 10 minutes. Linear diamagnetic influences have been removed from this data.	6-30
6.21.	Coercive field strengths at 5 and 300 K for various annealing conditions of Ni-implanted ZnO.	6-31
6.22.	Remanent field strengths at 5 and 300 K for various annealing conditions of Ni-implanted ZnO.	6-32

Figure	Page
6.23. Temperature-dependent magnetization for ZnO implanted with Ni and annealed as indicated for 10 minutes in O ₂ flowing at 10 sccm. Note that the <i>y</i> axis spans the same range of magnetic moment despite the fact that background offset causes a difference in absolute values.	6-33
6.24. Cathodoluminescence spectra of ZnO implanted with Ni and annealed as indicated in the figure for 10 minutes. Samples were cooled to approximately 5 K for these measurements.	6-35
6.25. Variable field measurements (raw data) for a ZnO thin film implanted with Fe and annealed as indicated for 10 minutes in O ₂ flowing at 25 sccm.	6-38
6.26. Variable field measurements (corrected to remove diamagnetism) for ZnO thin film implanted with Fe and annealed as indicated in O ₂ flowing at 25 sccm for 10 minutes.	6-39
6.27. Coercive field strengths at 5 and 300 K for various annealing conditions of an Fe-implanted ZnO epitaxial thin film.	6-41
6.28. Remanent field strengths at 5 and 300 K for various annealing conditions of an Fe-implanted ZnO epitaxial thin film.	6-42
6.29. Temperature-dependent magnetization for ZnO implanted with Fe and annealed as indicated in the figure for 10 minutes in O ₂ flowing at 25 sccm. Note that the <i>y</i> axis spans the same range of magnetic moment despite the fact that background offset causes a difference in absolute values.	6-43
6.30. Photoluminescence spectra, collected at approximately 10 K, of ZnO implanted with Fe and annealed as indicated for 10 minutes in O ₂ flowing at 25 sccm.	6-45
7.1. An SEM image of ZnO nanotips as-grown on a quartz substrate.	7-2
7.2. Raw data from magnetic hysteresis SQUID measurements of Mn-implanted ZnO nanotips on quartz annealed as indicated in O ₂ flowing at 25 sccm.	7-4

Figure	Page
7.3. Magnetic hysteresis data for ZnO nanotips grown on quartz, implanted with Mn and annealed as indicated in the figure in an atmosphere of O ₂ flowing at 25 sccm. Linear diamagnetic influences have been removed from this data.	7-6
7.4. Coercive field strengths at 5 and 300 K for various annealing conditions of Mn-implanted ZnO nanotips grown on quartz.	7-7
7.5. Remanent field strengths at 5 and 300 K for various annealing conditions of Mn-implanted ZnO nanotips grown on quartz substrates.	7-8
7.6. Temperature-dependent magnetization for ZnO nanotips implanted with Mn and annealed as indicated in the figure in O ₂ flowing at 25 sccm. Note that the <i>y</i> axis spans the same range of magnetic moment despite the fact that background offset causes a difference in absolute values.	7-9
7.7. Photoluminescence spectra of ZnO implanted with Mn and annealed as indicated in O ₂ flowing at 25 sccm. The samples were cooled to ~10 K for these measurements.	7-11
7.8. Raw data from magnetic hysteresis SQUID measurements of Fe-implanted ZnO nanotips on quartz annealed as indicated in O ₂ flowing at 25 sccm. Note that the measurement from the as-grown sample at 300 K is not displayed because the signal was overcome by noise.	7-13
7.9. Magnetic hysteresis data for ZnO nanotips grown on quartz, implanted with Mn and annealed as indicated in the figure in an atmosphere of O ₂ flowing at 25 sccm. Linear diamagnetic influences have been removed from this data. Note that the measurement from the as-grown sample at 300 K is not displayed because the signal was overcome by noise.	7-14
7.10. Coercive field strengths at 5 and 300 K for various annealing conditions of Mn-implanted ZnO nanotips grown on quartz. Measurements that are suspect due to a noisy signal are partially obscured in the figure.	7-15

Figure	Page
7.11. Remanent field strengths at 5 and 300 K for various annealing conditions of Mn-implanted ZnO nanotips grown on quartz substrates. Measurements that are suspect due to a noisy signal are partially obscured in the figure.	7-16
7.12. Temperature-dependent magnetization for ZnO nanotips implanted with Fe and annealed as indicated in the figure for 10 minutes in O ₂ flowing at 25 sccm. Note that the <i>y</i> axis spans the same range of magnetic moment despite the fact that background offset causes a difference in absolute values.	7-18
7.13. Photoluminescence at ~10 K of ZnO nanotips on quartz implanted with Fe and annealed as indicated for 10 minutes in O ₂ flowing at 25 sccm.	7-19
7.14. A scanning electron microscope image of ZnO nanotips grown on a <i>c</i> -Al ₂ O ₃ substrate [74].	7-21
7.15. Raw data from magnetic hysteresis SQUID measurements of Mn-implanted ZnO nanotips grown on <i>c</i> -Al ₂ O ₃ and annealed as indicated in O ₂ flowing at 25 sccm.	7-23
7.16. Magnetic hysteresis data for ZnO nanotips grown on <i>c</i> -Al ₂ O ₃ , implanted with Mn and annealed as indicated for 10 minutes in O ₂ flowing at 25 sccm. Linear magnetic influences have been removed from this data.	7-24
7.17. Coercive field strengths at 5 and 300 K for various annealing conditions of Mn-implanted ZnO nanotips grown on sapphire.	7-25
7.18. Remanent field strengths at 5 and 300 K for various annealing conditions of Mn-implanted ZnO nanotips grown on sapphire substrates.	7-26
7.19. Temperature-dependent magnetization for ZnO nanotips grown on <i>c</i> -Al ₂ O ₃ implanted with Mn. Samples are annealed as indicated in O ₂ flowing at 25 sccm for 10 minutes. Note that the <i>y</i> axis spans the same range of magnetic moment despite the fact that background offset causes a difference in absolute values.	7-27

Figure		Page
7.20.	Photoluminescence spectra of ZnO nanotips grown on <i>c</i> -Al ₂ O ₃ , implanted with Mn and annealed as indicated for 10 minutes in a 25 sccm O ₂ flow. PL measurements were taken at approximately 10 K.	7-29
7.21.	Raw data from magnetic hysteresis SQUID measurements of Fe-implanted ZnO nanotips grown on sapphire annealed as indicated in O ₂ flowing at 25 sccm.	7-31
7.22.	Magnetic hysteresis data for ZnO nanotips grown on <i>c</i> -Al ₂ O ₃ implanted with Fe and annealed as indicated in the figure in a 25 sccm flow of O ₂ . Linear diamagnetic influences have been removed from this data.	7-33
7.23.	Coercive field strengths at 5 and 300 K for various annealing conditions of Fe-implanted ZnO nanotips grown on sapphire. Data that is suspect due to a virtually non-magnetic characteristic in hysteresis is partially obscured.	7-34
7.24.	Remanent field strengths at 5 and 300 K for various annealing conditions of Fe-implanted ZnO nanotips grown on sapphire substrates. Data that is suspect due to a virtually non-magnetic characteristic in hysteresis is partially obscured.	7-35
7.25.	Temperature-dependent magnetization for ZnO nanotips on <i>c</i> -Al ₂ O ₃ implanted with Fe. Samples are annealed as indicated in a 25 sccm flow of O ₂ . Note that the <i>y</i> axis spans the same range of magnetic moment despite the fact that background offset causes a difference in absolute values.	7-36
7.26.	Photoluminescence spectra taken at ~10 K from ZnO nanotips grown on <i>c</i> -Al ₂ O ₃ , implanted with Fe and annealed as indicated in the figure in O ₂ flowing at 25 sccm.	7-38
7.27.	An SEM image of ZnO nanotips as-grown on a glass substrate.	7-40
7.28.	Raw data from magnetic hysteresis SQUID measurements of Fe-implanted ZnO nanotips grown on glass and annealed as indicated for 10 minutes in O ₂ flowing at 25 sccm.	7-41

Figure	Page
7.29. Magnetic hysteresis data for ZnO nanotips grown on glass, implanted with Fe and annealed as indicated in O ₂ flowing at 25 sccm for 10 minutes. Linear dia- and para-magnetic influences have been removed from this data. Note that the samples annealed at 675 and 725 °C were subjected to a maximum applied magnetic field of 10 kOe in an attempt to find magnetic saturation in them, which affects the scaling and appearance of these measurements relative to the others in the figure.	7-43
7.30. Coercive field strengths at 5 and 300 K for various annealing conditions of Fe-implanted ZnO nanotips grown on glass.	7-44
7.31. Remanent field strengths as a percentage of saturation magnetization at 5 and 300 K for various annealing conditions of Fe-implanted ZnO nanotips grown on glass. Values that are erroneously small due to large M _S values are partially obscured in the figure.	7-45
7.32. Temperature-dependent magnetization for ZnO nanotips grown on glass and implanted with Fe. Samples are annealed as indicated in a 25 sccm flow of O ₂ for 10 minutes. Note that the <i>y</i> axis spans the same range of magnetic moment despite the fact that background offset causes a difference in absolute values.	7-46
7.33. Photoluminescence spectra, collected at ~10 K, of ZnO nanotips grown on glass, implanted with Fe, and annealed as indicated in the figure in O ₂ flowing at 25 sccm.	7-48
8.1. Schematics of a proposed structures for utilizing electron spin to modulate current output. (a) The device proposed by Datta and Das [23]. (b) A similar device using wide-bandgap semiconductors and fabricated using ion implantation.	8-8
8.2. Real space energy band diagrams of metal–insulator–semiconductor diodes that could be used to test the carrier dependence of magnetic ordering in transition-metal-implanted semiconductors.	8-11

List of Tables

Table		Page
3.1.	Ion doses, in $\frac{\text{ions}}{\text{cm}^2}$, for the transition metals implanted in the various semiconductor materials studied in this research. All implantations are performed at 200 keV and room temperature.	3-2
A.1.	Materials and transition metal dopants reported in literature (as cited in the appropriate block) for useful properties as a DMS.	A-1

List of Symbols

Symbol		Page
GaN	Gallium Nitride	1-2
ZnO	Zinc Oxide	1-2
T_C	Curie Temperature	2-3
H_c	Coercive Field	2-3
B_R	Remanent Field	2-4
M_S	Saturation Magnetization	2-4
K	Kelvins	2-9
k_B	Boltzmann's Constant	2-14
N_2	Nitrogen Gas	3-2
AlN	Aluminum Nitride	3-2
Ta	Tantalum	3-2
O_2	Oxygen Gas	3-2
ϕ_0	Magnetic Flux Quantum	3-3
h	Plank's Constant	3-3
e	Electron Charge	3-3
T	Torr	3-6
Mg	Magnesium	4-1
μ_B	Bohr Magneton	4-5
eV	Electron-Volt	4-8
(D^0, X)	Neutral Donor-Bound Exciton	4-8
DAP	Donor-Acceptor Pair	4-10
Zn_i	Zn Interstitial	6-6
V_O^+	Singly Ionized Oxygen Vacancy	6-7
V_{Zn}	Zinc Vacancy	6-36
Sc	Scandium	A-1
Ti	Titanium	A-1

Symbol		Page
V	Vanadium	A-1
Cr	Chromium	A-1
Fe	Iron	A-1
Co	Cobalt	A-1
Cu	Copper	A-1
Ga	Gallium	A-3
Zn	Zinc	A-3
N	Nitrogen	A-3
O	Oxygen	A-3
Al	Aluminum	A-6
<i>g</i>	Landé Splitting Factor	A-9
Li	Lithium	A-10

List of Abbreviations

Abbreviation		Page
DoD	Department of Defense	1-1
TM	Transition Metal	1-2
DMS	Diluted Magnetic Semiconductor	1-2
SG	spin glass	2-3
ZFC	Zero-Field-Cooled	2-3
FC	Field-Cooled	2-3
MCD	Magnetic Circular Dichroism	2-3
XRD	X-Ray Diffraction	2-5
LED	Light Emitting Diode	2-5
2DEG	Two-Dimensional Electron Gas	2-7
GMR	Giant Magnetoresistance	2-8
TMR	Tunneling Magnetoresistance	2-8
AHE	Anomalous Hall Effect	2-8
SQUID	Superconducting Quantum Interference Device	2-8
PL	Photoluminescence	2-8
EL	Electroluminescence	2-8
CL	Cathodoluminescence	2-8
PLD	Pulsed Laser Deposition	2-10
<i>M-H</i>	Magnetization versus Magnetic Field	2-11
BMP	Bound Magnetic Polaron	2-14
keV	Kilo-Electron-Volt	3-1
sccm	Standard Cubic Centimeters per Minute	3-2
PMT	Photomultiplier Tube	3-6
LHe	Liquid Helium	3-9
DAP	Donor-Acceptor Pair	4-8
MOCVD	Metal-Organic Chemical Vapor Deposition	7-1

Abbreviation		Page
SEM	Scanning Electron Microscope	7-1
TES	Two-Electron Satellite	7-10
MIS	Metal–Insulator–Semiconductor	8-10
FM	Ferromagnetic	A-2
AFM	Antiferromagnetic	A-2
LSDA	Local Spin Density Approximation	A-2
LMTO-TB	Linear Muffin-Tin Orbital–Tight Binding	A-5
CLMBE	Combinatorial Laser Molecular Beam Epitaxy	A-6
MR	Magnetoresistance	A-6
RF	Radio Frequency	A-7
LHe	Liquid Helium	A-8
LMBE	Laser Molecular Beam Epitaxy	A-8
RTA	Rapid Thermal Annealing	A-8
VSM	Vibrating Sample Magnetometer	A-9
ECR	Electron-Cyclotron-Resonance	A-11
EHE	Extraordinary Hall Effect	A-12

HIGH-TEMPERATURE FERROMAGNETISM IN TRANSITION METAL IMPLANTED WIDE-BANDGAP SEMICONDUCTORS

I. Introduction

1.1 Motivation

The future miniaturization of electronic devices will require the electronics industry to cease relying solely on the charge of a carrier to store and convey information, and to look also at the spin degree of freedom [137]. The term “spintronics” (spin transport electronics) has come to encompass all electronics in which exploitation of electron spin is important to device operation [87]. Important new spintronic applications may include quantum computation [22] with rapidly reprogrammable logic [92] and quantum communication [18]. The realization of room-temperature spintronics will also improve the existing state of data storage by increasing processing speed, increasing integration density, decreasing power consumption, and eliminating memory volatility [86–88, 137]. Practical spintronics will also allow the fabrication of spin transistors and optical emitters with controlled polarization [87, 88] as well as next generation sensors [24, 28, 86]. Of particular interest to the Department of Defense (DoD) is the fact that spintronic devices also show resistance to radiation effects [138].

Clearly, the advent of the devices described above will contribute to the Air Force’s and DoD’s core competency of information superiority. Information superiority is enhanced by any technology that improves our ability to collect, process, and disseminate information without interruption [129, 130]. The capabilities mentioned above will enhance the speed and efficiency of both ground- and space-based information systems as well as increasing reliability through non-volatility and radiation hardness [138].

Before spintronic devices can begin to improve our defensive posture in reliable and meaningful ways, however, the properties of the materials most likely to be used in their manufacture must be understood. Currently, some of the most promising materials for use in spintronic applications are gallium nitride (GaN) and zinc oxide (ZnO) semiconductors doped with transition metals (TMs) [27–30, 32, 37, 59, 87, 88, 94, 100, 102, 103, 117, 123, 128, 133, 134, 147].

1.2 Brief Background

1.2.1 Challenges

The viability of spintronic devices depends on technology that will allow efficient spin injection, spin-dependent and spin-independent transport, manipulation of spin and detection of spin states, and spin-polarized currents [22, 48, 87, 88, 133, 137]. Each of these needs has solutions in the exploitation of materials that exhibit magnetic semiconductor properties.

The aforementioned progress and innovation requires materials that exhibit the familiar semiconductor properties as well as magnetic properties that will interact with electron spin [32]. As a class, materials that meet the criteria of having both semiconductor and magnetic properties are referred to as diluted magnetic semiconductors (DMS). DMS materials such as (Ga,Mn)As have been available for some time [78], but practical spintronics will require operation outside of the cryogenic regime (120 K is the theoretical limit GaAs-based DMSs [28, 30]).

1.2.2 Current State of Research

The pursuit of a room-temperature magnetic semiconductor has already led researchers to dope ZnO and GaN with several different transition metals using various doping methods. The previous experiments are discussed more fully in section A.2. There have been many findings of magnetic hysteresis persisting well above room temperature, but it has recently become apparent that these findings may not hold

relevance for fabricating practical spintronic devices. The factors necessary for successful spintronic device fabrication are discussed more fully in section 2.2.5.

1.3 Problem Statement

Despite encouraging results, implanting ZnO or GaN with transition metals to produce magnetic semiconductors is far from being characterized to an extent that will allow engineering of magnetic properties. There is a marked lack of theoretical knowledge and several competing models attempting to explain DMS phenomena. Further work must be undertaken to refine theories of ferromagnetism in semiconductors by doping materials with a variety of transition metals. The effects of ion implantation for DMS fabrication also require further characterization, including investigation of annealing conditions subsequent to implantation. The variation of annealing conditions must be observed for a variety of implanted species in order to make meaningful comparisons of the magnetic properties of each DMS as well as to determine optimal annealing conditions for each dopant/material combination. Finally, the true presence of ferromagnetism and the interaction of charge carriers with the implanted magnetic species must be verified in order to mount an effective investigation. A study which addresses these questions is essential to the advancement of the material science upon which spintronics is based. Such a study is undertaken in the work presented here. The study encompasses several transition metals, using ion implantation exclusively and a thorough search of viable annealing temperatures for activating transition metals without causing clustering. The purpose of this search is not to determine which materials and processing methods will be useable in the manufacture of spintronic systems based on DMS material, rather the purpose is to determine whether ferromagnetism can be induced in wide-bandgap semiconductors in a way that will allow for their use in making and characterizing novel spintronic devices. With this goal in mind, the wisest use of time and resources is to perform preliminary testing, without multiple repetitions, on a variety of materials and processing methods to see which show the most promise. This lays the groundwork for

those that wish to fabricate devices or further test DMS materials, so that they know where their efforts are most likely to be rewarded.

1.4 Results of This Research

Magnetic hysteresis and the absence of spin-glass phases have been achieved by implanting transition metal ions into wide-bandgap semiconductors. In many of the materials tested, these magnetic effects persist to room temperature. This offers proof that ion-implanted wide bandgap semiconductors are a viable method for implementing practical spintronics. Among the most promising materials for creating spintronic devices using ion implantation are p -GaN:Mn, $\text{Al}_{0.35}\text{Ga}_{0.65}\text{N}:\text{Cr}$, epitaxial ZnO implanted with Mn, and Fe-implanted ZnO nanotips grown on sapphire. Some of the other samples, even though they are not mentioned as the most promising, show clear signatures of ferromagnetism. The work reported in subsequent chapters shows that there is a variety of options available for implantation-based fabrication of DMS material with ferromagnetism persisting to room temperature. As progress is made toward realizing practical spintronic devices, the work reported here will be useful for determining material combinations and implantation conditions that will yield the needed materials.

II. Background

2.1 Terminology

The following terms are used commonly in discussions of magnetism and magnetic materials. Their use varies in different contexts, so it is important to define the way in which they will be used in this document.

Diamagnetism: The tendency for an object to respond to a magnetic field by producing its own weak magnetic field antiparallel to the applied magnetic field. This phenomenon arises from a change in the electrons' orbital angular momentum in response to an applied magnetic field [55,80].

Paramagnetism: A reaction to an applied magnetic field in which matter subjected to the field produces a field parallel to the applied magnetic field. Pauli paramagnetism (also called free-electron paramagnetism) occurs because of an energy difference between spin states of free electrons in a system, and is independent of temperature [17]. Curie (also known as bound-electron) paramagnetism arises in solids due to the intrinsic dipole moment of atoms with incomplete electron subshells (*e.g.*, the transition metals) and is a strong function of temperature [127].

Superparamagnetism: A phenomenon that occurs when tiny particles of a ferromagnetic material are present in a host material. In the presence of an external magnetic field, the particles behave like a paramagnetic ion but, due to interactions and a partially-filled *d*-shell, have an unusually large magnetic moment [106]. In field-dependent measurements of superparamagnetic systems, saturation and a large magnetic response are still observed, but hysteresis is not present because of the coherent rotation of the magnetic domains [12]. This type of response is illustrated in figure 2.1.

Ferromagnetism: The state of ordered alignment of magnetic moments in a material that gives it a net magnetization. This is illustrated in part (a) of figure 2.2 [80].

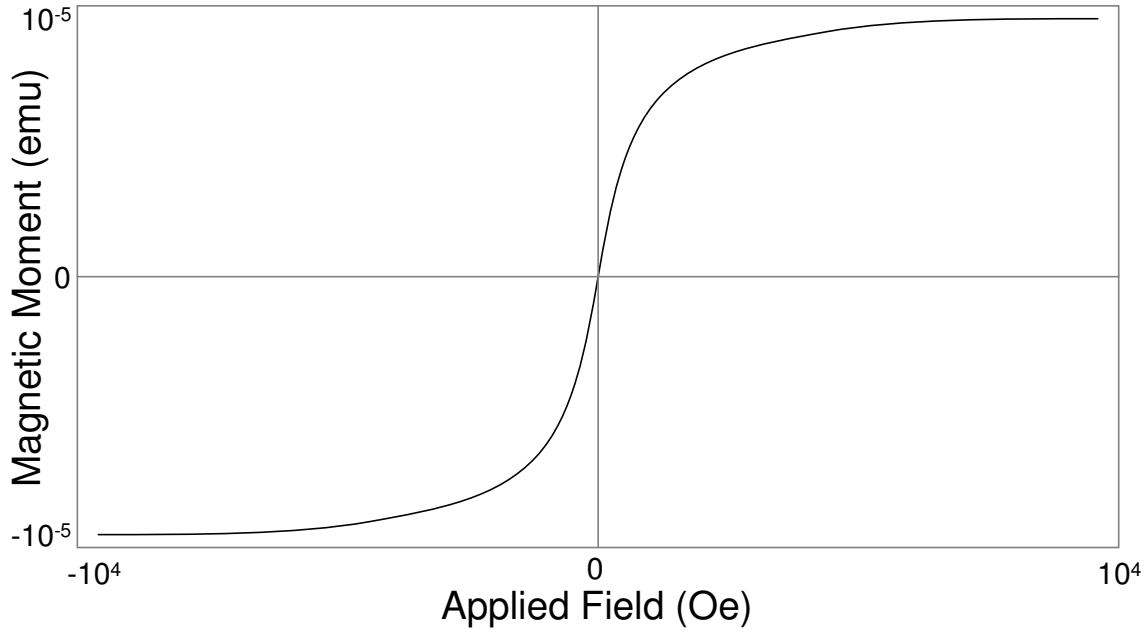


Figure 2.1 Illustration of the magnetic response of a superparamagnetic material while the applied magnetic field is varied. This is a theoretical illustration modelled after Bean [12].

Antiferromagnetism: The state of ordered alignment of magnetic moments in a material where adjacent domains are oriented antiparallel to one another resulting in zero net magnetization. This type of ordering is illustrated in figure 2.2(b) [80].

Ferrimagnetism: The state of ordered alignment of magnetic moments in a material where adjacent domains are oriented antiparallel but do not have the same magnitude, hence there is a net magnetization present. This type of ordering is illustrated in figure 2.2(c) [80].

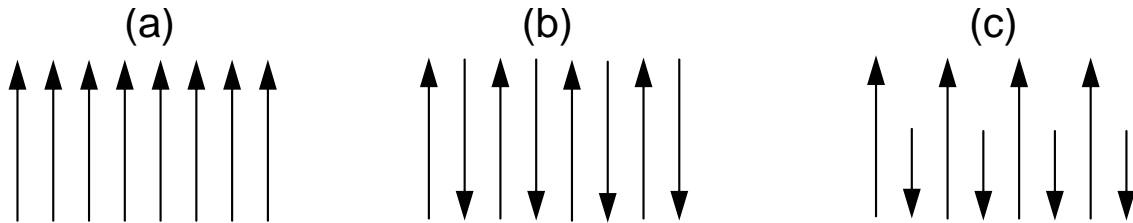


Figure 2.2 Local ordering of magnetic moments in (a) a ferromagnet, (b) an anti-ferromagnet, and (c) a ferrimagnet. After O'Reilly [80].

Curie Temperature (T_C): The temperature below which a material exhibits spontaneous magnetic ordering (Ferromagnetic, Antiferromagnetic or Ferrimagnetic properties) [55]. Above T_C , thermal effects cause the loss of magnetic ordering and materials revert to a paramagnetic state [127].

spin glass (SG): A material that draws its magnetic properties from the frustration of antiferromagnetic ordering. Simplistically, it is a case where three spins are present and the lowest energy ordering is antiferromagnetic—two of the spins can align antiparallel to one another, but the third cannot align itself antiparallel to either of the other two without aligning itself parallel (in a higher energy state) to one of the first two spins [81]. The presence of a spin-glass state is evident in magnetization-versus-temperature graphs where the zero-field-cooled (ZFC) trace diverges from the field-cooled (FC) trace and has a cusp at low temperatures [25]. The presence of a spin-glass phase can also be detected by a cusp in temperature-dependent susceptibility measurements [38].

(*s*)*p*-*d* Hybridization: The coupling of spins in the *d*-shell of transition metal dopants with the band electrons in the *s*- and/or *p*-shells of the host semiconductor. These interactions lead to the unique optical and transport properties of DMSs as well as ordered magnetic behavior [4]. Achieving (*s*)*p*-*d* hybridization is critical to the realization of DMS devices because such devices depend on free carriers with coordinated spins. The free carrier spins in the *s*- and *p*-orbitals of the host semiconductor are coordinated by interaction with the *d*-shells of the transition metal dopants [3].

Magnetic Circular Dichroism (MCD): The difference in absorption of left- and right-circularly-polarized light of a given photon energy. This preferential absorption is a direct indicator of the magnitude and polarity of Zeeman splitting as well as an indication that the (*s*)*p*-*d* exchange interaction is occurring in the sample [3].

Coercive Field (H_c): In field dependent magnetic measurements, H_c is the amount of magnetic field that must be applied in order to bring the sample's magnetization

back to zero after applying a magnetic field in the opposite direction. This quantity is illustrated in figure 2.3. In this research, the reported values of H_c will generally include the total width of the hysteresis loop at the point where the magnetic moment from the sample is zero ($-H_c$ to $+H_c$ in figure 2.3).

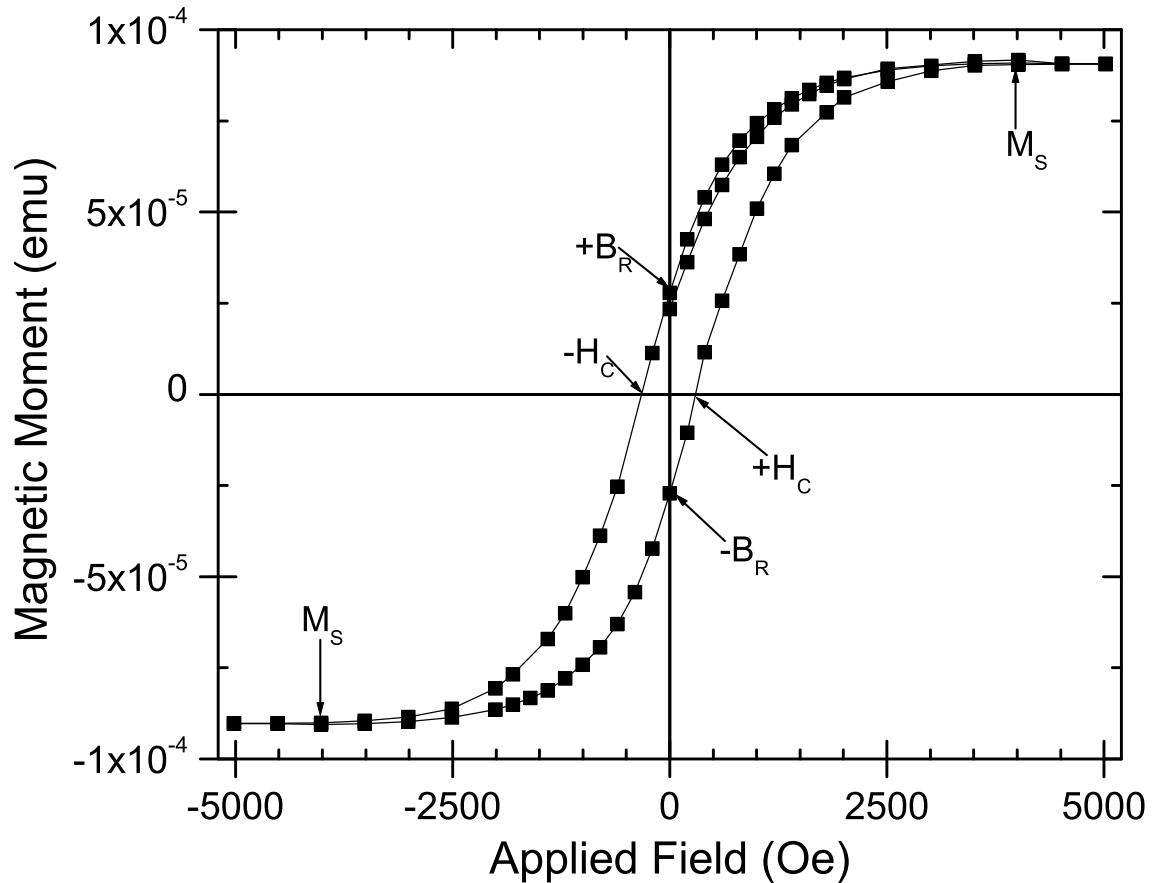


Figure 2.3 A magnetic hysteresis loop with the coercive (H_c) and remanent (B_R) fields and saturation magnetization (M_S) labelled for reference purposes. This magnetization-versus-applied-field measurement was taken from an epitaxial ZnO sample implanted with Fe and annealed at 625 °C for 10 minutes. The contribution of background diamagnetism was removed from this data.

Remanent Field (B_R): The magnetic moment that persists when the magnetic field applied to a sample is lowered to zero. B_R is labelled in figure 2.3 to illustrate the remanent field in a magnetic hysteresis measurement.

Saturation Magnetization (M_S): The maximum magnetization for a sample. This phenomenon occurs when every unpaired electron spin in the sample is aligned

[108]. In a variable field measurement (such as the one shown in figure 2.3), saturation is characterized by a constant magnetic moment emanating from the sample even when the applied magnetic field continues to increase. In this research, a change in magnetization of less than 2.5 % between applied magnetic field steps (usually 500 Oe) is used as a guide for determining saturation values.

Secondary Phase Formation: The phenomenon in doped compound semiconductors where the dopant bonds preferentially with one of the semiconductor's component atoms to form a new compound rather than substituting for one of the species comprising the compound semiconductor. Examples relevant to this work include GaMn, MnN, and ZnMn₂O₄. These and a variety of other compounds are ferromagnetic with high T_C and can cause false positives in magnetic measurements. Fortunately, prevalent secondary phases are detectable by X-ray diffraction (XRD).

Clustering: The tendency of implanted ions to form islands of pure dopant. Like secondary phase formation, this presents a problem when clusters of a material have a magnetic response that mimics or counters that of the DMS that is being fabricated. The likelihood of this phenomenon increases with increasing annealing temperature and with increasing implantation dose.

2.2 Spintronics Challenges

2.2.1 Spin Injection

The term spin injection refers to the ability to put carriers that already possess a spin polarization into a semiconductor device. One way to accomplish this is to pass current through a ferromagnetic DMS thereby causing spin-polarized carriers to be swept into the adjacent non-magnetic semiconductor. This approach is explored by Ohno *et al.* [79] using p-type GaMnAs as the ferromagnetic layer and a forward bias to inject spin-polarized holes into a light emitting diode (LED) structure. Figure 2.4a shows the structure of their device.

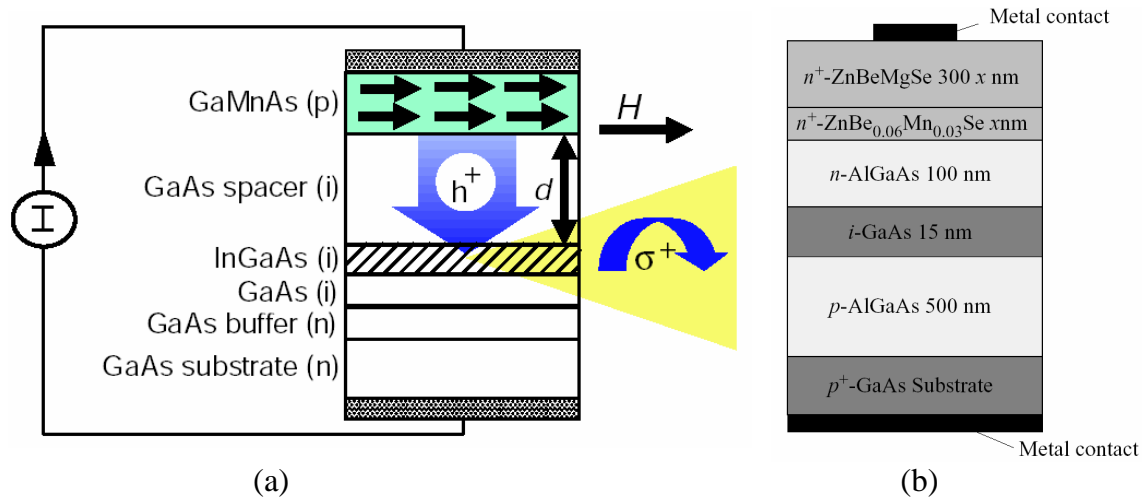


Figure 2.4 Configurations for semiconductor-based electrical spin injectors, (a) using a ferromagnetic DMS layer [79], and (b) leveraging giant Zeeman splitting [104].

Another semiconductor-based spin injector reported by Schmidt *et al.* [104] uses $\text{ZnBe}_{0.06}\text{Mn}_{0.03}\text{Se}$ as a spin-polarized carrier injector. The structure of this device is depicted in figure 2.4b. The $\text{ZnBe}_{0.06}\text{Mn}_{0.03}\text{Se}$ material exhibits giant Zeeman splitting (a separation in energy between formerly degenerate spin states [71, p. 173]) at low temperature under an external magnetic field. In this material, the large splitting leads to “relaxation of *all* conduction electrons into the lower Zeeman level.” Again, the now spin-polarized carriers, electrons in this case, are swept into the non-magnetic semiconductor. This giant Zeeman splitting alignment scheme has the added advantage that it can inject a completely spin-polarized current into the underlying material, whereas injection through a ferromagnetic material allows only partial spin polarization [104].

Spin-polarization in a semiconductor can also be induced optically. Circularly polarized light used to excite electrons out of the valence band will preferentially populate one spin polarization in the conduction band of a semiconductor [58].

2.2.2 Spin Transport

2.2.2.1 Spin-Dependent Transport

Carriers of a given spin may move about a material more easily than carriers of the opposite spin. This occurs because of an imbalance of spin populations at the Fermi level. The carriers that exist at the Fermi level will move about the crystal more easily so, if there is a greater density of states for one spin direction, carriers with their spin aligned in that direction should demonstrate greater mobility [92]. Since this differentiation between states is common in ferromagnetic materials, the use of a DMS to accommodate spin-dependent carrier transport is a natural development.

2.2.2.2 Spin-Independent Transport: Maintaining Spin Coherence

In some cases, it is desirable to move charge carriers around a material and preserve their organic spin without regard to its direction. An electric field will move these carriers by their charge, but normal spin relaxation mechanisms will still cause them to lose spin coherence [52]. By irradiating a two-dimensional electron gas (2DEG) in a semiconductor with a circularly polarized laser pulse, Kikkawa and Awschalom [51] were able to extend spin coherence times by two orders of magnitude while moving groups of spin-coherent electrons through a semiconductor. Future research must also address mechanisms for extending spin lifetime in a DMS without external intervention.

2.2.3 Spin Manipulation

Spin manipulation is the ability to change the magnetic state of a material or the spins of free carries in a material [133]. The ability to dynamically manipulate either of these properties is expected to allow progress in quantum computing by allowing for the advent of spin-based logic [22].

There are several ways in which spin manipulation can be realized. One way to accomplish this is by controlling the availability of holes in a material where the degree of ferromagnetic response is dependent on the presence of free holes [77]. Similar to

optical spin injection discussed in section 2.2.1, polarized optical pulses can also be used to rotate electron spins using the optical Stark effect [114].

2.2.4 Spin Detection

As discussed in section 2.2.1 and section 2.2.2.1, it is possible to discriminate between spin polarities with respect to carrier transport. This may be useful for the purpose of detecting carrier spin based on giant magnetoresistance (GMR) or tunneling magnetoresistance (TMR). Low magnetic coercivity electrical contacts with drastic differences in resistivity or tunneling probability based on spin polarization would enable measurements of current where the magnitude depends on the spin of the carriers being measured [133]. These measurements could then carry information in the same manner in which currents carry information in charge-based devices with the added dimension of spin information being included.

Other methods of spin detection, more practical for laboratory use than integrated electronics, are anomalous hall effect (AHE) measurements, superconducting quantum interference device (SQUID) magnetometry, vibrating sample magnetometry and detection of circular polarization in photoluminescence (PL), electroluminescence (EL) or cathodoluminescence (CL). These detection mechanisms fall more in line with measurement techniques and as such will be discussed in Chapter III.

2.2.5 Relevant Factors for Spintronic Device Fabrication

While it is important to demonstrate hysteresis in variable field measurements, the apparent ferromagnetism demonstrated thereby can have sources other than the perfect formation of a DMS. These other sources include clustering, secondary phase formation, or any other fabrication outcome which does not produce *sp-d* hybridization. Interaction between the transition metal dopant and the conduction or valence band of the semiconductor is necessary for spin injection, spin manipulation, and spin-dependent optical emission. Hybridization is the process that allows the charge carriers in the semiconductors to interact with the partially filled *d*-orbital of the tran-

sition metal dopant. Therefore, detection of *sp-d* interaction is necessary to verify the usefulness of DMS materials for spintronic device fabrication.

2.3 Promising Materials

Although many transition-metal-doped semiconductor materials exhibit magnetic properties, particularly at cryogenic temperatures, wide bandgap materials show the greatest potential to allow T_C to rise above 300 Kelvin (K). This is illustrated graphically in figure 2.5, where the results of T_C calculations are presented for a variety of semiconductors doped with Mn. Theoretical calculations have also been performed with other transition metal dopants as discussed in appendix A.1.

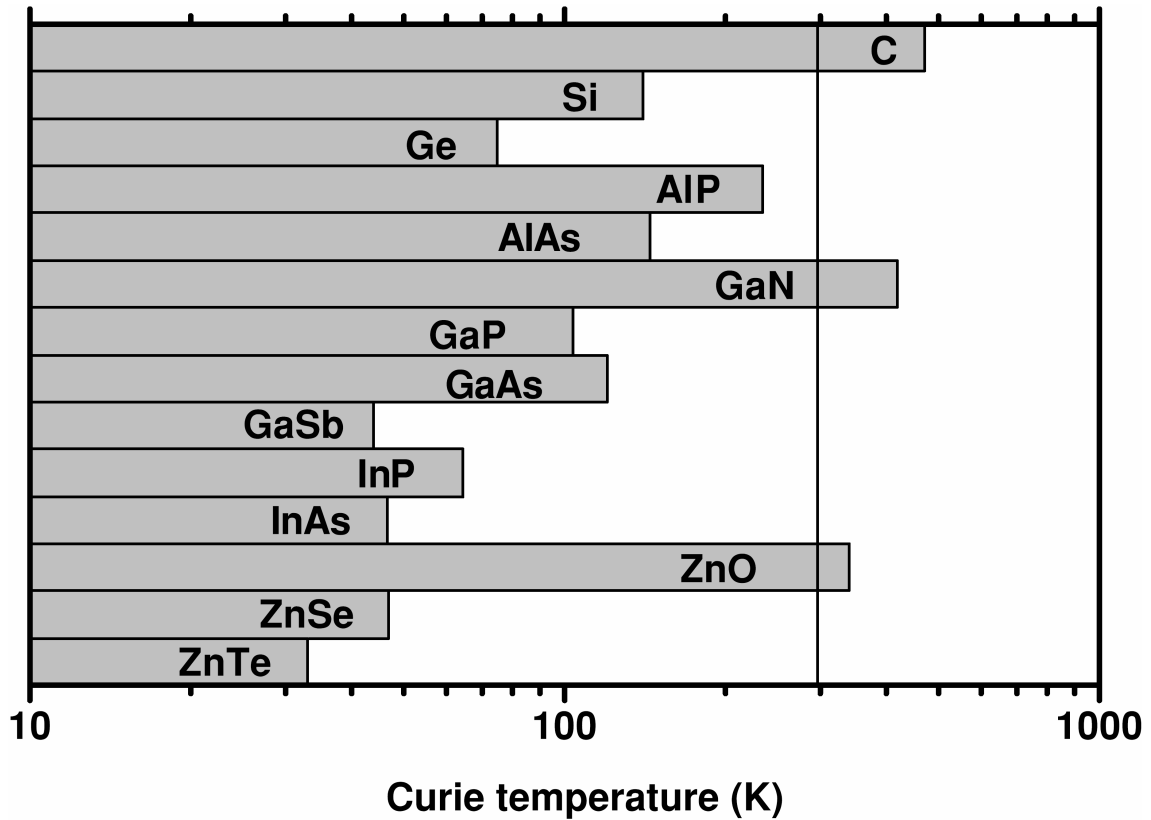


Figure 2.5 Computed values of the Curie temperature (T_C) for various p-type semiconductors containing 5% Mn and $3.5 \times 10^{20} \frac{\text{holes}}{\text{cm}^3}$ [30].

As shown in figure 2.5, wide bandgap materials tend to show the highest propensity for room temperature ferromagnetism. This is verified by experiment as discussed

in section 2.4, appendix A.2, and chapters IV through VII. The reason for high- T_C potential in wide bandgap materials is because lighter elements on the anion sublattice allow for greater p - d hybridization and reduce spin-orbit coupling [28,29].

2.4 Prior Art

There have been a number of experiments reported and theoretical calculations made concerning the implantation of transition metals into ZnO and GaN. A comprehensive list and a summary of these experiments and calculations are given in Appendix A, and a brief recapitulation of the experiments most similar to the ones reported in this dissertation is given here. A brief summary of the results reported in chapters IV through VII is also given in Appendix C.

2.4.1 Relevant Experiments Involving ZnO

Chromium: Several attempts to grow $\text{Zn}_{1-x}\text{Cr}_x\text{O}$ ($x = 0.012-0.25$) failed to demonstrate magnetic ordering [5, 47, 120, 128]. Satoh and Kobayashi did produce ferromagnetic $\text{Zn}_{0.7}\text{Cr}_{0.3}\text{O}$ with $T_C = 400$ K [102] as evidenced by SQUID measurements. This latter experiment used pulsed laser deposition (PLD) to grow the Cr-doped ZnO. In the literature surveyed, Cr ion implantation has not been reported. In this research, Cr-implanted ZnO has demonstrated ferromagnetism by coercive fields above 200 Oe persisting to room temperature for several annealing conditions.

Manganese: Several attempts to demonstrate FM ordering in $\text{Zn}_{1-x}\text{Mn}_x\text{O}$ were initially unsuccessful [20, 36, 47, 103, 120, 128, 142]. Several magnetic circular dichroism (MCD) measurements showed indications of spin splitting due to sp - d exchange interactions in $\text{Zn}_{1-x}\text{Mn}_x\text{O}$ ($x < 0.35$) [5, 37]. There were also successes reported for $\text{Zn}_{1-x}\text{Mn}_x\text{O}$ with FM ordering up to a temperature of 300 K [44, 50, 53]. Interestingly, the best results of this bunch are reported by Heo *et al.* who used ion-implantation to dope their samples with Mn. The work presented here shows FM ordering of Mn-implanted ZnO above 300 K under

proper annealing conditions. This research also reports implantation of Mn into ZnO nanotips. Although it is similar to work reported by Ip *et al.* [46], there are also several elements that differentiate this research from Ip's: larger coercive fields, a variety of different substrates, different annealing conditions, and a more regular structure to the nanotips (different ZnO growth methods).

Iron: So far, films of $\text{Zn}_{1-x}\text{Fe}_x\text{O}$ have shown no evidence of ferromagnetism [47] nor shown AFM ordering at low temperature [142]. Neither of these reports indicate the use of ion implantation to fabricate $\text{Zn}_{1-x}\text{Fe}_x\text{O}$. In this research, ion implantation yielded samples with strong coercive fields at low temperatures that persisted, although in a diminished state, to 300 K. Furthermore, the work presented here is the first to report Fe implantation into ZnO nanotips. The results of this implantation were encouraging, but failed to show an optimal annealing temperature as clearly as the Fe-implanted epitaxial ZnO.

Nickel: Tabata, Ueda, *et al.* did not achieve ferromagnetism in their films of $\text{Zn}_{1-x}\text{Ni}_x\text{O}$ ($0.05 < x < 0.25$) [120, 128]. The MCD spectrum of $\text{Zn}_{0.970}\text{Ni}_{0.030}\text{O}$ indicated strong *sp-d* interactions [5]. At very low temperatures, FM ordering was shown in $\text{Zn}_{1-x}\text{Ni}_x\text{O}$ ($x = 0.03 - 0.25$) and superparamagnetism maintained to 300 K as reported by Wakano *et al.* [134]. Several reports of ferromagnetism persisting to 350 K for polycrystalline films formed from Ni-doped ZnO quantum dots as a precursor [93, 105]. Again, the work presented in this document is unique because there are no reports of ferromagnetism demonstrated in $\text{Zn}_{1-x}\text{Ni}_x\text{O}$ formed by ion implantation. This research demonstrates magnetic hysteresis with a coercive field width of 400 Oe persisting to 300 K in Ni-implanted ZnO annealed at 725 °C for 10 minutes.

2.4.2 Relevant Experiments Involving GaN

Chromium: Several groups have reported ferromagnetism slightly below [85], as well as above, room temperature [43, 62, 147] based on magnetization versus magnetic field ($M-H$). Lee *et al.* were able to fabricate GaCrN with ferromagnetism

persisting to 320 K by ion implantation [62]. Lee's group also reports that clustering and secondary phase formation were excluded as sources of the reported magnetic ordering. In the research reported in this document, ion implantation and a variety of annealing conditions are used to produce GaCrN samples with coercive field widths greater than 200 Oe at 300 K.

Manganese: Kuwabara *et al.* found a lack of ferromagnetic behavior in their samples of $\text{Ga}_{1-x}\text{Mn}_x\text{N}$ ($x < 0.02$) which they blame on a deficiency of free carriers [59]. Zajac *et al.* report AFM ordering and paramagnetic behavior in their films of $\text{Ga}_{1-x}\text{Mn}_x\text{N}$ ($x < 0.1$) [144, 145]. The MCD spectra obtained by Ando *et al.* indicate significant *sp-d* exchange interactions in $\text{Ga}_{0.932}\text{Mn}_{0.068}\text{N}$ [4]. Several others report FM ordering in $\text{Ga}_{1-x}\text{Mn}_x\text{N}$ from cryogenic temperatures to just below room temperature [63, 83, 94, 111–113, 125, 126]. Further experiments showed T_C s at and above room temperature [40, 95, 117, 123], with the highest T_C estimated at 940 K (measured to 750 K) for $\text{Ga}_{0.91}\text{Mn}_{0.09}\text{N}$ [116]. Some of these high T_C results, however, have since been attributed to clustering, secondary phase formation, or faulty measurements. More recent experiments show that Mn ion implantation is a viable method for producing ferromagnetism in GaN and that it can be enhanced by co-doping with nitrogen [9]. This research demonstrates agreement with previous results by demonstrating H_c widths of over 200 Oe persisting to room temperature. The temperature-dependent data collected in this work verifies that a ferromagnetic phase is dominant.

Nickel: Pearton *et al.* report Ni-doping of GaN by ion implantation. They achieved ferromagnetism below 185 and 45 K for implant doses of 3×10^{16} and $5 \times 10^{16} \frac{\text{ions}}{\text{cm}^2}$, respectively [90]. The research reported here finds room-temperature coercive field widths over 300 Oe for samples annealed at 25 °C higher temperature than those reported by Pearton *et al.* Unfortunately, magnetization-versus-temperature measurements show divergence of field-cooled (FC) and zero-field-cooled (ZFC) measurements at low temperature, which suggests that the results may be due to a spin-glass state.

2.4.3 Relevant Experiments Involving $\text{Al}_{0.35}\text{Ga}_{0.65}\text{N}$

Chromium: Frazier *et al.* report separation and low-temperature tracking of FC and ZFC measurements in $n\text{-Al}_{0.38}\text{Ga}_{0.62}\text{N}$ implanted with Cr and annealed at 1000 °C for 2 minutes. This indication of ferromagnetism was not duplicated in $p\text{-Al}_{0.13}\text{Ga}_{0.87}\text{N}:\text{Cr}$ and coercivity values were not reported [35]. The research reported here shows that Cr-implantation into $\text{Al}_{0.35}\text{Ga}_{0.65}\text{N}$ does produce magnetic hysteresis with coercivity increasing with annealing temperature, but it is troubling that, of the samples measured, the greatest coercive fields were measured in the as-implanted (unannealed) sample.

Manganese: The University of Florida DMS group has reported successful fabrication of ferromagnetic $p\text{-Al}_{0.13}\text{Ga}_{0.87}\text{N}:\text{Mn}$ by ion implantation. They report a coercivity of ~ 60 Oe for samples annealed at 1000 °C for 2 minutes [35,89]. The research reported in this dissertation shows that coercivities greater than 350 and 140 Oe are achievable at 5 and 300 K, respectively, for optimal annealing conditions, which are found to be lower temperature and longer time than those used by Frazier *et al.* [35].

Nickel: There are no reports available concerning doping AlGa_{0.65}N with Ni. This research shows clear hysteresis at both 5 K and room temperature for Ni-implanted $\text{Al}_{0.35}\text{Ga}_{0.65}\text{N}$ due to a ferromagnetic phase indicated by temperature-dependent-magnetization measurements. This research also shows sensitivity of the coercive field strength to annealing conditions.

2.5 Theory of Dilute Magnetic Semiconductors

There are two competing explanations for the occurrence of ferromagnetism in transition metal (TM) doped semiconductors. The first, called the mean-field theory or effective-medium theory, explains the phenomenon by attributing the coordination between TM ions in DMS material to the presence of a hole gas. This theory also necessarily assumes long-range spin–spin coupling among the TM dopant atoms [89].

A schematic illustration of this is shown in figure 2.6(a). Equation (2.1) is the formula for calculating the Curie temperature (T_C) in a material using the effective-medium theory [26].

$$T_C = \left[S(S+1)N_0I^2A_F\rho_d(\epsilon_F) \int d\zeta \tilde{x}(\zeta)|\varphi_0(\zeta)|^4/12k_B \right] - T_0. \quad (2.1)$$

In equation (2.1), S represents the value of the TM spins, N_0 is the number of spins participating in the interaction, $T_0 > 0$ and $\tilde{x} < x$ to account for antiferromagnetic interactions, the exchange integral $I \equiv \alpha$ or β depending on the band, the Fermi liquid parameter $A_F \geq 1$, ρ_d is the density of states at the Fermi level (ϵ_F), the envelope function of the relevant subband is represented by $\varphi_0(\zeta)$, and k_B is Boltzmann's constant.

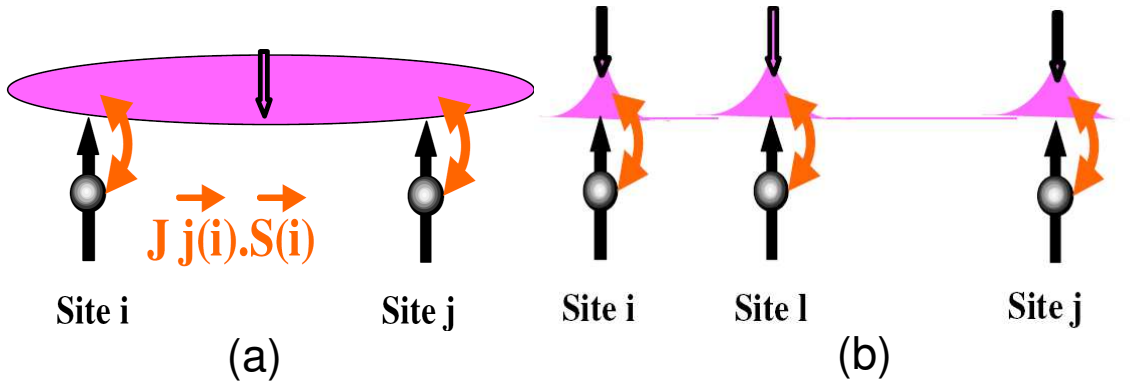


Figure 2.6 Illustration of the two most prevalent explanations for ferromagnetism in transition metal implanted semiconductors: (a) the mean-field theory; (b) the bound magnetic polaron theory [89].

The second class of theories used to explain ferromagnetism in semiconductors are based on the bound magnetic polaron (BMP) model. The BMP model, illustrated in figure 2.6(b), allows for magnetic coordination between TM atoms without a high concentration of free holes in the material. Carriers localize around TM atoms or clusters thereof, forming a BMP. As the material's temperature is lowered, these BMPs enlarge to the point where they overlap (at the Curie temperature) and facilitate magnetic coordination between the TM dopants [89]. In the case of BMP theory,

T_C can be predicted by equation (2.2).

$$T_C = \frac{S(S+1)}{3k_B}(12I_1 + 6I_2). \quad (2.2)$$

In equation (2.2), I_1 and I_2 represent exchange constants between nearest and next-nearest neighbors, respectively, k_B is Boltzmann's constant, and S is the value of the localized spins [68].

Some of the work reported in this document tends to support the BMP theory. The primary evidence supporting the BMP theory is the fact that ferromagnetism is observed in material that is not p -type. The $\text{Al}_{0.35}\text{Ga}_{0.65}\text{N}$ and ZnO are not doped with donors or acceptors, so they are most assuredly n -type [67, 69]. Ferromagnetic ordering in n -type material is also widely reported in the literature, with specific examples available in appendix A.2. This work does not, however, necessarily contradict the mean-field models of ferromagnetism. The magnetic ordering in p -GaN is one evidence that free holes have some role in coordinating ferromagnetism.

2.6 Conclusion

From the literature produced concerning wide-bandgap spintronics, it is clear that there is research remaining at all levels from basic physics to device production that will benefit from further investigation. This review demonstrates the need for the research described in this document. It also informs the reader of the physics pertinent to this area of study and the challenges that DMSs will allow us to overcome.

III. Experimental Methods

The following discussion details the methods used to fabricate and characterize the transition-metal-implanted semiconductors investigated in this research.

3.1 Ion-Implantation

Ion implantation is a relatively simple and inexpensive method of doping semiconductors after growth. It allows the growth of a thin film of the desired semiconductor without the added complication of doping during growth. This is particularly important for transition metal doping because the tendency for these materials to cluster restricts growth temperature. Ion implantation avoids these problems by allowing a substrate, thin film, or nanostructure to be grown under optimal conditions and then have energetic, charged atoms of the desired dopant introduced through the surface of the material. As these implanted ions enter the material they will dope, they lose some of their energy through collisions with the nuclei and electron clouds of atoms in the semiconductor crystal lattice. Electronic collisions do not displace atoms in the host semiconductor crystal because the resulting energy is dissipated by exciting electrons to higher energy levels, creating electron-hole pairs, or ionizing an atom in the host crystal. Nuclear collisions cause damage to the lattice, but this damage can be repaired by annealing as discussed in section 3.2 [119].

All ion implantation executed in conjunction with this research was performed by Implant Sciences Corporation (Wakefield, MA). The doses of implanted ions, which were varied for the different samples, are shown in table 3.1. Some implantation conditions were uniform for all samples: the ions were implanted with an energy of 200 keV and the implant was performed at room temperature (~ 300 K).

Table 3.1 Ion doses, in $\frac{\text{ions}}{\text{cm}^2}$, for the transition metals implanted in the various semiconductor materials studied in this research. All implantations are performed at 200 keV and room temperature.

Species Implanted	Material					
	<i>p</i> -GaN	Al _{<i>x</i>} Ga _{1-<i>x</i>} N <i>x</i> = 0.35	ZnO Film	ZnO nanotips on		
				Quartz	Sapphire	Glass
Fe			5×10^{16} †	5×10^{16}	5×10^{16}	5×10^{16}
Mn	5×10^{16}	5×10^{16}	5×10^{16} †‡	5×10^{16}	5×10^{16}	5×10^{16}
Cr	5×10^{16}	5×10^{16}	5×10^{16} †			
Ni	3×10^{16}	3×10^{16}	3×10^{16} †			

†First epitaxial ZnO growth from Rutgers University

‡Second epitaxial ZnO growth from Rutgers University

3.2 Thermal Annealing

As mentioned in section 3.1, annealing is necessary to remove damage caused by ion implantation.

3.2.1 Annealing of *p*-GaN and Al_{0.35}Ga_{0.65}N

The nitride samples were annealed in an Oxy-Gon annealing furnace. Nitrogen gas (N₂) was flowed at a rate of $2 \frac{\text{L}}{\text{min}}$ in order to minimize loss of nitrogen from the *p*-GaN or Al_{0.35}Ga_{0.65}N crystal. These losses were further minimized by the use of a 500-Å cap of aluminum nitride (AlN) on the Al_{0.35}Ga_{0.65}N samples which was not removed until after annealing. To prevent damage during annealing, the samples were wrapped face-to-face with tantalum (Ta) wire. Each *p*-GaN sample had the epitaxial *p*-GaN layer pressed against the AlN cap layer of one of the Al_{0.35}Ga_{0.65}N samples implanted with the same transition metal. The samples were then bound together using Ta wire to ensure that the samples would act as proximity caps for one another during the heat treatment.

3.2.2 Annealing of ZnO

The ZnO samples were annealed in a Mini-M tube furnace manufactured by Blue M. Oxygen gas (O₂) was flowed at a rate of 25 standard cubic centimeters per minute (sccm) during all annealing to minimize damage caused by the outgassing of

oxygen from the ZnO crystal lattice. Because many of the ZnO samples were nanotips, they could not be annealed face-to-face in a proximity cap configuration because of the likelihood that the samples would bond during annealing and the high possibility of damage to the nanotips resulting from binding the samples in this configuration. The epitaxial ZnO samples could have been annealed using a proximity cap, but this was not attempted because satisfactory results were obtained using only an O₂ overpressure to minimize annealing damage.

3.3 Superconducting Quantum Interference Device (SQUID) Magnetometry

The premier technique for determining the magnetic properties of a sample is by using a Superconducting Quantum Interference Device (SQUID) for magnetic characterization. This is evidenced by the preponderance of research cited in sections 2.4 and A.2 in which SQUID magnetometry provided evidence of magnetic ordering in the samples being studied.

SQUID magnetometers operate by exposing a pick-up ring of superconducting material containing one or more Josephson junctions to a magnetic field. A simple schematic of such an apparatus is depicted in figure 3.1(a). The Josephson junction is a region of material that is not intrinsically superconducting, but is thin enough that tunneling effects cause the ring to behave as though it were composed entirely of superconducting material. The superconductivity of the junction, however, is not as robust as that of the bulk superconductor: its ability to emulate a superconductor ceases with small magnetic fields and low current density [49]. When a superconducting ring is exposed to a magnetic field, a current begins to circulate about the ring, but no magnetic flux is admitted to the center of the ring. If the ring contains a Josephson junction and the magnetic field is sufficiently strong, this circulating current will exceed the critical current of the junction and the junction will revert to normal, non-superconducting behavior. When this happens, one magnetic flux quantum ($\phi_0 = \frac{h}{2e} = 2.07 \times 10^{-15}$ Wb) is admitted to the ring, which then decreases the circulating current and allows the junction to become superconducting once again. In a strong

magnetic field, this process repeats itself causing a periodic variation in the current circulating around the loop. By monitoring this variation, it is possible to detect extremely small changes in the magnetic field to which the loop is exposed [127].

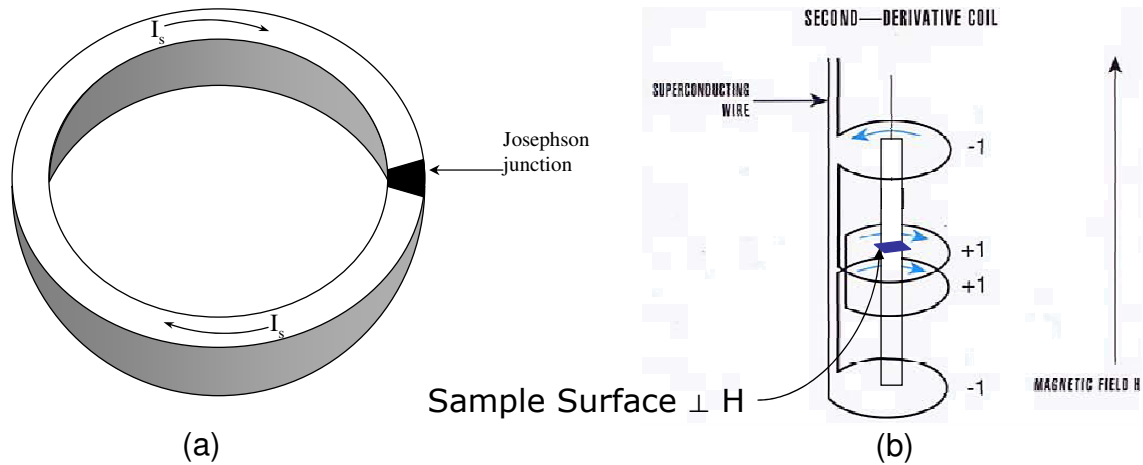


Figure 3.1 (a) Simple schematic of a SQUID pick-up loop used for detecting weak magnetic fields and small changes in magnetic fields. After Turton [127]. (b) A second-order gradiometer made of superconducting wire [70]. This is the configuration used in Quantum Design’s Magnetic Property Measurement System, which is the system used to make the magnetic measurements reported in this research.

In the SQUID system used for this research, the sample is moved through a superconducting second-order gradiometer which reduces the noise detected due to fluctuations in the applied magnetic field. A schematic of a second-order gradiometer is depicted in figure 3.1(b). The Josephson junction is part of the superconducting loop that forms the gradiometer and is located inside a magnetic shield approximately 11 cm below the magnet that provides the applied field on the sample. This configuration shields the SQUID detector from the magnetic field applied perpendicular to the surface of the sample and allows the SQUID output voltage to function as a highly linear conversion of the current induced by the sample in the superconducting gradiometer. This set-up allows detection of magnetic moments on the order of one-thousandth of a flux quantum [70]. By comparison, the earth’s magnetic field through a $5 \text{ mm} \times 5 \text{ mm}$ area (the typical area of samples used in this study) is about 500 thousand flux quanta.

In the experiments reported with this work, variable field or magnetic hysteresis measurements were made by stepping the applied magnetic field from zero to 2 kOe in steps of 200 Oe, then from 2 kOe to 5 kOe in steps of 500 Oe, and in steps of 1000 Oe to a maximum field of 10 kOe for selected samples. All magnetic fields are applied perpendicular to the sample surface. This allows for high resolution measurement near the origin where coercive and remanent fields are determined as well as a faster search for saturation and high-field behavior. For these measurements, the magnetic field is swept at a constant rate and allowed to slightly overshoot the target field in order to avoid oscillation at the stopping point.

The variable-temperature measurements were made by cooling the sample to 5 K with no applied field for the zero-field-cooled (ZFC) measurements. A magnetic field of 500 Oe is then applied perpendicular to the surface of the sample to enhance its magnetic signature and make the measurements less noisy. The temperature is then swept to 50 K at a rate of $2.5 \frac{\text{K}}{\text{min}}$ with measurements taken every 5 K. From 50 to 350 K, the temperature is swept at a rate of $7.5 \frac{\text{K}}{\text{min}}$ with measurements taken every 10 K. Upon reaching a temperature of 350 K, the sample is cooled back to 5 K under an applied magnetic field of 500 Oe with measurements being taken as described above for the respective temperature ranges in order to collect field-cooled (FC) data. The temperature sweep rates are also varied identically for the FC and ZFC measurements in the respective temperature ranges. In general, the measurements occur quickly enough that the temperature sweep is not stopped for the magnetization measurement. However, some of the samples with weaker signals require that the magnetization measurements be taken in “settle” mode, where the temperature is allowed to stabilize at the values discussed above and the measurement is completed before the temperature is swept to the next value.

3.4 *Optical Characterization*

3.4.1 *Cathodoluminescence*

Cathodoluminescence (CL) measurements are performed by exciting a sample with an electron beam and then observing the spectrum emitted by the sample. The exciting electron beam is emitted from a Kimball Physics EMG-12 Electron Gun, accelerated by a potential of 10 kV supplied by a Kimball Physics EGPS-12 power supply, and focused to a spot 600 to 850 μm in diameter. For the measurements in this study, a beam current of approximately 50 μA is used. The chamber containing the samples under test and the electron gun is evacuated to a pressure of 7×10^{-8} Torr (T). The samples were cooled to approximately 6 K using a closed cycle helium compressor and a “cold finger.” The sample temperature was controlled and measured using a Lakeshore 330 Temperature Controller. The radiation leaving the samples was captured by the optics shown in figure 3.2 and focused into a Spex 500M $\frac{1}{2}$ -meter spectrometer with 500- μm -wide entrance and exit slits. The spectrometer steps through the desired wavelength range in 2- \AA steps transmitting the captured light at each wavelength into a GaAs photomultiplier tube (PMT) manufactured by Products for Research, Inc., biased at 1500 V, and cooled to a temperature of -30 to -40 $^{\circ}\text{C}$ with liquid nitrogen.

In this research, CL provides much of the same data as photoluminescence (PL). Unlike PL, there is little feedthrough from the excitation source, so there is far less noise in the resulting spectral measurements. CL measurements, however, are not appropriate for ZnO nanotips for two reasons. The primary reason for this restriction is the need for a grounding bar to keep excess electrons from charging the sample and thus deflecting incoming excitation electrons. This grounding bar would likely crush the nanotips on samples so grown. The low conductivity across the sample’s face (due to the fact that the nanotips are independent columns on an insulating substrate) would likely cause the tips to charge and either damage the material or deflect incoming excitation electrons.

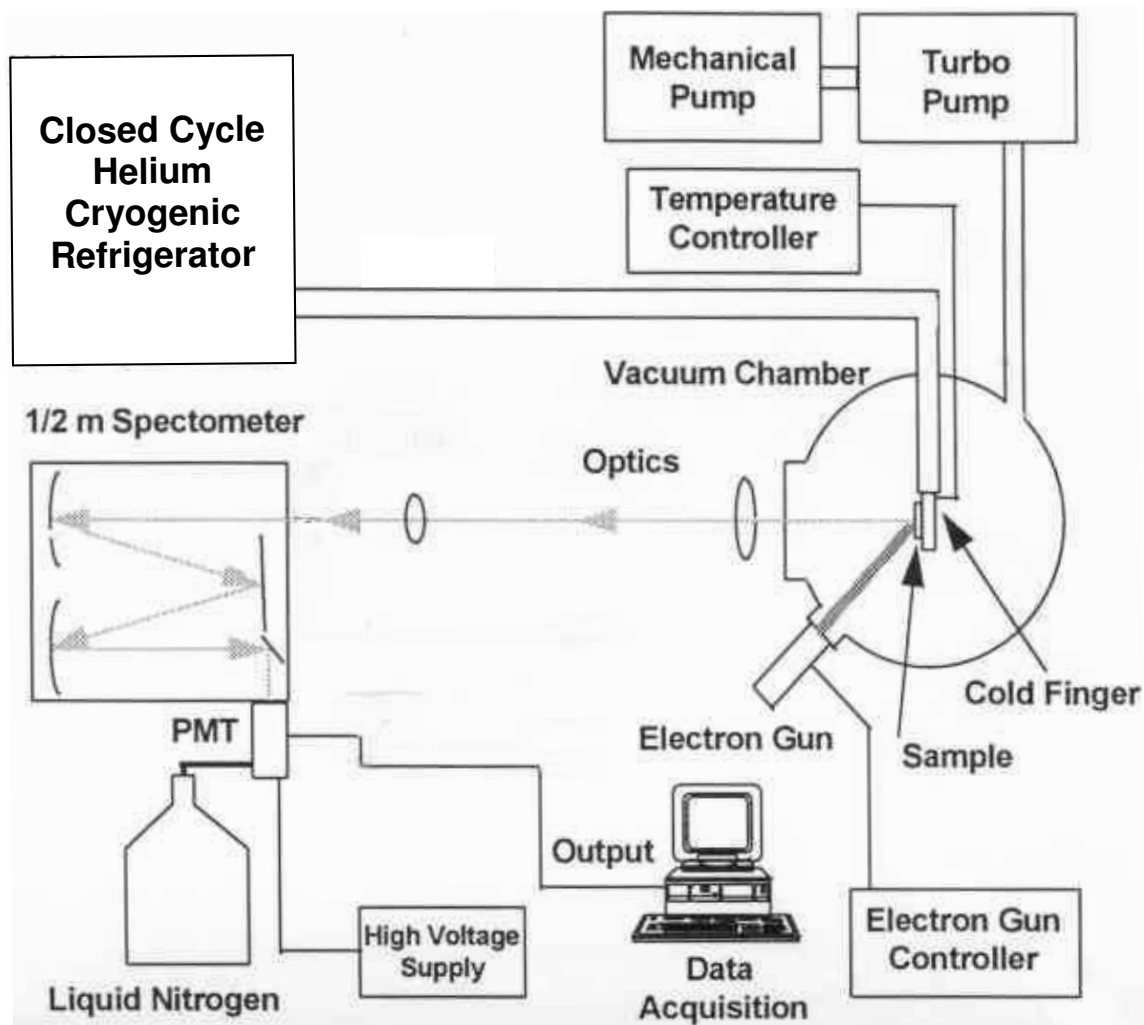


Figure 3.2 Schematic diagram of the cathodoluminescence measurement apparatus used to collect optical data.

3.4.2 Photoluminescence

The basic premise of PL is that optical radiation with a photon energy greater than the bandgap of the semiconductor under study excites electrons from the semiconductor's valence band into the conduction band where the electrons cool and then return to the valence band or to an impurity energy level. When these electrons fall to lower energy levels, they may emit a photon with energy equal to that of the energy difference between an impurity energy level and the valence or conduction band. A diagram of this system is presented in figure 3.3.

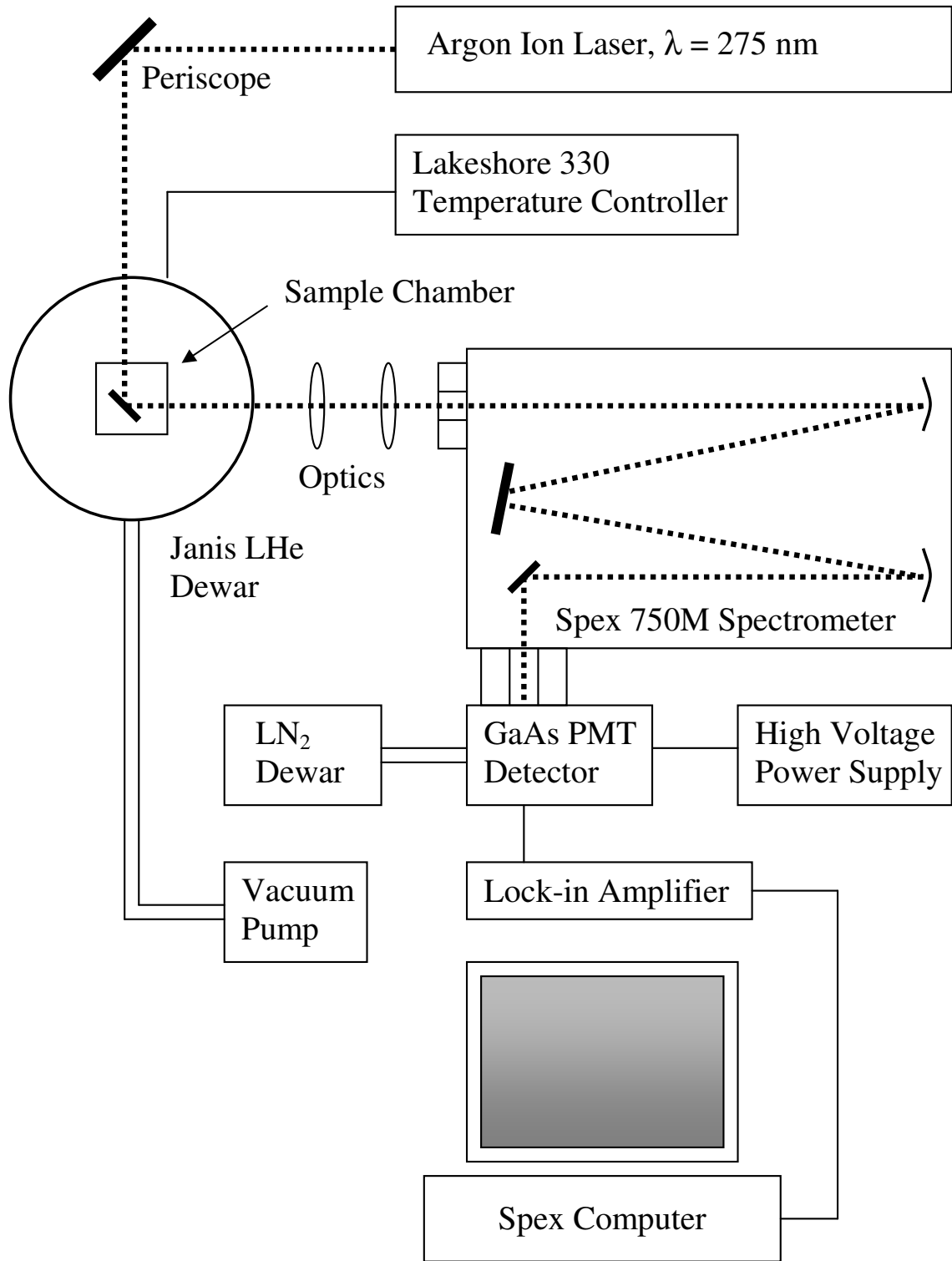


Figure 3.3 Schematic diagram of the photoluminescence measurement apparatus used to collect optical data.

In the work reported here, PL was performed with a SpectraPhysics 2085-20 argon-ion laser tuned to an emission wavelength of 275 nm. The laser power transmitted to the sample is approximately $\frac{1}{2}$ Watt. The sample is cooled with liquid helium (LHe) in a Janis 100T optical cryostat to a temperature between 2.1 and 300 K, depending on how much LHe is allowed into the sample chamber and the settings of the Lakeshore 330 temperature controller. The radiation emitted from the sample under test is collected by a system of lenses and focused into a Spex 750M grating-based spectrometer. The spectrometer sorts (by energy) the photons emitted by the sample and sends them into a Products for Research, Inc. GaAs photomultiplier tube PMT cooled to -30 to -40 °C, which records the emission intensity for each photon energy.

The information gleaned from PL measurements shows the effectiveness of annealing in recovering the damage induced by ion implantation. The PL plots also show the relative density of radiative defects or impurities and can qualitatively indicate the presence of non-radiative defects.

3.5 X-Ray Diffraction

X-ray diffraction (XRD) is a technique that is useful for detecting the presence of secondary phases or clusters in ion implanted semiconductors. In this analysis technique, a sample is irradiated with collimated X-rays which are then diffracted at an angle based on the distance between atoms in the crystal [56, Ch. 3]. In order to obtain these measurements, the sample and the X-ray detector are rotated so as to keep incident and reflected beam angles equal with respect to the sample surface. This setup is illustrated in figure 3.4. Whenever the crystal planes align so that the distance between crystal planes leads to constructive interference, a strong reflection or XRD peak occurs [41, Sec. 9.6]. The measurements reported in this research were made by collaborators at Rutgers University, so comprehensive characterization of all samples at all annealing conditions is not available.

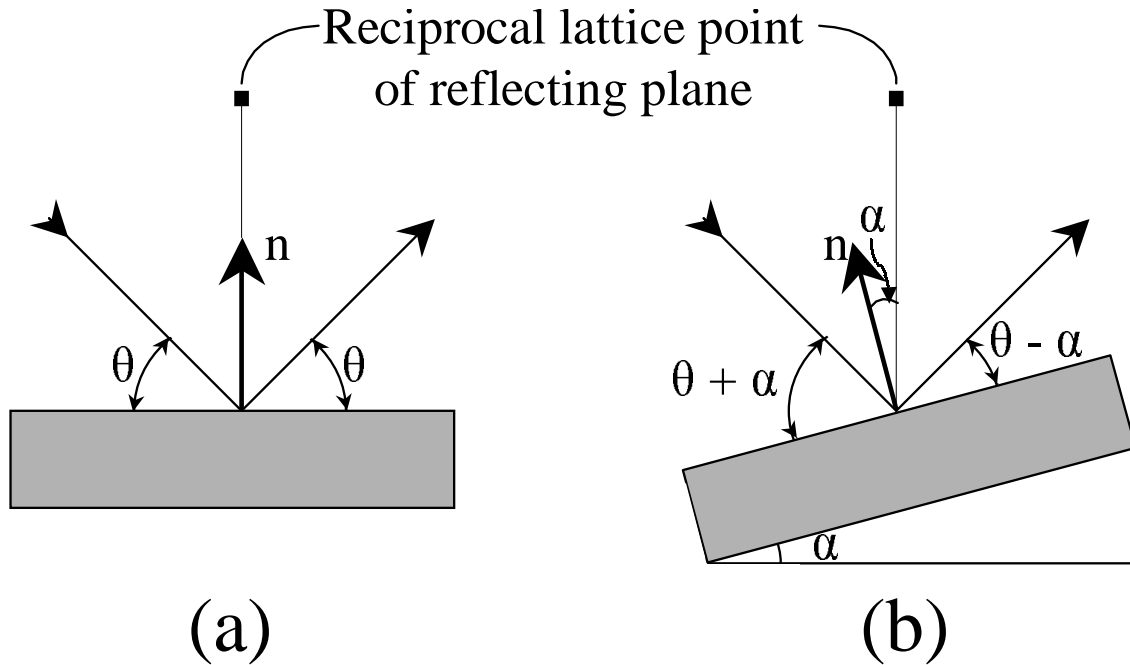


Figure 3.4 Configuration for XRD measurements on a single crystal thin film when: (a) the reciprocal lattice vectors of the reflecting planes are parallel to the surface normal; and (b) the asymmetrical case where reciprocal lattice vectors are aligned at an angle α to the sample surface normal (after Hammond [41, Fig. 9.16]).

The angular location of XRD peaks reveals the interatomic lattice spacing and structural information about, the lattice and, hence, provides definite information concerning the lattice composition. The peaks recorded in an XRD measurement are compared with those of known substances (either measured or calculated) in search of a match in peak location, shape, and (to a lesser degree) intensity. This allows confirmation that the expected material is present as well as detection of any unwanted secondary phases such as those listed in appendix B [41, Sec. 10.3]. The presence of clusters, or precipitates, is most clearly indicated by broadening and symmetry loss in the XRD peaks. This corresponds to a distortion of the X-ray refraction at the reciprocal lattice points [10].

While PL tends to reveal the damage remaining after ion implantation and subsequent annealing, XRD is useful in identifying the resultant crystal structure after thermal annealing during which implantation damage is being repaired. The

absence of XRD features associated with secondary phases and clustering does not guarantee their total absence from the material, but it does help to preclude their dominance as a source of macroscopic magnetic properties, and is thus important to this research because it helps determine the source of the magnetic effects seen in these semiconductors.

IV. Characteristics of Transition Metal Implanted

p-type Gallium Nitride

A 1- μm film of GaN was grown on a buffer layer of AlN on sapphire. The GaN was *p*-doped by incorporating magnesium (Mg) during growth to a level which results in a free hole concentration of $3 - 4 \times 10^{17} \frac{\text{holes}}{\text{cm}^3}$ at room temperature. The growth was performed by EpiPlus (Kyonggido, Korea).

Transition-metal-implanted *p*-GaN showed signatures of ferromagnetism that were generally dependent on annealing conditions. This material shows some hope of providing room-temperature ferromagnetism for the fabrication of DMS-based devices. The strongest coercive and remanent fields were found in Ni-implanted *p*-GaN (section 4.3), but the results that were most consistently sensitive to anneal temperature are given by the Mn-implanted samples (section 4.1). The *p*-GaN implanted with Cr (section 4.2) did not demonstrate consistent magnetic behavior for the implant and annealing conditions used in this experiment.

4.1 Manganese-implanted Gallium Nitride

p-GaN was implanted with Mn to a dose of $5 \times 10^{16} \frac{\text{ions}}{\text{cm}^2}$ at room temperature with an implantation energy of 200 keV. The strongest coercive and remanent fields are found when the Mn-implanted sample is annealed at 725 °C for 5 minutes. This annealing condition also produces a separation in field-cooled (FC) and zero-field-cooled (ZFC) temperature-dependent magnetization with low-temperature tracking. Although annealing at 725 °C for 5 minutes also results in significant recovery of cathodoluminescence (CL) intensity at the bandedge in *p*-GaN:Mn, this condition is not optimal for luminescence recovery.

4.1.1 Magnetic Hysteresis Measurements

Direct measurements of the magnetic moment in Mn-implanted *p*-GaN were undertaken using a SQUID magnetometer as detailed in section 3.3. Figure 4.1 shows the hysteresis data as measured. The data collected from these measurements show

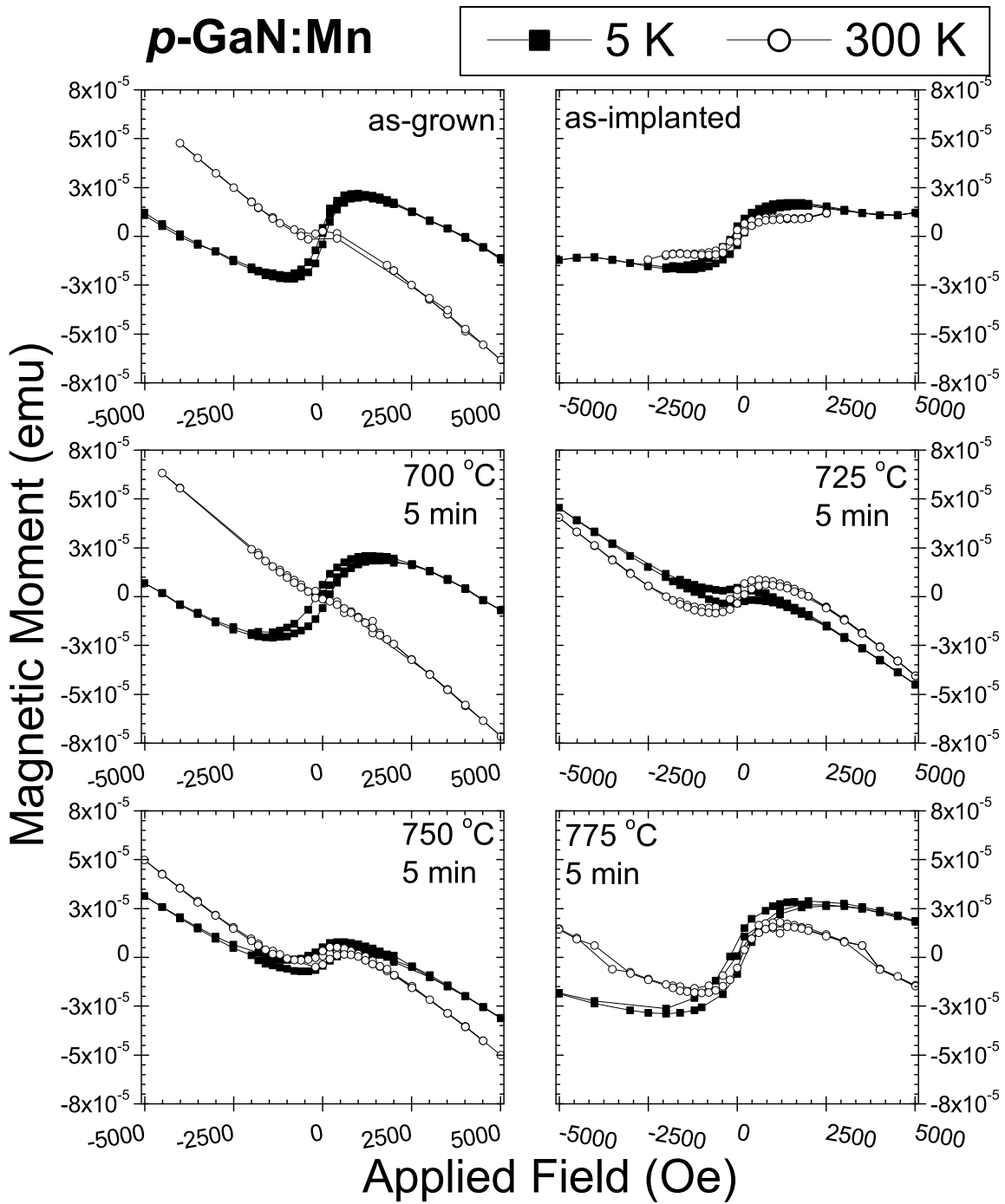


Figure 4.1 Raw magnetic hysteresis data from SQUID measurements of Mn-implanted *p*-GaN annealed as indicated for 5 minutes in N₂ flowing at 2 $\frac{L}{min}$.

a diamagnetic component that is attributable to the sapphire substrate and thus, this diamagnetic component must be corrected in order to obtain the true magnetic properties of the sample. The background diamagnetism present in the sample prior to the introduction of Mn is clear in the as-grown hysteresis measurement result shown in figure 4.1.

These SQUID measurements demonstrate hysteresis and hence the presence of coercive (H_c) and remanent (B_R) fields. Unfortunately, the uncorrected data presented in figure 4.1 will give slightly erroneous values for coercive fields because the tilt induced by underlying diamagnetism will cause the zero magnetization line to cross the hysteresis loop at an angle. Therefore, a correction to the raw data is necessary to allow meaningful, numerical comparisons of H_c and B_R among the samples characterized in this manner. The SQUID data presented in figure 4.2 have the linear diamagnetic influences arising from the substrate removed. Diamagnetism is removed using a MATLAB[®] routine that determines the amount of rotation about the origin necessary to make the magnetization values at the two greatest applied magnetic fields (both positive and negative) equal in value. Each data point is then rotated by this amount so that saturation magnetization (M_S) becomes apparent and accurate values for coercive and remanent fields can be ascertained.

The corrected data corresponding to the uncorrected magnetic moment data in figure 4.1 are shown in figure 4.2. This data demonstrates not only the greater coercive and remanent field strengths of the samples annealed at 725 and 750 °C, but also shows that they have the cleanest signals in measurements of magnetic moment. The most interesting feature of these measurements is the saturation magnetization that is greater at 300 K than at 5 K in the sample annealed at 725 °C for 5 minutes. This phenomenon is most likely due to the presence of a spin-glass state in which coordinated magnetic moments are “frozen” in a non-optimal configuration at low temperature, but free to follow the applied magnetic field at higher temperatures.

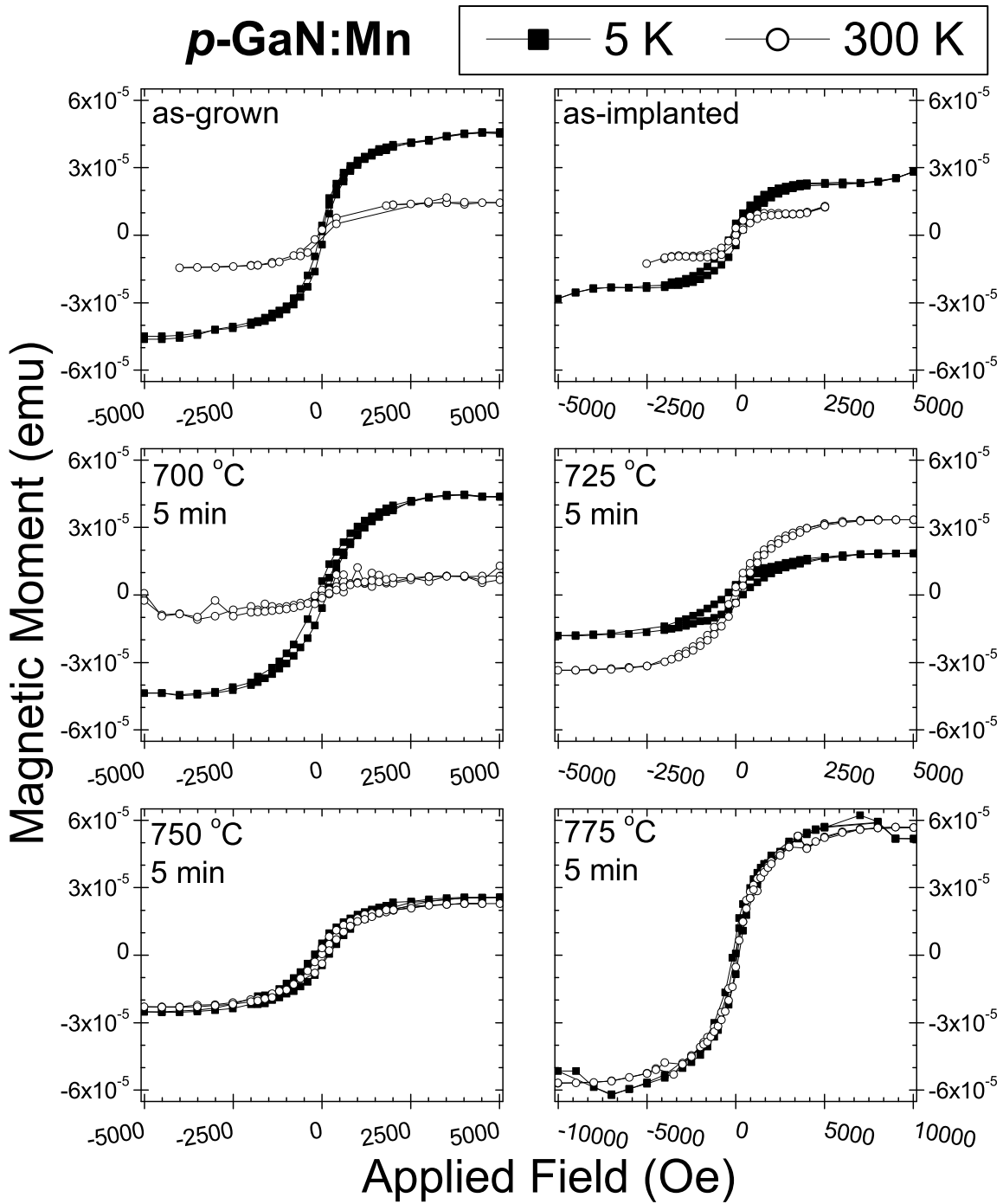


Figure 4.2 Magnetic hysteresis data for *p*-GaN implanted with Mn: as-implanted and annealed as indicated. Linear diamagnetic influences have been removed from this data.

The numerical results of these hysteresis measurements are summarized in figure 4.3, which indicates that the maximum coercive field (H_c) at 5 K for p -GaN:Mn occurs when it is annealed at 725 °C for 5 minutes. However, maximum H_c at room temperature occurred after annealing at 750 °C. As a function of the Bohr magneton (μ_B), The saturation magnetization (M_S) for the sample annealed at 750 °C corresponds to a values of 0.20 and 0.18 μ_B per Mn atom at temperatures of 5 and 300 K, respectively. The theoretical maximum effective magneton number for Mn^{2+} in an insulating crystal is 5.9 [8, Table 31.4], which indicates that a vast majority of the implanted Mn atoms are not participating in ferromagnetic ordering.

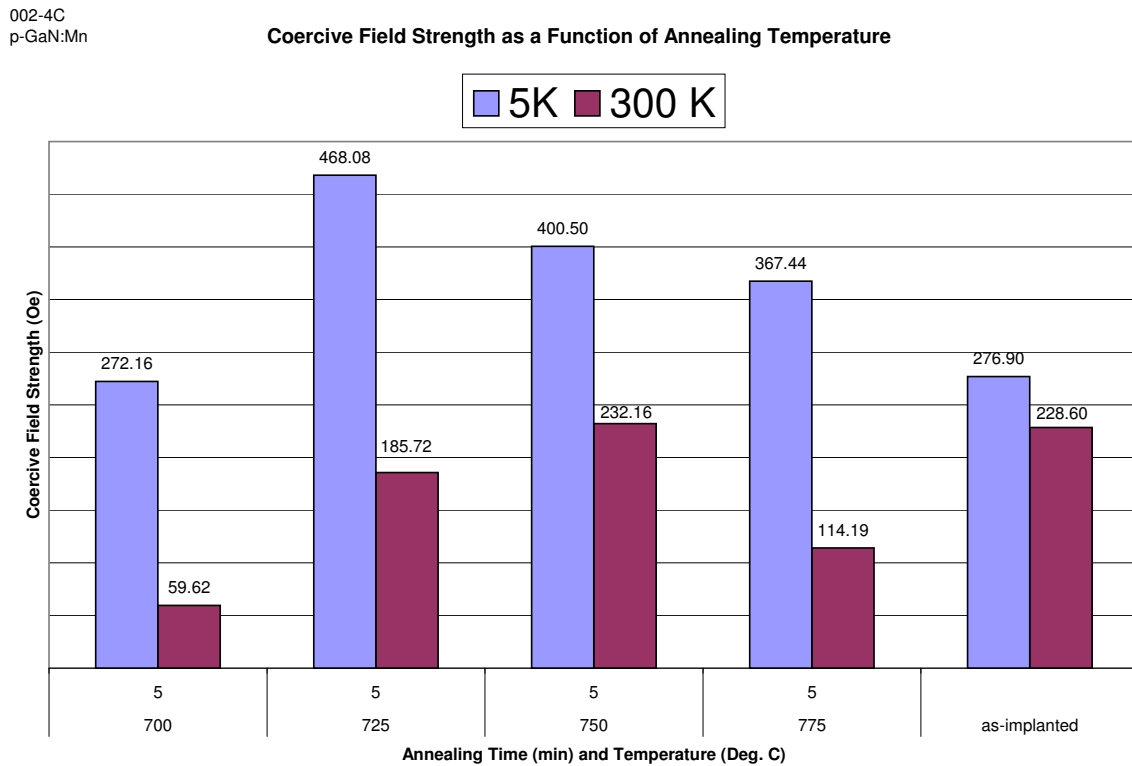


Figure 4.3 Coercive field strengths at 5 and 300 K for various annealing conditions of Mn-implanted p -GaN.

The remanent field strengths, B_R , charted in figure 4.4 correlate well with the H_c data. Similar to the H_c data, the strongest B_R at 5 K occurs when the sample is annealed at 725 °C for 5 minutes, but the greatest B_R at room temperature occurs in the sample annealed at 750 °C for 5 minutes. The 300 K measurement for the

sample annealed at 700 °C for 5 minutes is an anomalous data point that results from the removal of strong diamagnetic influences from a sample that is virtually entirely diamagnetic. For reference purposes, as-implanted H_c and B_R values are included in figures 4.3 and 4.4, respectively. The magnetism arising from this sample is attributed to interstitial Mn atoms where spin coordination is a result of the lowest energy state of the individual atoms in which the 5 d -orbital electrons are in the same spin state being influenced by the applied magnetic field. This atomic magnetic response is useless from a DMS standpoint because there is no magnetic coordination or interaction with the conduction or valence bands of the host semiconductor.

002-4C
p-GaN:Mn

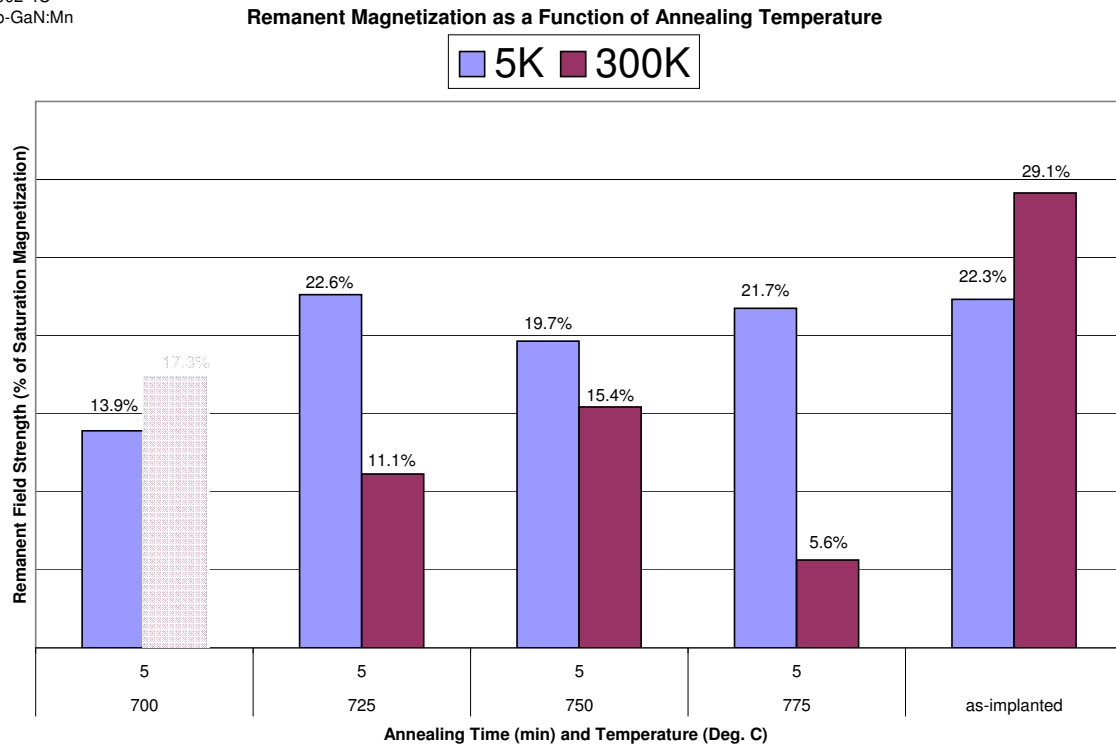


Figure 4.4 Remanent field strengths at 5 and 300 K for various annealing conditions of Mn-implanted p -GaN.

4.1.2 Temperature-Dependent Magnetization

Both FC and ZFC magnetization-versus-temperature measurements for p -GaN implanted with Mn are shown in figure 4.5. For the sample annealed at 700 °C, the FC and ZFC magnetization measurements are separated and increase together as the

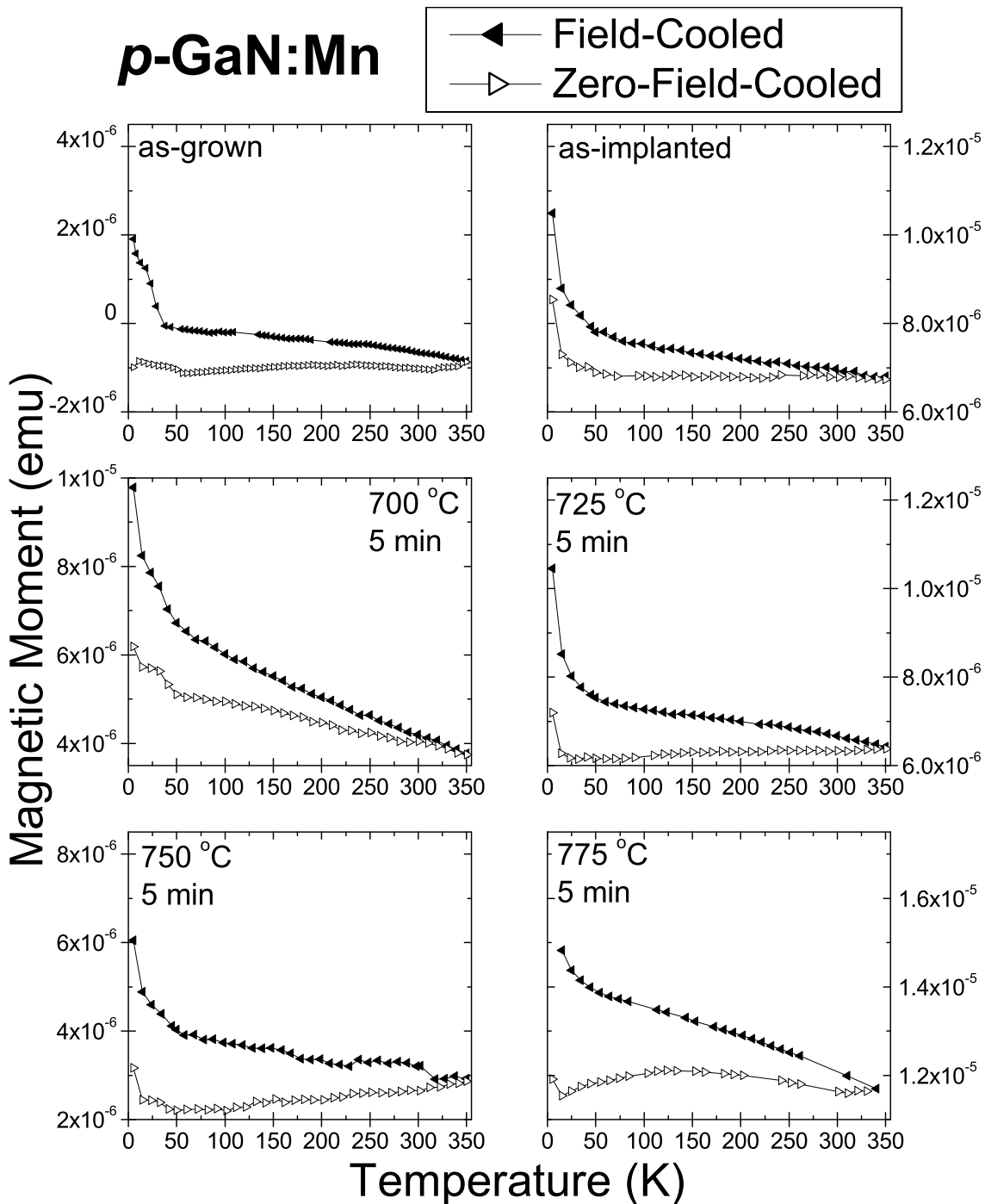


Figure 4.5 Temperature-dependent magnetization for *p*-GaN implanted with Mn and annealed as indicated for 5 minutes in N₂ flowing at 2 $\frac{\text{L}}{\text{min}}$. Note that the *y* axis spans the same range of magnetic moment despite the fact that background offset causes a difference in absolute values.

measurement temperature decreases. In the samples annealed at 725 and 750 °C, there is a mild increase in ZFC magnetization with increasing temperature. This increase is negligible and probably occurs due to the continued application of a 500-Oe magnetic field as temperature is increased during ZFC magnetization measurements. All of the samples annealed at temperatures below 775 °C show markedly higher magnetization values at measurement temperatures below 50 K for both FC and ZFC measurements. This indicates the presence of a ferromagnetic phase in each of the samples annealed at lower temperatures. The dominance of a spin-glass phase is evident in the sample annealed at 775 °C. This is demonstrated by the presence of a peak in the ZFC magnetization near 150 K [89]. This is further verified by the hysteresis data presented in figure 4.2, where the magnetic behavior is best characterized as superparamagnetic.

In keeping with the indications of ferromagnetism discussed above, the sample that has the cleanest magnetization signal and strongest separation of FC and ZFC measurements is the sample annealed at 725 °C for 5 minutes. The fact that the separation in FC and ZFC measurements is present across the entire range of temperatures measured is a strong indication that this material has a magnetic ordering temperature above room temperature.

4.1.3 Optical Measurements

CL measurements of Mn-implanted *p*-GaN samples are shown in figure 4.6 for various annealing temperatures. The CL spectra showed the most effective damage recovery at 750 °C for 5 minutes.

The as-grown sample shows a broad luminescence around 3.16 eV, which is consistent with donor-acceptor pair (DAP) peaks in GaN. The presence of this feature is most likely due to the heavy Mg doping that was performed during the growth of this sample. The photoluminescence from the as-implanted sample shows a minuscule peak around 3.49 eV, which is attributable to the neutral donor-bound exciton (D^0, X) peaks in GaN. There is also broad luminescence with a peak around 2.54 eV that

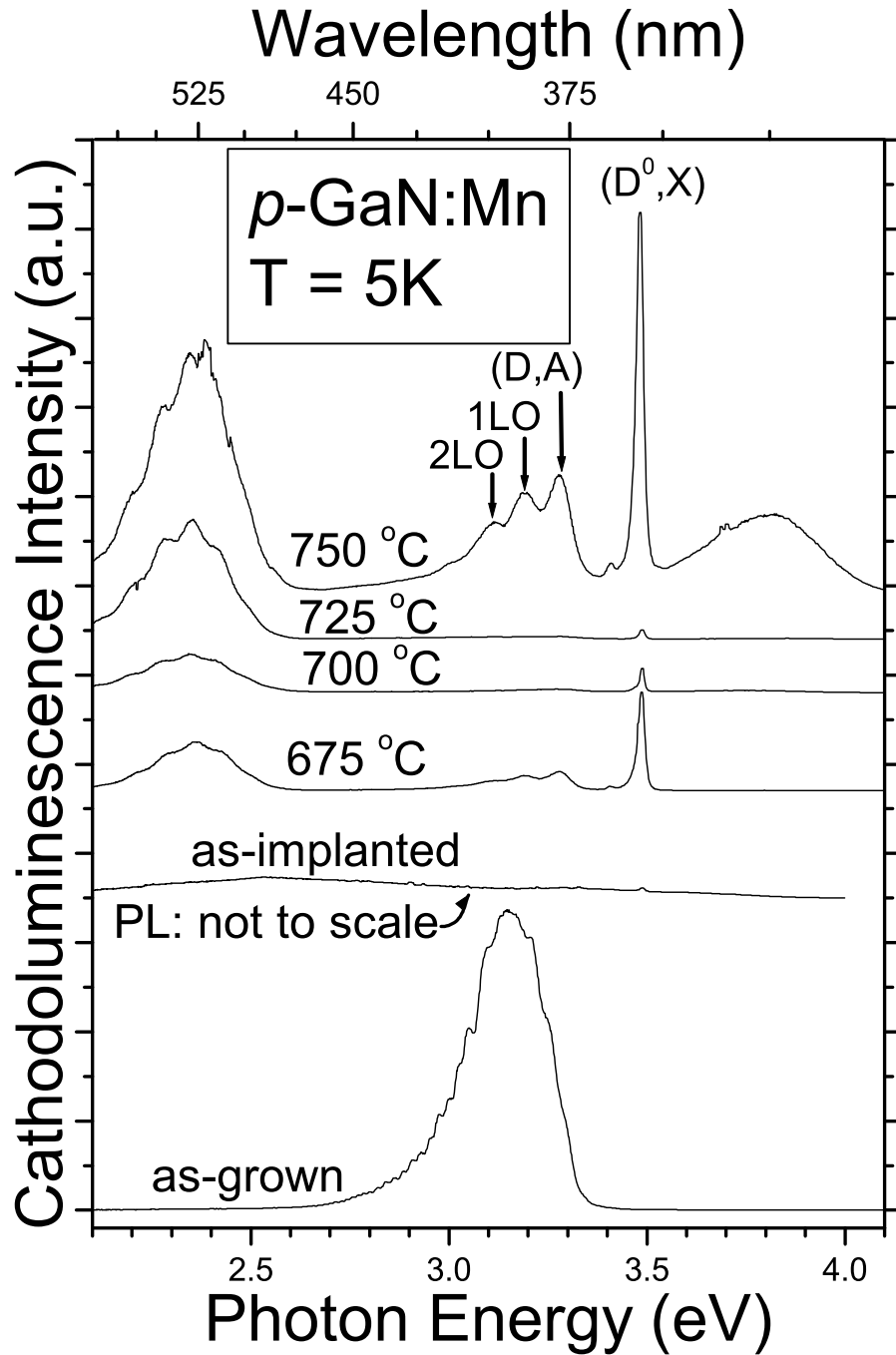


Figure 4.6 Cathodoluminescence and photoluminescence spectra of *p*-GaN implanted with Mn and annealed as indicated for 5 minutes in N₂ flowing at 2 $\frac{\text{L}}{\text{min}}$. Note that the as-grown and as-implanted samples are PL spectra and are not to scale with the annealed samples for which CL spectra were collected. The PL and CL spectra were collected from samples cooled to ~ 10 and ~ 5 K, respectively.

results from the incomplete removal of plasma lines from the exciting laser at those wavelengths. Plasma lines are individually suppressed back to a baseline level, but when they dominate the luminescence of a sample, the baseline is somewhat elevated by the merger of their tails.

The samples showed increasing luminescence with increasing anneal temperature. Most notable is the recovery of the band-edge feature at 3.49 eV, which is again attributed to a neutral donor-bound exciton. The brightness of this feature decreases in the sample annealed at 725 °C for 5 minutes compared to the sample annealed at 700 °C, but is the dominant feature in the sample annealed at 750 °C. This evolution of the (D^0,X) peak is somewhat anomalous and does not correlate well with the magnetic data presented above. The small feature visible in the CL measurement on the sample annealed at 750 °C just below the 3.49 eV peak is centered around 3.41 eV. The 3.41-eV feature is attributed to a defect-bound exciton [33].

In the sample annealed at 750 °C for 5 minutes, there is a clear donor-acceptor pair (DAP) peak at 3.28 eV. The peaks below this feature, in both energy and luminescent intensity, are spaced approximately 90 meV apart. This separation corresponds to the LO phonon energy in GaN [109]. Therefore, these features are attributed to phonon replicas of the DAP peak. This peak is also present in the samples annealed at 700 and 725 °C, but its magnitude is far less and it is broadened such that the phonon replicas are not resolved.

Another feature unique to the annealed samples is the presence of a blue-green luminescence centered around 2.4 eV. The luminescence from this feature increases with increasing annealing temperature. The continued increase in blue-green luminescence with annealing temperature is attributed to increasing incorporation of Mn into the *p*-GaN crystal lattice. Although slightly different in photon energy, this is similar to the luminescence results reported for Si-implanted $\text{Al}_{0.25}\text{Ga}_{0.75}\text{N}$ [98].

The broad luminescence centered around 3.8 eV and most visible in the sample annealed at 750 °C is attributed to Al-N-O complexes near the interface between the

p-GaN and the Al₂O₃ substrate [118]. The data presented in figure 4.6 indicates that these complexes are sensitive to annealing conditions. As far as crystal lattice damage recovery and magnetic properties are concerned, these complexes are inconsequential because they tend to occur in the Al₂O₃ substrate.

The most intense CL, the sharpest band-edge recovery, and the emergence of a feature at 3.28 eV were seen in the sample annealed at 750 °C. These facts indicate that the best implant damage recovery from this group of samples occurs when the sample is annealed at 750 °C for 5 minutes. This sample also has the strongest coercive field at room temperature, which suggests a good correlation between crystal damage recovery and signs of ferromagnetism in Mn-implanted *p*-GaN. Both good recovery of implant damage and the strongest magnetic properties occur for the same samples annealed at 725 and 750 °C for 5 minutes indicating that ferromagnetism in this material is probably due to the product of true magnetic interactions between the host *p*-GaN and the implanted Mn.

4.2 Chromium-implanted Gallium Nitride

p-GaN was implanted with Cr to a dose of $5 \times 10^{16} \frac{\text{ions}}{\text{cm}^2}$ at room temperature with an implant energy of 200 keV. Although signs of ferromagnetism are present, this material does not seem to be particularly sensitive to annealing temperature. Annealing does enhance the magnetic properties of these samples, but not in a predictable or consistent manner. This lack of a trend in the data indicates that the magnetic properties of this material may not be a product of *sp-d* hybridization, which diminishes its usefulness as a magnetic semiconductor.

4.2.1 Magnetic Hysteresis Measurements

SQUID measurements were used to determine the magnetization of the Cr-implanted *p*-GaN under a variable applied magnetic field. The raw data from these measurements is presented in figure 4.7. The raw hysteresis data shows very little separation between the positive- and negative-going magnetic field sweeps at room

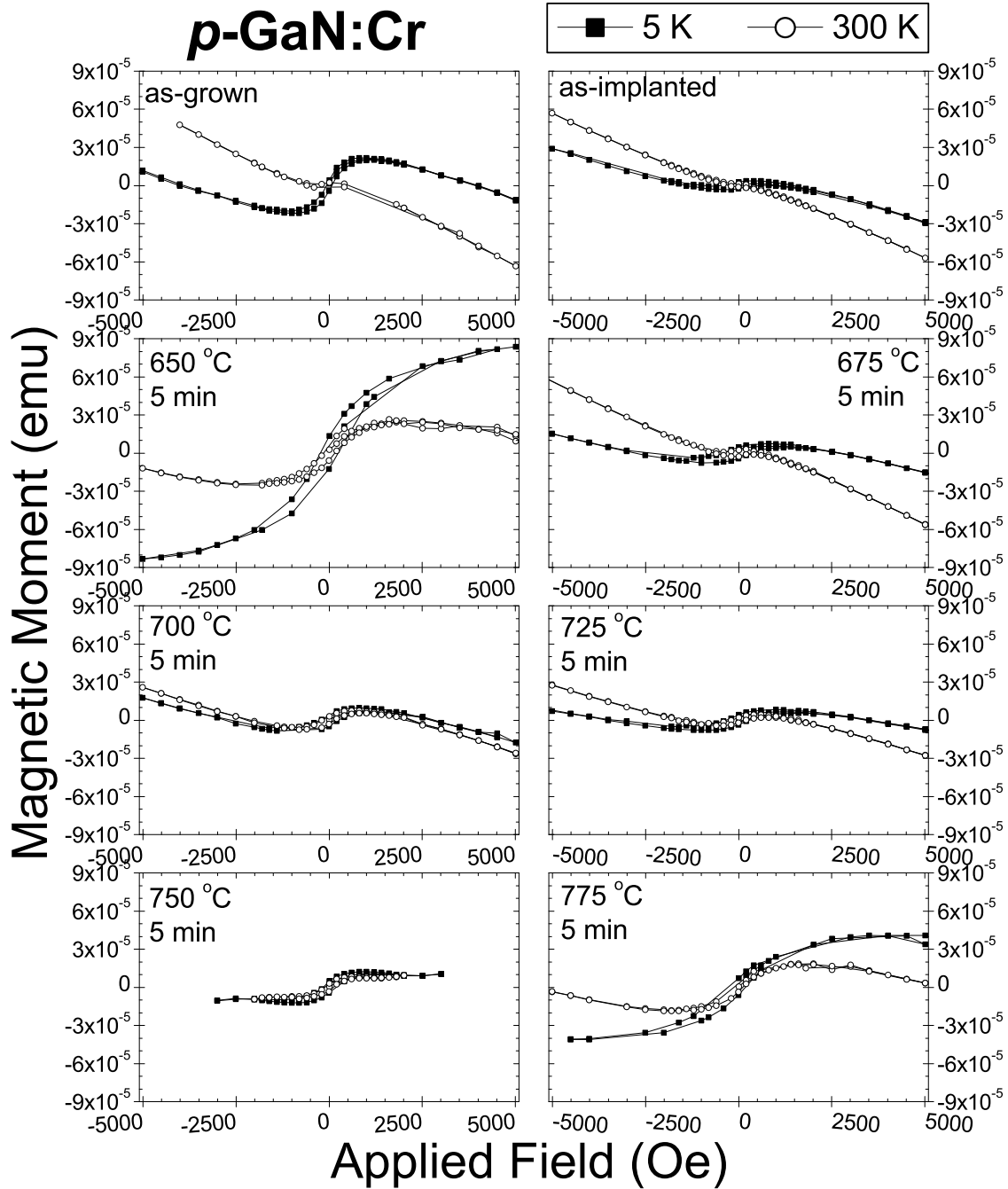


Figure 4.7 Raw data from magnetic hysteresis SQUID measurements of Cr-implanted *p*-GaN as-implanted and annealed as indicated for 5 minutes in N₂ flowing at 2 $\frac{L}{min}$.

temperature. For all but the sample annealed at 650 °C for 5 minutes, the magnetic behavior is best described as superparamagnetism riding on a diamagnetic background. The sample annealed at 650 °C also shows a saturation magnetizations of 0.57 and 0.38 μ_B per Cr atom at 5 and 300 K, respectively. The calculated maximum effective magneton for Cr^{2+} is 4.8 [8, Table 31.4]. Furthermore, the samples (except the one annealed at 650 °C) show similar responses regardless of annealing temperature. This insensitivity to annealing conditions is an indication that Cr-implanted GaN is not demonstrating ferromagnetic properties commensurate with a good DMS. Given the characteristic of the as-grown sample (superparamagnetism riding on a diamagnetic background), the behavior of many of the implanted and annealed samples indicate that Cr is not being incorporated into them in a way that significantly alters the magnetic properties of the *p*-GaN.

The variable field measurements taken on *p*-GaN:Cr are shown in figure 4.8 after correcting the diamagnetic component arising from the sapphire substrate. At room temperature, even the modified data does not show the separation in hysteresis characteristic of ferromagnetic materials. There is clear saturation in all of the samples, but this certainly does not indicate interaction of the implanted Cr with the host *p*-GaN.

The width of the coercive fields (H_c) at both 5 and 300 K is shown in figure 4.9 for the range of annealing temperatures utilized in this experiment. This data seems to indicate that the coercivity of *p*-GaN implanted with Cr is not very sensitive to annealing conditions, and this insensitivity may indicate deleterious effects, such as secondary phase formation or clustering, that are similar across a range of annealing temperatures. The magnetic characteristics of some possible secondary phases are given in Appendix B.

The absence of a clear optimal annealing temperature in figure 4.9 is countered in the remanent field data plotted in figure 4.10 for low temperature measurements. For the measurements made at 5 K, the greatest remanent field, as a percentage of

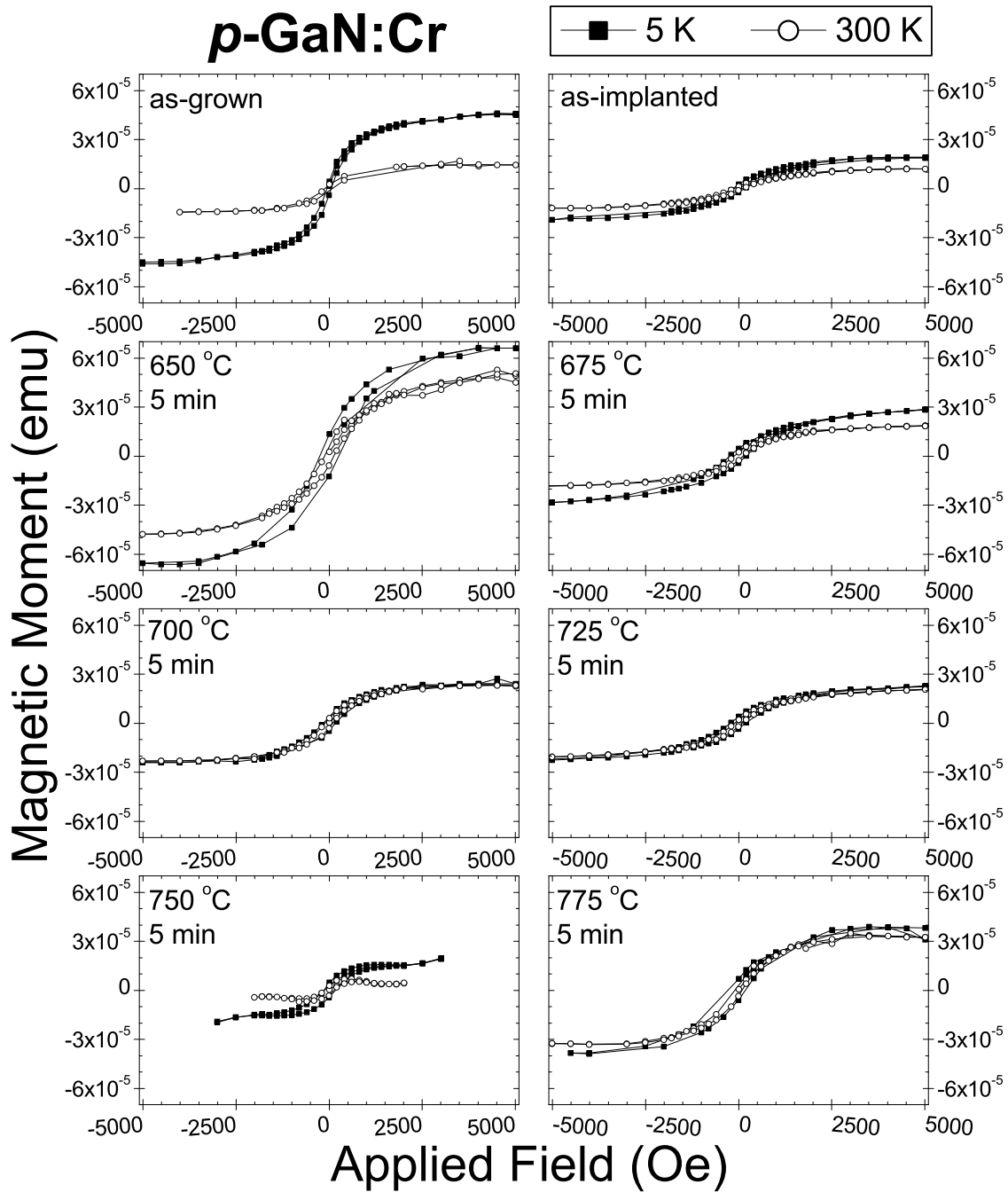


Figure 4.8 Magnetic hysteresis data for *p*-GaN implanted with Cr and annealed as indicated. Linear diamagnetic influences have been removed from this data.

Coercive Field Strength as a Function of Annealing Temperature

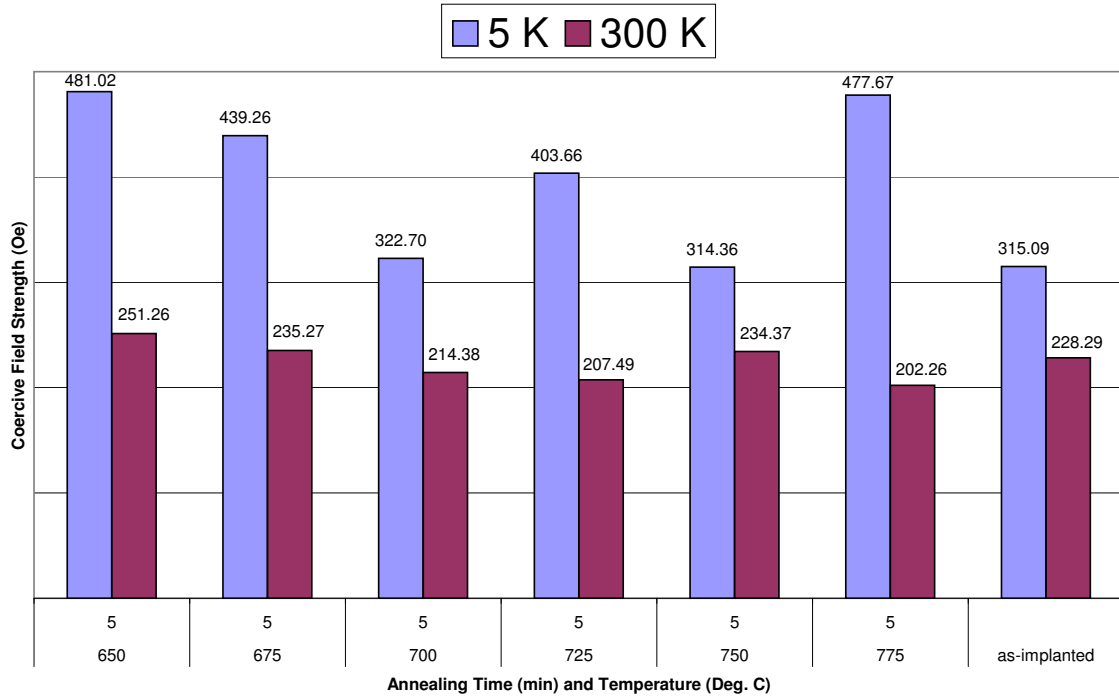


Figure 4.9 Coercive field strengths at 5 and 300 K for various annealing conditions of Cr-implanted *p*-GaN.

saturation magnetization, occurs when the Cr-implanted *p*-GaN is annealed at 750 °C for 5 minutes. For the room temperature variable field measurements, there is little distinction among the various annealing conditions, but the maximum occurs when the sample is annealed at 700 °C for 5 minutes. This lack of distinction bodes ill for the hope of true DMS behavior in which ferromagnetism arises from *sp-d* hybridization for this material system.

4.2.2 Temperature-Dependent Magnetization

FC and ZFC magnetization were also measured while temperature was varied for the *p*-GaN samples implanted with Cr. The results of these measurements are depicted in figure 4.11.

The as-implanted sample shows virtually no magnetic character as evidenced by the lack of separation between FC and ZFC magnetization for this sample. The

Remanent Magnetization as a Function of Annealing Temperature

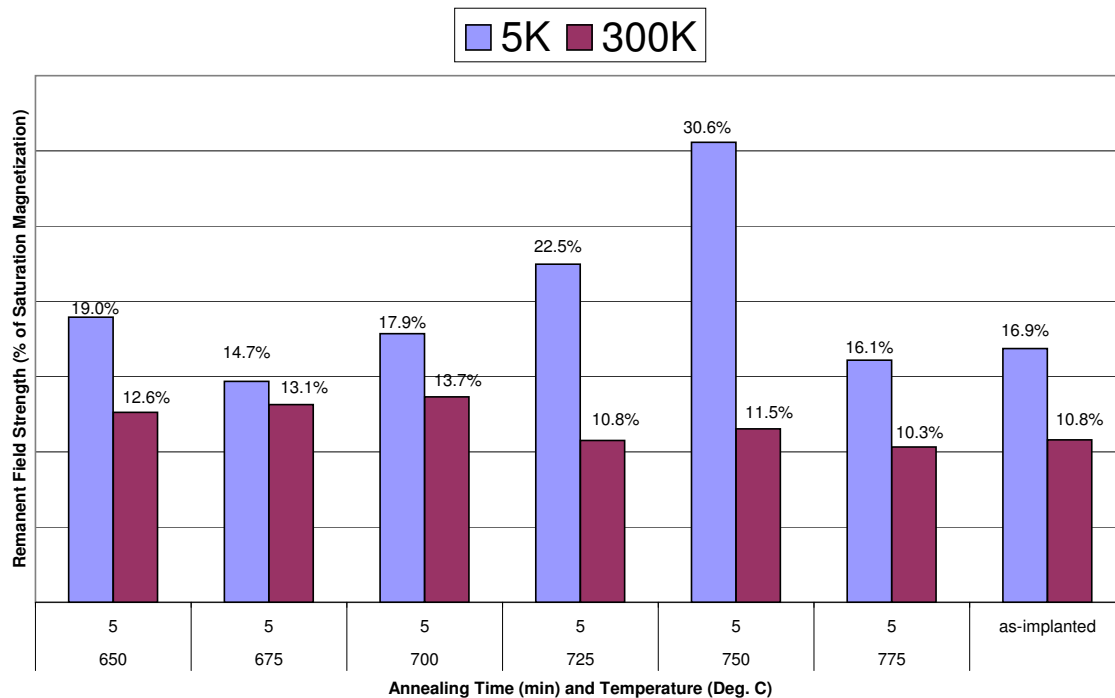


Figure 4.10 Remanent field strength as a function of saturation magnetization at 5 and 300 K for various annealing conditions of Cr-implanted *p*-GaN.

divergence of FC and ZFC measurements in the samples annealed at 650, 700, and 775 °C for 5 minutes is an indication that any magnetic ordering seen at low temperature in these samples is most likely the result of a spin-glass phase. This is especially apparent because of the “hump” in ZFC magnetization for the sample annealed at 775 °C, which is a clear indication of spin-glass behavior [89].

The sample annealed at 675 °C for 5 minutes shows a clear transition at a temperature of 75 K. The rapid decrease of FC magnetization at 75 K and lack of separation between FC and ZFC measurements above this temperature indicate that the sample loses its magnetic ordering above 75 K. However, the definite loss of magnetic ordering implies that order is present below this temperature, so there may be useful DMS behavior in this material albeit at temperatures too low for practical devices.

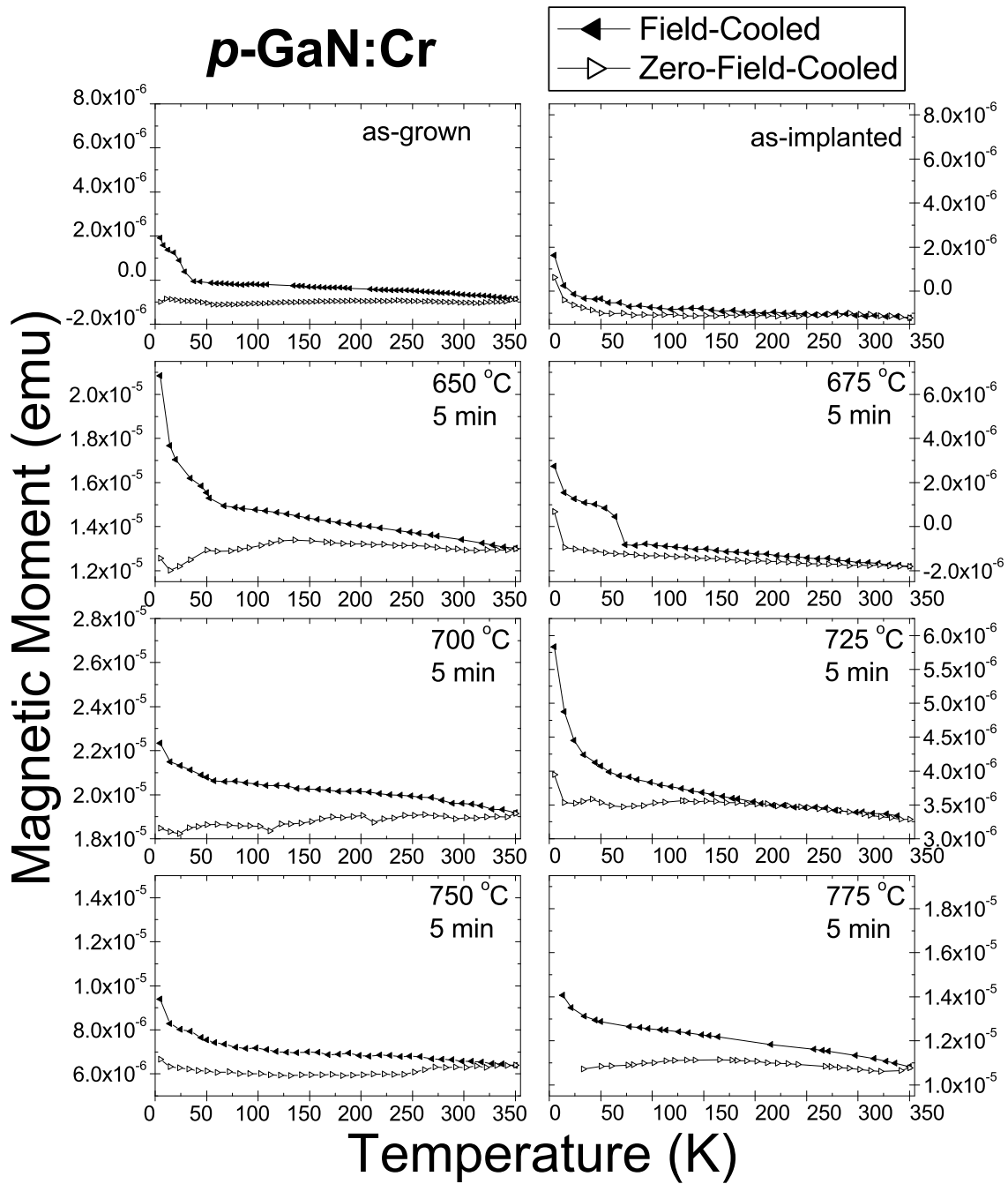


Figure 4.11 Temperature-dependent magnetization for p -GaN implanted with Cr and annealed as indicated. Note that the y axis spans the same range of magnetic moment despite the fact that background offset causes a difference in absolute values.

There is also a lack of significant separation between FC and ZFC magnetization in the sample annealed at 725 °C for 5 minutes. Although there is a small gap at temperatures below 150 K, there is not a clear transition temperature as is the case in the sample annealed at 675 °C. The temperature-dependent magnetization of the sample annealed at 725 °C indicates that magnetic ordering is not dominant, if it is present at all.

The only sample of *p*-GaN:Cr that may demonstrate magnetic ordering persisting to near room temperature is the one annealed at 750 °C for 5 minutes. Temperature-dependent magnetization measurements from this sample show clear separation of FC and ZFC magnetization up to approximately 273 K, and the FC and ZFC measurements track upward together at low temperatures. The convergence of FC and ZFC magnetization above 273 K occurs as a result of a change in the ZFC values, and the fact that CrN is known to be antiferromagnetic (AFM) with an ordering temperature of 273 K [82], indicates the presence of a secondary phase in this material. Obviously, an AFM phase does not dominate the sample as evidenced by the hysteresis observed in figure 4.7. The disordering of this AFM phase above 273 K allows ferromagnetism to dominate more completely and results in this sample showing the least difference in H_c between 5 and 300 K measurements (see figure 4.9).

The somewhat anomalous behavior demonstrated in the temperature-dependent magnetization measurements of Cr-implanted *p*-GaN undermine potential claims that this material is truly a dilute magnetic semiconductor. Although there does appear to be some ordering in the sample annealed at 750 °C for 5 minutes, this ordering may have AFM alignment as its source. This material exemplifies a case where direct magnetic measurements are not sufficient to characterize the material as a DMS. Other measurements that are beyond the scope of this research, such as anomalous Hall effect and magnetic circular dichroism, would be useful for more complete characterization of *p*-GaN:Cr.

4.2.3 Optical Measurements

Damage recovery in *p*-GaN:Cr annealed at various temperatures was determined by CL and PL measurements. The resulting spectra are presented in figure 4.12.

The as-grown sample shows a broad luminescence around 3.16 eV, which is consistent with (DAP) peaks in GaN brought on by heavy Mg doping that was performed during the growth of this sample. As expected, the ion implantation greatly reduces the luminescence emanating from the sample. There is a noticeable luminescence peak at 3.25 eV that is associated with a donor-acceptor pair (DAP) transition. This peak is much more prominent in the sample annealed at 750 °C for 5 minutes, but is still broad because of incomplete lattice recovery under these annealing conditions.

A prominent feature in all of the samples, though only with a much smaller scale for the as-implanted samples, is the broad luminescence peak around 3.8 eV. These broad luminescence peaks around 3.8 eV arise from Al-N-O complexes near the AlN/Al₂O₃ interface [118].

The dominant feature in the samples annealed at 700 and 750 °C is a broad blue-green luminescence centered around 2.46 and 2.38 eV, respectively. This broad peak is also present in the same region of the sample annealed at 725 °C for 5 minutes, but is much lower in intensity and far from the dominant feature of that sample. The fact that this feature is not consistent and does not increase in intensity with anneal temperature seems to indicate that it does not appear as a result of Cr incorporation in the *p*-GaN lattice. This feature reveals a deep level emission that is attributed to Mg doping in GaN [66]. Note that the asymmetry in the sample annealed at 700 °C for 5 minutes was induced by placement of an optical filter to prevent duplication of shorter wavelength features. Unfortunately, this filter also causes some attenuation, even at the longer wavelengths that the filter is designed to pass, so there is an immediate drop in luminescent intensity at 2.374 eV where the filter was inserted.

The sharpest, most noticeable band-edge peak, occurs when the sample is annealed at 725 °C for 5 minutes. The band-edge peak occurs at an energy of 3.364-eV.

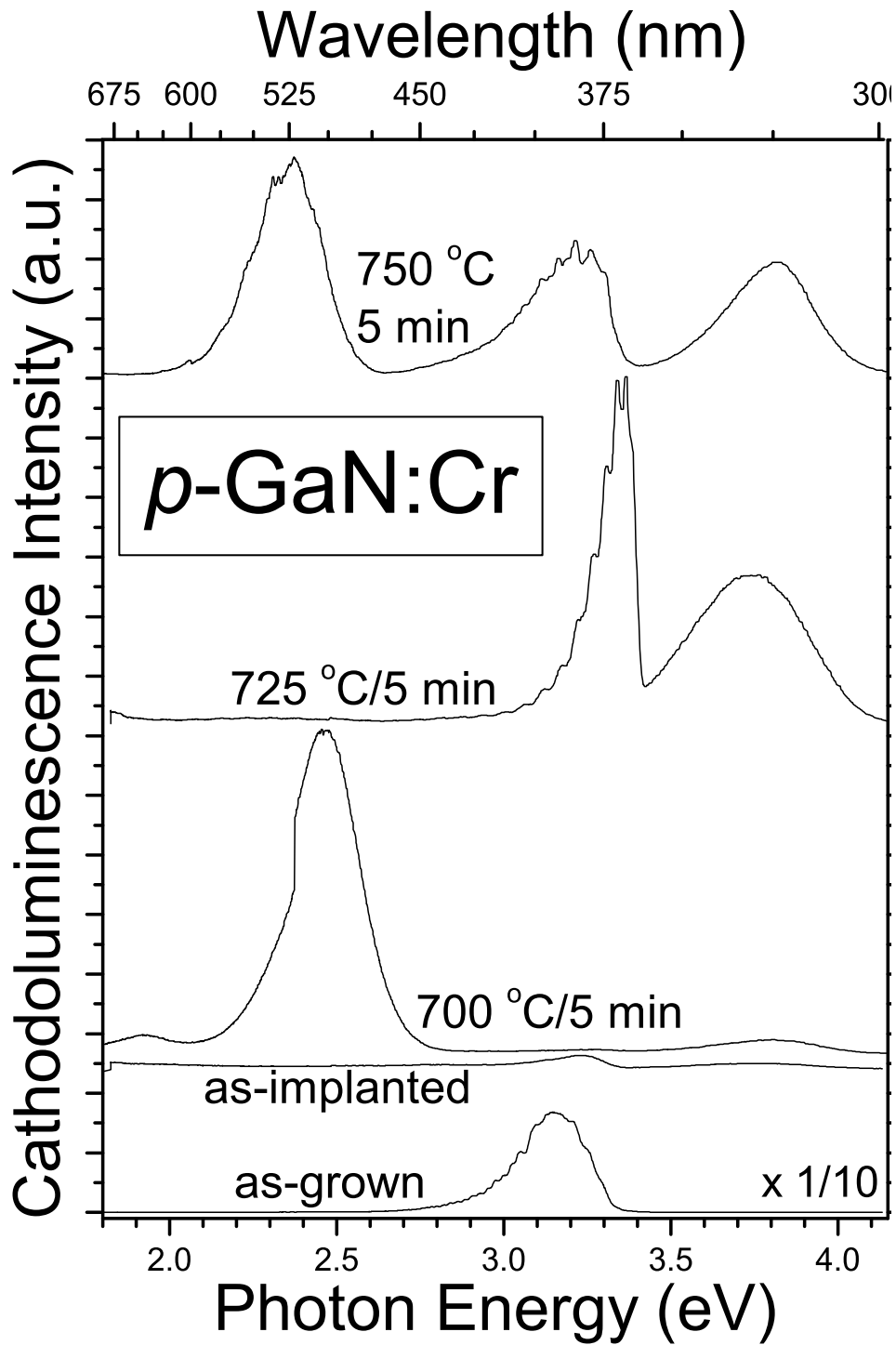


Figure 4.12 Cathodoluminescence spectra, collected from samples cooled to approximately 5 K, of *p*-GaN implanted with Cr and annealed as indicated in a $2 \frac{\text{L}}{\text{min}}$ flow of N_2 for 5 minutes.

The 3.364 eV peak is attributed to a strongly localized exciton tied to a crystal defect level [135]. The shoulders on the low-energy side of this feature are attributed to the etalon effect. Overall, this material is probably of low quality: the sharp near-band-edge luminescence is made possible by crystal defects. This observation confirms that good crystal quality is necessary for magnetic ordering in these materials and helps explain the weaker magnetic properties of the sample annealed at 725 °C with respect to those annealed at 700 and 750 °C.

4.3 Nickel-implanted Gallium Nitride

Ni was implanted into *p*-GaN to a dose of $3 \times 10^{16} \frac{\text{ions}}{\text{cm}^2}$ at room temperature with an implant energy of 200 keV. The lower Ni dose was used because a previous report indicates that a dose of $3 \times 10^{16} \frac{\text{ions}}{\text{cm}^2}$ gives better magnetic performance than a dose of $5 \times 10^{16} \frac{\text{ions}}{\text{cm}^2}$ [90]. This lower implantation dose has the added benefit of mitigating the formation of Ni clusters in the annealed material.

Ni-implantation and subsequent annealing of *p*-GaN causes the material to exhibit evidence of ferromagnetism. Unfortunately, there are some anomalies in the data, which may portend a non-DMS source for some of the magnetic properties observed. There is a possibility that the observed ferromagnetism in the sample annealed at 675 °C for 5 minutes originates from true DMS behavior. The evidence for this comes from the low-temperature and temperature-dependent behavior seen in the direct magnetic measurements of this material.

4.3.1 Magnetic Hysteresis Measurements

The raw hysteresis data is presented in figure 4.13. From this figure, it is apparent that all of the samples present indications of ferromagnetism at low temperatures, but there is a vast difference in the samples when variable field measurements are taken at room temperature.

The room-temperature variable field measurement of the as-grown and as-implanted samples reveal a strong diamagnetic character. This is also the case in

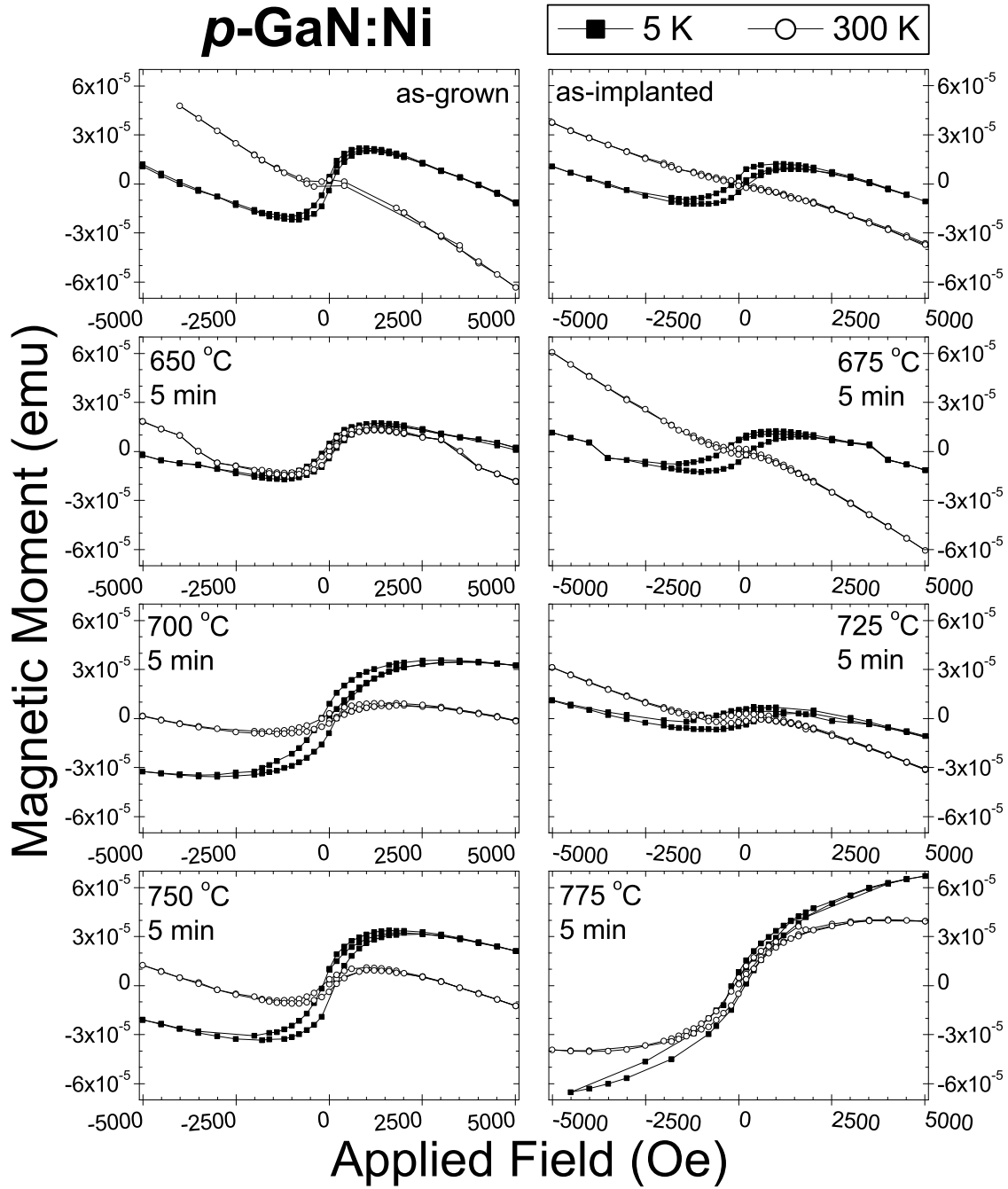


Figure 4.13 Raw data from magnetic hysteresis SQUID measurements of Ni-implanted *p*-GaN annealed as indicated for 5 minutes in N₂ flowing at 2 $\frac{L}{min}$.

the sample annealed at 675 °C for 5 minutes in N₂ flowing at 2 $\frac{\text{L}}{\text{min}}$. The sample annealed at 650 °C, while showing magnetic saturation, does not show much separation in 5 K hysteresis measurements, so, much like the as-grown sample, it is best characterized as superparamagnetic at low temperatures. For the samples annealed from 700 to 775 °C for 5 minutes, all show separation between positive- and negative-going legs of the hysteresis loop so that meaningful values can be determined for the coercive and remanent fields. In the sample annealed at 775 °C for 5 minutes, the raw data in figure 4.13 shows that there is virtually no diamagnetic background at room temperature and the background at low temperature is paramagnetic. The simplest explanation for this phenomenon is that there are defects or complexes in the samples that are annealed out with increasing effectiveness as annealing temperature is increased. The trends of decreasing diamagnetism can be seen in all of the *p*-GaN samples as evidenced in figures 4.1 and 4.7, as well as figure 4.13. In general, diamagnetic components decrease as annealing temperature increases to the point where the background may even exhibit paramagnetism when annealed at a relatively high temperature.

In order to determine meaningful values of H_c and B_R , the raw hysteresis data needs to be rotated about the origin so that the magnetization measurements level out after the saturation value is reached. This ensures that the hysteresis loop is measured correctly for the purpose of determining coercive and remanent fields. This process is discussed in greater detail in section 4.1.1.

The hysteresis data with linear dia- and para-magnetic influences removed is shown in figure 4.14. This view of the data makes the hysteretic behavior discussed above more apparent. The samples annealed at 700 and 725 °C may appear to have lower coercive fields in this figure because the scale was enlarged to show that magnetic saturation was clearly achieved in these samples. As an artifact of the rotation to remove diamagnetic influences, the as-implanted sample, as well as the one annealed at 675 °C, show a more ferromagnetic character than what is actually present.

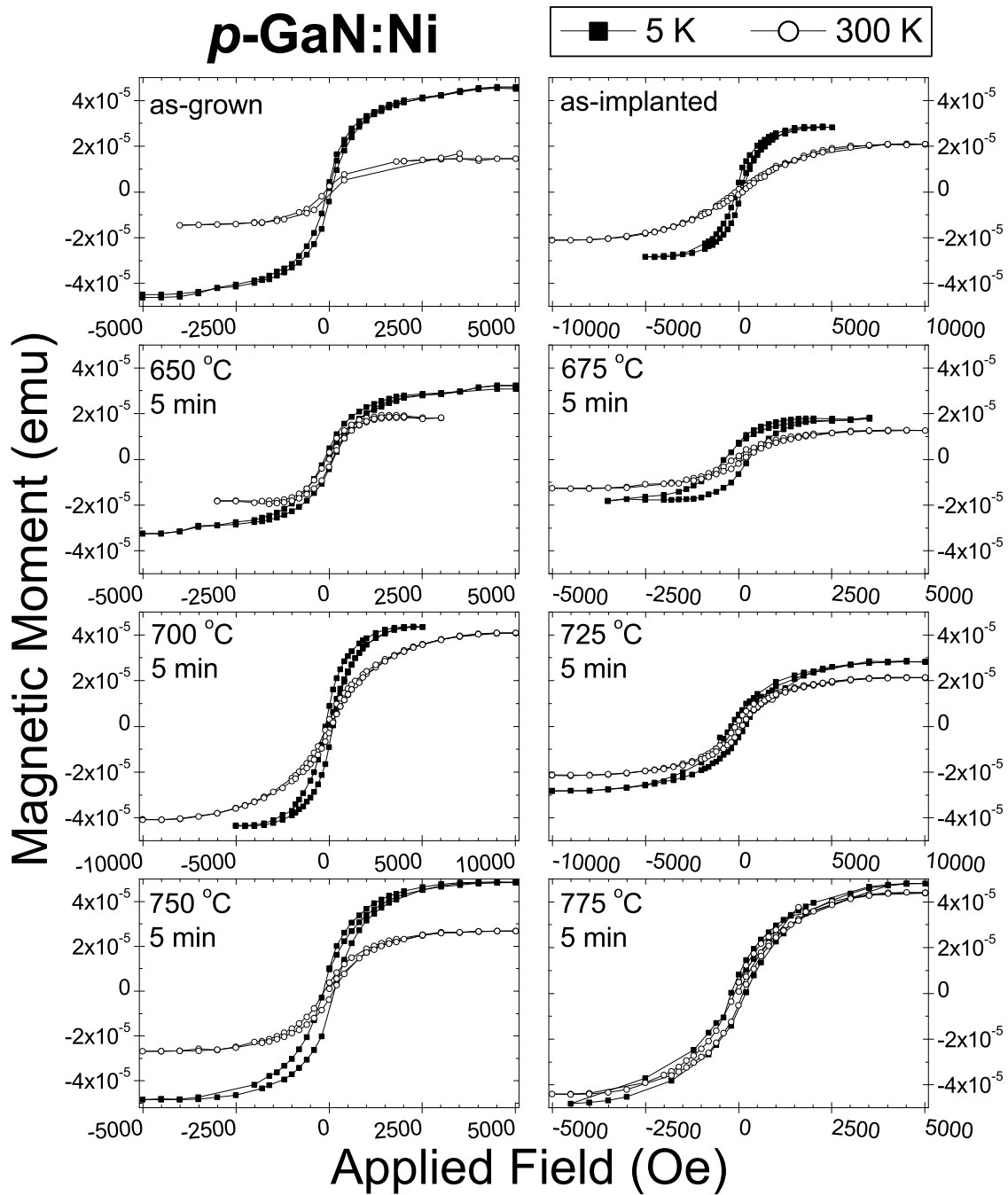


Figure 4.14 Magnetic hysteresis data for *p*-GaN implanted with Ni and annealed as indicated. Linear magnetic influences have been removed from this data. Note that the horizontal scale is doubled for the samples annealed at 700 and 725 °C as well as the as-implanted sample.

A summary of the H_c data collected during variable field measurements is presented in figure 4.15. It is clear from the data collected at room temperature that the strongest coercive field is produced in the sample annealed at 725 °C for 5 minutes. This sample also shows M_S values of $0.51 \mu_B$ per Ni atom at 5 K and $0.39 \mu_B$ per Ni atom at 300 K. The calculated maximum magneton for Ni^{2+} is $3.2 \mu_B$ [8, Table 31.4]. The data presented in figure 4.15 for the sample annealed at 675 °C is erroneous due to the fact that even after background subtraction, the zero-crossings of the hysteresis loop are still slanted rather than crossing the x axis at a sharp angle. The correction necessary to allow perpendicular (to the x axis) zero-crossings would prevent calculation of the saturation magnetization.

002-4B
p-GaN:Ni

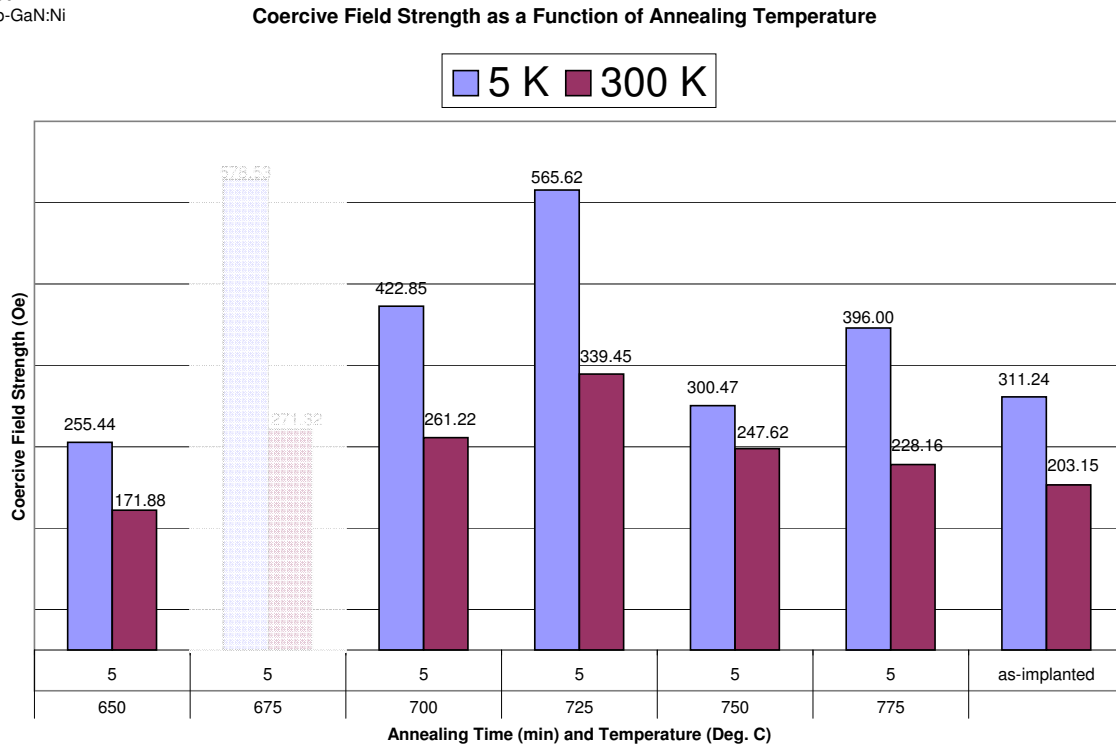


Figure 4.15 Coercive field strengths at 5 and 300 K for various annealing conditions of Ni-implanted p -GaN. The data for the sample annealed at 675 °C is obscured because of an artifact of the diamagnetism correction algorithm.

In the case of Ni-implanted p -GaN, remanent field data does not seem to be a reliable figure of merit. The remanent field strengths are reported in figure 4.16 and

are weak and erratic. There is no clear trend in B_R , and the greatest values occur in samples with weaker coercive fields and other indications of non-ferromagnetic (spin-glass) behavior in the temperature-dependent magnetization measurements as discussed in the following section.

002-4B
p-GaN:Ni

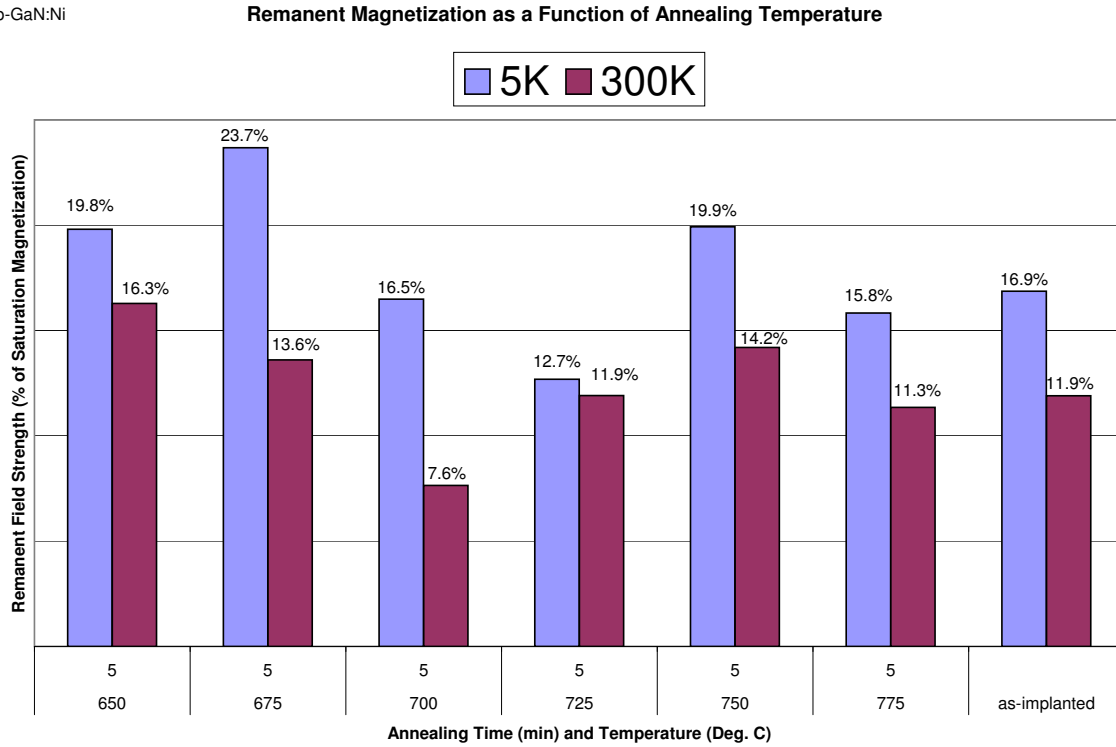


Figure 4.16 Remanent field strengths at 5 and 300 K for various annealing conditions of Ni-implanted p -GaN.

4.3.2 Temperature-Dependent Magnetization

Magnetization-versus-temperature data for the Ni-implanted p -GaN was collected and are displayed in figure 4.17. In these samples, there is a clear separation and divergence of the ZFC and FC measurements at low temperature for the samples annealed at and above 725 °C. This divergence is indicative of a spin-glass phase being the dominant magnetic feature over any ferromagnetic phase [89].

Even though the Ni-implanted p -GaN annealed at 675 °C shows strong coercive and remanent fields at low temperature, this behavior diminishes rapidly with increasing temperature as shown in figure 4.13. This behavior is echoed in figure 4.17 where

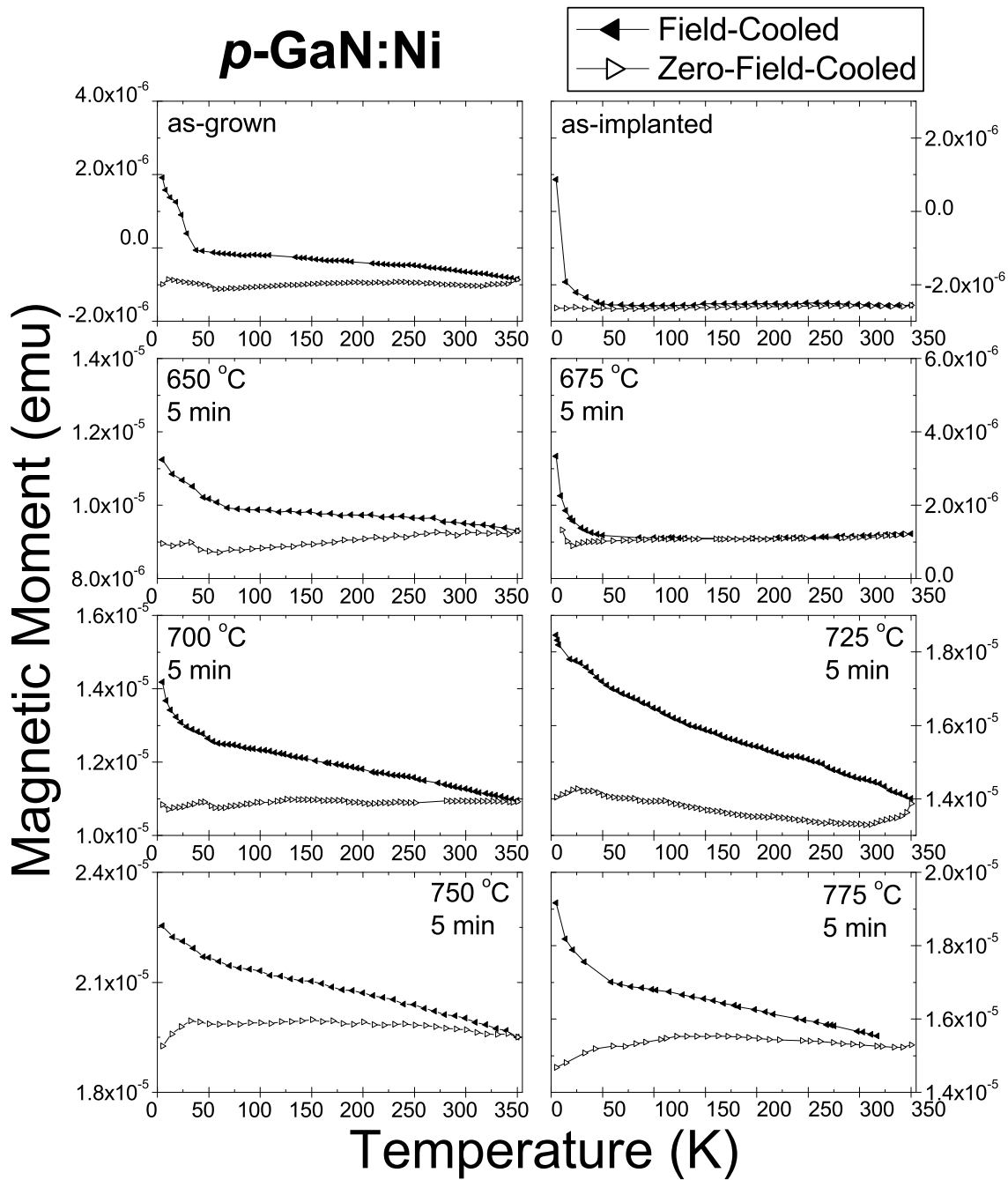


Figure 4.17 Temperature-dependent magnetization for *p*-GaN implanted with Ni and annealed as indicated for 5 minutes. Note that the *y* axis spans the same range of magnetic moment despite the fact that background offset causes a difference in absolute values.

the FC and ZFC magnetization measurements converge quickly at 100 K indicating a lack of ferromagnetic ordering above this temperature. The samples annealed at 650, 700, and 725 °C for 5 minutes maintain separation in FC and ZFC magnetization values up to 350 K, and those annealed between 700 and 750 °C for 5 minutes show significant increases in FC–ZFC separation versus the as-grown sample. The persistence of ferromagnetism to room temperature is also apparent in figures 4.13 and 4.14 where hysteresis is apparent at 300 K for these samples. The coercivity measured is small, however, which contributes to the inconsistency in the magnetic behavior of this material.

4.3.3 Optical Measurements

Spectra from CL measurements of the p -GaN:Ni samples are shown in figure 4.18. Implant damage is recovered, from an optical standpoint, for samples annealed at 700 °C for 5 minutes. While there is a recovery of a broad feature near the bandedge, the CL spectrum is dominated by Al-N-O complexes (3.8 eV) in the Al₂O₃ substrate [118] and blue-green luminescence. In the sample annealed at 675 °C the blue-green luminescence occurs at a photon energy of 2.36 eV and there is also a broad, weak luminescence in the violet at 3.10 eV.

Both the violet and blue-green luminescence bands in the sample annealed at 675 °C are attributed to the activation of implanted Ni impurities. Although slightly different in energy, these CL features are similar to those reported for Si-implanted Al_{0.25}Ga_{0.75}N [98]. In the work of Ryu *et al.* increasing intensity in the broad mid-bandgap peaks indicated greater and greater activation of the implanted silicon. It is believed that a similar phenomenon is occurring in Ni-implanted p -GaN since the 2.36-eV and 3.10-eV peaks are not present in the as-grown sample and only manifest themselves after annealing at 675 °C for 5 minutes. In the context of the direct magnetic measurements, the activation of implanted Ni after annealing at 675 °C is reasonable and allows some hope that p -GaN:Ni annealed under these conditions is a true DMS.

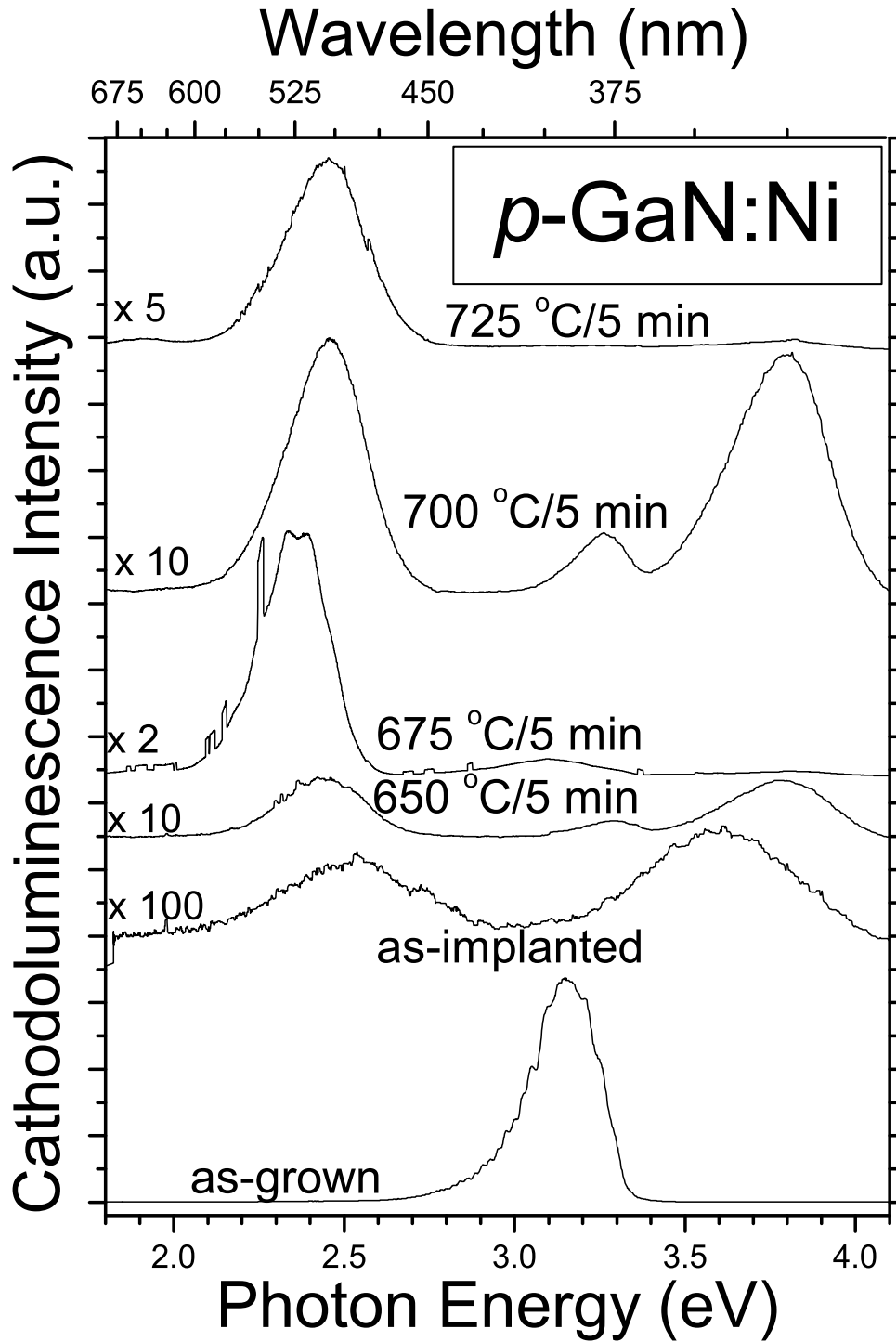


Figure 4.18 Cathodoluminescence spectra of $p\text{-GaN}$ implanted with Ni and annealed as indicated for 5 minutes in N_2 flowing at $2 \frac{\text{L}}{\text{min}}$. These measurements were taken at approximately 5 K.

4.4 Conclusions

Transition metal implantation into *p*-GaN is an effective method of creating a wide-bandgap semiconductor with ferromagnetic properties that persist to room temperature. In the Mn-implanted samples, the magnetic properties follow a trend that indicates optimum annealing occurs at a temperature of 725 °C for a 5 minute anneal. At this annealing condition, a saturation magnetic moment of 1.8×10^{-5} emu, coercive field width of 468 Oe, and remanent field value of 23% of saturation were obtained. The *p*-GaN:Cr does not show this sort of consistency in magnetic properties, so there is doubt that this material is demonstrating true DMS behavior, rather this sample shows superparamagnetism. Although the Ni-implanted *p*-GaN lacks consistent trending, there is some evidence that the sample annealed at 675 °C for 5 minutes may be a true DMS at low temperatures. However, most of the *p*-GaN:Ni samples show spin-glass properties.

Overall, the tendency for *p*-GaN doped with transition metals to show ferromagnetic properties persisting to room temperature is encouraging. As Mn- and Ni-doped *p*-GaN are further characterized, they will likely be found suitable for DMS device fabrication. *p*-GaN:Cr may also show some promise, but a different set of implant and/or annealing conditions are necessary to produce the consistency necessary for confidence in the magnetic properties of this material.

V. Characteristics of Transition Metal Implanted

Aluminum Gallium Nitride

1- μm thick $\text{Al}_{0.35}\text{Ga}_{0.65}\text{N}$ was grown on an AlN buffer layer which was grown on a sapphire substrate. The $\text{Al}_{0.35}\text{Ga}_{0.65}\text{N}$ was also capped with a 500- \AA layer of amorphous AlN. The material was not intentionally doped, but probably exhibits *n*-type conductivity due to unintentional impurities such as oxygen and silicon [69]. Based on the results of the characterization detailed below, using Mn-, Cr-, and Ni-implanted $\text{Al}_{0.35}\text{Ga}_{0.65}\text{N}$ to fabricate DMS material is viable. There are some anomalies and possible issues with reproducibility in this material system, but the overall quality of the material indicates that it should be included in further studies and device work moving forward.

5.1 Manganese-implanted Aluminum Gallium Nitride

A dose of $5 \times 10^{16} \frac{\text{ions}}{\text{cm}^2}$ Mn ions were implanted into $\text{Al}_{0.35}\text{Ga}_{0.65}\text{N}$ at room temperature with an energy of 200 keV. The resulting material produced convincing signs of ferromagnetism when annealed at 750 $^\circ\text{C}$ and higher for 5 minutes in N_2 flowing at 2 $\frac{\text{L}}{\text{min}}$. The strongest indications of ferromagnetism in $\text{Al}_{0.35}\text{Ga}_{0.65}\text{N}:\text{Mn}$ occurred when it was annealed at 775 $^\circ\text{C}$, which suggests that even higher temperature anneals may enhance magnetic properties. However, the sample annealed at 775 $^\circ\text{C}$ did display the onset of an undesirable spin-glass phase, which could be bolstered by hotter annealing. The samples annealed at and below 725 $^\circ\text{C}$ showed weaker signs of ferromagnetism overall. Overall, $\text{Al}_{0.35}\text{Ga}_{0.65}\text{N}$ implanted with Mn shows great promise as a room-temperature DMS and is undoubtedly one of the materials that will form the basis for spintronic device research.

5.1.1 Magnetic Hysteresis Measurements

Variable field measurements of the samples are shown in figure 5.1 for the annealing conditions used in this experiment. The presence of a diamagnetic background is apparent in all of the samples with the exception of the 5-K measurement of the

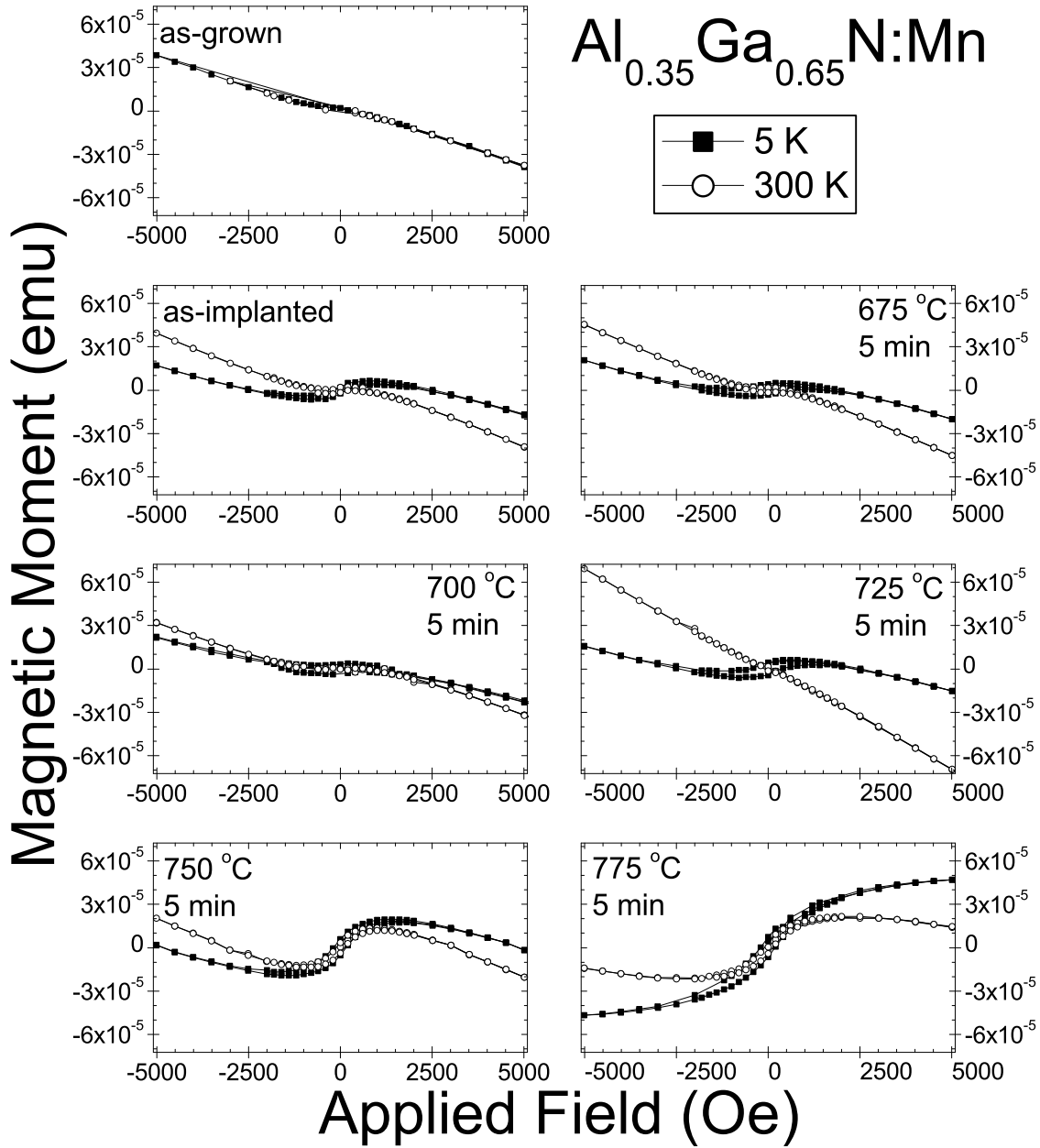


Figure 5.1 Raw data from magnetic hysteresis SQUID measurements of Mn-implanted $\text{Al}_{0.35}\text{Ga}_{0.65}\text{N}$ annealed as indicated in N_2 flowing at $2 \frac{\text{L}}{\text{min}}$.

sample annealed at $775 \text{ }^\circ\text{C}$ for 5 minutes. Furthermore, the room-temperature hysteresis measurements in the samples annealed at $725 \text{ }^\circ\text{C}$ and less can be characterized as diamagnetic behavior even though there is some token saturation and a small separation of the positive- and negative-going legs of the hysteresis loop. This behavior

indicates that the higher annealing temperatures (750 and 775 °C) are more likely to produce ferromagnetic behavior in Mn-implanted $\text{Al}_{0.35}\text{Ga}_{0.65}\text{N}$.

The raw data presented in figure 5.1 gives a sense of which samples show ferromagnetism. To quantify the ferromagnetic properties of these samples by the strength of coercive and remanent fields (H_c and B_R , respectively), it is necessary to remove the linear diamagnetic influence that is so prominent. Without this correction, data presented in figure 5.1 will give slightly erroneous values for coercive fields because the tilt induced by underlying diamagnetism will cause the zero magnetization line to cross the hysteresis loop at an angle. The SQUID data presented in figure 5.2 have the linear diamagnetic influences arising from the substrate removed. Diamagnetism is removed using a MATLAB[®] routine that determines the amount of rotation about the origin necessary to make the magnetization values at the two greatest applied magnetic fields (both positive and negative) equal in value. Each data point is then rotated by this amount so that saturation magnetization (M_S) becomes apparent, and accurate values for coercive and remanent fields can be ascertained. This method of removing linear magnetic background influences is not flawless as it tends to assign erroneously large values to H_c strengths when the sample is largely diamagnetic or paramagnetic. The problem in these samples is that the slope of the magnetization-versus-applied-field line is less as magnetic saturation is approached because of the small M_S values. When the hysteresis loop is rotated to remove diamagnetism, these gently sloped lines result in a wider area between zero crossings than the more nearly vertical lines that result in a sample less dominated by diamagnetism. This effect is clear in the contrast between corrected variable field measurements of the samples annealed at 725 and 750 °C as shown in figure 5.2.

The most striking feature of the data with background linear magnetic influences removed is the doubling of M_S for the samples annealed at 750 and 775 °C compared to the other samples. For the sample annealed at 775 °C for 5 minutes, M_S values of 0.41 and 0.37 μ_B per Mn atom were achieved at 5 and 300 K, respectively. The maximum calculated magneton value for Mn^{2+} is 5.9 μ_B per atom [8, Table 31.4]. This behavior

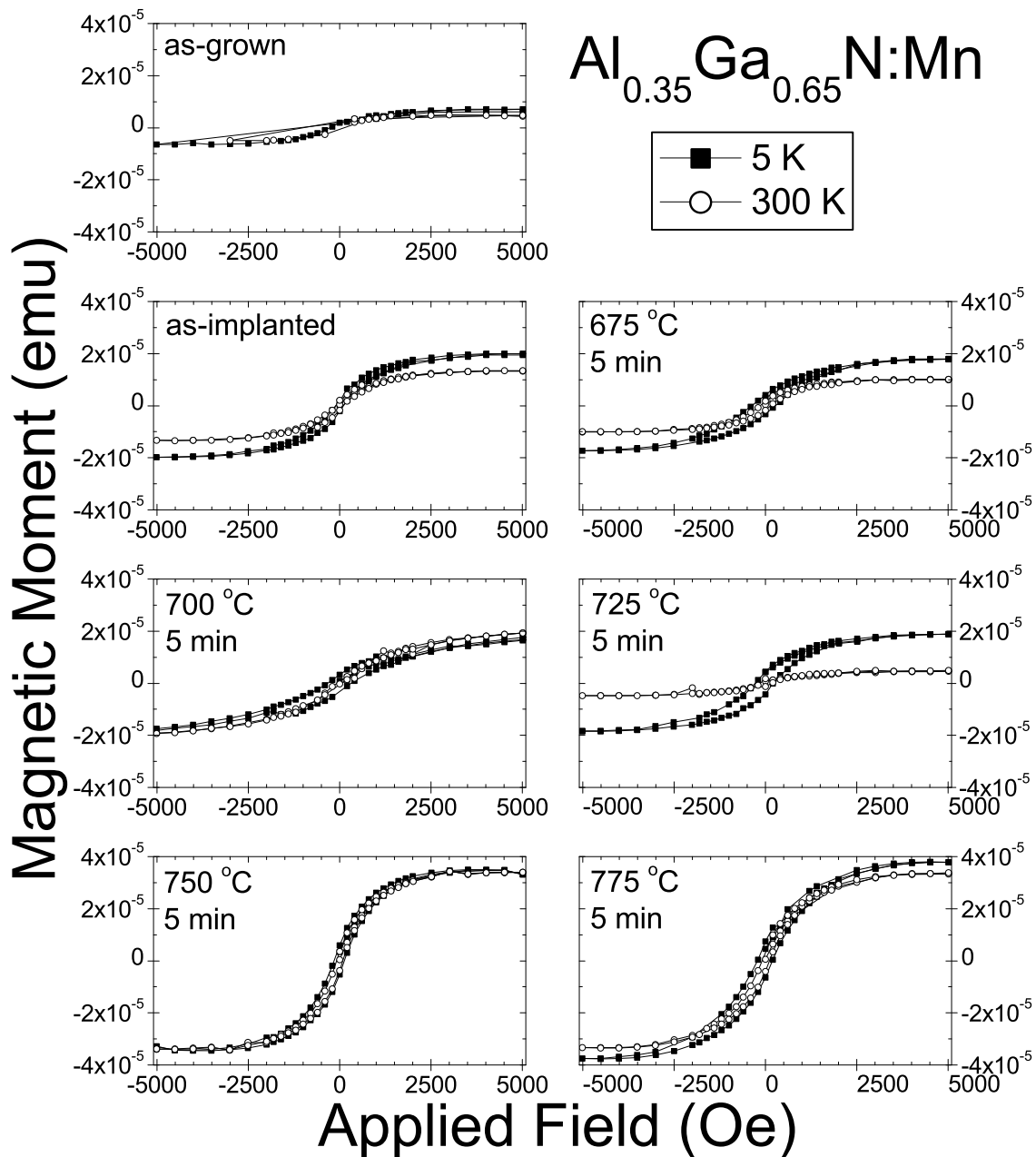


Figure 5.2 Magnetic hysteresis data for $\text{Al}_{0.35}\text{Ga}_{0.65}\text{N}$ implanted with Mn and annealed as indicated. Linear diamagnetic influences have been removed from this data.

indicates that Mn-implanted $\text{Al}_{0.35}\text{Ga}_{0.65}\text{N}$ should be annealed at a temperature of 750 °C or higher if the Mn is to be incorporated in a way that yields ferromagnetism. The larger saturation values also allow for a more accurate determination of H_c as discussed above.

Figure 5.3 presents a summary of the coercive field (H_c) strengths obtained using various annealing temperatures. Being aware of the artifacts of the background subtraction scheme detailed previously, the numerical values presented in figure 5.3 are false except for those reported for the samples annealed at 750 and 775 °C for 5 minutes.

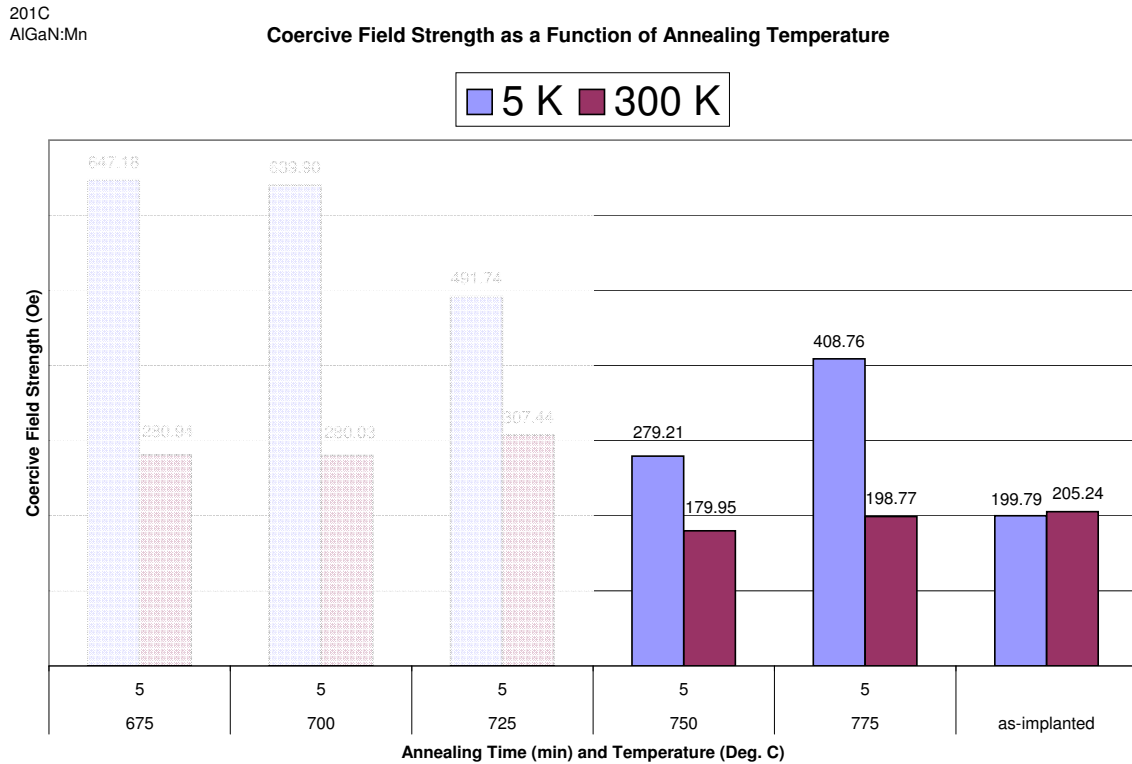


Figure 5.3 Coercive field strengths at 5 and 300 K for various annealing conditions of Mn-implanted Al_{0.35}Ga_{0.65}N. The data that have been skewed by the background subtraction process are obscured in this figure.

Remanent field strength measurements tend to be less sensitive to the rotation about the origin used to remove linear diamagnetic influences. The reason that B_R is less sensitive to the rotation can be explained geometrically: the orders of magnitude difference between the x and y axes means that the rotation necessary causes far less translation along the x axis than along the y axis, which means the value being measured directly above the origin does not change greatly after rotation. Unfortunately, saturation magnetization values are subject to gross errors resulting from

the rotation algorithm, so the values of B_R reported in figure 5.4 are not reported as magnetization values rather than as a percentage of M_S .

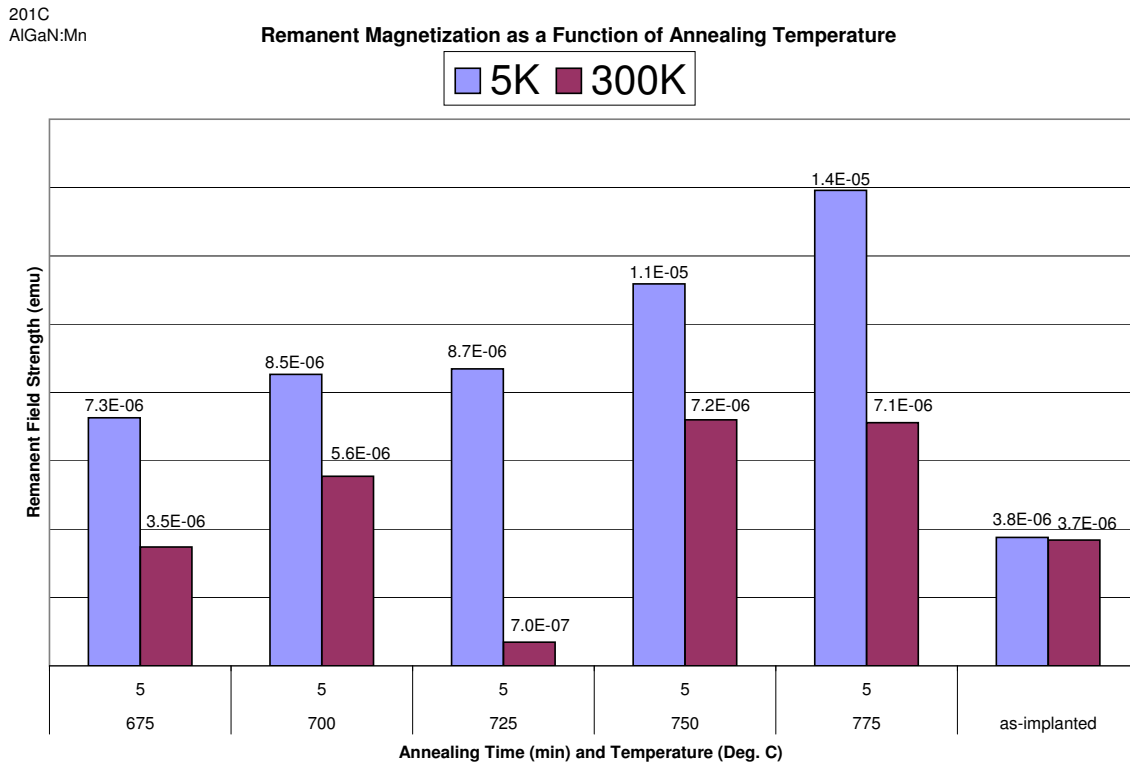


Figure 5.4 Remanent field strength differences at 5 and 300 K for various annealing conditions of Mn-implanted *p*-GaIn. Note that this data is presented as magnetization values in emu, not as a percentage of saturation magnetization as in the other figures reporting B_R .

The remanent field strengths of the samples tend to increase with increasing anneal temperature as shown in figure 5.4. This suggests that the optimal annealing temperature lies at the high end of the range of annealing temperatures tested. The increase in B_R at higher annealing temperatures corroborates the evidence seen in figures 5.1 and 5.2 (wider hysteretic separation and greater saturation magnetization) that the samples annealed at and above 750 °C are ferromagnetic.

5.1.2 Temperature-Dependent Magnetization

The magnetization-versus-temperature measurements for this sample are shown in figure 5.5. This data reveals a separation between zero-field-cooled (ZFC) and field-cooled (FC) magnetization that is approximately 50% greater at 100 and 300 K in

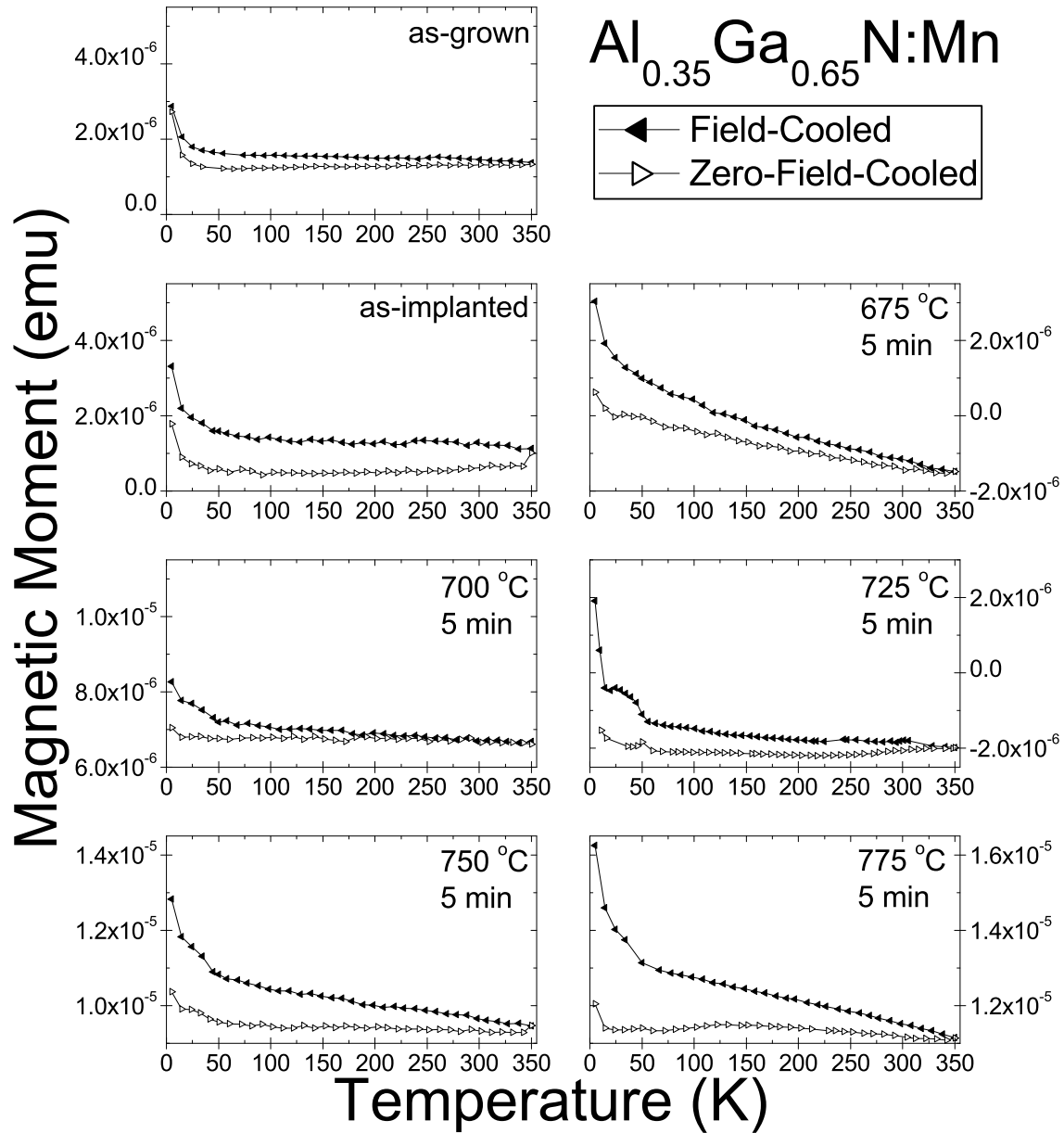


Figure 5.5 Temperature-dependent magnetization for $\text{Al}_{0.35}\text{Ga}_{0.65}\text{N}$ implanted with Mn and annealed as indicated for 5 minutes in N_2 flowing at $2 \frac{\text{L}}{\text{min}}$. Note that the y axis spans the same range of magnetic moment despite the fact that background offset causes a difference in absolute values.

the samples annealed at 750 and 775 °C than in the other samples. This separation is an indication of ferromagnetism, so these measurements are yet another sign that the samples annealed at and above 750 °C for 5 minutes incorporate the implanted Mn better than those annealed at lower temperatures.

In the sample annealed at 775 °C for 5 minutes, there is a broad peak in ZFC magnetization around 150 K. This is indicative of a spin-glass state in the material [89], but the relative insignificance of this peak compared to the separation in FC and ZFC magnetization and compared to the low-temperature rise in magnetization for both FC and ZFC measurements suggests that the sample is dominated by a ferromagnetic phase despite the presence of a spin-glass phase.

There is a cusp at 50 K in the sample annealed at 725 °C. This could also be indicative of spin-glass behavior, but is more likely a result of freezing oxygen that has either contaminated the sample space in the magnetometer or adsorbed to the surface of the $\text{Al}_{0.35}\text{Ga}_{0.65}\text{N}$. The conclusion that it is freezing oxygen is based on the fact that it occurs at 50 K [6] and that the dominant characteristic of the sample seen in variable field measurements is diamagnetic.

5.1.3 *Optical Measurements*

Cathodoluminescence spectra of the Mn-implanted $\text{Al}_{0.35}\text{Ga}_{0.65}\text{N}$ were collected at a temperature of approximately 5 K and are presented in figure 5.6. The band-edge peak for the as-grown $\text{Al}_{0.35}\text{Ga}_{0.65}\text{N}$ occurs around 4.4 eV. This is slightly larger than expected [73], so the Al content may be slightly higher than 35%. This band-edge feature is suppressed when Mn is implanted and is not recovered for any of the annealing conditions used in this experiment.

The as-implanted sample also shows a broad blue-green luminescence peak centered around 2.5 eV. This peak is attributed to defect-recombination bands in the unimplanted sample [91]. In the annealed $\text{Al}_{0.35}\text{Ga}_{0.65}\text{N}:\text{Mn}$ samples, the luminescence around 2.5 eV persists and becomes even stronger with its maximum intensity occurring in the sample annealed at 725 °C for 5 minutes. The jagged appearance

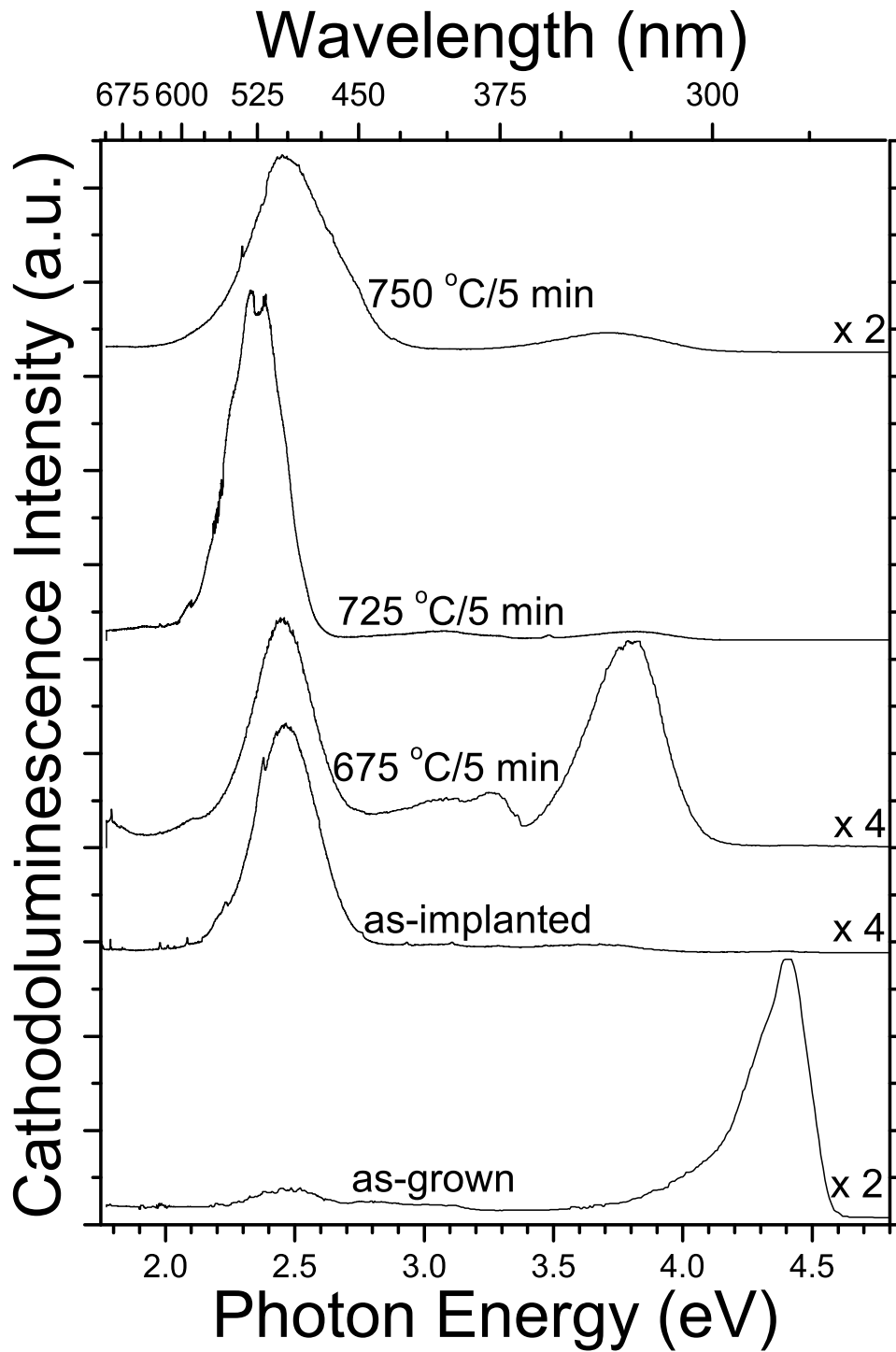


Figure 5.6 Cathodoluminescence spectra, collected from samples cooled to ~ 5 K, of $\text{Al}_{0.35}\text{Ga}_{0.65}\text{N}$ implanted with Mn and annealed at the indicated temperatures for 5 minutes in N_2 flowing at $2 \frac{\text{L}}{\text{min}}$.

of the top of this peak is due to the etalon effect induced by the index of refraction difference among the $\text{Al}_{0.35}\text{Ga}_{0.65}\text{N}:\text{Mn}$, the AlN buffer layer below it, and the vacuum above it. The increase in the blue-green luminescence with implantation is due to the fact that ion implantation produces a greater density of the defects related to this luminescence. The blue-green luminescence increases with annealing because annealing removes some of the non-radiative, light-absorbing defects before the damage related to the 2.5-eV feature is repaired. As evidenced in figure 5.6 for the sample annealed at 750 °C for 5 minutes, the blue-green luminescence starts to abate when the annealing temperature is sufficient to remove the radiative defects that cause it.

The sample annealed at 675 °C for 5 minutes shows a weak, broad luminescence with peaks at 3.3 and 3.1 eV. Though weaker, the 3.1-eV feature is also present in the sample annealed at 725 °C, and is due to incorporation of Mn into the $\text{Al}_{0.35}\text{Ga}_{0.65}\text{N}$. Similar 3.3-eV features are reported for transition-metal-implanted AlGaN and attributed to defects or complexes involving implanted Mn [91]. Since this luminescence declines in samples annealed at higher temperatures, it is possible to remove these defects or complexes and allow for the implanted Mn to be well-incorporated into the $\text{Al}_{0.35}\text{Ga}_{0.65}\text{N}$ crystal lattice.

Another defect-related feature that is common to all of the implanted samples is the broad peak around 3.5 eV. This peak is attributed to Al-N-O complexes which, in GaN, usually occur near the interface with the sapphire substrate [118], but in this case could occur virtually anywhere in the sample due to the AlN buffer layer, the Al content of the semiconductor film, and the pervasiveness of O as an unintended dopant. The intensity of this defect varies among the samples because of the effects of annealing on it, its location within the crystal and the penetration of the electron beam used to excite the sample.

5.2 Chromium-implanted Aluminum Gallium Nitride

Chromium ions were implanted into $\text{Al}_{0.35}\text{Ga}_{0.65}\text{N}$ with an implantation energy of 200 keV to a dose of $5 \times 10^{16} \frac{\text{ions}}{\text{cm}^2}$ at ambient temperature. Cr-implanted

$\text{Al}_{0.35}\text{Ga}_{0.65}\text{N}$ also shows clear signs of ferromagnetism under two sets of annealing conditions. Unfortunately, these are at non-consecutive annealing temperatures (725 and 775 °C), which indicates that competing magnetic phases, as seen in the temperature-dependent magnetization measurements (shown in figure 5.12) may play a role. As far as future DMS application work goes, $\text{Al}_{0.35}\text{Ga}_{0.65}\text{N}:\text{Cr}$ has shown desirable properties and should be integrated into initial device studies.

5.2.1 *Magnetic Hysteresis Measurements*

Variable field measurements of Cr-implanted $\text{Al}_{0.35}\text{Ga}_{0.65}\text{N}$ were made using a SQUID magnetometer at both 5 and 300 K. Data from hysteresis measurements, presented in figure 5.7, shows that coercive fields (H_c) and saturation magnetization (M_S) both increase with increasing annealing temperature. There is also a noticeable decrease in the dominance of background diamagnetism as annealing temperature increases. This decrease in diamagnetism may be a result of annealing effects on the substrate and $\text{Al}_{0.35}\text{Ga}_{0.65}\text{N}$ film or the strengthening of ferromagnetism as annealing temperature increases. Regardless of the background behavior, the trend of increasing H_c and M_S make it apparent that ferromagnetism becomes stronger with higher anneal temperatures (at least up to 775 °C) in Cr-implanted $\text{Al}_{0.35}\text{Ga}_{0.65}\text{N}$.

The hysteresis loops with diamagnetic substrate contributions removed are shown in figure 5.8. The rotation to remove linear magnetic influences is performed primarily to allow more accurate measurements of H_c , B_R , and M_S . As detailed in section 5.1.1, the diamagnetic background is subtracted by rotating all of the data points about the origin by the amount necessary to make the magnetic measurements above saturation level with the x axis. Subtracting the background makes the trends discussed above (increasing H_c and M_S with increasing annealing temperature) more apparent.

The results of the variable field measurements, in terms of H_c , are presented in figure 5.9. In the case of the room-temperature measurement on the sample annealed at 675 °C for 5 minutes, the background subtraction causes an erroneously large value

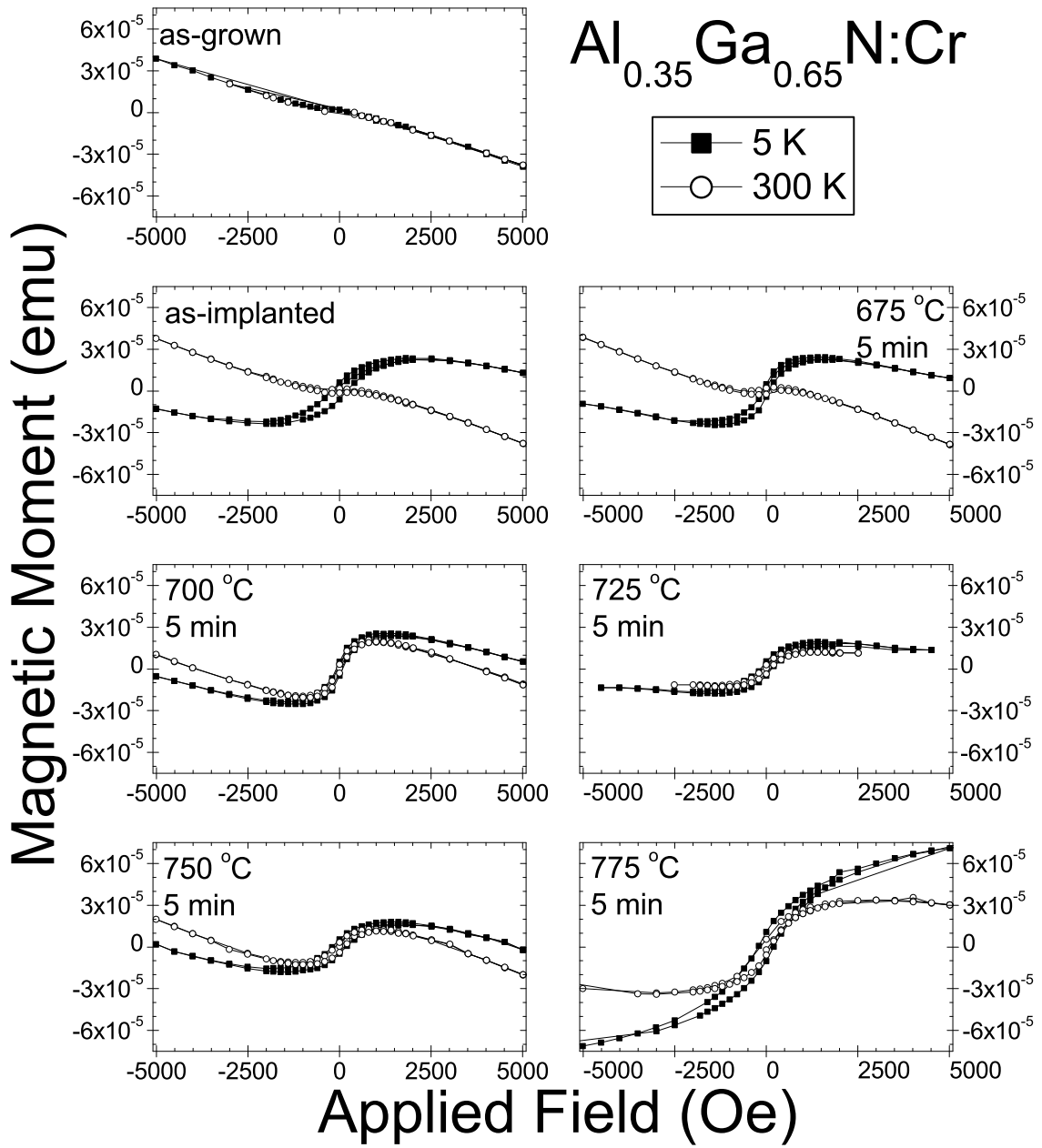


Figure 5.7 Raw data from magnetic hysteresis SQUID measurements of Cr-implanted $\text{Al}_{0.35}\text{Ga}_{0.65}\text{N}$ annealed as indicated for 5 minutes in N_2 flowing at $2 \frac{\text{L}}{\text{min}}$.

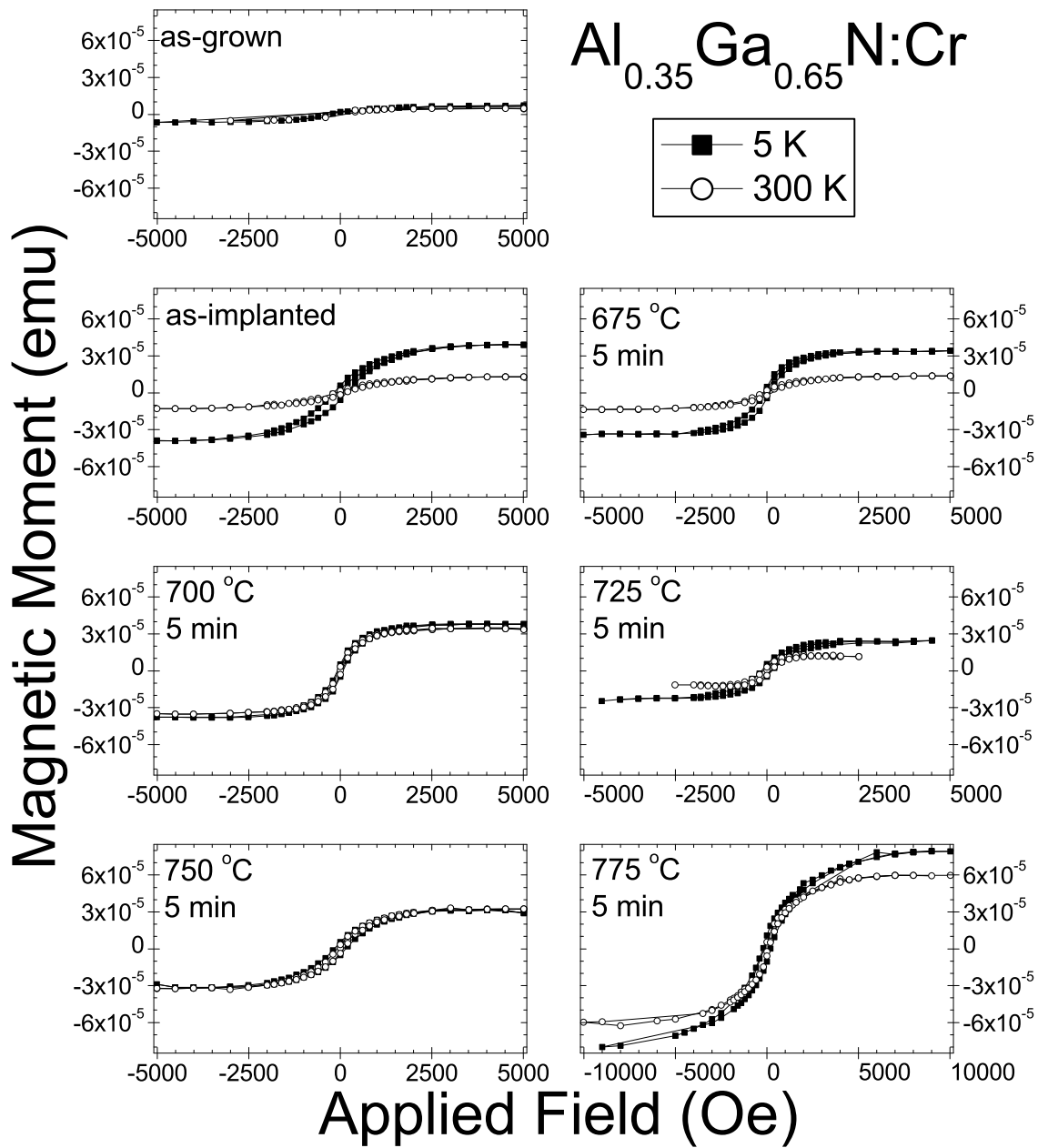


Figure 5.8 Magnetic hysteresis data for $\text{Al}_{0.35}\text{Ga}_{0.65}\text{N}$ implanted with Cr and annealed as indicated in N_2 flowing at $2 \frac{\text{L}}{\text{min}}$ for 5 minutes. Linear diamagnetic influences have been removed from this data.

Coercive Field Strength as a Function of Annealing Temperature

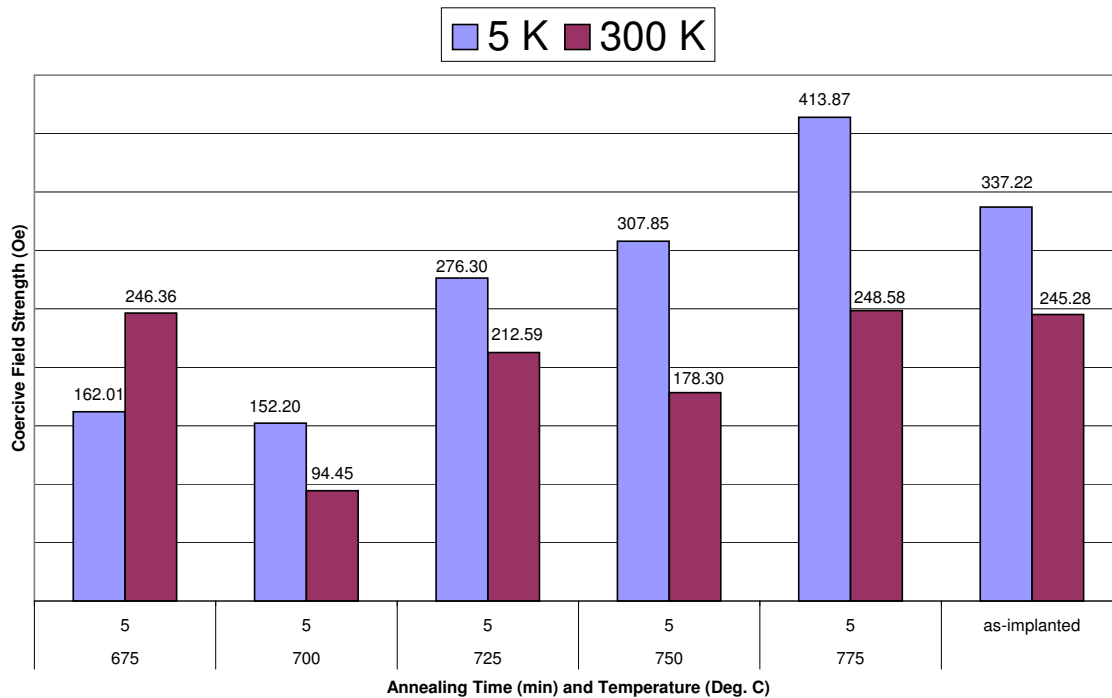


Figure 5.9 Coercive field strengths at 5 and 300 K for various annealing conditions of Cr-implanted $\text{Al}_{0.35}\text{Ga}_{0.65}\text{N}$.

for H_c due to the very weak saturation magnetization. Section 5.1.1 contains a more detailed discussion of this effect. Given that the numerical value assigned to the room-temperature measurement of the sample annealed at 675 °C for 5 minutes is incorrect, the data displayed in figure 5.9 show a clear trend of increasing coercivity with increasing annealing temperature for measurements taken at both 5 and 300 K.

The remanent field strengths determined from variable field measurements are charted in figure 5.10. This data again shows a trend toward the strongest B_R at the highest annealing temperature. From the measurements presented in figures 5.7 and 5.8, this is expected due to the high M_S values seen in the sample annealed at 775 °C for 5 minutes. Specifically, the M_S values seen in this sample are 1.1 and 0.67 μ_B per Cr atom (maximum calculated for Cr^{2+} is 4.8) [8, Table 31.4].

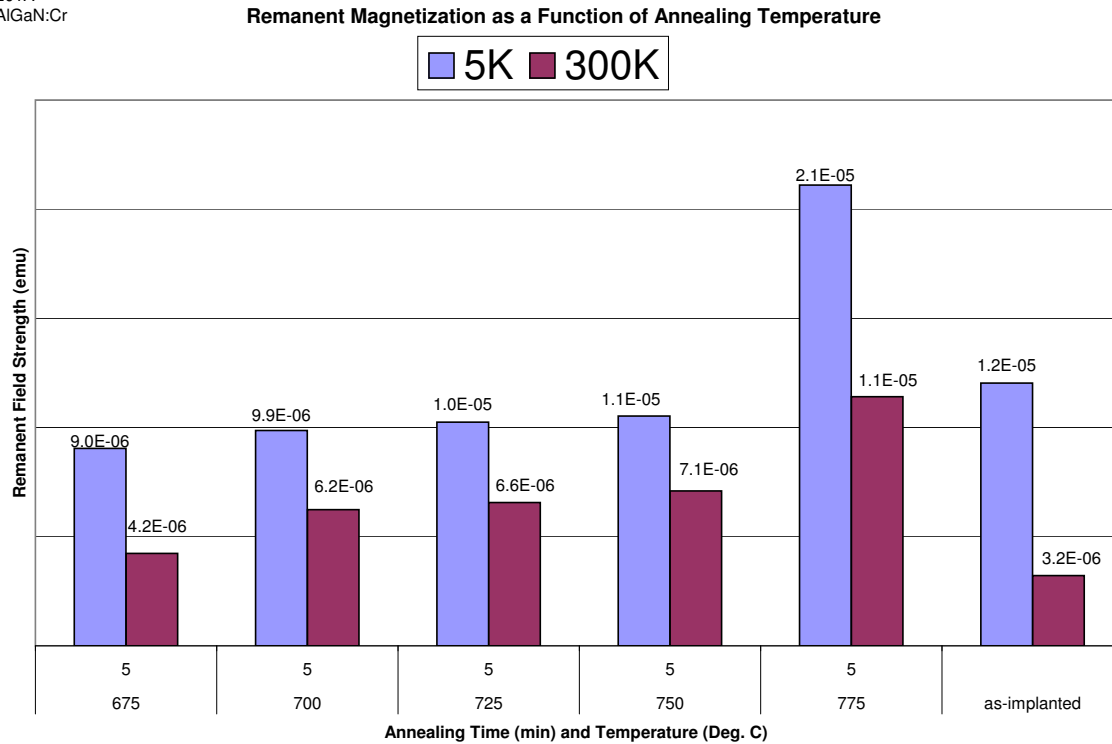


Figure 5.10 Remanent field magnetization values at 5 and 300 K for various annealing conditions of Cr-implanted $\text{Al}_{0.35}\text{Ga}_{0.65}\text{N}$. Note that this is raw data and not presented as a function of saturation magnetization.

When remanent fields are calculated as a percentage of saturation magnetization, the results are different. As seen in figure 5.11, the greatest B_R as a percentage of M_S is produced in the sample annealed at 725 °C for 5 minutes.

The hysteresis data for both the sample annealed at 725 °C and the one annealed at 775 °C show clean signals with respectable saturation values. The difference in peak remanency depending on whether raw values or percentage of saturation is used indicates that there may be a secondary phase present in one of the samples. Variable temperature measurements and X-ray diffraction will help determine whether this is the case and which sample is most likely to exhibit true DMS behavior.

5.2.2 Temperature-dependent Magnetization

Magnetization-versus-temperature measurements for $\text{Al}_{0.35}\text{Ga}_{0.65}\text{N}$ implanted with Cr are presented in figure 5.12. The data indicates a dominant ferromagnetic

Remanent Magnetization as a Function of Annealing Temperature

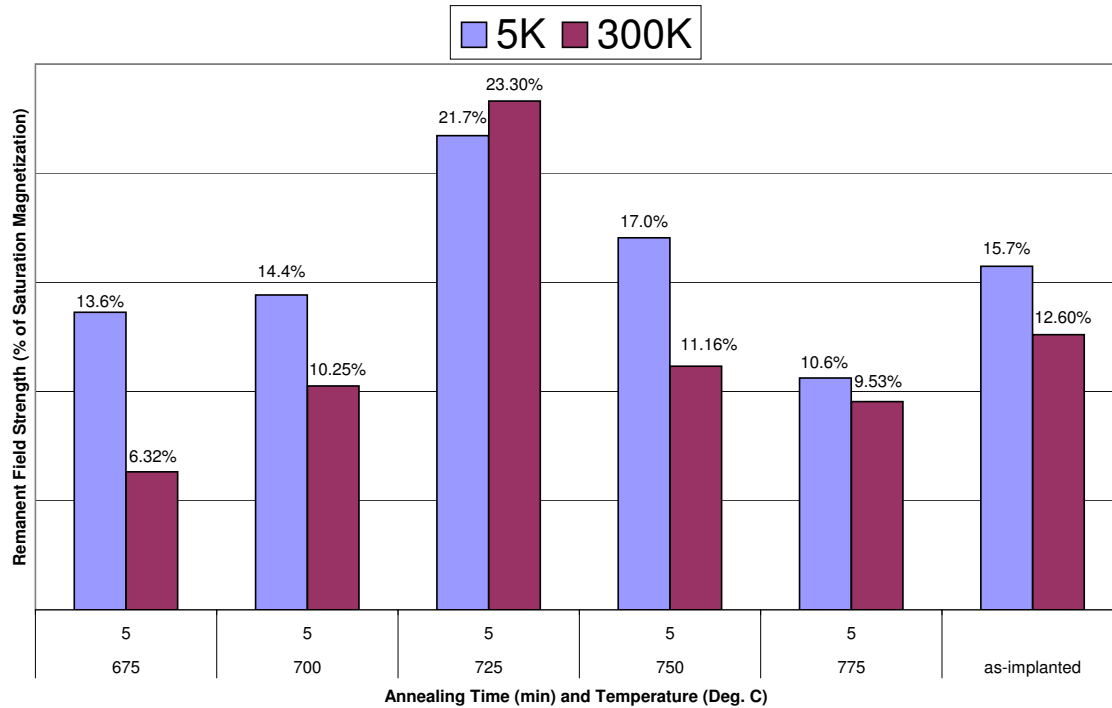


Figure 5.11 Remanent field strengths as a function of M_S at 5 and 300 K for various annealing conditions of Cr-implanted $\text{Al}_{0.35}\text{Ga}_{0.65}\text{N}$.

phase in the samples annealed between 700 and 750 °C. In these samples, the ZFC magnetization varies only a little except for the upward trend at low temperatures. This tracks well with the FC magnetization below 50 K. This behavior, along with the separation between FC and ZFC magnetization at all temperatures in this measurement, indicates that ferromagnetism is dominant for $\text{Al}_{0.35}\text{Ga}_{0.65}\text{N}:\text{Cr}$ annealed between 700 and 750 °C.

Despite the relatively clean signal, the strength of the magnetization (as judged by the difference in FC and ZFC measurements) from the as-implanted sample is far less than for the annealed samples, particularly at higher temperatures. The absence of a spin-glass in the as-implanted sample is not altogether surprising: the sparse Cr interstitials that are likely to dominate the magnetic characteristics of such a sample are not able to coordinate themselves into a spin-glass state (as defined in

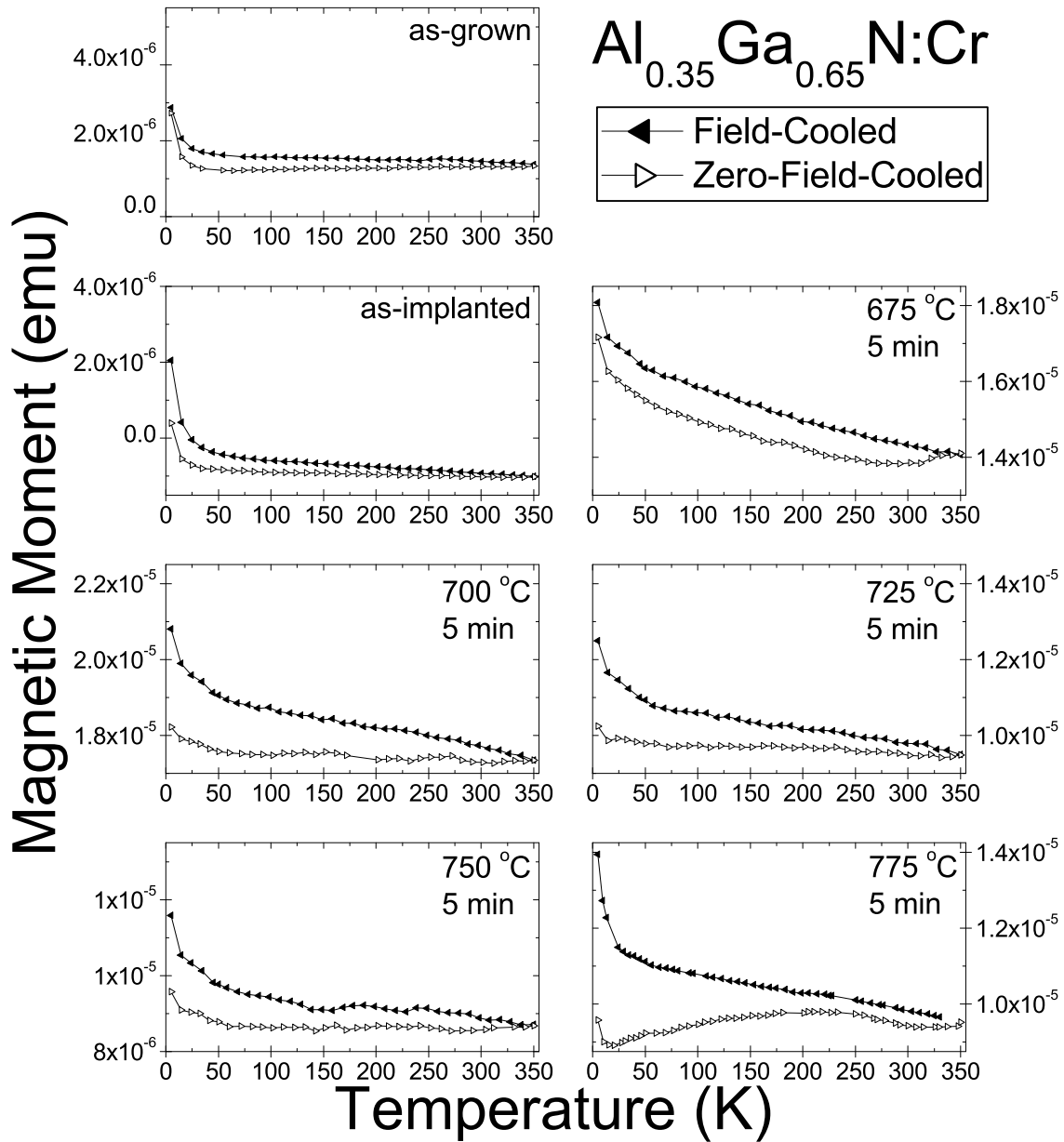


Figure 5.12 Temperature-dependent magnetization for $\text{Al}_{0.35}\text{Ga}_{0.65}\text{N}$ implanted with Cr. Samples were annealed in N_2 flowing at $2 \frac{\text{L}}{\text{min}}$ at the temperatures indicated for 5 minutes. Note that the y axis spans the same range of magnetic moment despite the fact that background offset causes a difference in absolute values.

section 2.1), but will more likely display superparamagnetism due to their partially-filled d -shells [12, 106].

The sample annealed at 675°C shows some separation in FC and ZFC magnetization, but the near linear decrease in magnetic moment with increasing temperature

indicates that paramagnetism is the dominant characteristic of this sample. This corroborates the variable field measurement for this sample presented in figure 5.8 where there is a small H_c value is also indicative of superparamagnetism.

There is an unsustained increase in ZFC magnetization values as the measurement temperature is raised for the sample annealed at 775 °C for 5 minutes. This indicates the presence of a spin-glass phase [89]. The spin-glass phase is dominated by ferromagnetism at low temperature as evidenced by the upward track of both ZFC and FC magnetization data. The spin-glass magnetic behavior is most likely the result of secondary phase formation due to hotter annealing conditions. As further evidence of the conclusion that a spin-glass has been formed under these annealing conditions, this phenomenon was also seen in Cr-implanted *p*-GaN annealed at 775 °C. Likely secondary phases of the materials studied in this research and their magnetic properties are discussed in Appendix B.

The presence of a spin-glass phase in the sample annealed at 775 °C and the clearly ferromagnetism-dominated variable temperature measurement of the sample annealed at 725 °C for 5 minutes indicate that the sample annealed at 725 °C may be the true DMS despite its lesser H_c and M_S values.

5.2.3 Optical Measurements

The cathodoluminescence data for the various annealing temperatures is presented in figure 5.13. CL measurements of $\text{Al}_{0.35}\text{Ga}_{0.65}\text{N}:\text{Cr}$ show that implantation damage recovery increases with increasing annealing temperature. The primary area of the optical damage recovery is the blue-green luminescence centered around 2.5 eV.

As expected, this CL data shows that ion implantation causes damage resulting in the disappearance of the band-edge peak and the suppression of all luminescence except for a small, broad peak at 3.8 eV. The strength of the broad luminescence at 3.8 eV in the as-implanted sample suggests that it arises from Al-N-O complexes at the Al_2O_3 interface [118]. The signature of these complexes is present in all of the Cr-implanted samples, but is strongest in the sample annealed at 675 °C for 5

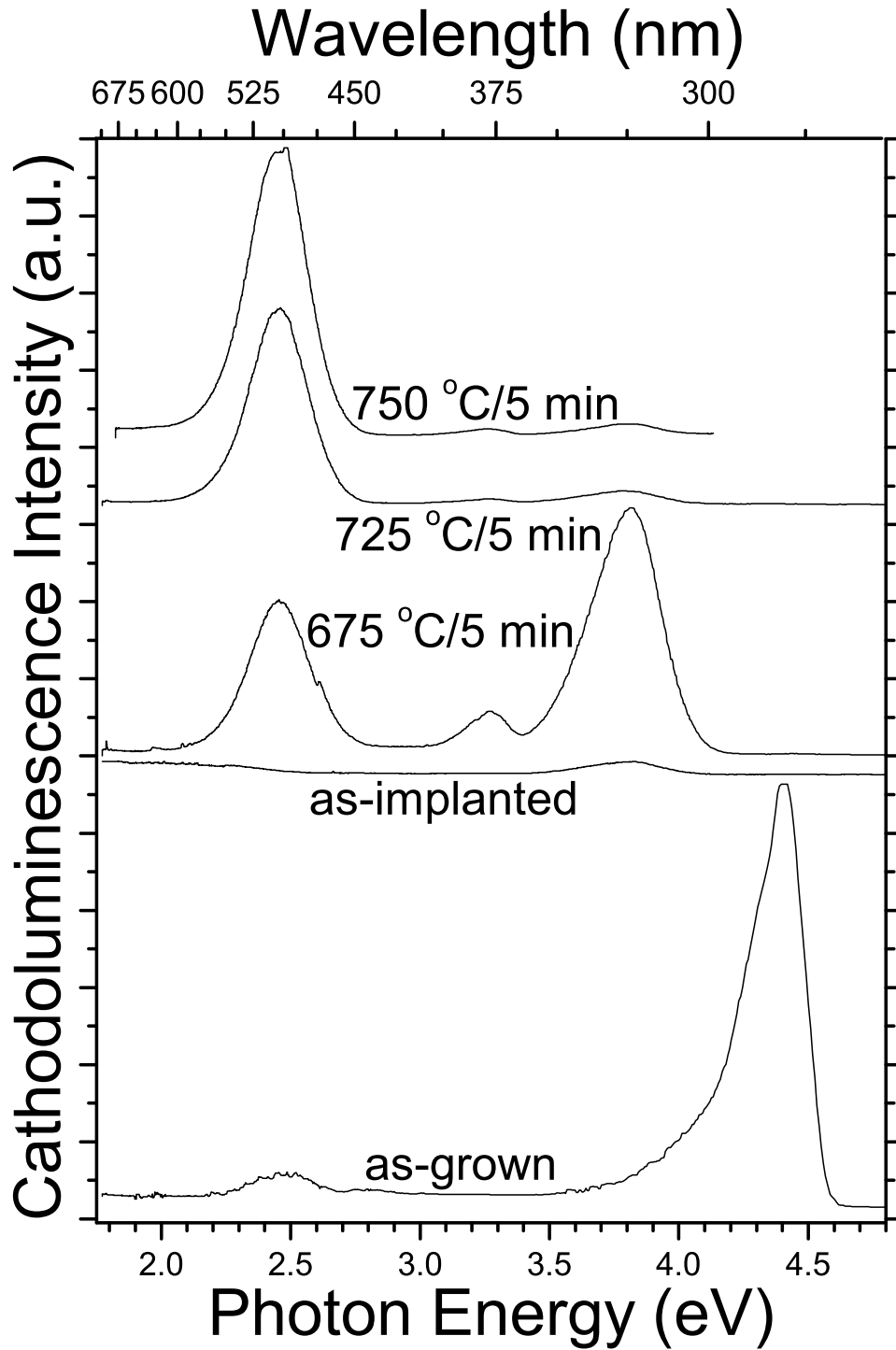


Figure 5.13 Cathodoluminescence spectra of Al_{0.35}Ga_{0.65}N implanted with Cr and annealed as indicated for 5 minutes in N₂ flowing at 2 $\frac{\text{L}}{\text{min}}$. CL measurements were taken at approximately 5 K.

minutes. Annealing at this temperature is apparently favorable for the formation of this defect in $\text{Al}_{0.35}\text{Ga}_{0.65}\text{N}$ as shown by its prevalence in figures 5.6 and 5.19 which verify that the 3.8-eV luminescence is strongest in the sample annealed at 675 °C regardless of the implanted transition metal.

Another CL feature that is most prominent in the sample annealed at 675 °C and present to a lesser degree in the remaining annealed samples is the small peak at 3.27 eV. This peak is attributed to a donor-acceptor pair DAP [16]. As annealing temperature is increased, the DAP transition becomes less visible. This is likely due to increased absorption by the defect that leads to the blue-green luminescence centered around 2.5 eV.

The luminescent intensity in the blue-green region (2.5 eV) increases with annealing temperature and is strongest when the sample is annealed at 750 °C for 5 minutes. In the case of Si-implanted AlGa_{0.65}N, the increasing strength of mid-gap luminescence in this range indicates greater levels of dopant incorporation into the crystal lattice [98]. The same is likely true concerning incorporation of Cr into the $\text{Al}_{0.35}\text{Ga}_{0.65}\text{N}$ crystal lattice, particularly since magnetic coordination, which also depends on crystal quality, is strongest in the samples annealed at and above 725 °C.

5.3 Nickel-doped Aluminum Gallium Nitride

The $\text{Al}_{0.35}\text{Ga}_{0.65}\text{N}$ samples were implanted with Ni to a dose of $3 \times 10^{16} \frac{\text{ions}}{\text{cm}^2}$ at room temperature with an implantation energy of 200 keV. This lower dose showed a higher magnetic ordering temperature than samples doped to $5 \times 10^{16} \frac{\text{ions}}{\text{cm}^2}$ in reports about Ni-implanted *p*-Ga_{0.65}N [90]. The lower dose also reduces the probability of clustering during annealing.

Ni-implanted $\text{Al}_{0.35}\text{Ga}_{0.65}\text{N}$ shows ferromagnetic behavior when annealed at a temperature of 700 °C for 5 minutes in a $2 \frac{\text{L}}{\text{min}}$ flow of N₂. There are other annealing conditions that produce signatures of ferromagnetism in this material, but the indications are somewhat conflicting. Given the character of the data collected, it is

possible that annealing another Ni-implanted $\text{Al}_{0.35}\text{Ga}_{0.65}\text{N}$ sample under the same conditions would produce a more definite signature of ferromagnetism. Yield and repeatability problems have been noted in attempts to fabricate DMS material [120], so it may be that $\text{Al}_{0.35}\text{Ga}_{0.65}\text{N:Ni}$ is sensitive to some unknown variable that is not well controlled in this experiment. Regardless of the difficulty in determining optimal annealing conditions, the unmistakable magnetic properties of this material make it a candidate for continuing DMS work.

5.3.1 *Magnetic Hysteresis Measurements*

Variable field measurements of $\text{Al}_{0.35}\text{Ga}_{0.65}\text{N:Ni}$ were obtained and the results are shown in figure 5.14. These measurements reveal that the sample annealed at 700 °C for 5 minutes demonstrates the greatest dominance of ferromagnetism over the background diamagnetism as well as the highest saturation magnetization. These measurements also show that the magnetic signatures of ferromagnetism (hysteretic separation and saturation) persist to room temperature in the samples annealed between 675 and 775 °C.

In order to ensure accurate measurements of the coercive field (H_c) and saturation magnetization (M_S) values, the raw hysteresis data presented in figure 5.14 need to have the dia- or para-magnetic background subtracted. Linear magnetic influences are removed by rotating all of the data points around the origin so that the linear region that occurs after M_S has been reached is parallel to the x axis. The background subtraction process is detailed more fully in section 5.1.1. In cases where there is a discontinuity in the data, such as the $\text{Al}_{0.35}\text{Ga}_{0.65}\text{N:Ni}$ sample annealed at 650 °C for 5 minutes, the magnetization data collected above the applied magnetic field where the discontinuity occurs is ignored for the purpose of determining the amount of rotation necessary to eliminate the background diamagnetism.

The data processed to remove ferromagnetism are depicted in figure 5.15. The corrected data make the dominance of M_S in the sample annealed at 700 °C for 5 minutes even more clear. An M_S of $1.8 \mu_B$ per Ni atom was observed at both 5

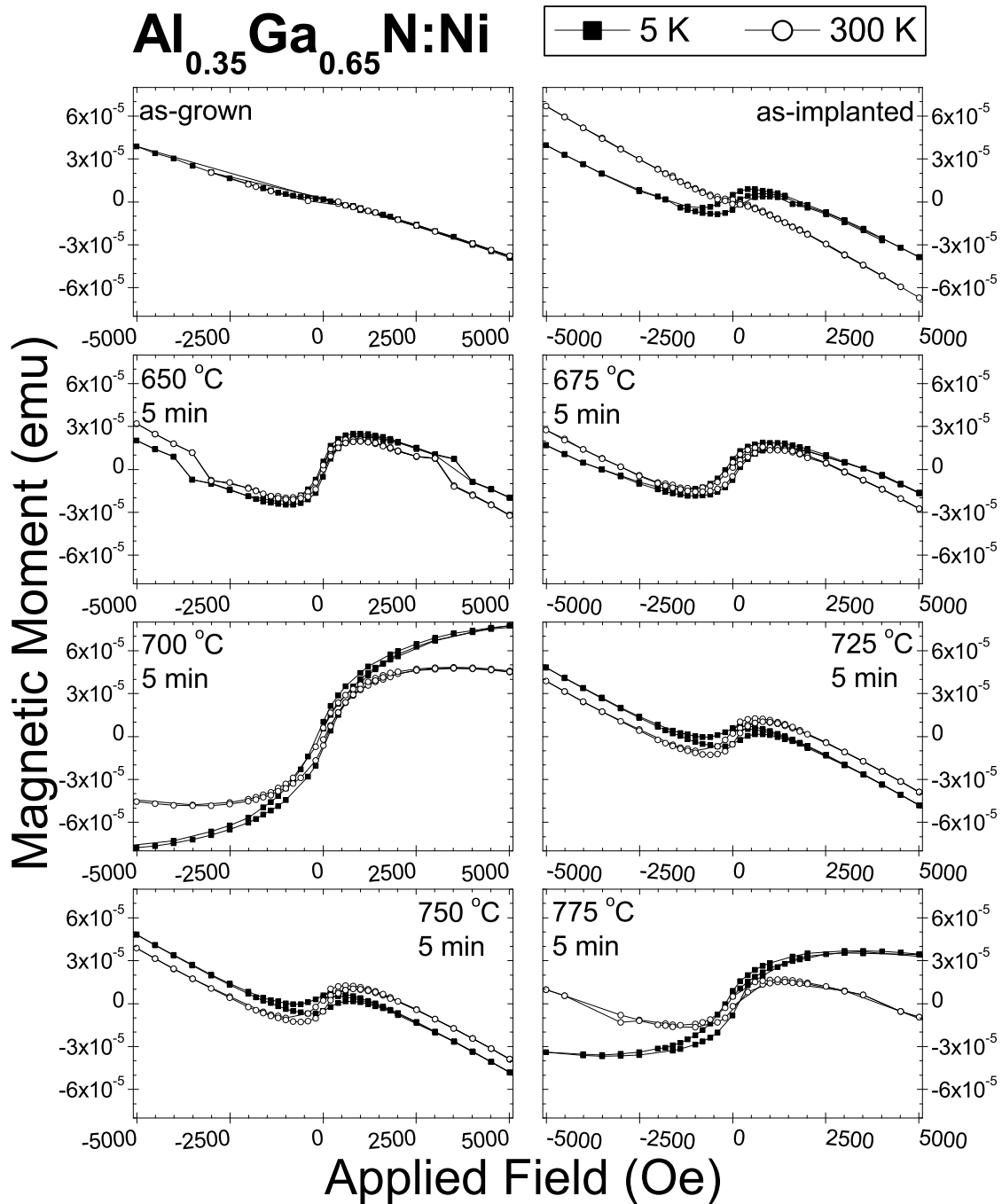


Figure 5.14 Raw data from magnetic hysteresis SQUID measurements of Ni-implanted Al_{0.35}Ga_{0.65}N annealed as indicated in N₂ flowing at 2 $\frac{L}{min}$ for 5 minutes.

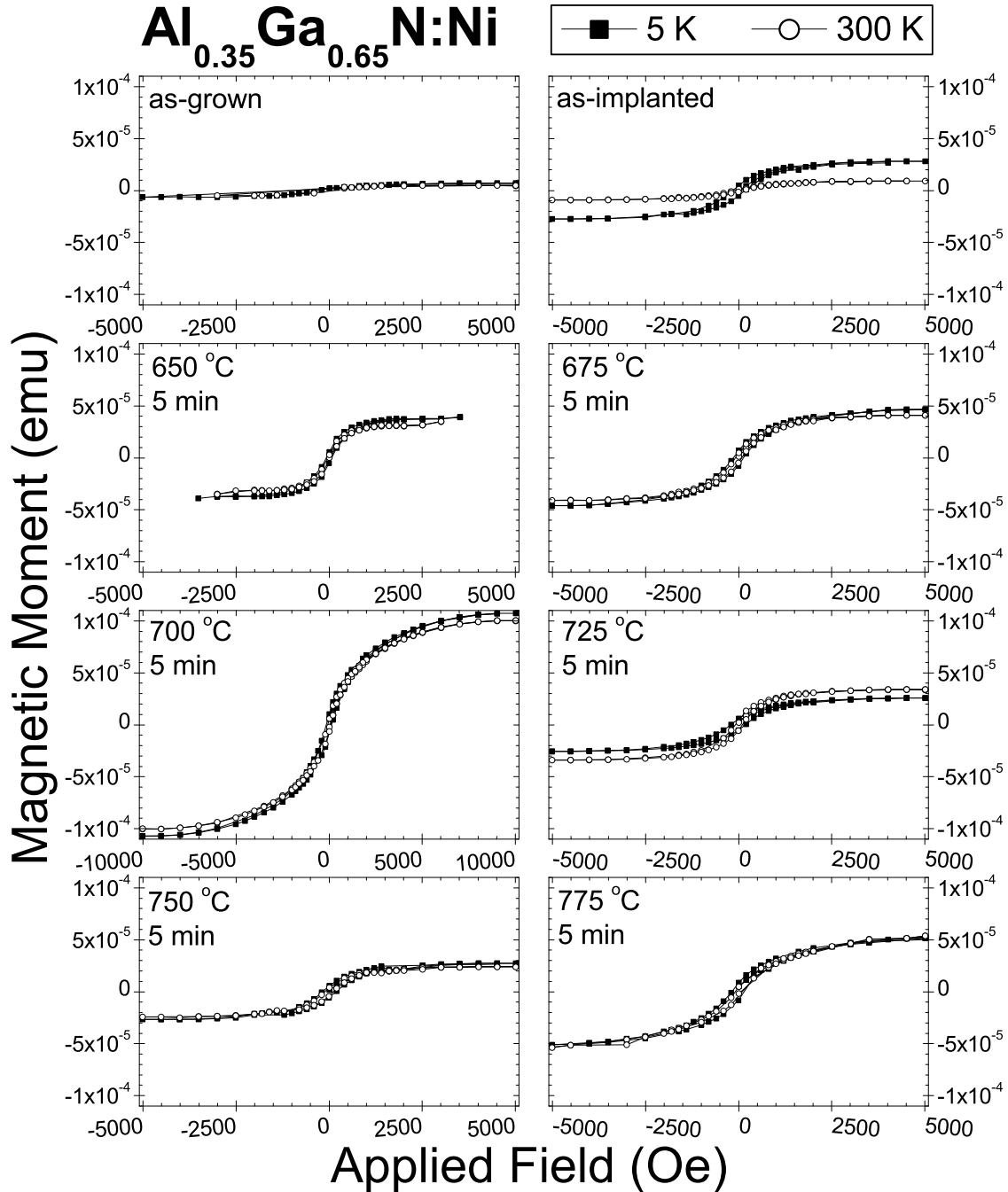


Figure 5.15 Magnetic hysteresis data for Al_{0.35}Ga_{0.65}N implanted with Ni and annealed as indicated for 5 minutes in a 2 $\frac{\text{L}}{\text{min}}$ flow of N₂. Linear diamagnetic influences have been removed from this data.

and 300 K in this sample. The calculated maximum effective magneton number for Ni^{2+} is 3.2 [8, Table 31.4]. H_c for this sample may appear smaller in figure 5.15, but this is because the applied field scale has been increased to 1 T in order to show the full measure of magnetic saturation in this sample. An applied magnetic field of 1 T was also necessary to positively define M_S in the sample annealed at 775 °C, even though the magnetization proved to be less at saturation than for the sample annealed at 700 °C for 5 minutes. Higher applied magnetic fields were not necessary in the other samples as shown by the highly linear magnetization response after reaching saturation in both the corrected and uncorrected data, figures 5.14 and 5.15, respectively. From the appearance of the hysteresis data, the best annealing temperature for this sample is 700 °C.

In figure 5.16, the numerical values of H_c determined from the variable field measurements with diamagnetism removed are reported. These values, however, are

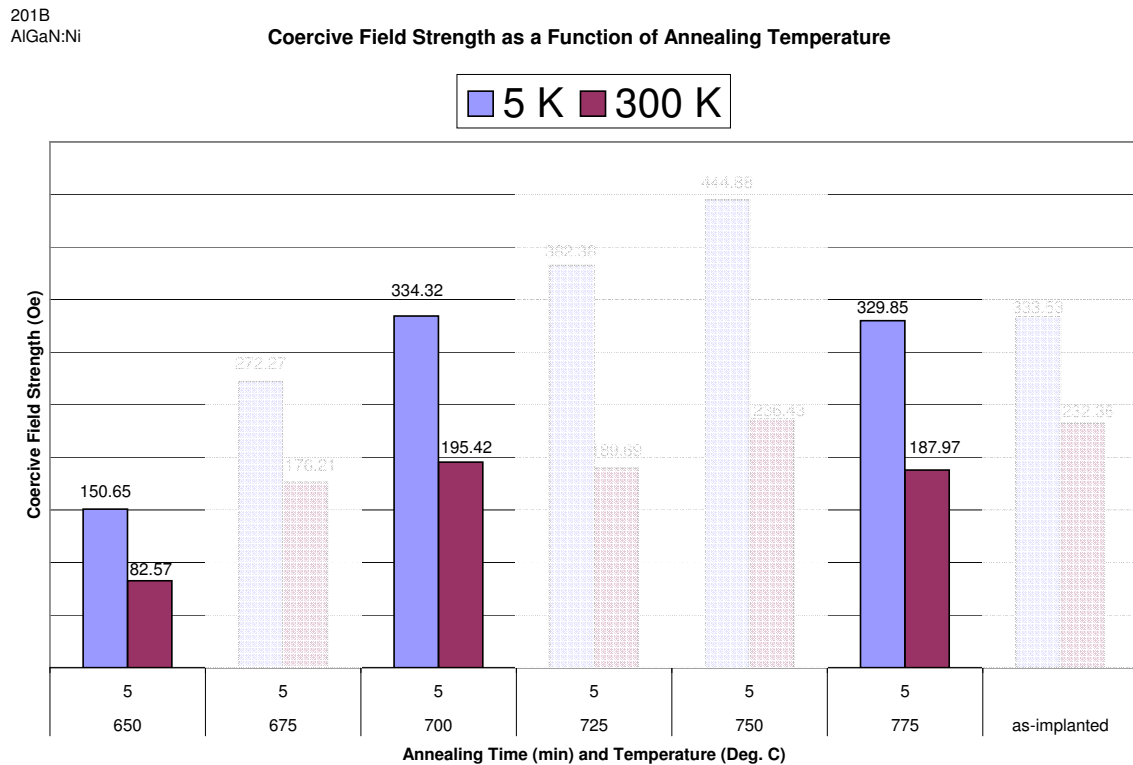


Figure 5.16 Coercive field strengths at 5 and 300 K for various annealing conditions of Ni-implanted $\text{Al}_{0.35}\text{Ga}_{0.65}\text{N}$.

misleading because of the tilt present near the zero magnetization crossings. From figure 5.15, it is apparent that the only annealing temperatures for which a reasonable coercivity value could be calculated are those annealed at 650, 700, and 775 °C. When only the measurements under these conditions (those not obscured in figure 5.16) are considered, it is clear that the maximum H_c values at both 5 and 300 K are obtained when the sample is annealed at 700 °C for 5 minutes. The fact that the H_c values determined for the sample annealed at 775 °C are similar to those for the 700 °C annealed sample means that further metrics are needed in order to determine which annealing conditions are most favorable for creating a ferromagnetic semiconductor.

The remanent field strengths are shown for the various annealing conditions in figure 5.17. This data points to the sample annealed at 700 °C for 5 minutes as the one with the strongest remanent field at both 5 and 300 K. The artifacts of

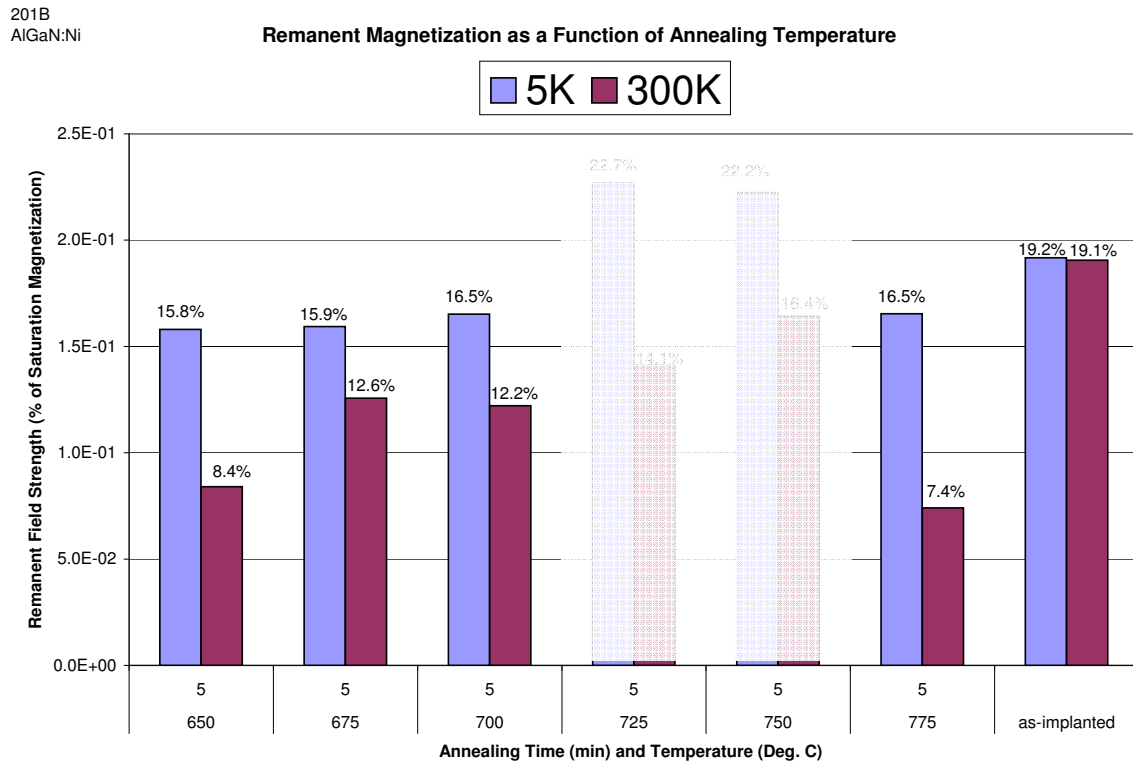


Figure 5.17 Remanent field strengths at 5 and 300 K for various annealing conditions of Ni-implanted Al_{0.35}Ga_{0.65}N.

background subtraction that cause erroneous H_c values also produce inaccuracies in M_S , so the raw B_R data is given in figure 5.17 rather than B_R as a percentage of M_S .

5.3.2 *Temperature-Dependent Magnetization*

Both field-cooled and zero-field-cooled magnetization-versus-temperature measurements for Ni-implanted $\text{Al}_{0.35}\text{Ga}_{0.65}\text{N}$ are presented in figure 5.18. The as-implanted sample shows divergence between FC and ZFC magnetization at low temperature, which verifies the lack of ferromagnetism demonstrated in the variable field measurements. For samples annealed at 725 °C and below, there is an upward tracking together between ZFC and FC measurements at low temperature, which indicates the presence of a ferromagnetic phase. However, this tracking is mild for the samples annealed at 650 and 675 °C. The cusps in the ZFC measurements for samples annealed at 700 and 725 °C indicate the presence of a spin-glass state that exists along with the ferromagnetic phase. The spin-glass state decays above approximately 250 K for the samples annealed at 650 and 700 °C and 75 K for the sample annealed at 725 °C. There is no low-temperature tracking between FC and ZFC magnetization for the sample annealed at 750 °C for 5 minutes, so there is no indication of ferromagnetism from the temperature-dependent measurements. The sample annealed at 775 °C for 5 minutes shows some indication of ferromagnetic ordering below 325 K, where there is separation between the FC and ZFC magnetization curves. As in many of the other samples, there is also a broad peak centered around 200 K that may indicate there is a spin-glass phase present in this sample as well.

For all of the samples, there is very little separation between FC and ZFC magnetization at high temperature. This suggests that the magnetic order that is present may be weak. From temperature-dependent magnetization data collected, it is difficult to determine an optimal set of annealing conditions. The hysteresis measurements inspired some doubt about which annealing conditions are optimal, but the overall indication is that annealing at 700 °C for 5 minutes is best.

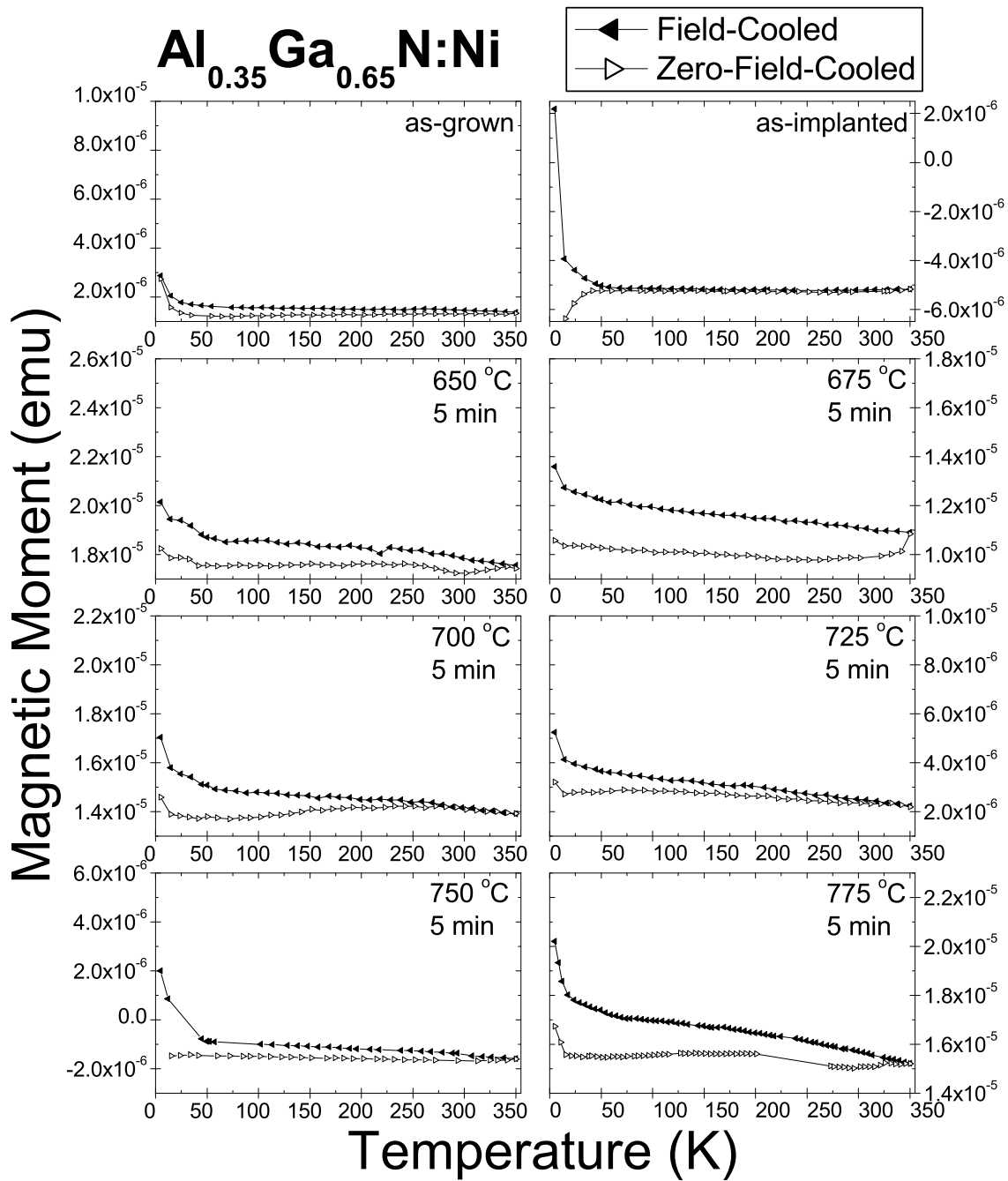


Figure 5.18 Temperature-dependent magnetization for $\text{Al}_{0.35}\text{Ga}_{0.65}\text{N}$ implanted with Ni. Samples are annealed as indicated in the figure for 5 minutes in N_2 flowing at $2 \frac{\text{L}}{\text{min}}$. Note that the y axis spans the same range of magnetic moment despite the fact that background offset causes a difference in absolute values.

5.3.3 Optical Measurements

The dependence of CL profiles on annealing temperature is illustrated in figure 5.19. The as-grown sample has a band-edge peak at 4.41 eV. A slightly lower value is predicted by measurement-based calculations for $\text{Al}_{0.35}\text{Ga}_{0.65}\text{N}$ [73], so the AlGaN may have a slightly higher mole fraction of aluminum than intended. Luminescence from the Ni-implanted $\text{Al}_{0.35}\text{Ga}_{0.65}\text{N}$ is almost totally squelched by the implantation process as shown in figure 5.19. An intense green luminescence dominates in the sample annealed at 650 °C and those annealed at or above 700 °C. The sample annealed at 675 °C for 5 minutes has its dominant luminescence peak in the UV near a photon energy of 3.8 eV. This peak is present in all of the annealed samples to some degree and is attributed to defects in the sapphire substrate [118]. As observed in the other $\text{Al}_{0.35}\text{Ga}_{0.65}\text{N}$ samples, and reported in sections 5.1.3 and 5.2.3, annealing at 675 °C tends to maximize the Al-N-O complexes near the Al_2O_3 interface. Annealing chamber contamination is eliminated as a source of these complexes because contaminants will not diffuse through the AlN capping layer and because this behavior is not universal in the *p*-GaN samples annealed at the same time as these samples. The small peak at 3.477 eV, which is most noticeable in the sample annealed at 700 °C for 5 minutes, is attributed to free excitons in GaN [84, 107]. The appearance of this feature indicates possible phase segregation in the sample annealed at 700 °C.

Annealing also leads to the emergence of a broad CL peak in the green region of the spectrum centered at 2.36 eV as well as a much less intense peak centered in the violet band at 3.10 eV. The jagged appearance of the 2.36-eV peaks is due to an etalon effect on the $\text{Al}_{0.35}\text{Ga}_{0.65}\text{N}$ thin film. Both the violet and green luminescence bands are related to the activation of implanted Ni impurities. Although slightly different in energy, these CL features are similar to those reported for Si-implanted $\text{Al}_{0.25}\text{Ga}_{0.75}\text{N}$ [98]. Increasing intensity in the broad mid-bandgap peaks indicated greater and greater activation of the implanted silicon. A similar phenomenon is occurring in $\text{Al}_{0.35}\text{Ga}_{0.65}\text{N}:\text{Ni}$ since the 2.36-eV and 3.10-eV peaks are not present in

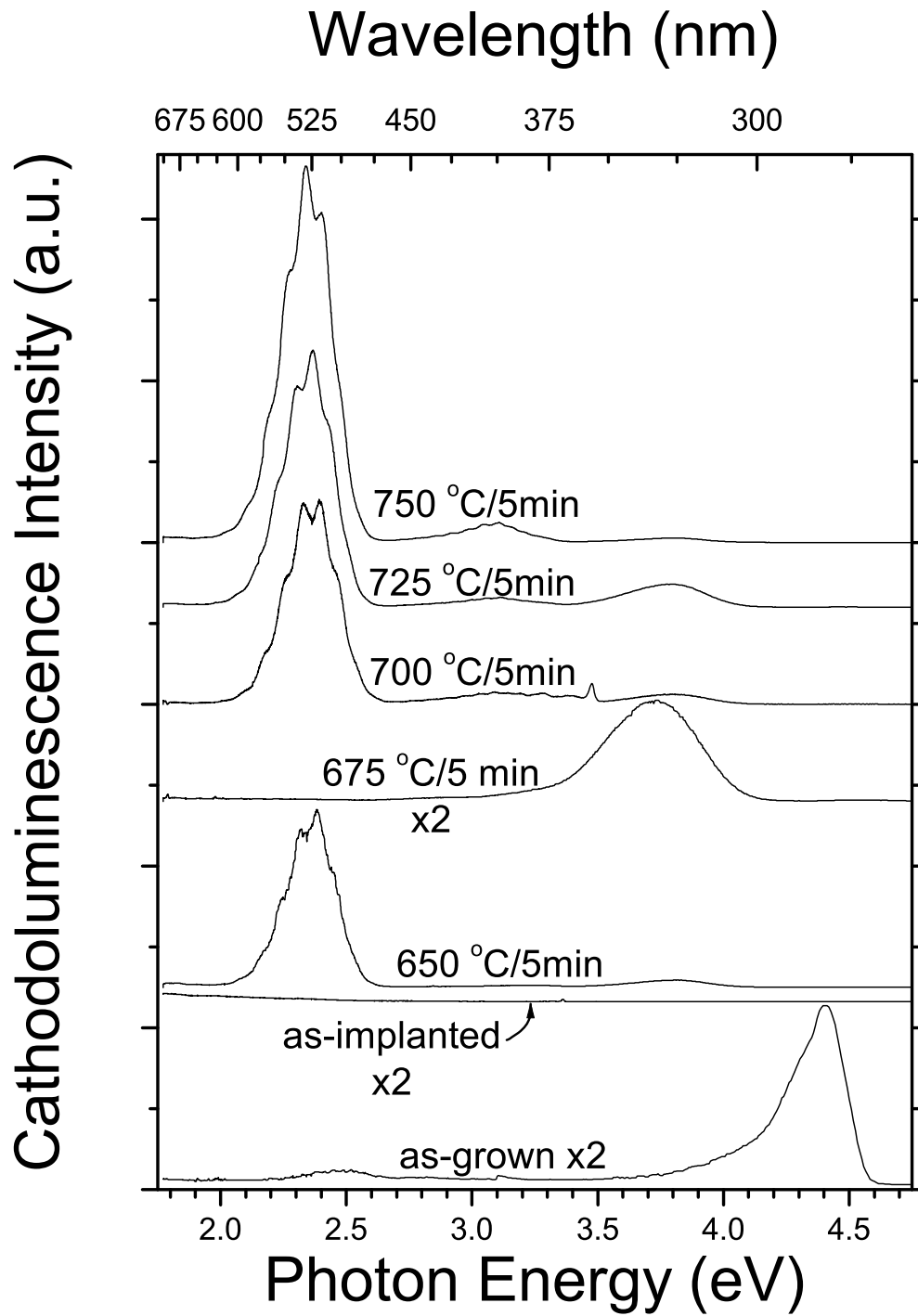


Figure 5.19 Cathodoluminescence spectra collected at ~ 5 K for $\text{Al}_{0.35}\text{Ga}_{0.65}\text{N}$ implanted with Ni and annealed as indicated for 5 minutes in N_2 flowing at $2 \frac{\text{L}}{\text{min}}$.

the as-grown sample and only manifest themselves after annealing. This luminescence feature bodes well for hopes that the sample is a true DMS if it is truly a sign of Ni-incorporation in the $\text{Al}_{0.35}\text{Ga}_{0.65}\text{N}$ lattice. However, the lack of band-edge recovery indicates a lack of crystal quality in the material unless the mid-gap luminescence at 2.36 eV is quenching the band-edge luminescence.

5.4 Conclusions

In this work, $\text{Al}_{0.35}\text{Ga}_{0.65}\text{N}$ is the material with the widest bandgap. The Al content of this material does not, however, give it a marked advantage in the strength of its magnetic properties. This lends credence to the theory that wide-bandgap semiconductors are suitable for DMS fabrication because of the anion species more so than the cation in the material [28, 29].

The most encouraging fact about transition-metal implanted $\text{Al}_{0.35}\text{Ga}_{0.65}\text{N}$ is that there are annealing conditions that produce a signature of ferromagnetism for each of the species implanted. The Mn-implanted $\text{Al}_{0.35}\text{Ga}_{0.65}\text{N}$ shows its most convincing signs of ferromagnetism in the samples annealed at the highest temperatures (750 and 775 °C). Annealing at 775 °C for 5 minutes produces coercive field widths (H_c) of 409 and 199 Oe and remanent field (B_R) values of 14×10^{-6} and 7×10^{-6} emu at 5 and 300 K, respectively. Of course, further experimentation with higher annealing temperatures is necessary to determine the optimal annealing conditions in this material, but the higher the annealing temperature, the more likely that clustering of the implanted Mn will occur.

Implanting $\text{Al}_{0.35}\text{Ga}_{0.65}\text{N}$ with Cr also produces signatures of ferromagnetism across a range of annealing temperature from 700 to 775 °C. Further characterization, such as magnetic circular dichroism, will be necessary to resolve which of the samples are showing true DMS behavior. When annealed at 775 °C for 5 minutes in flowing N_2 , Cr-implanted $\text{Al}_{0.35}\text{Ga}_{0.65}\text{N}$ shows an H_c of 414 and 249 Oe at 5 K and room temperature, respectively. This material also has a B_R greater than 20% of

saturation magnetization (M_S) at both temperatures and reasonable separation and low temperature tracking between FC and ZFC magnetization measurements.

In $\text{Al}_{0.35}\text{Ga}_{0.65}\text{N:Ni}$, the most convincing signs of ferromagnetism come from the sample annealed at 700 °C for 5 minutes, although there was difficulty in determining accurate values of H_c for the samples annealed at 725 and 750 °C. In these samples, H_c is estimated to be 350 Oe at 5 K and 200 Oe at 300 K. B_R does not appear highly sensitive to annealing temperature with values of $\sim 16\%$ (5 K) and $\sim 12\%$ (300 K) across the range of annealing temperatures. There is room for uncertainty about the nature of the magnetic behavior in these samples, especially because of the number of samples with indications from the temperature-dependent measurements of the presence of a spin-glass phase. MCD characterization will also help to answer questions about $\text{Al}_{0.35}\text{Ga}_{0.65}\text{N:Ni}$.

The experiments with $\text{Al}_{0.35}\text{Ga}_{0.65}\text{N}$ have proven that ion implantation is a viable technique for producing ferromagnetic properties in wide-bandgap semiconductors. These measurements, however, highlight the need for further characterization to determine whether there is *sp-d* hybridization and which annealing conditions maximize true DMS behavior.

VI. Characteristics of Transition Metal Implanted

Epitaxial Zinc Oxide

Epitaxial thin films of ZnO were grown on *r*-plane sapphire by collaborators at Rutgers University. There were two of these wafers used in this study: one had portions implanted with Mn and Fe, and the other had parts implanted with Cr, Ni, and Mn.

The difference between these two wafers is a major factor in the performance of the resulting material. The ZnO films on the second wafer implanted with Mn, Cr, and Ni all showed signs of ferromagnetism when annealed properly. CL measurements of these samples also showed good implant damage recovery, which bolsters the assertion that ferromagnetism in them is the result of interaction between the ZnO lattice and the implanted transition metal. While there was a lack of clear magnetic ordering in the Fe-implanted ZnO from the first film, there was enough evidence of magnetic activity that ZnO:Fe should be considered in future experiments.

6.1 Manganese-Implanted Zinc Oxide (First Run)

A ZnO thin film from the first wafer was implanted with Mn to a dose of $5 \times 10^{16} \frac{\text{ions}}{\text{cm}^2}$ at room temperature with an energy of 200 keV. The magnetic measurements taken from this sample did not seem to trend with annealing temperature, and PL measurements did not show recovery of band-edge features. Unfortunately, these facts indicate that this sample of Mn-implanted ZnO is not a ferromagnetic semiconductor and does not exhibit DMS behavior.

6.1.1 Magnetic Hysteresis Measurements

Variable field measurements performed on ZnO:Mn show a magnetic response that is only weakly dependent on annealing temperature. The results of these measurements are shown in figure 6.1. From the data, it is apparent that there is a strong diamagnetic background present in all of the samples. The raw data also reveals that the diamagnetic background is increasingly dominant over any ferromagnetism present as the annealing temperature increases. These measurements also reveal the

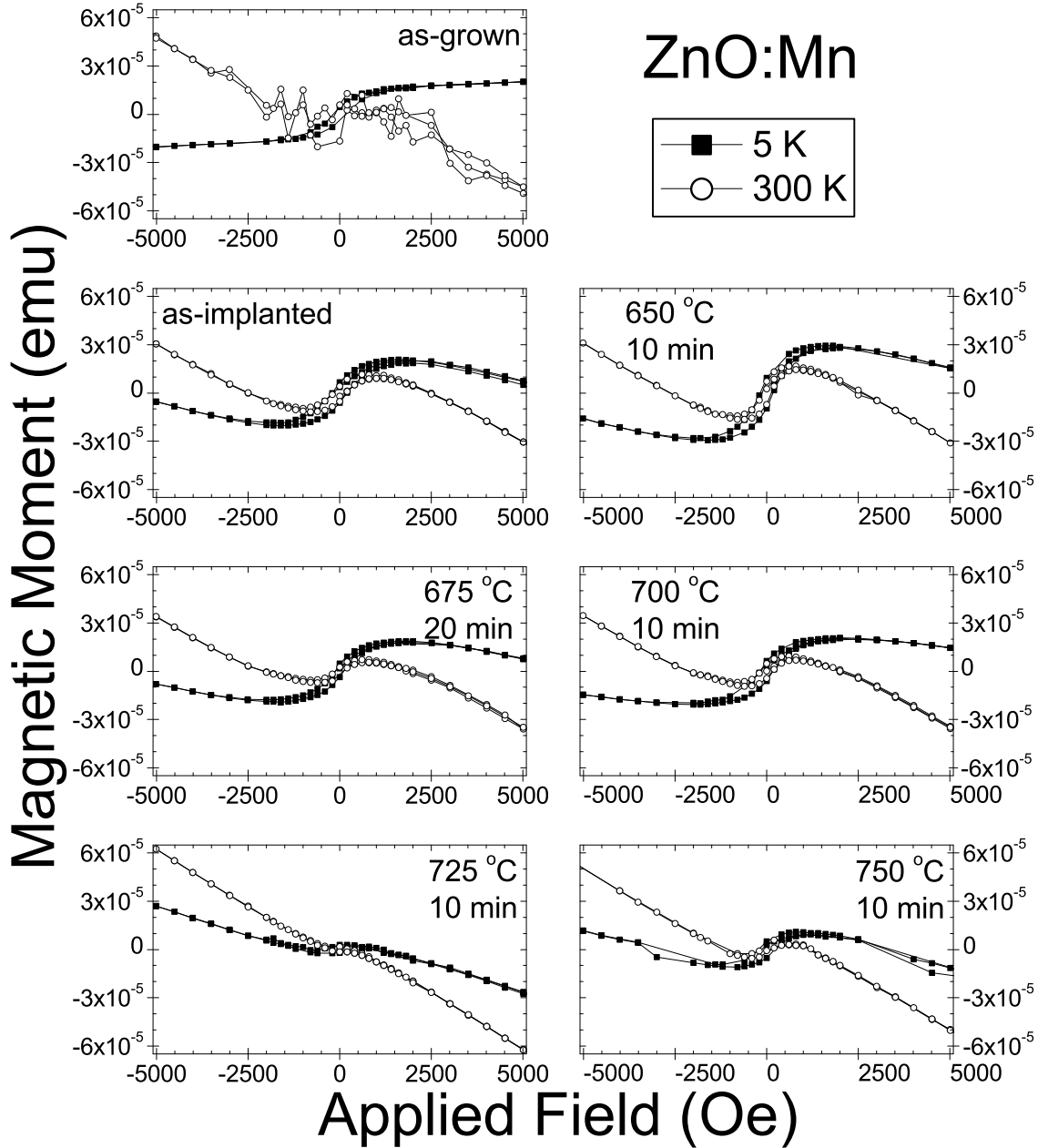


Figure 6.1 Raw data from magnetic hysteresis measurements of Mn-implanted ZnO annealed as indicated in O₂ flowing at 25 scfm.

presence of magnetic hysteresis and saturation, but none of the samples appear more ferromagnetic than the as-implanted sample.

In an attempt to determine whether magnetic ordering exists despite the strong diamagnetic background, the data in figure 6.2 is rotated about the origin by the

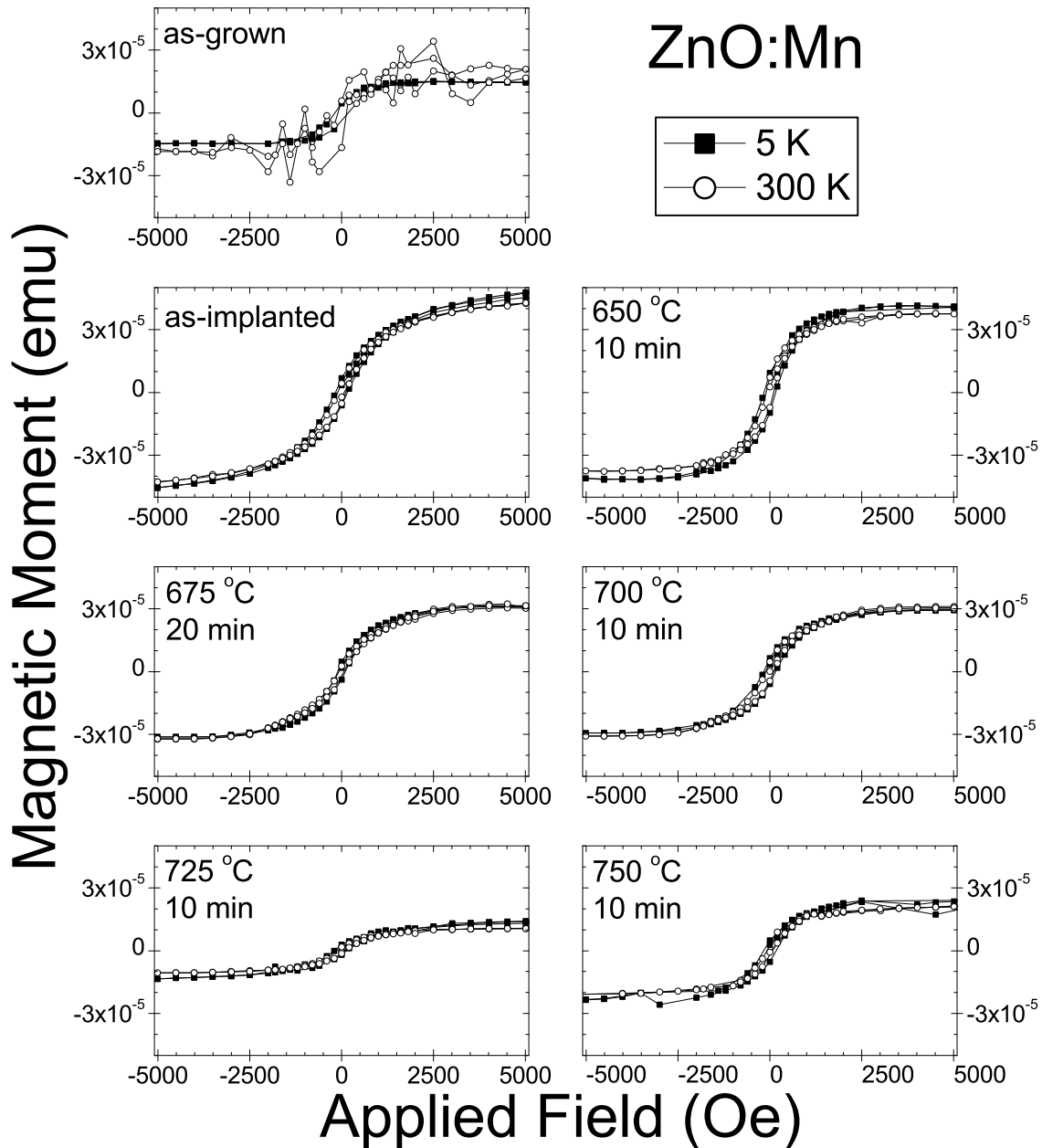


Figure 6.2 Magnetic hysteresis data for ZnO implanted with Mn and annealed in O_2 flowing at 25 sccm as indicated in the figure. Linear diamagnetic influences have been removed from this data.

amount necessary to bring the linear region above saturation parallel to the x axis. Diamagnetism is removed using a MATLAB[®] routine that determines the amount of rotation about the origin necessary to make the magnetization values above saturation as equal as possible. Each data point is then rotated by this amount so that saturation

magnetization (M_S) becomes apparent and accurate values for coercive and remanent fields can be ascertained.

Variable field measurement data with background diamagnetism removed shows a trend of decreasing saturation magnetization with increasing anneal temperature. The data displayed in figure 6.2 also show only negligible separation of between magnetization measured during the positive and negative sweeps of the applied magnetic field. These factors are further indications that these particular ZnO samples do not show ferromagnetism as a result of Mn-implantation.

The rotation to remove the diamagnetic background described above also allows for more accurate measurement of the coercive field (H_c) present in the samples. These measurements are charted in figure 6.3. There is no significant difference in coercivity among the samples based on annealing temperature. There is some difference based on annealing time in that the lone sample annealed for 20 minutes produces a noticeably

AC002B
epi ZnO:Mn

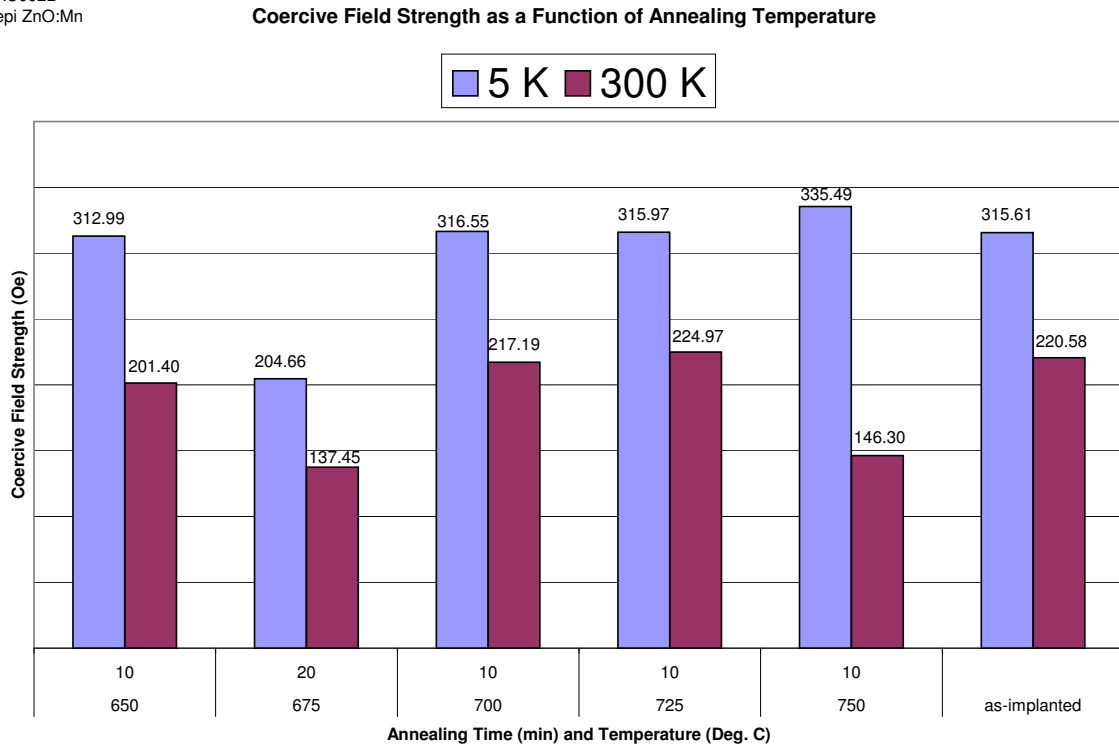


Figure 6.3 Coercive field strengths at 5 and 300 K for various annealing conditions of Mn-implanted ZnO.

weaker H_c value. Together with the fact that H_c does not increase from the as-implanted case, this lack of differentiation based on annealing temperature suggests that the magnetic properties do not arise from the incorporation of Mn into the ZnO crystal lattice. Without Mn incorporation, *sp-d* interaction is not possible, so the material cannot be a true DMS.

A chart summary of the numerical remanent field (B_R) data is presented in figure 6.4. This data echoes the trend, or lack thereof, seen in H_c measurements. Again, there is not a significant distinction in remanency based on annealing temperature. There is some trending in the room-temperature data, but this is basically a downward trend with increasing annealing temperature. Also similar to the H_c data, the B_R measurements show high sensitivity to annealing time: the sample annealed for 20 minutes shows much lower B_R values at both 5 and 300 K than any of the samples annealed under other conditions.

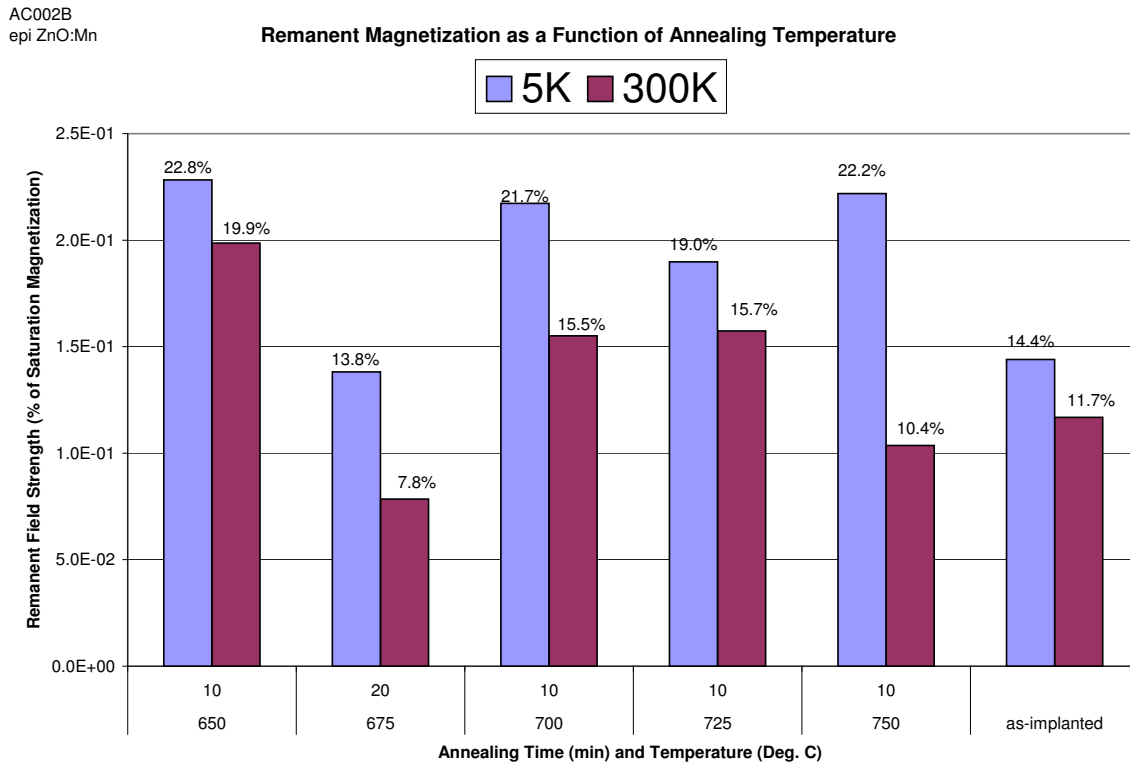


Figure 6.4 Remanent field strengths at 5 and 300 K for various annealing conditions of Mn-implanted ZnO.

6.1.2 *Temperature-Dependent Magnetization*

FC and ZFC measurements for Mn-implanted ZnO are shown in figure 6.5. The lack of separation between FC and ZFC magnetization in most of these samples indicates a basically non-magnetic character. The sample annealed at 675 °C for 20 minutes shows the greatest separation between FC and ZFC measurements despite that fact that it had the lowest values of H_c and B_R . This indication of ferromagnetism is contradictory with those reported for variable field measurements. The lack of agreement between the two characterization methods tends to indicate that the material does not meet the criteria of a good DMS.

The possibility also exists that 20 minutes of annealing is necessary for Mn activation in this material. A longer annealing time would be required if the material has a high defect density from crystal growth or was otherwise damaged before ion implantation. If it is the case that the material requires a longer annealing time, then the annealing temperature of 675 °C is sub-optimal. The reduction of magnetic behavior from the as-implanted values is common in this work for materials annealed above or below the optimum temperature. This hypothesis could be tested by annealing Mn-implanted ZnO samples from this wafer across the temperature range tested for a period of 20 minutes to see if the signatures of ferromagnetism increase in both variable field and variable temperature magnetization measurements. Unfortunately, Mn-implanted ZnO from the first wafer was not available to test this hypothesis.

6.1.3 *Optical Measurements*

Photoluminescence measurements of these samples were taken at a temperature of approximately 10 K, as described in section 3.4.2. The results of these measurements are shown in figure 6.6.

The PL data for the as-grown sample shows a near band-edge peak at 3.37 eV, which is typical for ZnO [72]. There are also broad luminescence peaks in the violet and red-orange regions of the spectrum. The violet luminescence centered around 2.9 eV is attributed to interstitial Zn (Zn_i) [65]. The smaller luminescence around

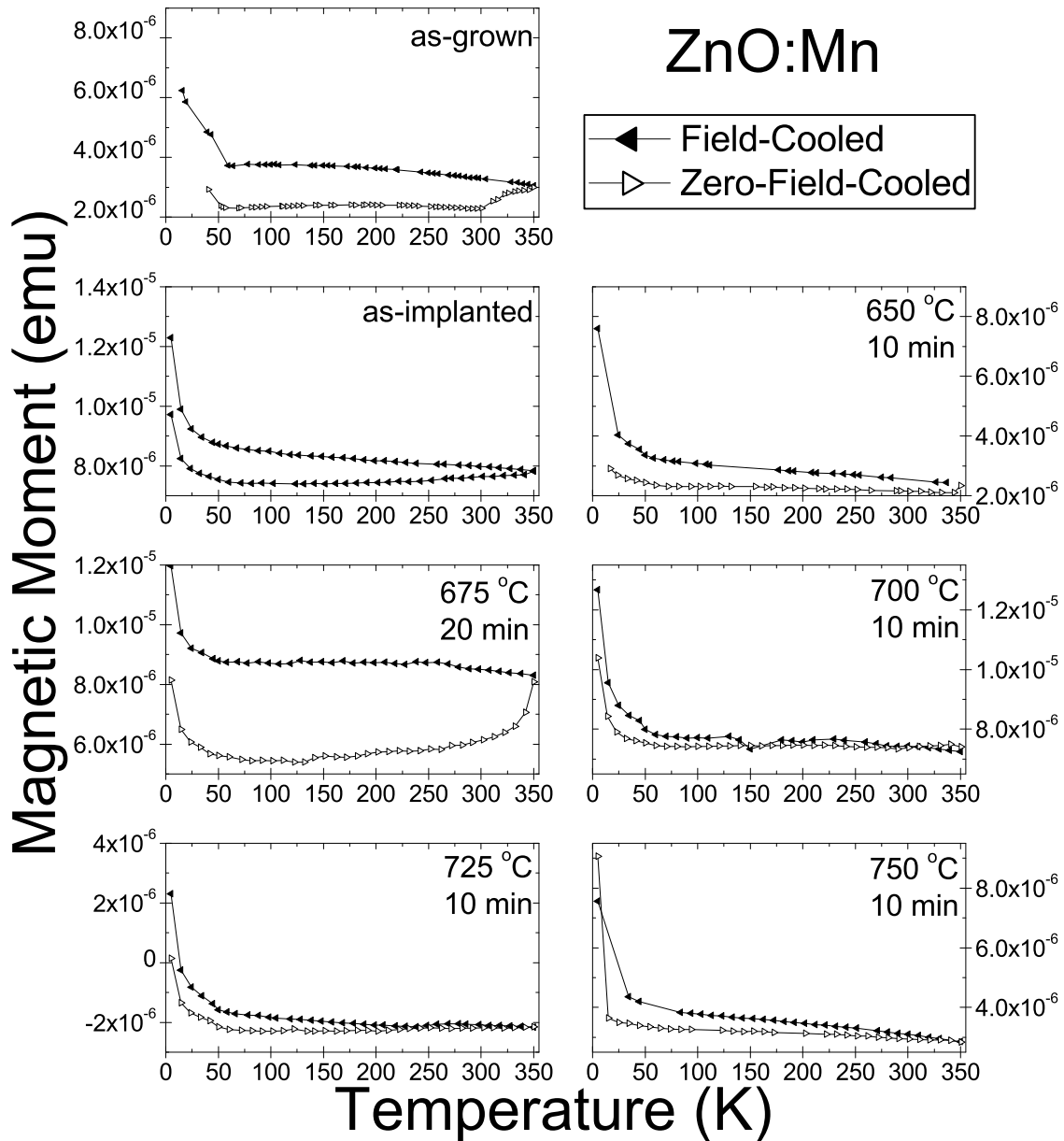


Figure 6.5 Temperature-dependent magnetization for ZnO implanted with Mn and annealed as indicated in the figure in O_2 flowing at 25 sccm. Note that the y axis spans the same range of magnetic moment despite the fact that background offset causes a difference in absolute values.

2 eV is attributed to transitions between the conduction band and singly ionized oxygen vacancies (V_O^+) [64]. The clear presence of Zn_i and V_O^+ in this ZnO before ion implantation suggests that the quality and crystallinity of this material is not good enough to produce a DMS.

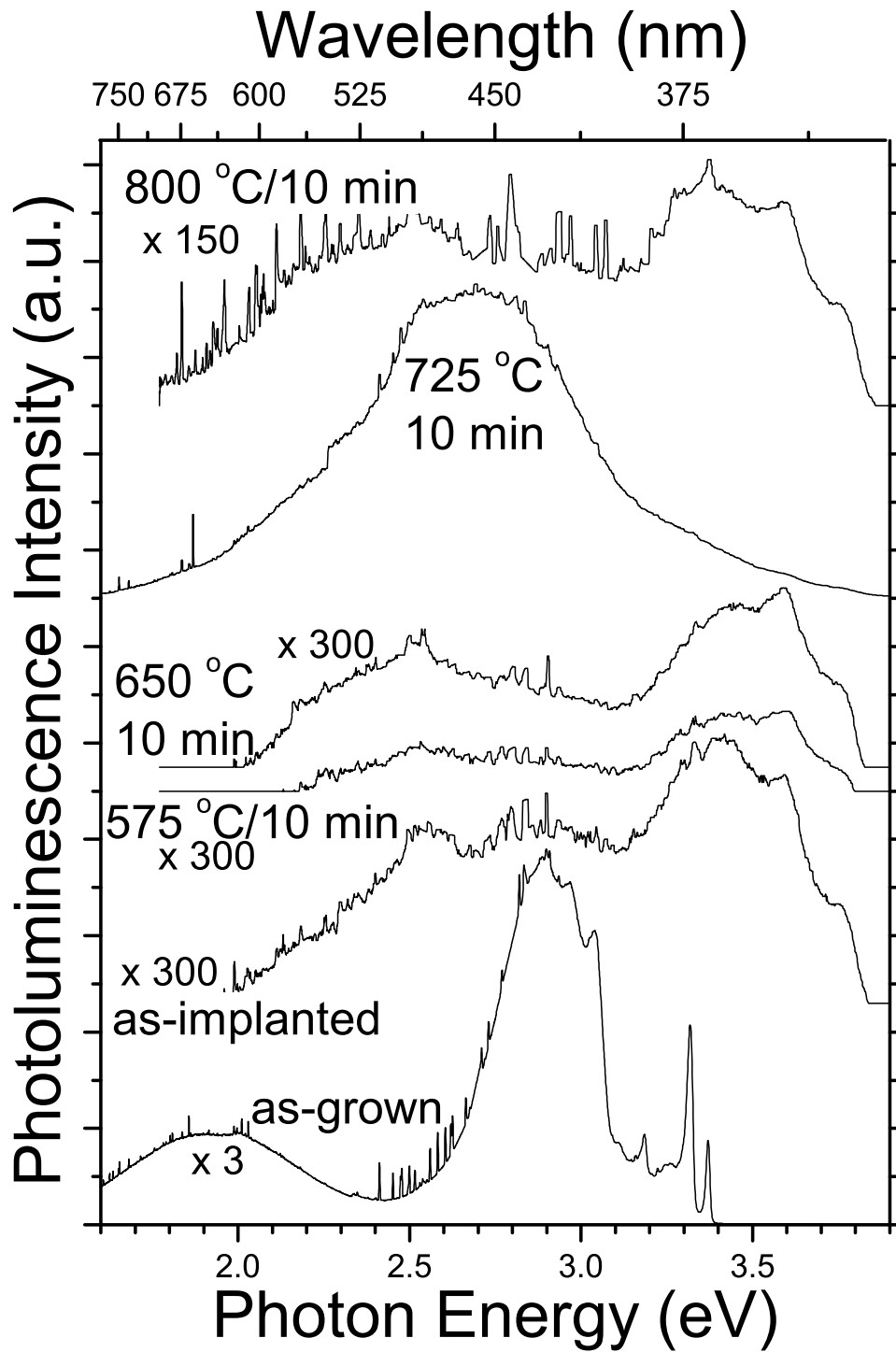


Figure 6.6 Photoluminescence spectra of ZnO implanted with Mn and annealed as indicated in the figure in O_2 flowing at 25 sccm for 10 minutes. The spectra are collected at a temperature of approximately 10 K.

All of the PL features in the as-grown samples are virtually eliminated by Mn implantation, even when the sample is subsequently annealed. The only sample that recovers brightness in the overall luminescence is the one annealed at 725 °C for 10 minutes. The PL spectra from the other implanted and annealed samples are best characterized as noise and are only shown at great magnification so that the reader will not believe that the reported data is the result of an obstruction in the optical path. In the single sample where luminescent intensity is recovered, the broad mid-bandgap nature of this PL feature indicates that recovery of the ZnO crystal lattice structure is incomplete. The lack of implant damage recovery in these Mn-implanted ZnO samples indicates that the crystal structure of the semiconductor has not been recovered and that Mn has not been incorporated into the ZnO lattice. These two facts indicate that the material will not produce useful DMS behavior.

6.2 *Manganese-Implanted Zinc Oxide (Second Run)*

Again, a ZnO thin film was implanted with Mn to a dose of $5 \times 10^{16} \frac{\text{ions}}{\text{cm}^2}$ at room temperature with an energy of 200 keV. This implantation occurred on the second ZnO wafer supplied by Rutgers University. The results from this wafer and implantation were markedly different from (and better than) those for a similar wafer reported in section 6.1. The difference in these results can be credited to the superior quality of the second ZnO thin film supplied by Rutgers. The higher crystal quality is evidenced primarily by CL measurements showing fewer defects in the as-grown samples and implant damage recovery in the annealed samples. Magnetic measurements suggest that the temperature that yields the strongest ferromagnetism over a 10-minute anneal lies between 650 and 675 °C. The performance of the second wafer received from Rutgers University shows that Mn-implanted ZnO behaves as a DMS and will be important to device work moving forward.

6.2.1 *Magnetic Hysteresis Measurements*

Variable field measurements on the ZnO:Mn are shown in figure 6.7. The hys-

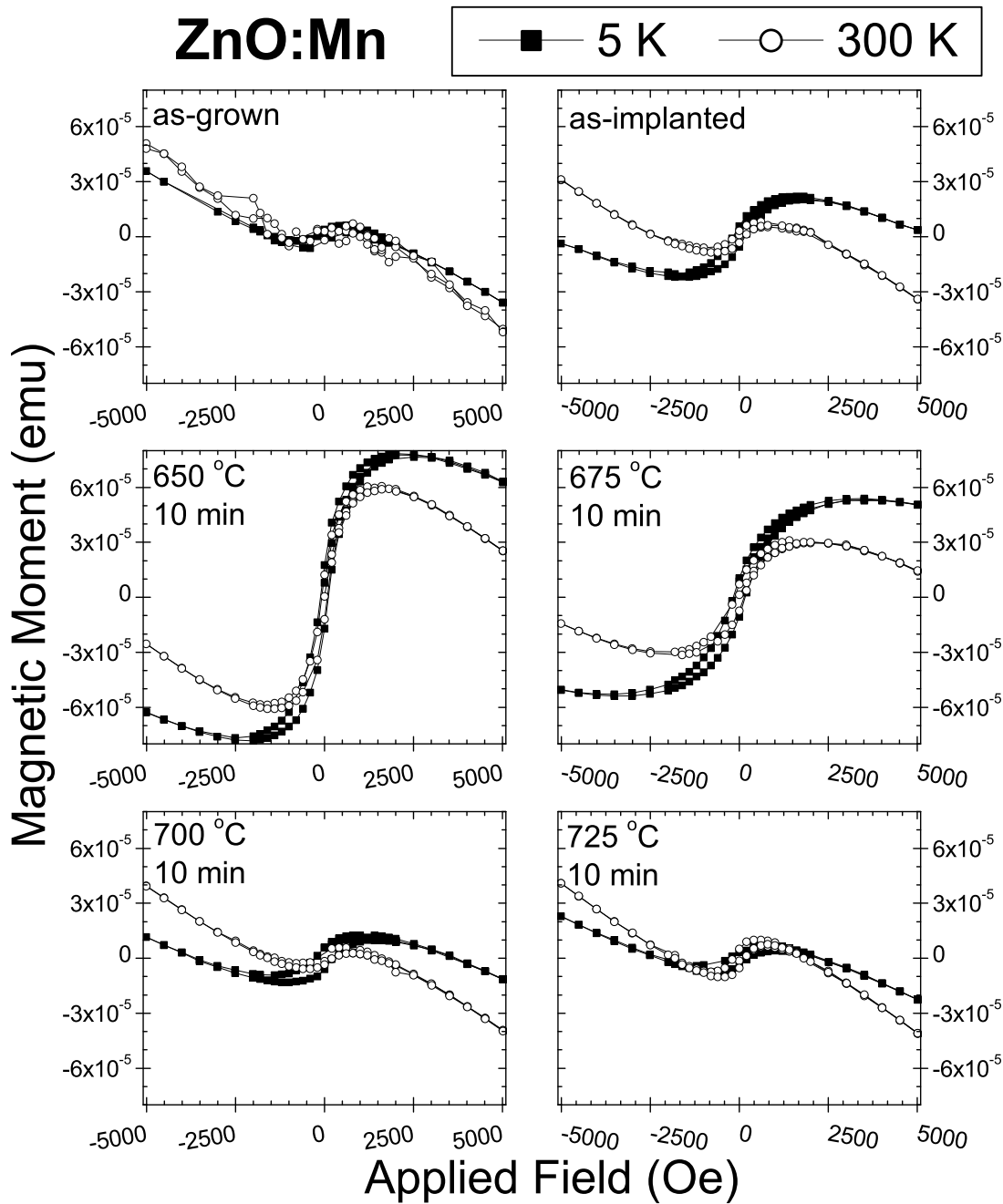


Figure 6.7 Raw data from magnetic hysteresis SQUID measurements of Mn-implanted ZnO annealed as indicated for 10 minutes in a 25 sccm flow of O₂.

teresis data shows separation in the positive- and negative-going sweeps of the applied magnetic field. They also show magnetic saturation with a clear trend toward decreasing saturation magnetization with increasing annealing temperature, the greatest saturation occurring in the sample annealed at 650 °C for 10 minutes in O₂ flowing

at 25 sccm. As expected with a Al_2O_3 substrate, there is a diamagnetic background. The greatest dominance of ferromagnetism over this diamagnetic background occurs in the sample annealed at 675 °C. Although the width of its coercive field (H_c) is less, the greatest saturation magnetization (M_S) is seen in the sample annealed at 650 °C for 10 minutes. The values of M_S for this sample are 0.85 and 0.76 μ_B at 5 and 300 K, respectively. The calculated moment for Mn^{2+} in an insulating crystal is 5.9 μ_B [8, Table 31.4]. The samples annealed at 700 and 725 °C demonstrate behavior comparable to that of the as-implanted sample, which suggests that higher annealing temperatures are not the most effective for Mn-incorporation in ZnO:Mn.

The diamagnetic contribution of the sapphire substrate is removed by rotating each data point in the variable field measurement around the origin by an equal angle. This angle is calculated based on the amount of rotation necessary to make the linear region of above-saturation magnetization values parallel with the x axis. This processing is performed in order to more accurately determine values for H_c , B_R , and M_S . Unfortunately, the process can also create artifacts that lead to erroneous numerical results for the above-mentioned quantities. In this case, the relatively low M_S and slow onset of saturation will lead to larger-than-actual H_c values being calculated for the samples annealed at 700 and 725 °C. This occurs because the legs of the hysteresis loop are tilted as they cross the zero magnetization line, which means that they are further apart than if the hysteresis loop was rotated so that the two legs cross the x axis at 90°.

Hysteresis data for ZnO:Mn with the diamagnetic background removed, which is shown in Figure 6.8, confirms that M_S tends to decrease with annealing temperature. This presentation of the data also shows that the coercive field is greatest in the sample annealed at 675 °C for 10 minutes.

The H_c values calculated from the hysteresis data with the diamagnetic background removed are shown in figure 6.9. The values of H_c that are suspect due to artifacts from the background correction algorithm are obscured in the figure. For

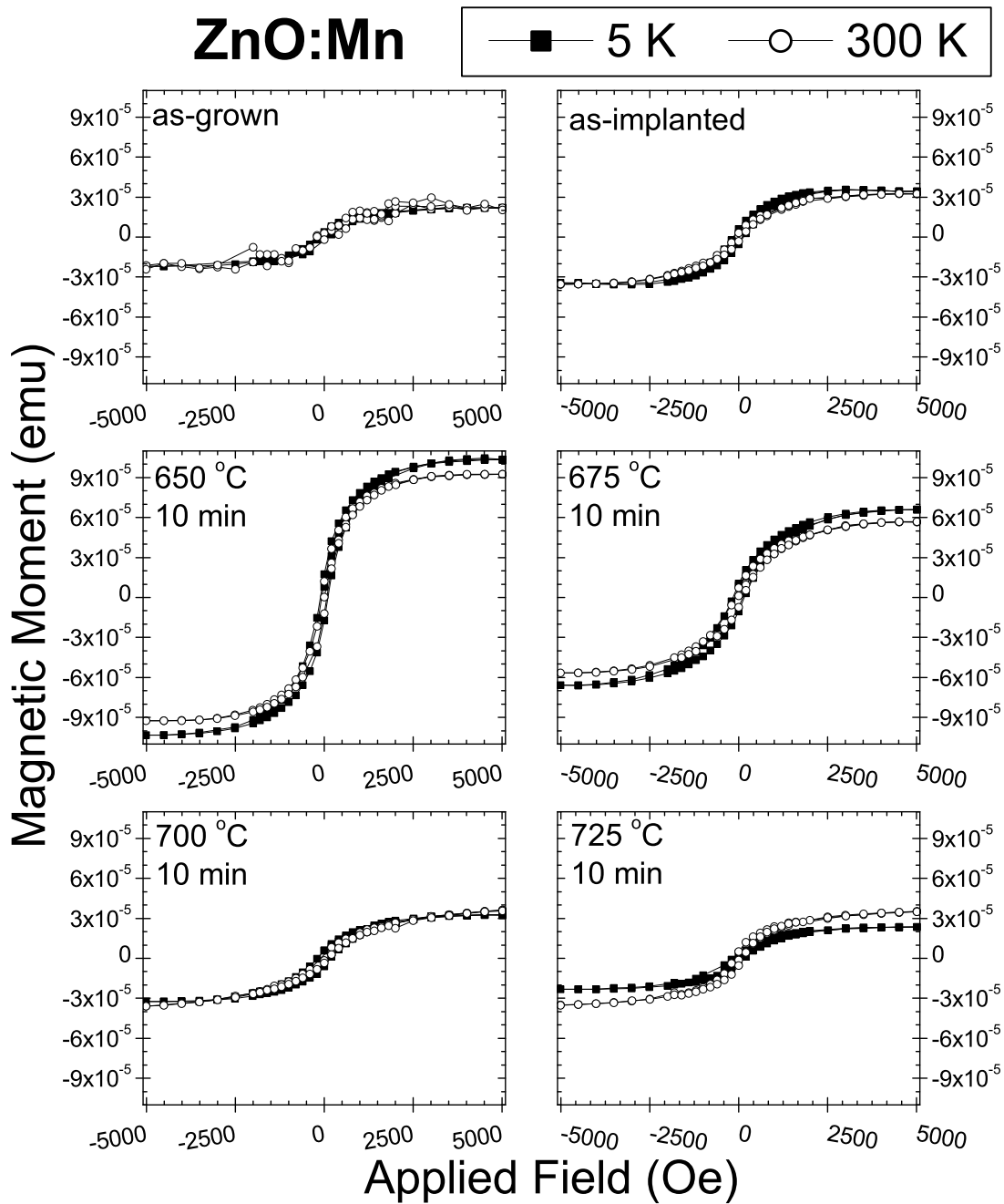


Figure 6.8 Magnetic hysteresis data for epitaxial ZnO implanted with Mn and annealed as for 10 minutes in O₂ flowing at 25 sccm. Linear diamagnetic influences have been removed from this data.

these samples, background removal causes the strength of the coercive fields to be overstated, so this data may not be directly compared to that collected from samples with higher saturation magnetization. From the samples on which valid measurements of H_c are available, the maximum coercive field is seen to occur in the sample annealed at 675 °C for 10 minutes at both 5 and 300 K.

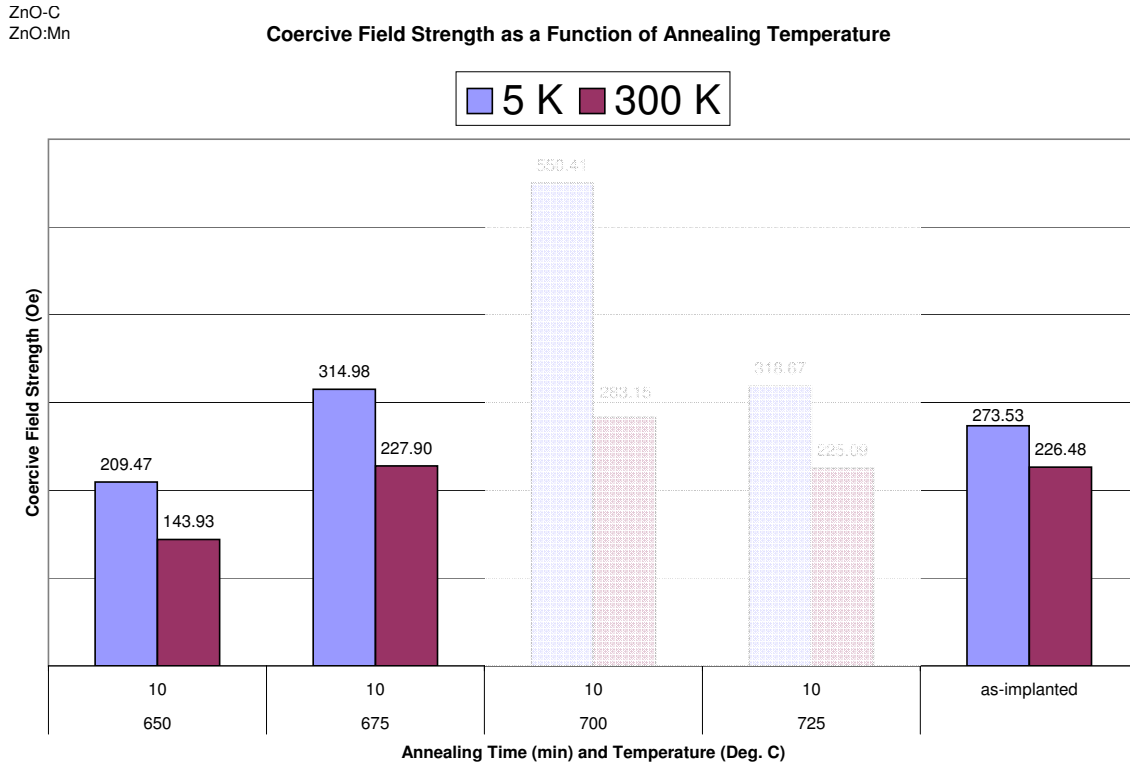


Figure 6.9 Coercive field strengths at 5 and 300 K for various annealing conditions of Mn-implanted ZnO. The values that are suspect due to artifacts from the background correction algorithm are obscured.

Remanent field strength is far less sensitive to the rotation used to remove diamagnetic background. The reason that B_R is less sensitive to the rotation can be explained geometrically: the orders of magnitude difference between the x and y axes means that the rotation necessary causes far less translation along the x axis than along the y axis, which means the value being measured directly above the origin does not change greatly after rotation.

B_R for this material is less sensitive to annealing conditions, and has a minimum in the sample annealed at 700 °C for 10 minutes. Figure 6.10 shows the values of B_R calculated as a percentage of M_S . The data for the sample annealed at 725 °C is obscured because the disparity in sensitivity to rotation between B_R and M_S causes these values to be erroneously large. These measurements indicate that the samples annealed at 650 and 675 °C have equal B_R values at room temperature.

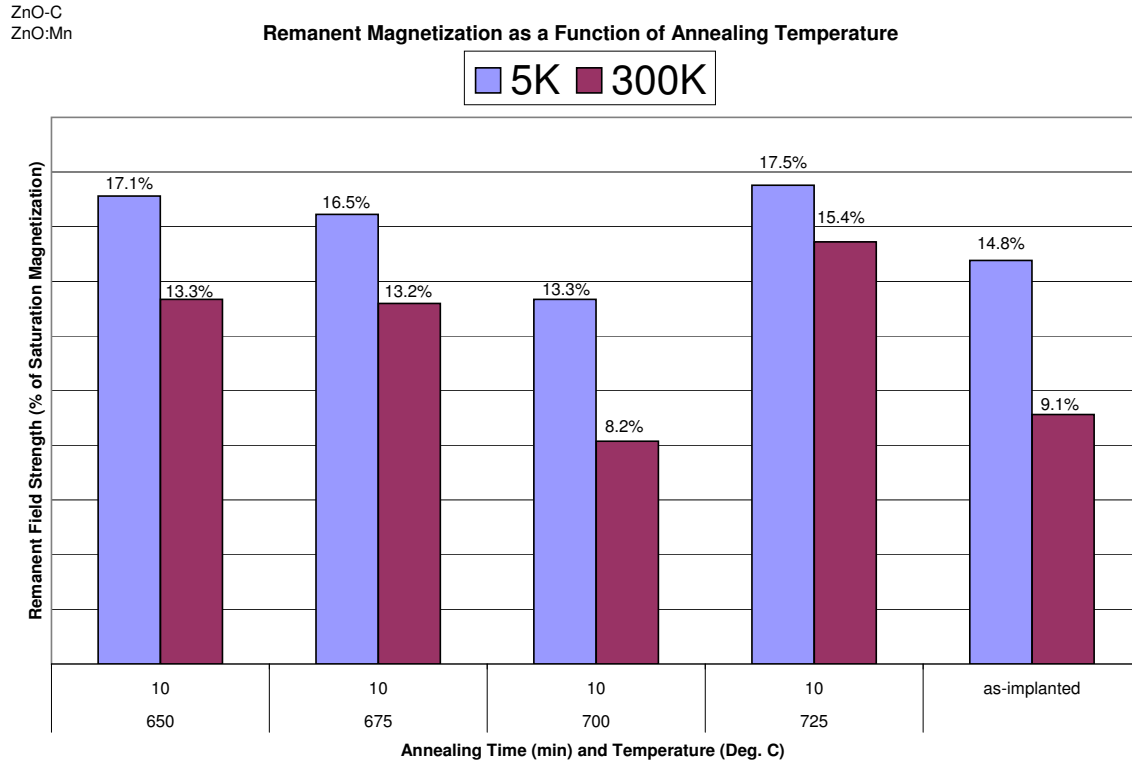


Figure 6.10 Remanent field strengths at 5 and 300 K for various annealing conditions of Mn-implanted ZnO. The data for the sample annealed at 725 °C is obscured because it is erroneously large due to the high sensitivity of M_S to the background subtraction process compared to B_R .

The appearance of the hysteresis loops in figures 6.7 and 6.8, as well as the calculated values of H_c and B_R (with allowance for background subtraction artifacts), indicates that annealing at the lower end of the range used in this experiment produces the best signatures of ferromagnetism in Mn-implanted ZnO. The fact that annealing at both 650 and 675 °C for 10 minutes causes favorable ferromagnetic behavior in

different measurements suggests that the optimum temperature may lie between the two.

6.2.2 Temperature-Dependent Magnetization

The magnetic response as temperature is varied in both field-cooled and zero-field-cooled measurements is shown in figure 6.11. Each of these samples displays some indication of ferromagnetism as all of the FC and ZFC measurements track upward together at low temperature. The feature of the temperature-dependent magnetization measurements that stratifies the samples by indications of ferromagnetism is the separation between FC and ZFC magnetization. The greatest separation occurs in the sample annealed at 675 °C for 10 minutes. The samples annealed at 650, 700, and 725 °C display less separation between FC and ZFC magnetization than even the as-implanted samples, which suggests that these are non-optimal annealing temperatures. The data presented in figure 6.11 corroborates the variable field measurement data presented in section 6.2.1 and leads to the conclusion that the best annealing temperature for inducing ferromagnetic behavior in Mn-implanted ZnO is between 650 and 675 °C.

6.2.3 Optical Measurements

Cathodoluminescence measurements on Mn-implanted ZnO are presented in figure 6.12. The quality of this material is shown by the strong near band-edge peak. The broad appearance in this peak is due to the contributions of both free and bound excitons to this luminescence feature [140]. In the as-grown sample, the peak is slightly red shifted because bound excitons are the primary source of the luminescence. The near band-edge peak is largely suppressed, though not eliminated by Mn implantation. Annealing at 650 °C for 10 minutes begins to restore the near band-edge peak, but it is noticeably displaced toward lower energy. Annealing at higher temperatures (675–725 °C) causes not only restoration, but also enhancement of the band-edge luminescence in the form of a brighter and slightly blue-shifted signal. These changes occur because the higher-energy free exciton transitions are

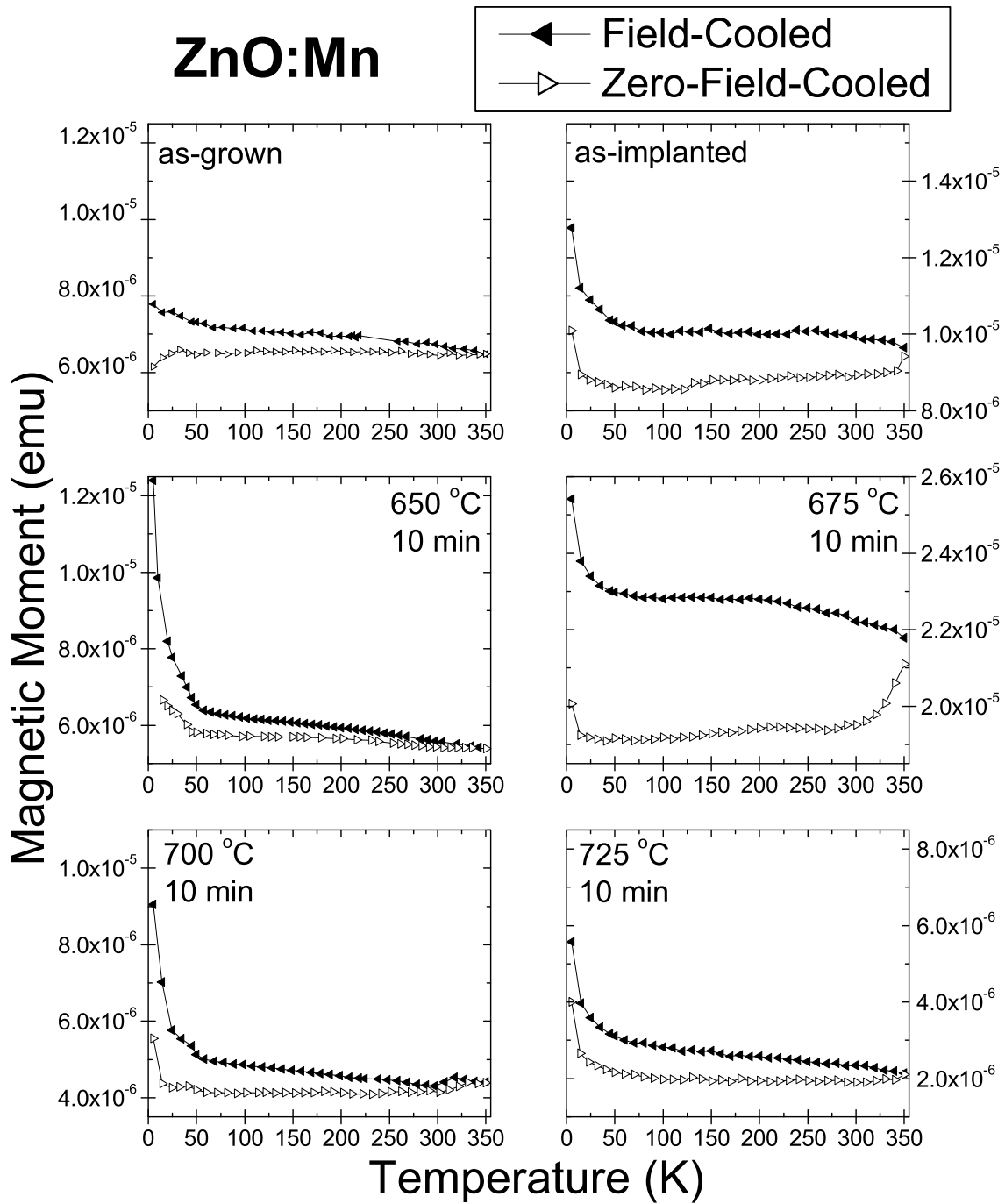


Figure 6.11 Temperature-dependent magnetization for ZnO implanted with Mn and annealed as indicated in the figure for 10 minutes in O₂ flowing at 25 sccm. Note that the y axis spans the same range of magnetic moment despite the fact that background offset causes a difference in absolute values.

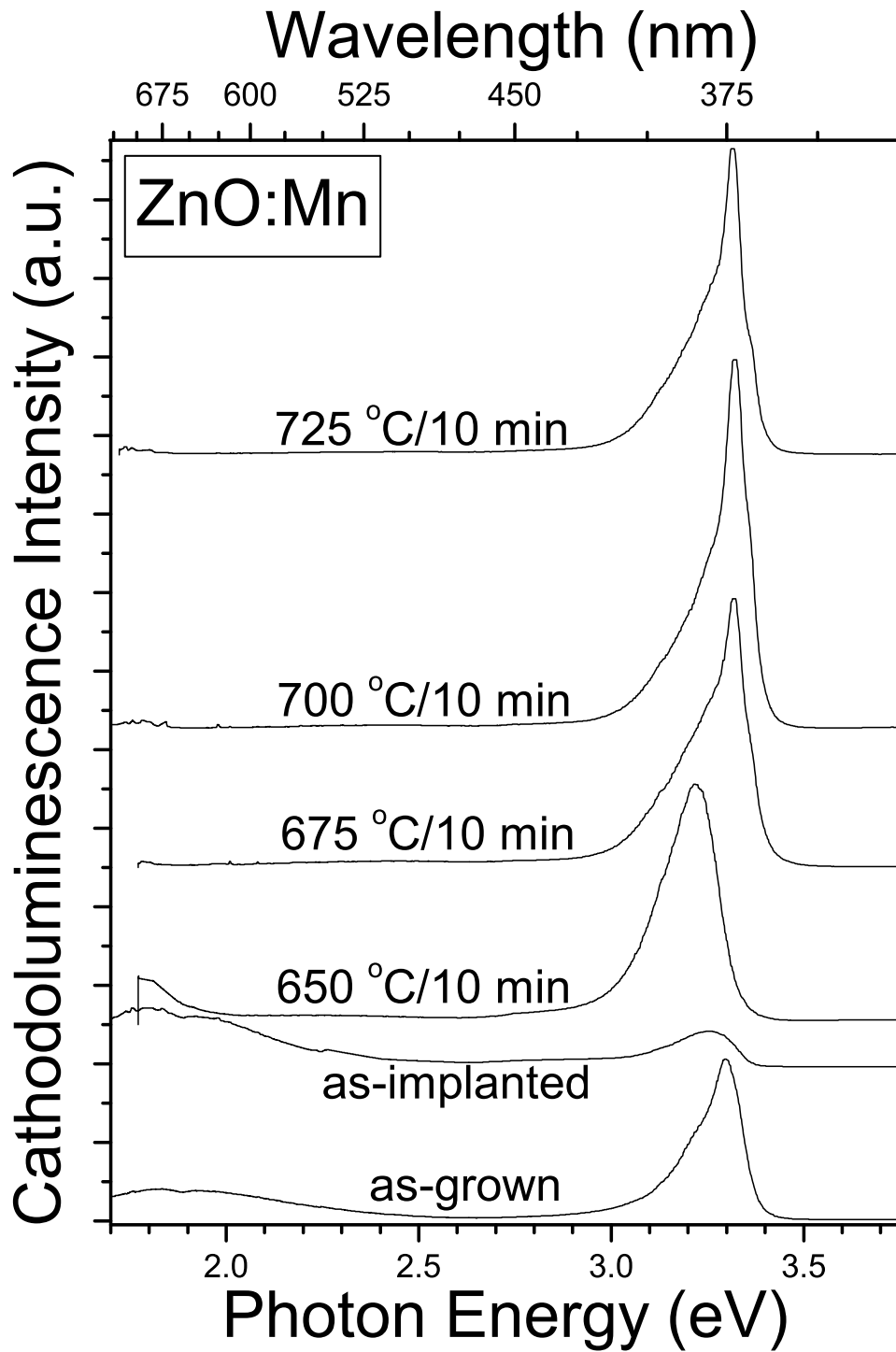


Figure 6.12 Cathodoluminescence spectra of ZnO implanted with Mn and annealed as indicated in a 25 sccm flow of O₂ for 10 minutes. The spectra were collected from samples cooled to approximately 10 K.

allowed once the defects from both growth and Mn implantation are annealed out at the higher temperatures.

The as-grown and as-implanted samples also both show a broad double peak in the red region of the spectrum with local maxima at 1.85 and 1.95 eV. This luminescence may be attributable to oxygen vacancies (V_O) [64], but the presence of V_O should tend to increase with annealing. Therefore, the presence of complexes (possibly involving hydrogen from the MOCVD precursors) is the most likely cause for these features.

The CL data presented show that crystallinity is recovered in the ZnO thin film for samples annealed above 675 °C. The magnetic data reported above show that samples annealed at 675 °C and below display the most desirable magnetic properties. Therefore, the best chance for the ferromagnetism reported for this material to be a result of Mn interaction with the ZnO crystal lattice occurs when the sample is annealed at 675 °C for 10 minutes in O₂ flowing at 25 sccm.

6.3 Chromium-Implanted Zinc Oxide

Epitaxial ZnO samples were implanted with Cr ions to a level of $5 \times 10^{16} \frac{\text{ions}}{\text{cm}^2}$ with a 200-keV implantation energy at room temperature. Annealing at and above 675 °C produced ferromagnetic properties in the samples, and the optimal annealing temperature for DMS production is between 700 and 725 °C. There is incomplete agreement concerning optimal annealing temperature among the characterization methods used, so any spintronic device work using ZnO:Cr should proceed with awareness that there may be repeatability or yield issues with this material. On a positive note, the unusually good implant damage recovery suggests that this material's magnetic properties are due to incorporation of Cr into the ZnO crystal lattice.

6.3.1 Magnetic Hysteresis Measurements

Variable field measurements of ZnO:Cr, as seen in figure 6.13, show that indications of ferromagnetism occur in the samples annealed at 725 and 750 °C. The sample

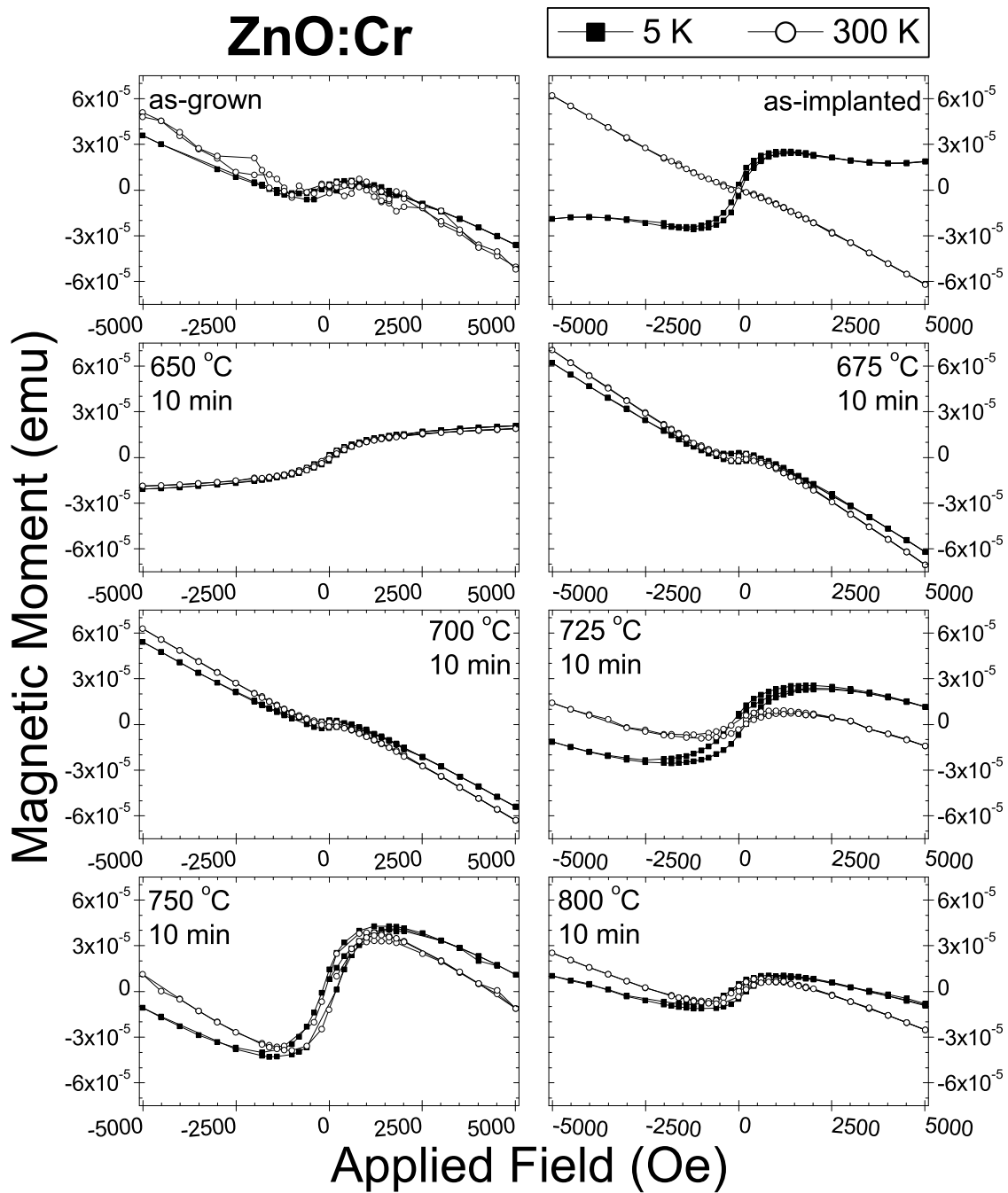


Figure 6.13 Raw data from magnetic hysteresis SQUID measurements of Cr-implanted ZnO annealed as indicated for 10 minutes in O₂ flowing at 25 sccm.

annealed at 650 °C for 10 minutes shows anomalous behavior, which is best characterized as superparamagnetic. This conclusion is verified by the temperature-dependent magnetization as discussed in section 6.3.2. The sample annealed at 750 °C shows the greatest saturation magnetization (M_S) and coercive fields (H_c) in measurements taken at both 5 and 300 K. Samples annealed above 750 °C show decreasing coercivity and saturation magnetization, which points to a more moderate temperature of 725–750 °C as the optimal for this material.

Figure 6.14 shows the hysteresis data with diamagnetism (paramagnetism in the case of the sample annealed at 650 °C) removed. The diamagnetic background is subtracted by rotating each data point about the origin by the amount necessary to make the linear region above saturation horizontal. Processing the data in this fashion allows for a more accurate calculation of H_c and M_S as well as a view of the data that is not obstructed by influences that may arise from the substrate and obscure the magnetic phenomena present in the Cr-implanted ZnO thin film. The data with linear magnetic influences removed serves to confirm that only the samples annealed at 725 and 750 °C for 10 minutes can reasonably be called ferromagnetic. Both of these samples have separation between the positive- and negative-going legs of the hysteresis loop, which is another indicator of ferromagnetic ordering.

The corrected variable field measurements on Cr-implanted ZnO allow for numerical values of H_c to be determined. Unfortunately, in the case of ZnO:Cr where background diamagnetism is strong and saturation magnetization is weak for the samples annealed at lower temperatures, the values determined are erroneously large. The error occurs due to the tilting of zero magnetization crossings after the background is subtracted. H_c values determined from the corrected data are plotted in figure 6.15 with the clearly erroneous data obscured (as determined from qualitative inspection of figures 6.13 and 6.14). Even the remaining data is somewhat suspect with the exception of that for the sample annealed at 750 °C. In short, numerical determination of H_c is not useful for this particular sample.

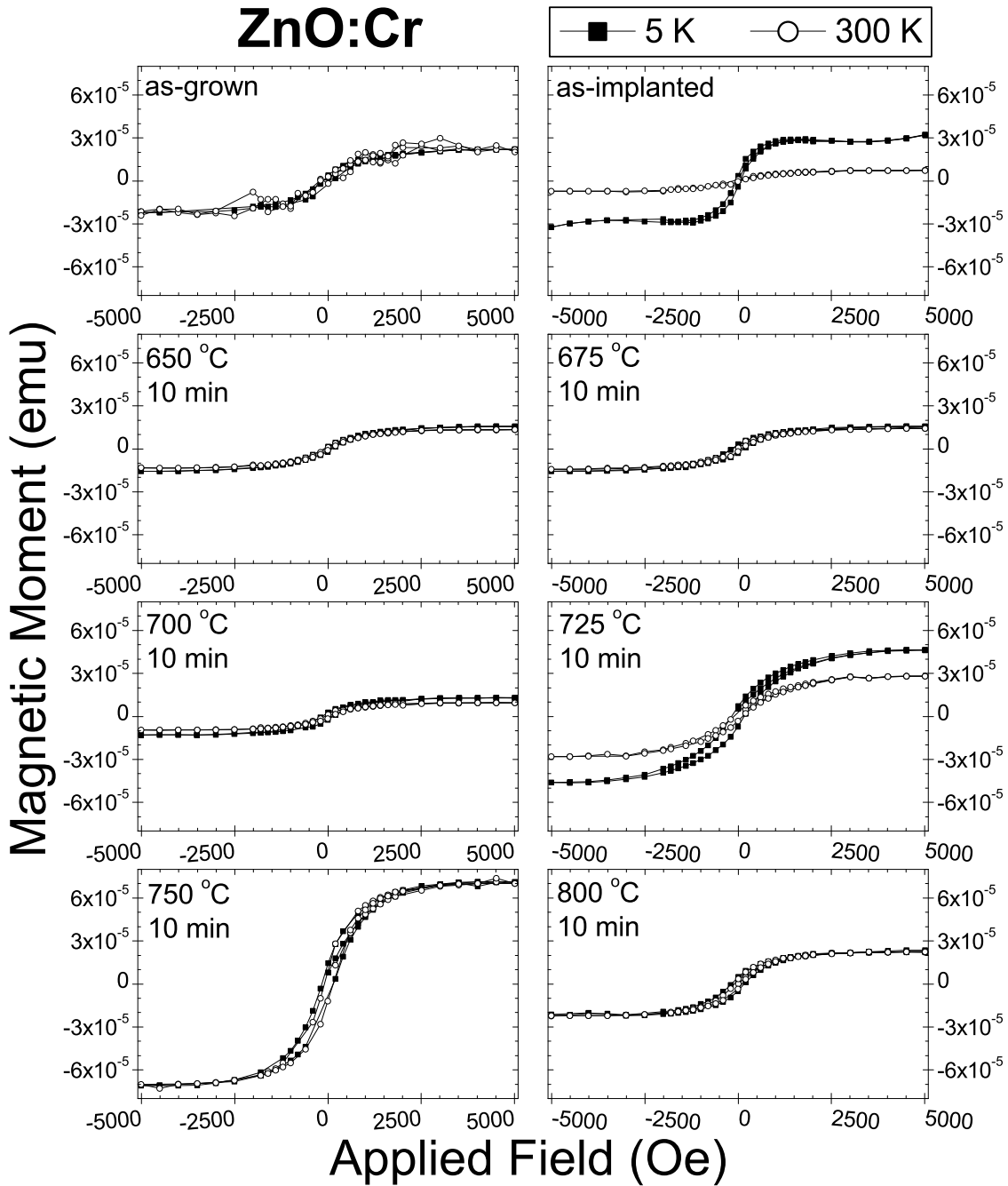


Figure 6.14 Magnetic hysteresis data for epitaxial ZnO implanted with Cr and annealed as indicated for 10 minutes in O_2 flowing at 25 sccm. Linear magnetic influences have been removed from this data.

Coercive Field Strength as a Function of Annealing Temperature

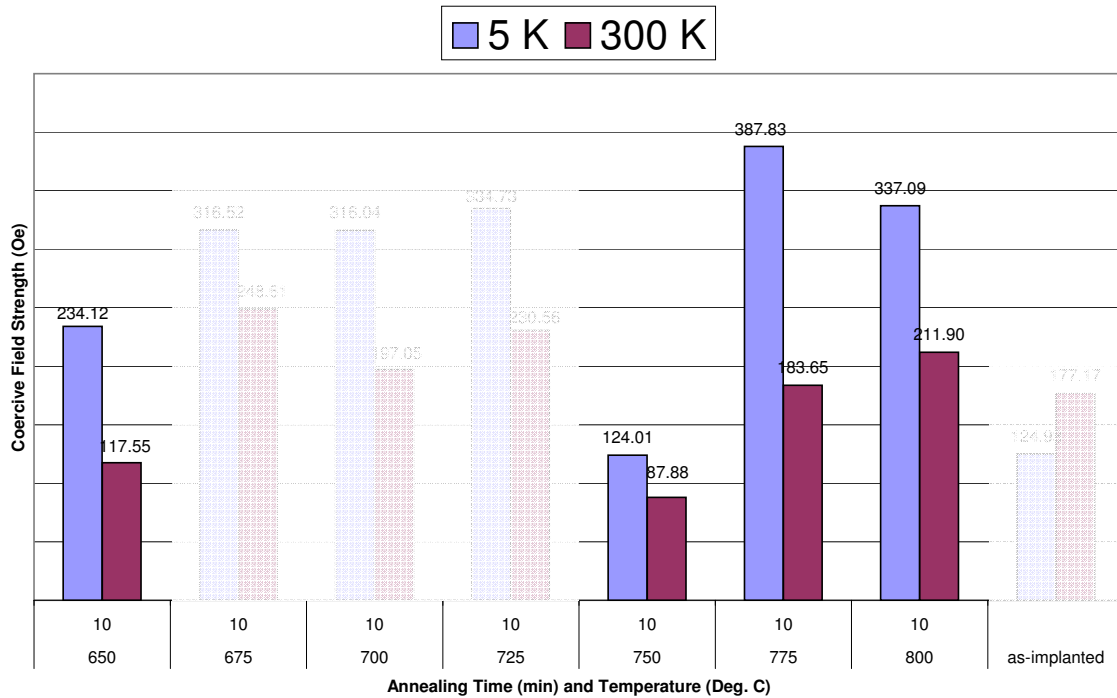


Figure 6.15 Coercive field strengths at 5 and 300 K for various annealing conditions of Cr-implanted ZnO.

Determination of the remanent field strength is not as sensitive to background subtraction processing because of the large difference in scale between the x and y axes (as explained in section 6.2.1). As shown in figure 6.16, the remanent field strengths point to the samples annealed at 725 and 750 °C as the ones that exhibit the greatest degree of ferromagnetism, particularly at room temperature where their values are nearly equal.

The variable field measurements performed on Cr-implanted ZnO demonstrate that an annealing temperature of 725 or 750 °C will produce ferromagnetic behavior. This is not to say that samples annealed at other temperatures are devoid of ferromagnetism, but they are dominated by diamagnetism, which makes it difficult to distinguish their behavior. The sample annealed at 750 °C shows greater saturation (~ 0.25 and $\sim 0.22 \mu_B$ per Cr^{2+} ion at 5 and 300 K, respectively; calculated maximum magneton of $4.8 \mu_B$ [8, Table 31.4]), a smaller, but probably more accurate, coerciv-

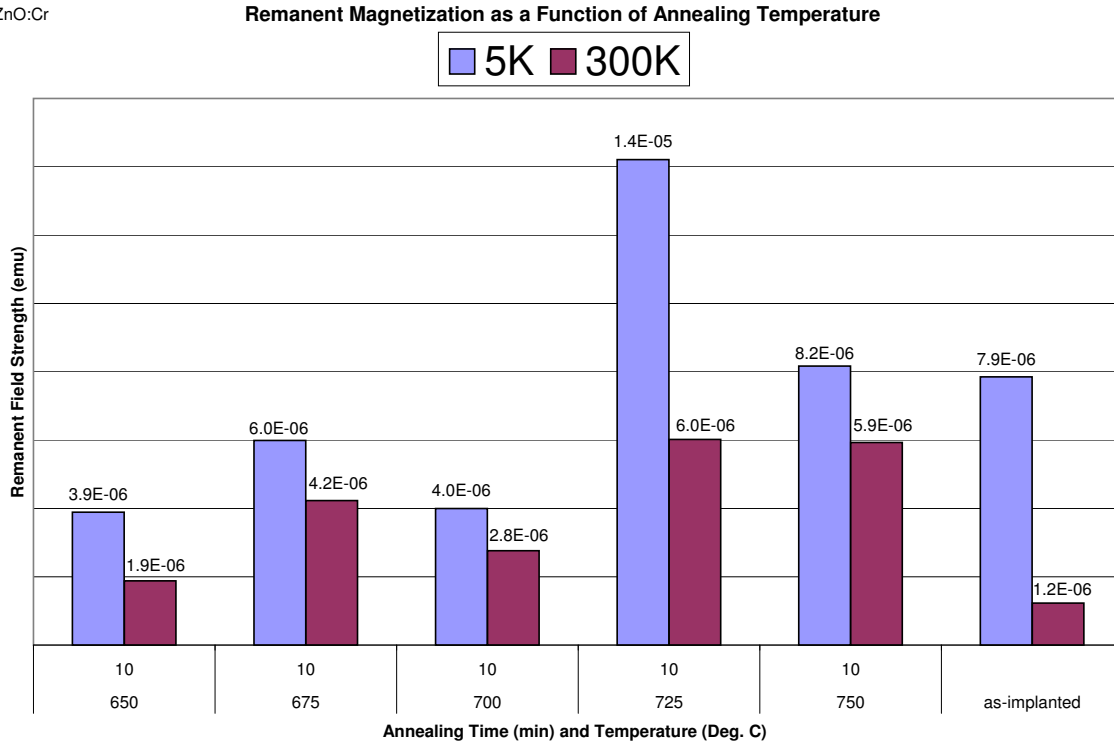


Figure 6.16 Remanent field strengths at 5 and 300 K for various annealing conditions of Cr-implanted ZnO. Note that these are raw sample magnetization values and not presented as a percentage of M_S .

ity and similar remanency at room temperature compared to the sample annealed at 725 °C. All of this suggests that optimal annealing for ferromagnetism in ZnO:Cr will be found somewhere between 725 and 750 °C when a 10 minute anneal is used.

6.3.2 Temperature-Dependent Magnetization

Temperature-dependent magnetization measurements were taken for the Cr-implanted ZnO in both ZFC and FC modes. The results of these measurements are depicted in figure 6.17. Annealing at 650 °C produces a superparamagnetic phase as evidenced by the divergence of FC and ZFC magnetization at low temperature as well as the behavior in hysteresis discussed above. The samples that were annealed at 675 and 700 °C show very little separation between FC and ZFC measurements particularly near room temperature, but they track together at low temperatures, which indicates that the samples may be weakly ferromagnetic. The sample annealed

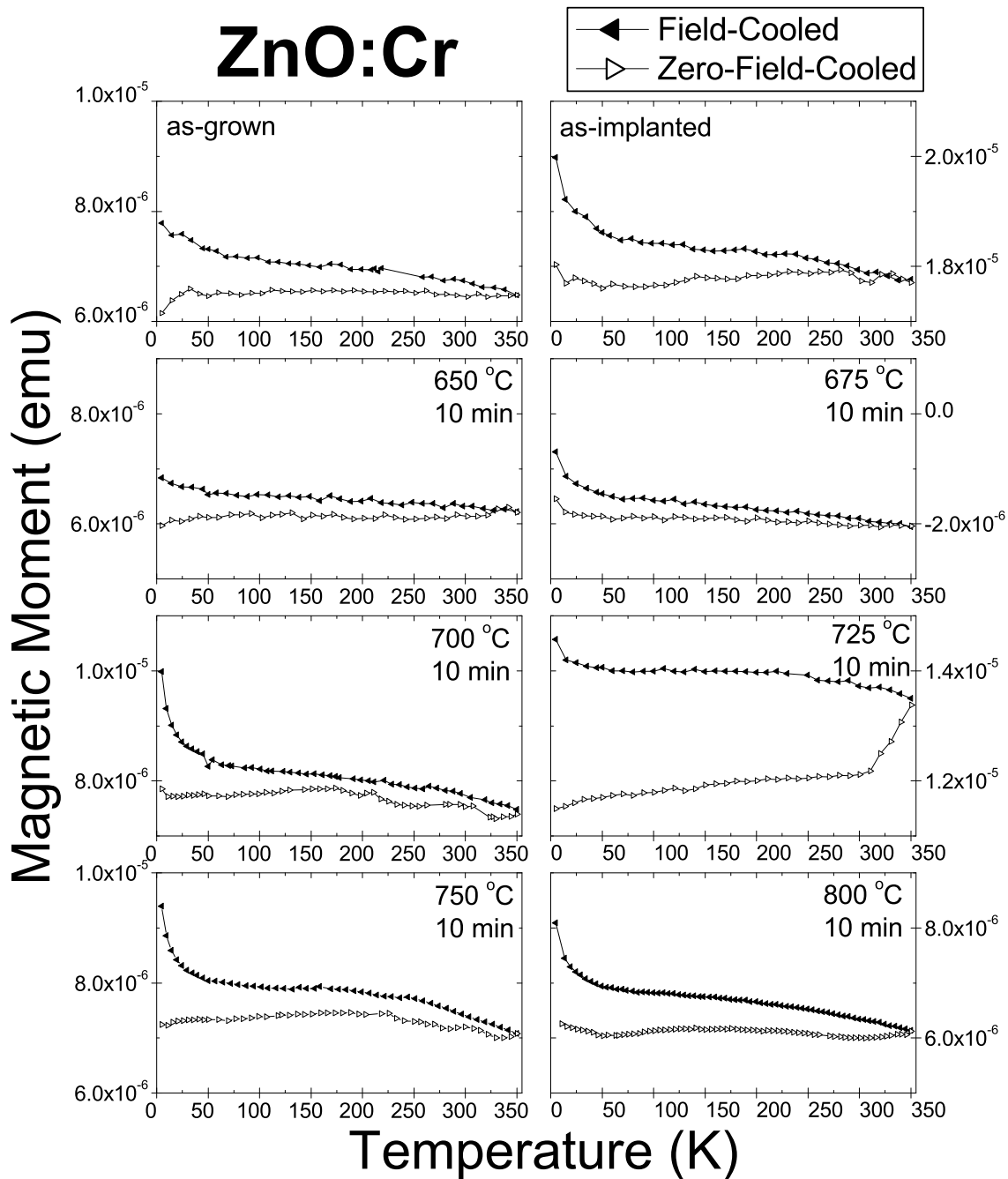


Figure 6.17 Temperature-dependent magnetization for ZnO implanted with Cr and annealed as indicated for 10 minutes in O₂ flowing at 10 sccm. Note that the y axis spans the same range of magnetic moment despite the fact that background offset causes a difference in absolute values.

at 725 °C for 10 minutes shows a wide separation between FC and ZFC magnetization measurements, but the measurements diverge at low temperature. Annealing at 750 °C for 10 minutes produces a small separation between FC and ZFC magnetization and an absence of low-temperature tracking. This behavior suggests the presence of a spin-glass phase with an ordering temperature around 225 K. Although there is moderate low-temperature tracking in the sample annealed at 800 °C, the FC-ZFC magnetization separation is small and there is still a broad “hump” in the ZFC measurement that indicates the possible presence of a spin-glass phase.

The facts delineated above point to two possible scenarios. The truly ferromagnetic samples may be those annealed at 675 and 700 °C for 10 minutes even though the ferromagnetism exhibited by these samples is weak. If this is the case, then ZnO implanted with Cr has limited potential usefulness as a dilute magnetic semiconductor. The other possible scenario is that strong ferromagnetism is achievable in ZnO:Cr, but there is a superparamagnetic phase in addition to the ferromagnetic phase found when annealing at 725 °C for 10 minutes. If this is the case, then processing that mitigates the superparamagnetic phase, which has yet to be discovered, must be utilized to fabricate useful DMS devices from ZnO:Cr.

6.3.3 Optical Measurements

Cathodoluminescence data for ZnO:Cr is shown in figure 6.18. The dominant feature in the as-grown sample is a near band-edge peak that is attributed to bound excitons [140]. Cr implantation causes a major reduction in luminescent output and broad emission in the red, green, and violet ranges. The near band-edge feature seen in the as-grown sample is quickly recovered with annealing. The most effective recovery, in terms of luminescent intensity near the band-edge, occurs in the sample annealed at 700 °C for 10 minutes. This peak gains its intensity and is broadened by additional emission from free excitons in addition to the bound-exciton emission seen in the as-grown sample [140]. Free-exciton emission is also detected in the sample annealed at 675 °C in the high-energy shoulder and is dominant in the sample annealed at 750 °C.

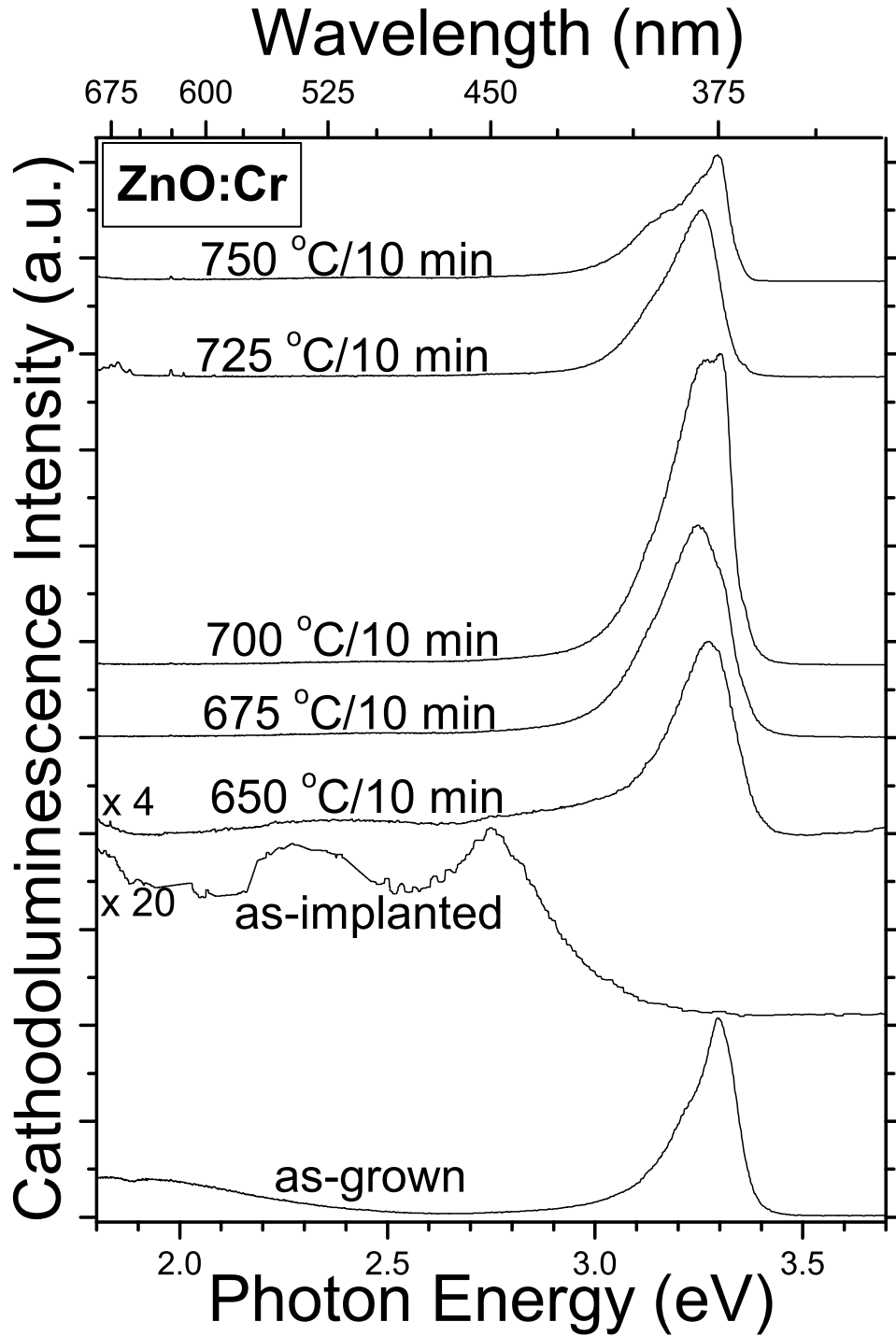


Figure 6.18 Cathodoluminescence spectra of ZnO implanted with Cr and annealed as indicated in O₂ flowing at 25 sccm for 10 minutes. CL measurements were taken at a temperature of approximately 5 K.

There is also a set of broad peaks at 1.85 and 1.95 eV in the as-grown sample. These are attributed to a complex (possibly hydrogen related) that is formed during the MOCVD growth of the samples. The defect is easily annealed away as seen by the fact that it does not appear in any of the annealed samples.

From CL measurements, the sample that appears to have the most crystalline structure is the one annealed at 700 °C for 10 minutes. This observation also implies that this sample will have the most effective incorporation of Cr into the crystal lattice which should lead to the highest probability for a true DMS. At this point, the evidence is rather conflicting, but it is probable that the optimal annealing temperature lies between 700 and 750 °C for ZnO implanted with Cr.

6.4 *Nickel-Implanted Zinc Oxide*

An epitaxial thin film of ZnO, from the second wafer provided by Rutgers University, was implanted at room temperature with Ni to a level of $3 \times 10^{16} \frac{\text{ions}}{\text{cm}^2}$ using an implantation energy of 200 keV. This lower implantation dose was chosen because of some previous results reported for Ni-implanted *p*-GaN [90] and to lower the probability of Ni cluster formation during annealing. The results of characterization measurements on this material are mixed with regard to optimal annealing conditions. The strongest coercive field is present in the sample annealed at 725 °C. The strongest remanent field and band-edge recovery in cathodoluminescence occurs in the sample annealed at 700 °C. Finally, the weakest indication of the a magnetic phase other than ferromagnetic in temperature-dependent measurements occurs in the sample annealed at 675 °C. The best annealing temperature for a 10-minute anneal on Ni-implanted ZnO is probably between 700 and 725 °C. The signs of magnetic ordering present in this material suggest that it will be useful in DMS-based device fabrication.

6.4.1 *Magnetic Hysteresis Measurements*

Variable field measurements of ZnO:Ni are shown in figure 6.19. The samples

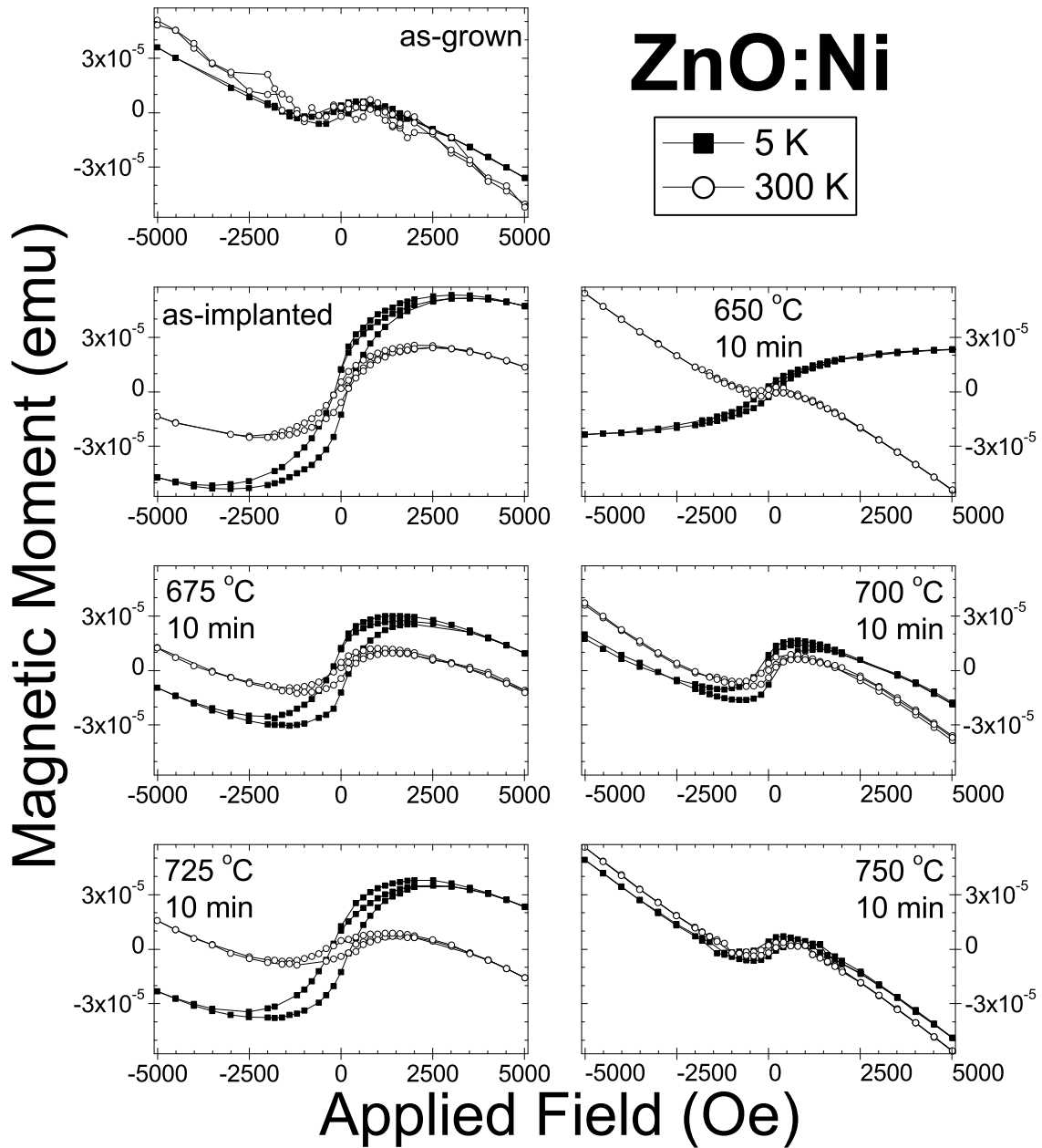


Figure 6.19 Raw data from magnetic hysteresis SQUID measurements of Ni-implanted ZnO annealed as indicated in the figure for 10 minutes in O₂ flowing at 25 sccm.

annealed in the temperature range from 675 to 725 °C show clear magnetic saturation and separation between the positive and negative sides of the hysteresis loop. The samples annealed outside this temperature range show superparamagnetism on a diamagnetic background—an overall downward slope with clear magnetic saturation. The 5-K measurement on the sample annealed at 650 °C for 10 minutes shows a magnetically neutral background, which probably arises from low-temperature ordering of Ni-related complexes or defects in this sample annealed under suboptimal conditions. The as-implanted sample shows signs of magnetic ordering in the hysteresis loop, but this is due to the activity of interstitial Ni resulting from the ion implantation, and not due to magnetic coordination utilizing the electronic structure of the semiconductor, which would be useful for fabricating DMS-based devices.

The diamagnetic background that is apparent in these measurements is removed by rotating each data point about the origin by the amount necessary to make the linear region above saturation magnetization parallel to the x axis. The results of the variable field measurements with background diamagnetism removed are shown in figure 6.20.

The background-free data serve to confirm the conclusions drawn from the raw hysteresis data. The samples annealed at 650 and 750 °C show a superparamagnetic character. The three samples annealed in the temperature range from 675 to 725 °C show separation in the legs of the hysteresis loop and comparable levels of magnetic saturation.

The main purpose for subtracting the background diamagnetism from the data depicted in figure 6.19 is to allow the assignment of an accurate numerical value to the quantities of coercive field (H_c), remanent field (B_R), and saturation magnetization (M_S). The values determined for H_c in ZnO:Ni under various annealing conditions are presented in figure 6.21. The H_c values confirm that the samples displaying the greatest ferromagnetism are those annealed between 675 and 725 °C for 10 minutes. These three samples have comparable H_c at 5 K, but the sample annealed at 725 °C is

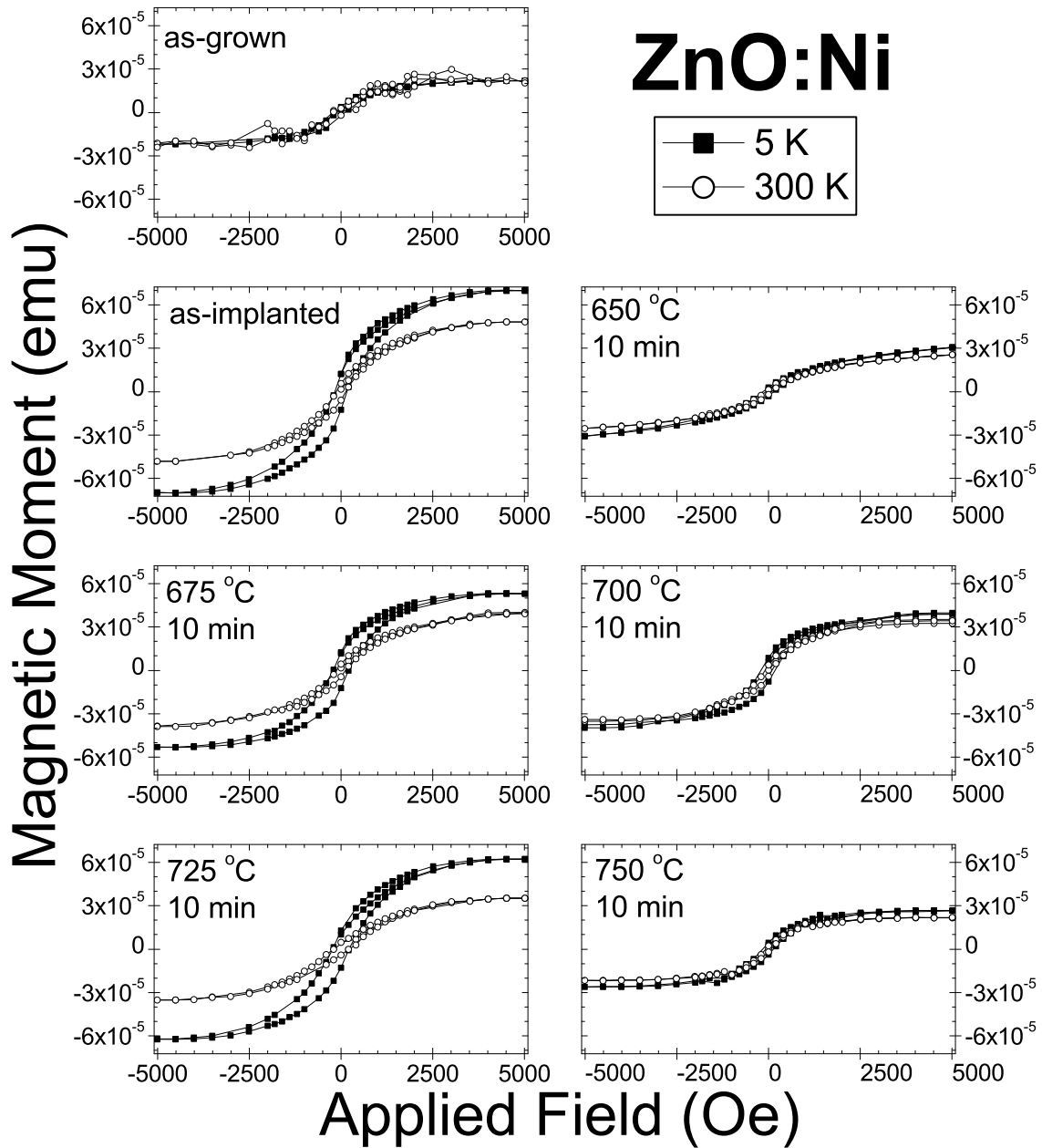


Figure 6.20 Magnetic hysteresis data for epitaxial ZnO implanted with Ni and annealed as indicated in O₂ flowing at 25 sccm for 10 minutes. Linear diamagnetic influences have been removed from this data.

the standout at room temperature. The sample annealed at 725 °C for 10 minutes also shows saturation values of 0.86 and 0.49 μ_B per Ni atom at 5 and 300 K, respectively, with a calculated maximum magneton for Ni²⁺ of 3.2 μ_B per Ni atom [8, Table 31.4].

ZnO:B
ZnO:Ni

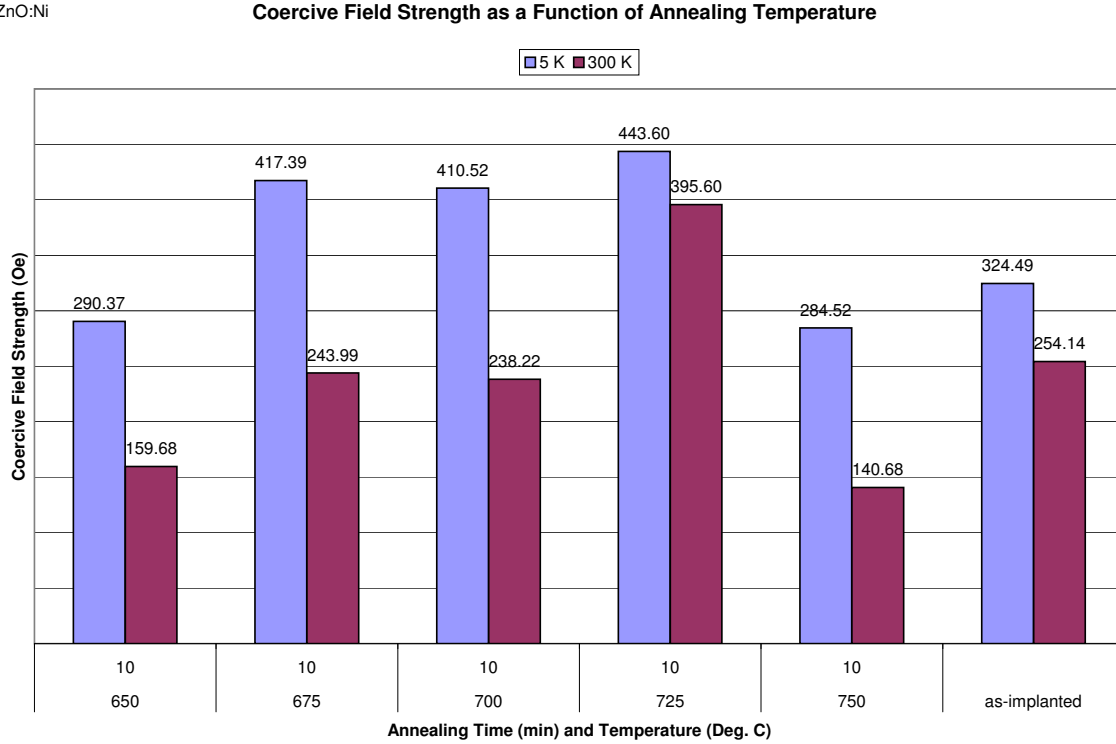


Figure 6.21 Coercive field strengths at 5 and 300 K for various annealing conditions of Ni-implanted ZnO.

Values of B_R are plotted in figure 6.22. For the purposes of maximizing remanency, the best annealing temperature is 700 °C, but strong B_R values even at room temperature are also noted for the samples annealed at 675 and 725 °C.

The variable field measurements for this material establish that annealing conditions in the range of 675 to 725 °C for a period of 10 minutes produce the strongest coercive and remanent fields. The fact that the greatest H_c occurs at an annealing temperature of 725 °C and the largest B_R value comes from the sample annealed at 700 °C suggests the possibility that the true optimum lies somewhere between these temperatures. In any case, it is possible to anneal Ni-implanted ZnO in such a way as to cause ferromagnetism persisting to room temperature.

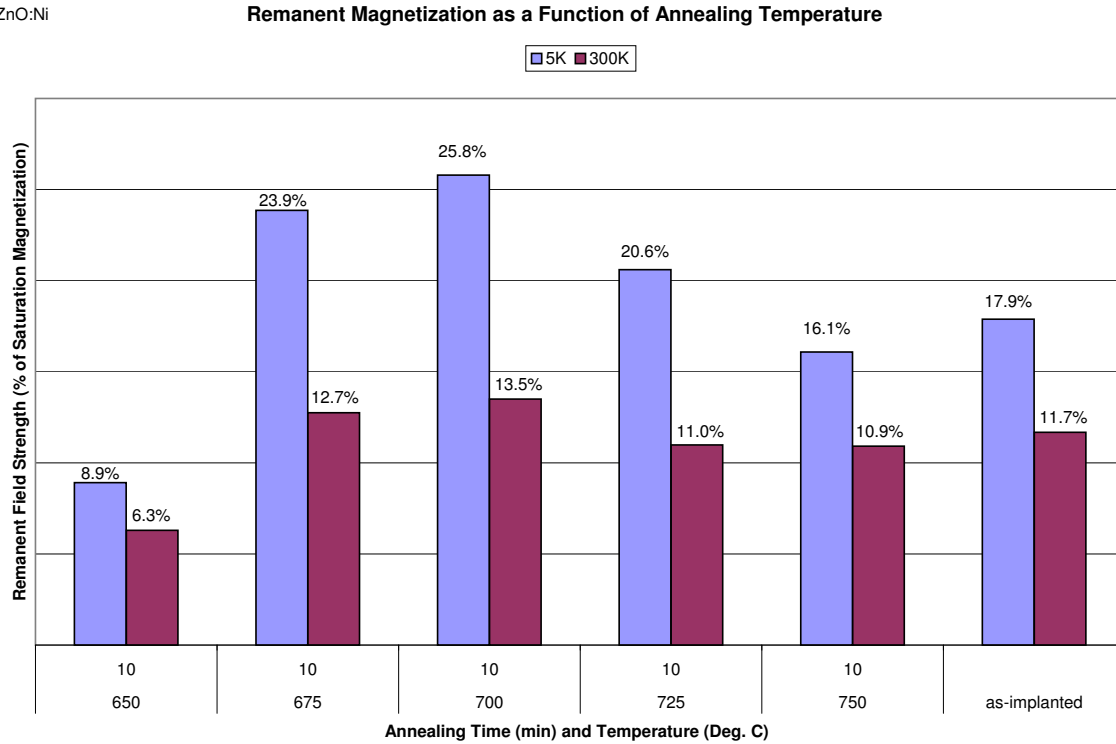


Figure 6.22 Remanent field strengths at 5 and 300 K for various annealing conditions of Ni-implanted ZnO.

6.4.2 Temperature-Dependent Magnetization

Plots of the magnetization-versus-temperature characteristics of ZnO:Ni are shown in figure 6.23 for each of the annealing conditions used in this experiment. The most striking and unique trend in this material is the tendency for ZFC magnetization to either plateau or diverge from FC magnetization at low temperature. This sort of behavior often indicates the absence of ferromagnetism in the material, but the properties revealed by the hysteresis measurements counter this. The true situation is probably frustrated ferromagnetism as evidenced by the fact that the FC and ZFC measurements track together at low temperatures before levelling or diverging in the samples annealed at 675 and 700 °C. Annealing temperatures above 700 °C show increasing divergence of low-temperature FC and ZFC magnetization. The annealed sample in which the levelling/divergence is least prominent is the one annealed at 675 °C for 10 minutes.

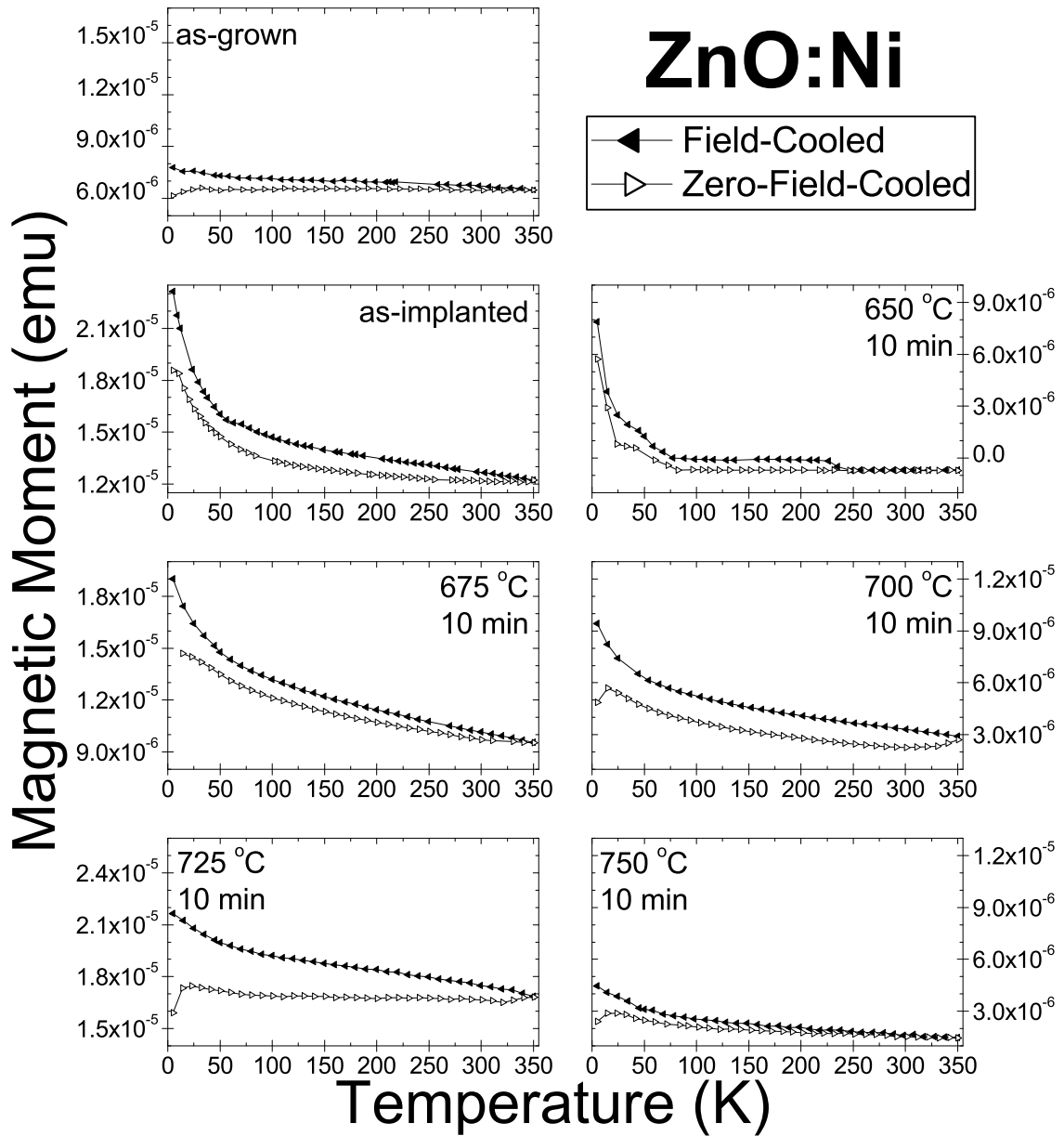


Figure 6.23 Temperature-dependent magnetization for ZnO implanted with Ni and annealed as indicated for 10 minutes in O₂ flowing at 10 sccm. Note that the y axis spans the same range of magnetic moment despite the fact that background offset causes a difference in absolute values.

The peculiar characteristics of the FC magnetization measurement on the sample annealed at 650 °C for 10 minutes can be attributed to the presence of two magnetic ordering points. Each abrupt change in magnetization (at 78 and 248 K) represents the onset of some sort of magnetic ordering as temperature is swept down-

ward in the presence of a 500 Oe applied magnetic field. These changes are not the product of anomalous measurements because viable measurements were taken even in the intermediate points of the slopes and equipment errors usually present themselves as abrupt changes. Despite the presence of some ordering at lower temperatures, the small separation between FC and ZFC magnetization, especially above 250 K, indicates a lack of strong ferromagnetism in ZnO:Ni annealed at 650 °C for 10 minutes.

The maximum separation between FC and ZFC magnetization, and ostensibly the strongest ferromagnetism, in Ni-implanted ZnO occurs when it is annealed at 725 °C. Unfortunately, this sample also displays a marked divergence of FC and ZFC magnetization at low temperature, which can indicate a lack of ferromagnetism. The presence of both of these features indicate that there are competing magnetic phases and that they reach an equilibrium that favors ferromagnetism when the sample is annealed around 700 °C. The unknown aspect of this competition is whether the material can exhibit true DMS behavior despite the presence of two magnetic phases—the test will come in future work where probing for *sp-d* hybridization and device fabrication will allow determination of whether the implanted Ni is interacting with free carriers in ZnO. Proposals for such work are presented in sections 8.2.1 and 8.2.2.1.

6.4.3 *Optical Measurements*

Cathodoluminescence spectra taken from the Ni-implanted ZnO annealed at various temperatures are shown in figure 6.24. The as-grown sample is dominated by a near band-edge peak at around 3.3 eV which arises from bound-exciton emission [140]. This peak is greatly suppressed by Ni implantation, but re-emerges after annealing, and matches the value from the as-grown sample when the Ni-implanted ZnO is annealed at 700 °C for 10 minutes.

There is also a double feature with peaks at 1.85 and 1.95 eV in the as-grown sample. This peak could be associated with oxygen vacancies [64], but is more likely

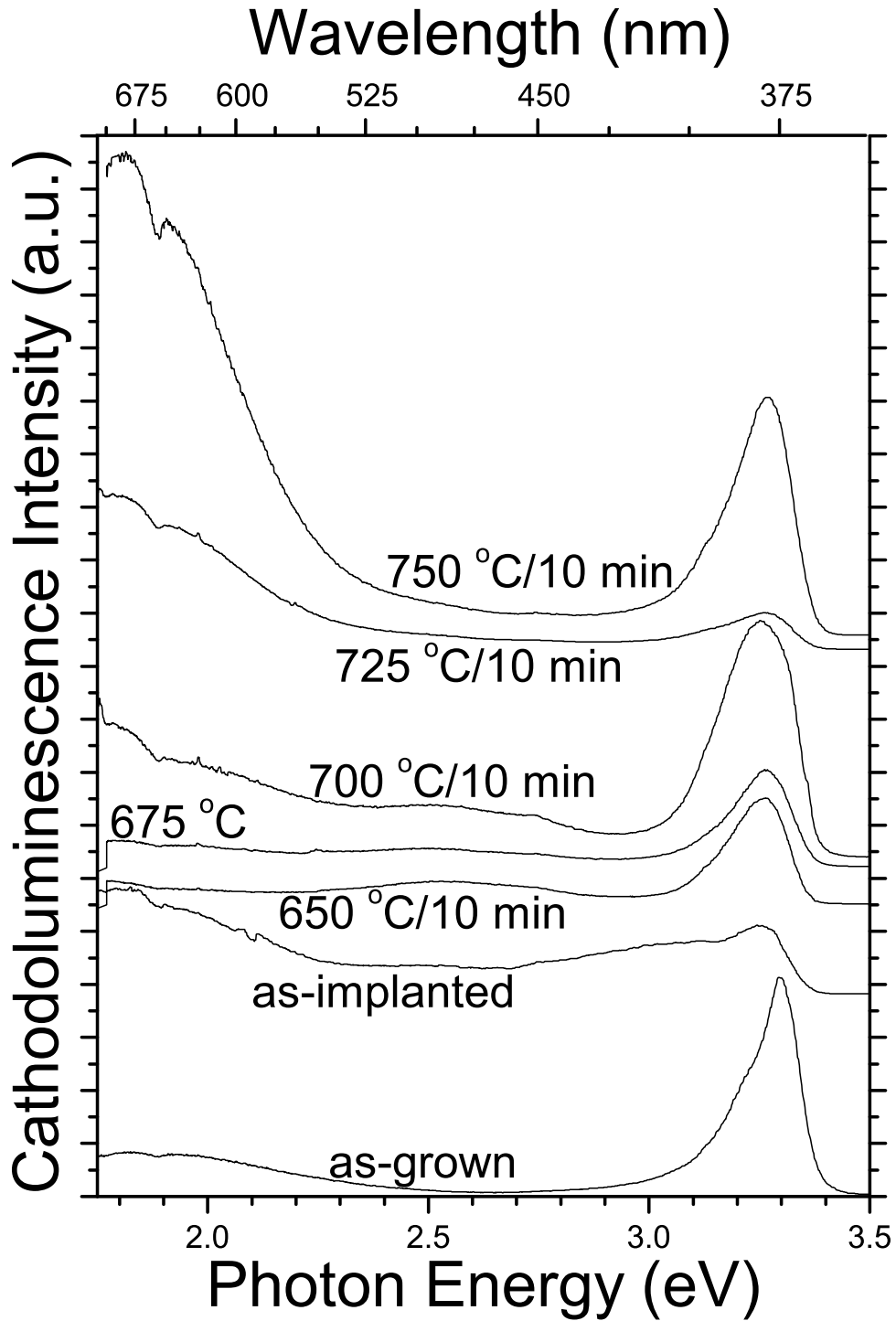


Figure 6.24 Cathodoluminescence spectra of ZnO implanted with Ni and annealed as indicated in the figure for 10 minutes. Samples were cooled to approximately 5 K for these measurements.

related to some other growth-dependent phenomenon like hydrogen complexes resulting from residue of the MOCVD precursors. With annealing after Ni implantation, this feature declines in intensity with respect to the band-edge feature up to an annealing temperature of 675 °C. The red luminescence increases again in the sample annealed at 700 °C, and it becomes dominant in the samples annealed at 725 and 750 °C. In the cases of Mn- and Cr-implanted ZnO, this feature disappeared with annealing. The reason for its persistence in ZnO:Ni is most likely connected to the fact that Ni was implanted to a dose of $3 \times 10^{16} \frac{\text{ions}}{\text{cm}^2}$ while the other two transition metals (TMs) were implanted to a level of $5 \times 10^{16} \frac{\text{ions}}{\text{cm}^2}$. The greater TM density in the sample quenches radiation from this defect in the other samples.

In the samples annealed from 650 to 700 °C, there is appears a broad blue luminescence centered at 2.6 eV. A transition between the conduction band and a zinc vacancy (V_{Zn}) is the probable source for this emission [57]. The presence of V_{Zn} is possible due to damage from Ni implantation. This damage is repaired by annealing at higher temperatures. The 2.6-eV feature is unique to the Ni-implanted ZnO samples. This may indicate a defect level related to Ni incorporation, but is more likely a result of the lower dopant dose allowing more radiative transitions than the higher doses of Mn and Cr that were used previously.

The behavior of the band-edge luminescence indicates that the crystal damage resulting from Ni implantation is best recovered by annealing at 700 °C for 10 minutes. This is consistent with the range of annealing temperatures that were seen in variable field and temperature measurements to produce desirable magnetic properties in ZnO:Ni. The true optimum may lie in between 700 and 725 °C, but the data clearly indicate that Ni-implanted ZnO can be induced to exhibit ferromagnetism.

6.5 Iron-Implanted Zinc Oxide

A thin epitaxial film of ZnO grown on *r*-Al₂O₃ from the first ZnO wafer provided by Rutgers University was implanted with Fe ions to a dose of $5 \times 10^{16} \frac{\text{ions}}{\text{cm}^2}$. The implantation was performed at room temperature with an implantation energy

of 200 keV. This experiment used a quadrant of the ZnO wafer from the first run by Rutgers. Unfortunately, as noted in section 6.1, the quality of the ZnO crystal in this sample was less than that of the second ZnO epitaxial thin film. Despite the lack of crystalline quality, there is a clear trend with annealing temperature for hysteresis-related indications of ferromagnetism in ZnO:Fe. The temperature-dependent measurements do not support the claims of ferromagnetism and photoluminescence measurements do not show convincing recovery of the implantation damage. Because of the known issues with the quality of this crystal and the fact that basic indications of ferromagnetism exist in ZnO:Fe, this material should be used in future DMS studies and will likely show a propensity for spintronic applications if the uncertainties of a lower-quality ZnO crystal can be eliminated.

6.5.1 Magnetic Hysteresis Measurements

The raw hysteresis data displayed in figure 6.25 show broad separation between the positive- and negative-going sides of the hysteresis loop for measurements made at 5 K for the samples annealed at 625 °C and less. Unfortunately, when variable field measurements are made at room temperature, the appearance of the hysteresis loops is best characterized as superparamagnetic since the hysteresis loops show high saturation but little separation. The high coercive field (H_c) and saturation magnetization (M_S) vanish in samples annealed at 650 °C and hotter for measurements taken at both 5 and 300 K.

The Fe-implanted ZnO also shows similar background diamagnetism for all of the samples upon which hysteresis measurements were taken. This background is attributed to the Al_2O_3 substrate.

In order to more accurately determine H_c and M_S values, the hysteresis data is rotated about the origin by the amount necessary to make the nearly linear region above M_S horizontal. Further discussion of the background subtraction methodology can be found in section 6.2. The variable field measurement data with the diamagnetic background removed is presented in figure 6.26.

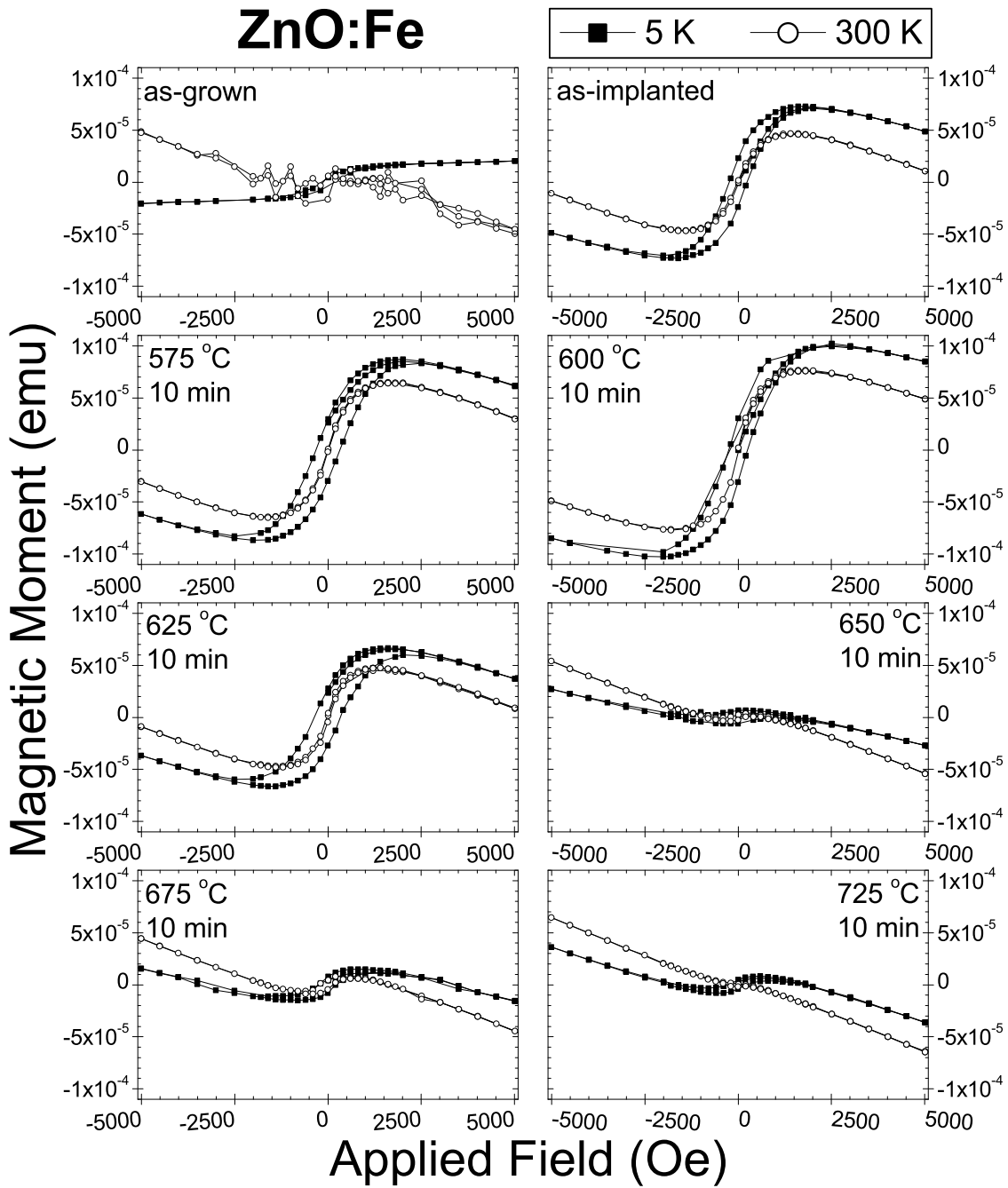


Figure 6.25 Variable field measurements (raw data) for a ZnO thin film implanted with Fe and annealed as indicated for 10 minutes in O₂ flowing at 25 sccm.

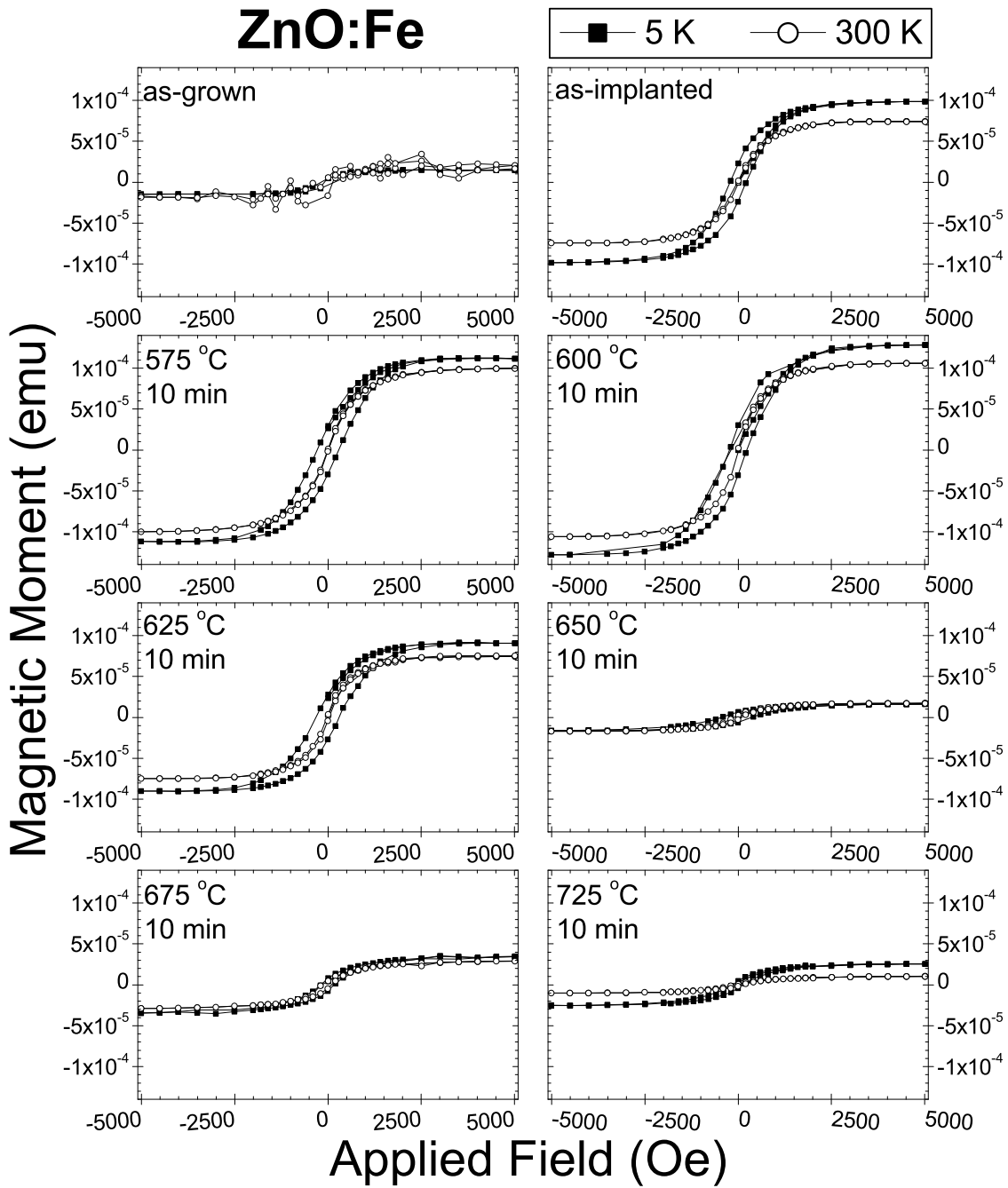


Figure 6.26 Variable field measurements (corrected to remove diamagnetism) for ZnO thin film implanted with Fe and annealed as indicated in O₂ flowing at 25 sccm for 10 minutes.

The corrected hysteresis measurements confirm the marked decrease in M_S in samples annealed at and above 650 °C versus those annealed at lower temperatures. The greatest M_S values of 1.1 and 0.73 μ_B per Fe atom occur when the sample is annealed at 600 °C for 10 minutes. The calculated maximum effective magneton number for Fe^{2+} is 5.4 [8, Table 31.4]. The data presented in figure 6.26 also further clarify the diminishing of hysteresis width between sample measured at 5 and 300 K.

The characteristics noted from variable field measurements on ZnO:Fe suggest that this material will not make a useful DMS, particularly since room temperature ferromagnetism is virtually non-existent. The fact that hysteresis measurements for all of the samples annealed at and below 625 °C show the same characteristics as the as-implanted sample demonstrates that the magnetism arising from these samples is not due to incorporation of Fe into the ZnO crystal lattice. The lack of magnetic saturation and hysteretic separation in the samples annealed at and above 650 °C suggests that these samples have an inherently non-magnetic character. The lack of coordination between Fe atoms that would allow a magnetic field implies that there is also no interaction between the implanted Fe and the ZnO conduction and valence bands.

The behavior of H_c as a function of annealing temperature at both 5 and 300 K is depicted in figure 6.27. The sample annealed at 650 °C for 10 minutes in flowing O_2 showed remarkable coercive field strength at cryogenic temperatures. Annealing at 675 °C for 10 minutes produced the strongest coercive field at room temperature. However, the H_c values for the samples annealed at and above 650 °C are not believable due their low-value, slow-onset saturation characteristics, which lead to a slant in the legs of the hysteresis loop as it crosses the zero magnetization line. Despite the apparent optimum annealing temperature for maximizing H_c , the evidence presented in figures 6.25 and 6.26 is overwhelming that ZnO:Fe is non-magnetic, or at best paramagnetic, at room temperature for the annealing conditions used in this experiment.

Coercive Field Strength as a Function of Annealing Temperature

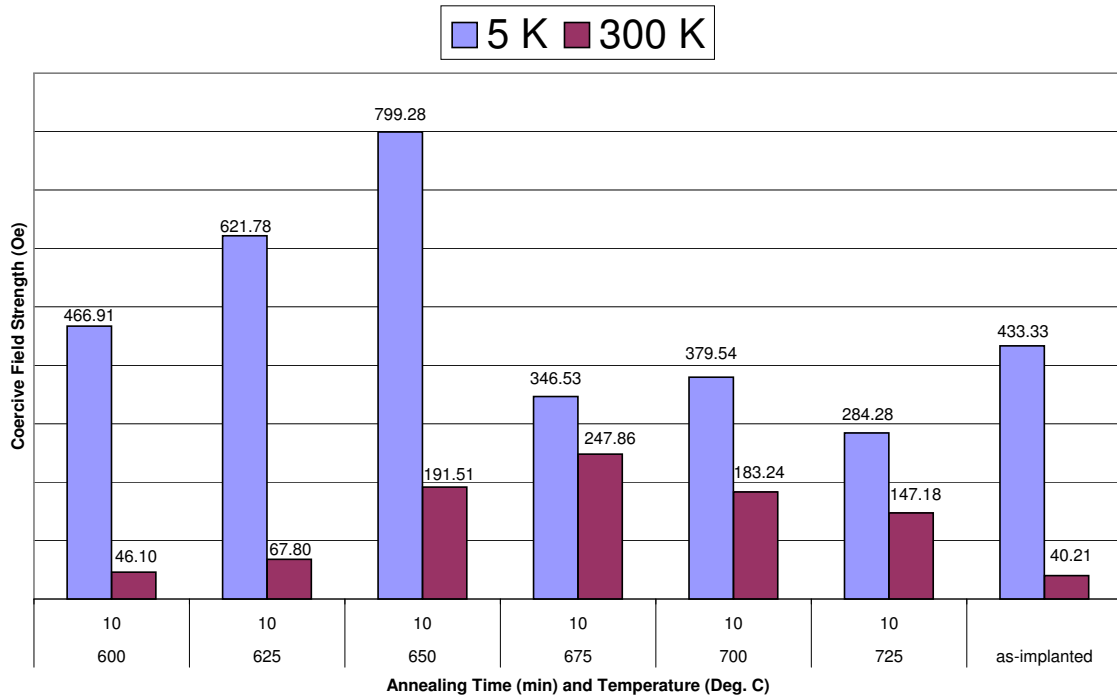


Figure 6.27 Coercive field strengths at 5 and 300 K for various annealing conditions of an Fe-implanted ZnO epitaxial thin film.

Remanent field strength (B_R) is less sensitive to artifacts from the background subtraction algorithm, so the data presented in figure 6.28 are valid measurements of B_R . The values determined for B_R follow a trend with 5-K measurements showing a maximum for the sample annealed at 650 °C for 10 minutes and room temperature measurements showing the strongest B_R occurring at 650 and 675 °C. While this data is useful for determining optimal annealing conditions to maximize B_R , this alone does not indicate the presence of ferromagnetism persisting to room temperature in Fe-implanted ZnO.

6.5.2 Temperature-Dependent Magnetization

FC and ZFC measurements are shown in figure 6.29. As in the variable field measurements, there is a noticeable difference between the samples annealed at and below 625 °C and those annealed at and above 650 °C in the variable temperature magnetization measurement. These differences are manifest in both the mag-

Remanent Magnetization as a Function of Annealing Temperature

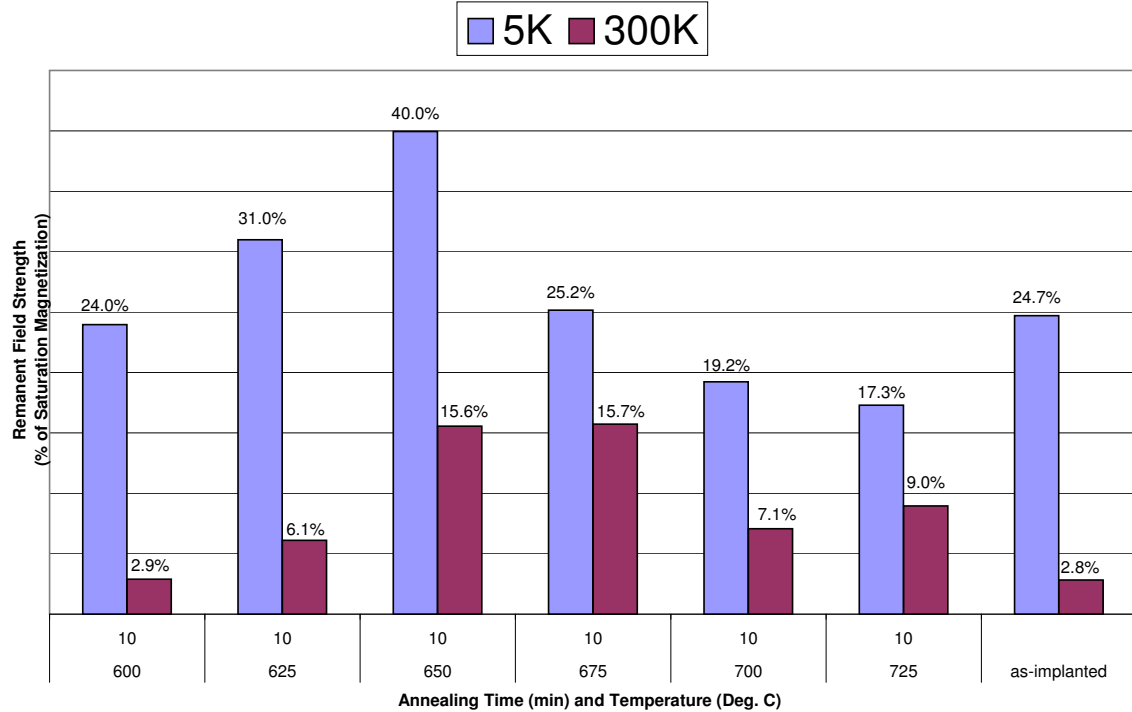


Figure 6.28 Remanent field strengths at 5 and 300 K for various annealing conditions of an Fe-implanted ZnO epitaxial thin film.

nititude of separation between FC and ZFC magnetization and the behavior of the low-temperature ZFC magnetization values.

The as-implanted sample and those annealed at less than 650 °C have a greater magnitude of FC–ZFC separation. Greater separation is normally an indication of ferromagnetism, but in this case, it is a by-product of the low-temperature divergence of FC and ZFC magnetization. Divergence at low temperature is an indication of a spin-glass phase [89]. The presence of a spin-glass state also explains the utter collapse of the hysteresis seen in figures 6.25 and 6.26 when the variable field measurement is taken at room temperature.

The minimal separation between FC and ZFC magnetization in samples annealed at and above 650 °C is also an indication that ferromagnetism is not present. Further evidence that these samples are not ferromagnetic is seen in the fact that

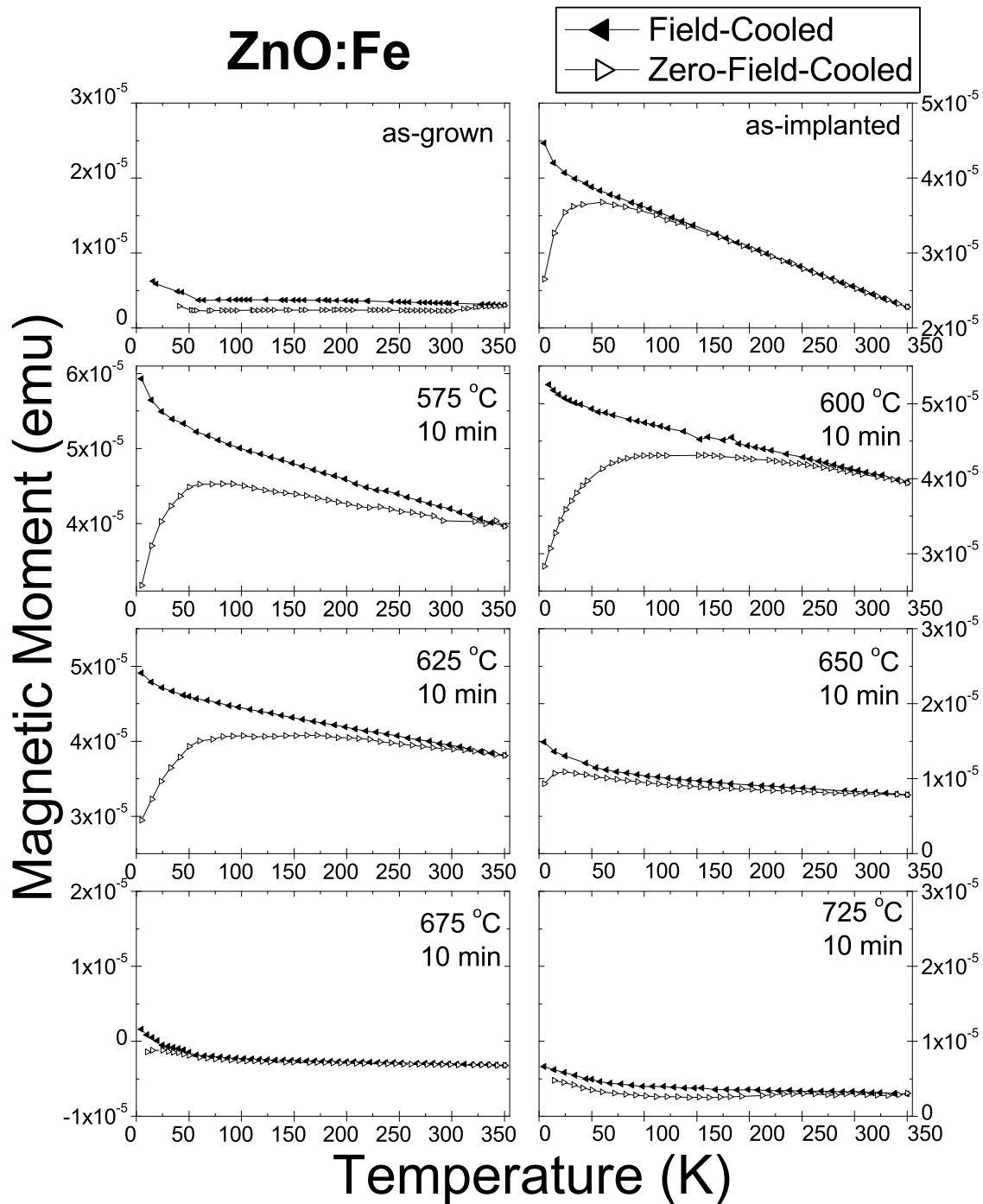


Figure 6.29 Temperature-dependent magnetization for ZnO implanted with Fe and annealed as indicated in the figure for 10 minutes in O₂ flowing at 25 sccm. Note that the *y* axis spans the same range of magnetic moment despite the fact that background offset causes a difference in absolute values.

most of them also show divergence between FC and ZFC magnetization at low temperatures.

The variable temperature measurements corroborate the conclusion drawn from the variable field measurements: ZnO:Fe is not ferromagnetic for the annealing conditions used in this experiment.

6.5.3 Optical Measurements

Photoluminescence measurements of the Fe-implanted ZnO thin film are displayed in figure 6.30. The PL data for the as-grown sample shows a near band-edge peak at 3.37 eV, which is typical for ZnO [72]. There are also broad luminescence peaks in the violet and red-orange regions of the spectrum. The violet luminescence centered around 2.9 eV is attributed to interstitial Zn (Zn_i) [65]. The smaller luminescence around 2 eV is attributed to transitions between the conduction band and singly ionized oxygen vacancies (V_O^+) [64]. The clear presence of Zn_i and V_O^+ in this ZnO before ion implantation suggests that the quality and crystallinity of this material is not good enough to produce a DMS.

For all implanted samples, regardless of annealing conditions, the total luminescence was greatly reduced and dominated by noise—notice that PL spectra from the implanted samples are magnified by a factor of 50 over the as-grown sample’s PL spectrum. The band-edge is not recovered with annealing and, in fact, becomes more and more obscured with increasing annealing temperature. Although recovery of implantation damage for Fe-implanted ZnO has been reported for samples annealed in a 2-hour stepped process with a maximum temperature of 1050 °C, such annealing would render magnetic results questionable because of the probability of clustering at these temperatures. Furthermore, annealing at higher temperatures would preclude comparison of these results with those for ZnO nanotips reported in Chapter VII because the nanotips tend to fuse together at temperatures above 800 °C.

It is possible that incorporation of Fe into ZnO creates a non-radiative trap within the bandgap of the semiconductor. See, for example, the work of Zhengwu

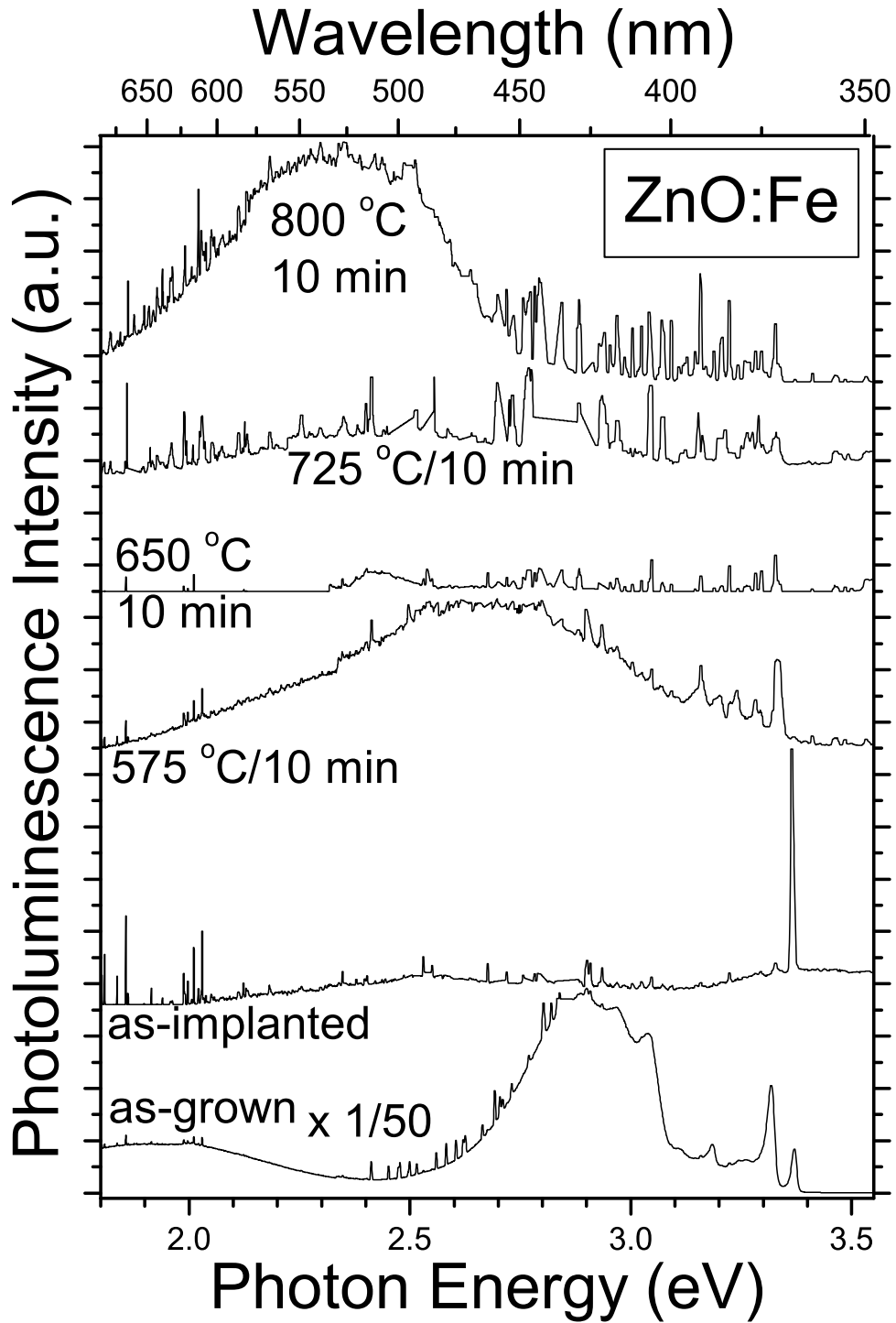


Figure 6.30 Photoluminescence spectra, collected at approximately 10 K, of ZnO implanted with Fe and annealed as indicated for 10 minutes in O₂ flowing at 25 sccm.

et al. where ZnO:Fe shows the weakest luminescence of the transition-metal-doped samples reported [47]. If the implanted Fe quenches luminescence when it is incorporated into the ZnO crystal lattice, then its effective incorporation does not guarantee ferromagnetic properties.

The broad blue luminescence seen in the sample annealed at 575 °C for 10 minutes can be attributed to anion (oxygen) vacancies in ZnO [19]. The broad green luminescence seen in the sample annealed at 800 °C for 10 minutes is characteristic of oxygen vacancies in ZnO [139]. These vacancies are caused by dissociation of the ZnO at higher temperatures. The fact that both of these slightly different blue-green PL features are attributed to oxygen vacancies is not surprising since a variety of researchers have reported native defect peaks related to V_O across a fairly broad range [19]. The broad luminescence around 2.9 eV in the as-grown film corresponds to the calculated value for Zn interstitials [65].

The magnetic measurements presented above show that Fe-implanted ZnO does not make a good DMS. The PL data offers a reasonable explanation for this behavior: low crystal quality prevents magnetic coordination among implanted transition metals.

6.6 Conclusions

Epitaxial thin films of ZnO implanted with transition metals show promise for applications requiring a DMS. Of the dopants investigated in this research, Mn showed the best indications of ferromagnetism when implanted into the higher quality of the two ZnO wafers. Annealing this material between 675 and 700 °C for 10 minutes produces coercive field widths (H_c) of at least 315 and 228 Oe at 5 and 300 K, respectively. Unfortunately, weak saturation magnetization (M_S) in this range of annealing temperatures prevents reliable measurements of remanent field (B_R) as a function of M_S .

Implanting Cr into ZnO also produced desirable ferromagnetic properties and may find use in DMS-based devices. H_c s of 335 and 230 Oe at 5 and 300 K, respectively, are achieved by annealing this material at 725 °C for 10 minutes. The maximum B_R of 14×10^{-6} emu at 5 K and 6×10^{-6} emu at 300 K and the greatest FC–ZFC separation are obtained under these conditions as well.

Competition between phases in the Ni-implanted ZnO leads to some indication of desirable magnetic behavior, but the lack of trending in field strengths with annealing temperature is troublesome. Still, the 700 to 725 °C range produces the maximum H_c and B_R values seen in this material. The greatest H_c s of 444 Oe (5 K) and 396 Oe (300 K) occur in the sample annealed at 725 °C for 10 minutes. The greatest B_R values of 26 and 13.5% occur in the sample annealed at 700 °C for 10 minutes. This material will provide an interesting instance in device fabrication to test the sensitivity of spintronic devices to the presence of non-ferromagnetic ordering in the DMS.

Another valuable insight gained from the experiments involving epitaxial ZnO is the sensitivity of magnetic properties to the quality of the semiconductor crystal. This is illustrated most strikingly in the two cases where Mn was implanted into ZnO thin films grown at different times. Unfortunately, the lack of crystal quality also prevented the Fe-implanted samples from clearly showing ferromagnetism. Because the sensitivity of magnetic properties to crystal quality, Fe cannot be ruled out as a possible dopant for DMS fabrication in ZnO.

*VII. Characteristics of Transition Metal Implanted
Zinc Oxide Nanotips Grown on Various Substrates*

ZnO nanotips were grown on quartz, sapphire, and glass substrates by metal-organic chemical vapor deposition (MOCVD). These nanotips are tiny pillars of single-crystal ZnO that rise from the substrate with little or no connection to one another. A scanning electron microscope (SEM) image of ZnO nanotips grown on quartz is shown in figure 7.1, and SEM images of nanotips grown on sapphire and glass are shown at the beginning of sections 7.2 and 7.3, respectively.

It is apparent from the lack of connection between pillars of ZnO seen in figure 7.1 that this sort of material cannot be easily used to make a device based on charge carrier movement. The isolation between individual nanotips may prove beneficial in certain applications. The most obvious applications for this sort of material is as a sensor. The vastly increased surface area of the nanotips over a conventional thin film would allow for added sensitivity to substances in the ambient air. The effects of interesting airborne substances on the magnetic properties of the transition-metal-doped ZnO is a matter for further investigation. Another application for such material is a data storage system based on magnetic writes and optical reads in order to leverage the speed advantages of each. A remanent field in the material induced by the magnetic write head could be optically read out by the Kerr rotation of a polarized beam.

Ion implantation and subsequent annealing result in a relatively uniform distribution of the implanted transition metal into the ZnO nanotips [45]. This leads to a more diluted concentration of the implanted transition metal, which may offer advantages in magnetic properties since they are sensitive to crystal quality.

In order to shorten the notation of the substrate upon which the ZnO nanotips were grown, the substrate will be noted in parentheses after ZnO. For example, Fe-doped ZnO nanotips grown on a sapphire substrate will appear as ZnO/(*c*-Al₂O₃):Fe.

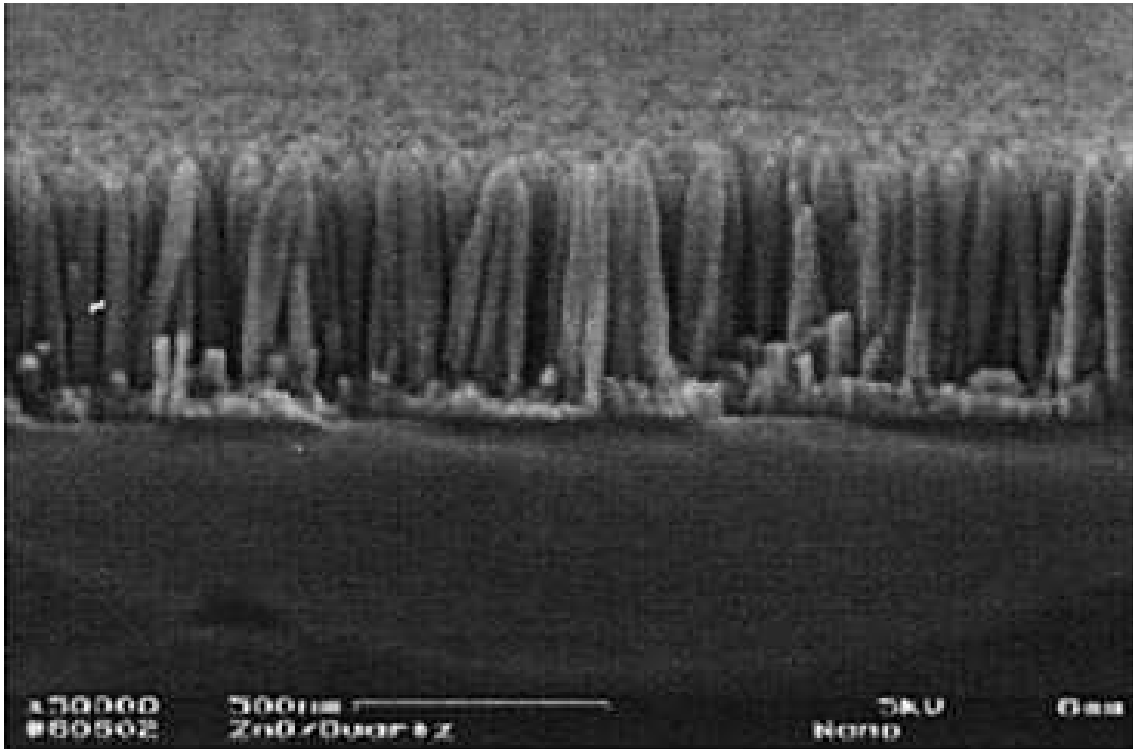


Figure 7.1 An SEM image of ZnO nanotips as-grown on a quartz substrate.

This notation is not meant to imply that the ZnO is an epitaxial thin film or that the substrate was implanted with any ions.

Consistent results are much more difficult to achieve in this material than in the epitaxial thin films of ZnO, *p*-GaN, and $\text{Al}_{0.35}\text{Ga}_{0.65}\text{N}$ reported in previous chapters. The most promising nanotips are those grown on quartz and implanted with Mn and those grown on *c*- Al_2O_3 and implanted with Fe. Common to both of these samples is the need for a 20-minute anneal time to produce the most desirable magnetic properties. The increased surface area of the ZnO nanotips compared to thin films accounts for this increased sensitivity to annealing conditions.

7.1 Zinc Oxide Nanotips on Quartz

ZnO nanotips were grown on a quartz substrate by MOCVD. The resulting structures are shown in figure 7.1. These ZnO nanotips were implanted with Mn and

with Fe. Both Mn- and Fe-implanted samples showed signs of ferromagnetism after annealing, but it was difficult to determine which annealing conditions were actually best. The Mn-implanted samples demonstrate agreement between the magnetic and optical measurements as to the best annealing conditions. The Fe-implanted ZnO/(quartz), however, shows some conflicting indications of which annealing conditions maximize ferromagnetism.

7.1.1 Manganese-Implanted ZnO Nanotips on Quartz

Mn was implanted into ZnO nanotips grown on a quartz substrate to a level of $5 \times 10^{16} \frac{\text{ions}}{\text{cm}^2}$ at room temperature with an implantation energy of 200 keV. The annealing condition that produces the most promising signatures of true DMS behavior is 675 °C for 20 minutes. Although coercive and remanent fields are highest in the sample annealed at 750 °C for 10 minutes, temperature-dependent magnetization and photoluminescence show that annealing at 675 °C for 20 minutes causes the implanted Mn to be well-incorporated into the ZnO crystal lattice.

7.1.1.1 Magnetic Hysteresis Measurements

The results of variable field measurements on Mn-implanted ZnO/(quartz) are shown in figure 7.2. Except for the sample annealed at 750 °C for 10 minutes, the ZnO/(quartz) samples implanted with Mn show superparamagnetism (samples annealed at 675 and 700 °C) or diamagnetism (as-implanted and samples annealed at 725 and 800 °C). The quartz substrate is the most likely cause of the diamagnetic background seen in all of the samples.

The ZnO/(quartz):Mn annealed at 750 °C for 10 minutes shows a sharp magnetic saturation and some separation between positive- and negative-going legs of the hysteresis loop. This particular sample also shows the most decisive dominance of ferromagnetic properties over the background diamagnetism. Some of the hysteretic separation is also due to the removal of data points where a high standard deviation ($> 10^{-6}$) exists between the three measurements taken. High standard deviation is

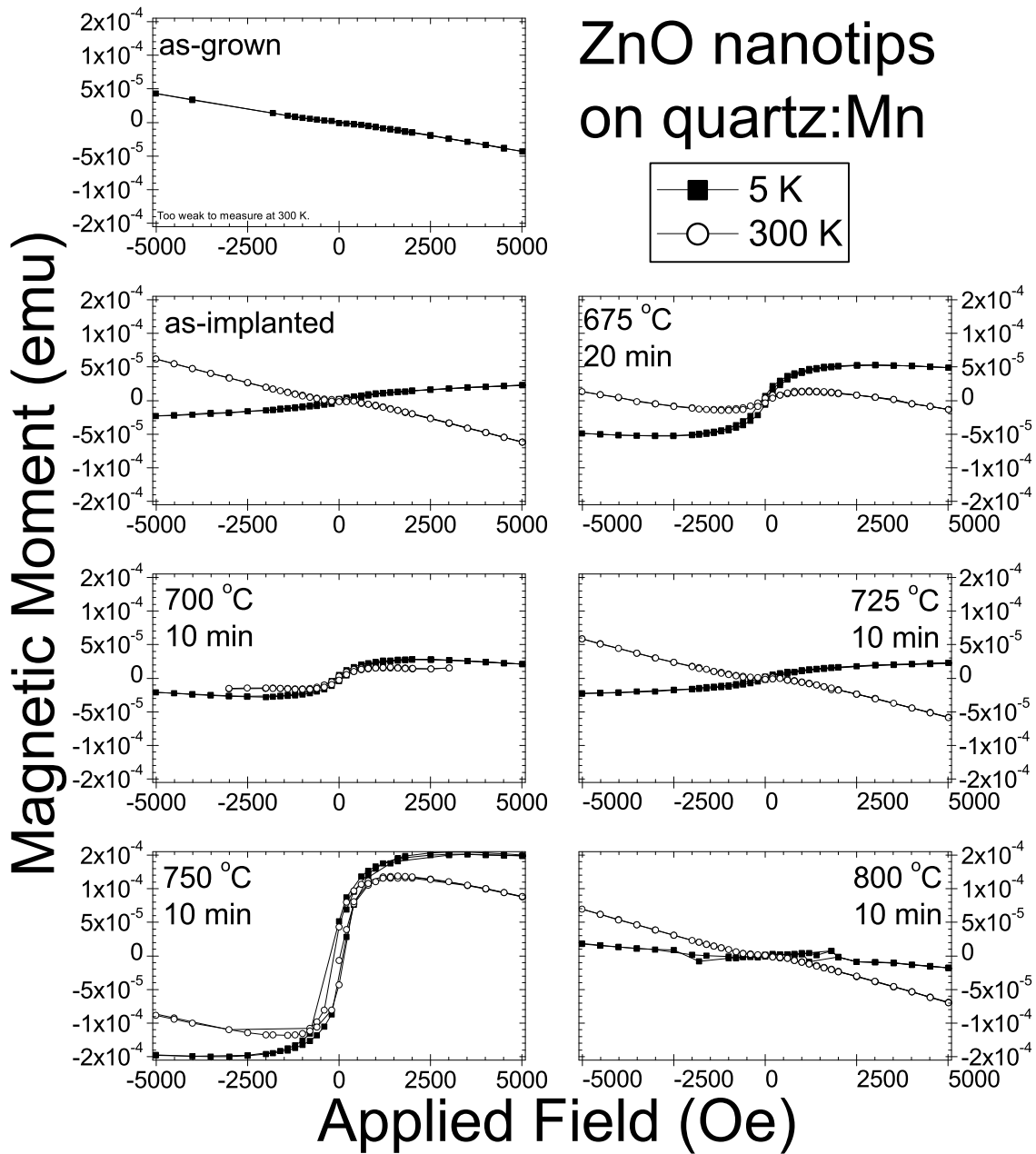


Figure 7.2 Raw data from magnetic hysteresis SQUID measurements of Mn-implanted ZnO nanotips on quartz annealed as indicated in O_2 flowing at 25 sccm.

usually indicative of a measurement error or environmental noise coupling into the SQUID signal amplifier. This leaves the negative-going leg of the measurement with fewer data points than it should have and possibly leads to a wider separation than is actually present.

The uncorrected data presented in figure 7.2 will give slightly erroneous values for coercive field (H_c) because the tilt induced by underlying diamagnetism will cause the zero magnetization line to cross the hysteresis loop at an angle. Therefore, a correction to the raw data is necessary to allow meaningful, numerical comparisons of H_c and among the samples characterized in this manner. The SQUID data presented in figure 7.3 have the linear diamagnetic influences arising from the substrate removed. Diamagnetism is removed using a MATLAB[®] routine that determines the amount of rotation about the origin necessary to make the magnetization values as nearly equal in value as possible. Each data point is then rotated by this amount so that saturation magnetization (M_S) becomes apparent and accurate values for H_c can be ascertained. Remanent field (B_R) values are not as sensitive to the diamagnetic background, but B_R data presented is determined from the variable field measurements with background diamagnetism subtracted.

With background diamagnetism removed, all of the samples display superparamagnetism. There are large M_S values and a small coercivity apparent in the samples annealed at 675 °C for 20 minutes and at 750 °C for 10 minutes. M_S for the sample annealed at 750 °C holds at approximately 1.1 μ_B per Mn atom for measurements performed at both 5 and 300 K. The calculated maximum is 5.9 μ_B for Mn^{2+} [8, Table 31.4]. While these samples represent the best of the ZnO/(quartz):Mn group, their ferromagnetic characteristics are not convincing.

Variable field measurements of ZnO/(quartz):Mn show that the greatest coercive field width at room temperature is obtained when the Mn-implanted sample is annealed at 750 °C for 10 minutes. The H_c value for this sample reported in figure 7.4 is most likely inflated due to missing data points in the hysteresis loop.

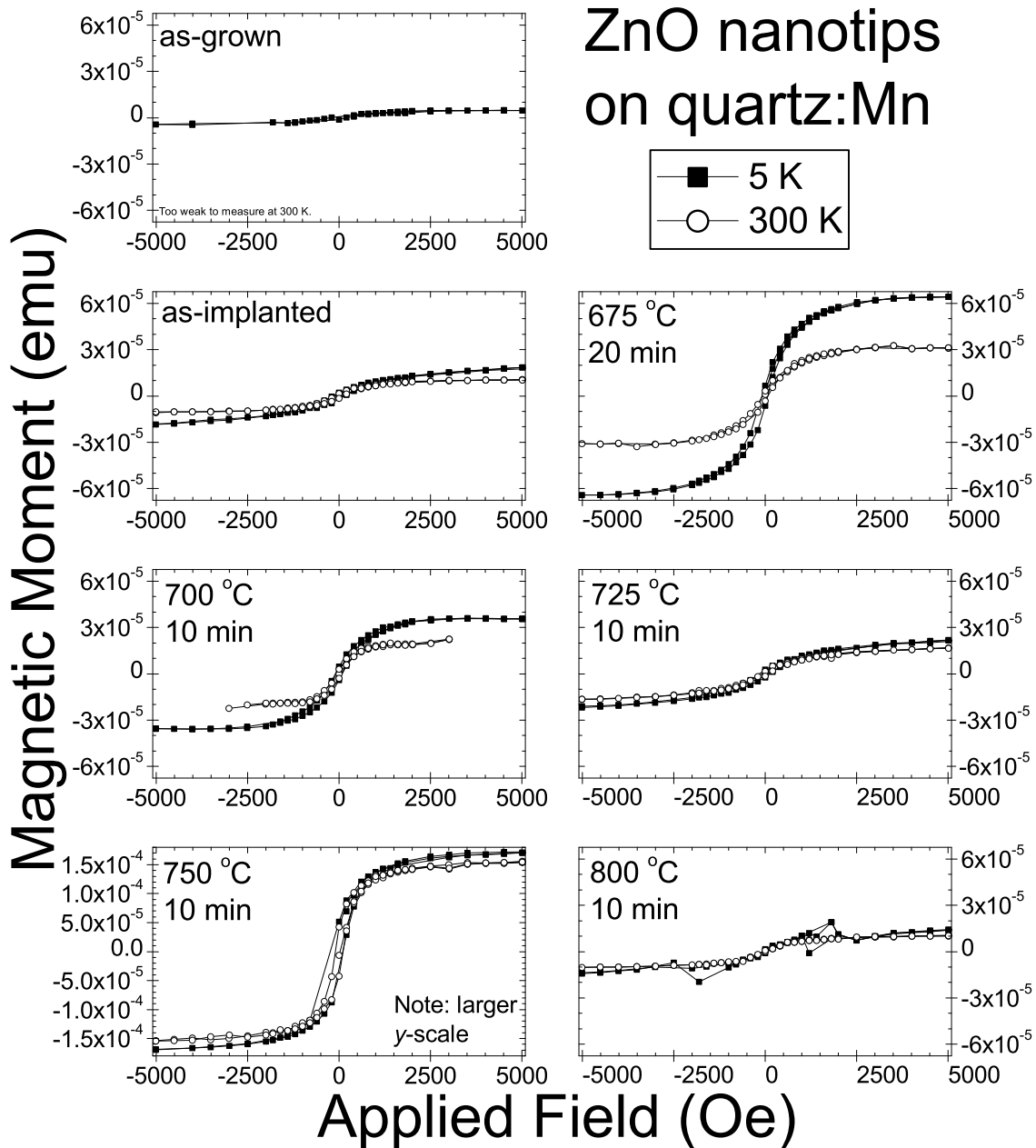


Figure 7.3 Magnetic hysteresis data for ZnO nanotips grown on quartz, implanted with Mn and annealed as indicated in the figure in an atmosphere of O₂ flowing at 25 sccm. Linear diamagnetic influences have been removed from this data.

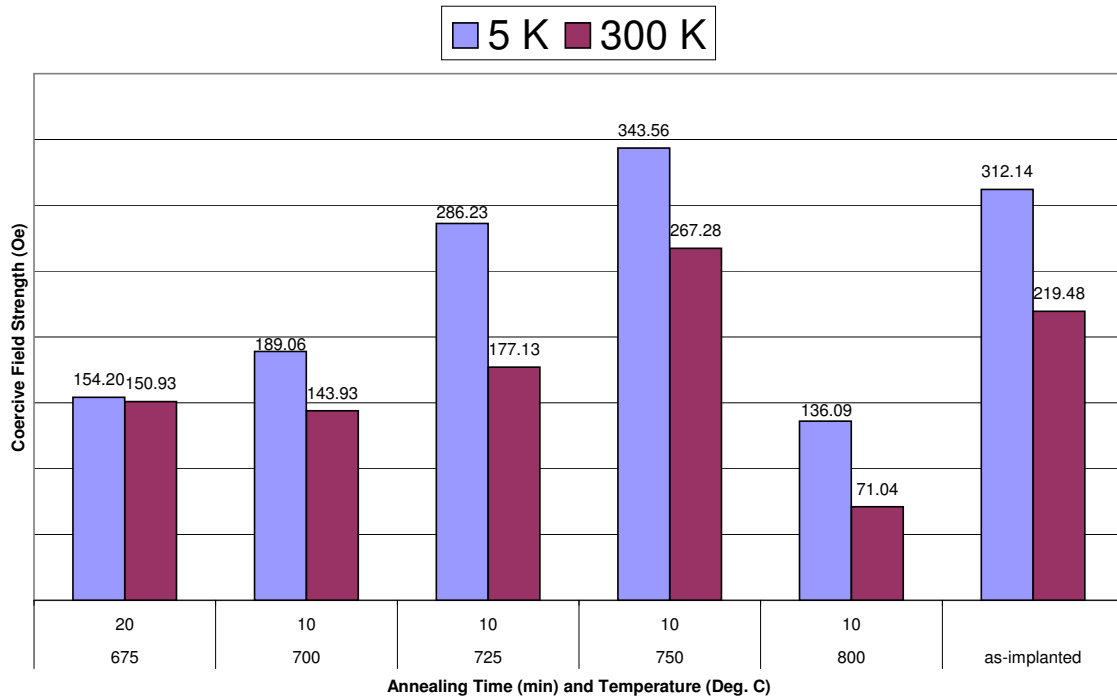


Figure 7.4 Coercive field strengths at 5 and 300 K for various annealing conditions of Mn-implanted ZnO nanotips grown on quartz.

The B_R values determined for the Mn-implanted ZnO/(quartz) samples are displayed in figure 7.5. This data shows the greatest remanency also occurs when the sample is annealed at 750 °C for 10 minutes. The fact that B_R is calculated as a percentage of M_S means that the high value reported for this sample is not merely a result of its high saturation magnetization.

From variable field measurements, it appears that there are at least two annealing conditions that induce ferromagnetism in Mn-implanted ZnO/(quartz). This is a reasonable result since the sample annealed at the lower temperature (675 °C) was annealed for twice as long (20 minutes versus 10 minutes) as the sample annealed at the higher temperature (750 °C). Given the superparamagnetic characteristic of the hysteresis loops, the nature of these ferromagnetic indicators will be investigated further in the following sections.

Remanent Magnetization as a Function of Annealing Temperature

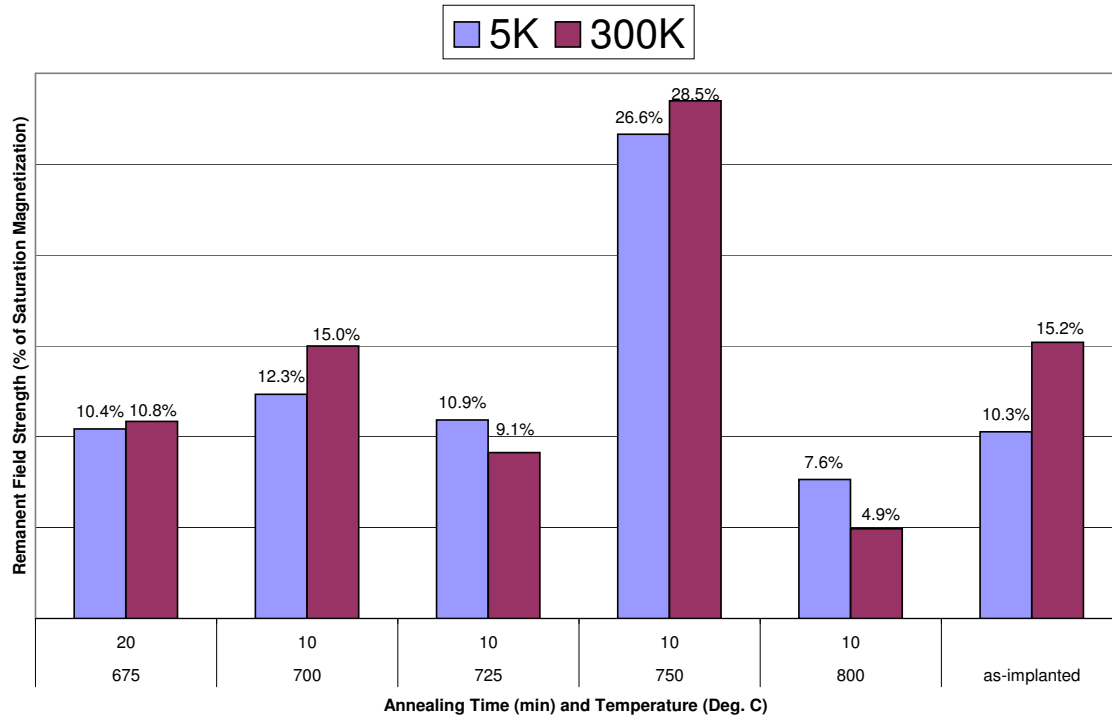


Figure 7.5 Remanent field strengths at 5 and 300 K for various annealing conditions of Mn-implanted ZnO nanotips grown on quartz substrates.

7.1.1.2 Temperature-Dependent Magnetization

Variable temperature SQUID measurements reveal the absence of a spin-glass phase in all of the ZnO/(quartz):Mn samples. In fact, the data presented in figure 7.6 show that a ferromagnetic phase dominates the Mn-implanted ZnO nanotips except for the sample annealed at 750 °C for 10 minutes. The ferromagnetism is indicated by the fact that there is separation between the FC and ZFC magnetization measurements and that the magnetization values track together at low temperature. The lack of ferromagnetism in the sample annealed at 750 °C is indicated by the gap between FC and ZFC magnetization being smaller than even the gap in the as-implanted sample.

The greatest separation between FC and ZFC magnetization occurs in the ZnO/(quartz):Mn when it is annealed at 675 °C for 20 minutes. Despite weaker signs of ferromagnetism in variable field measurements, temperature-dependent measure-

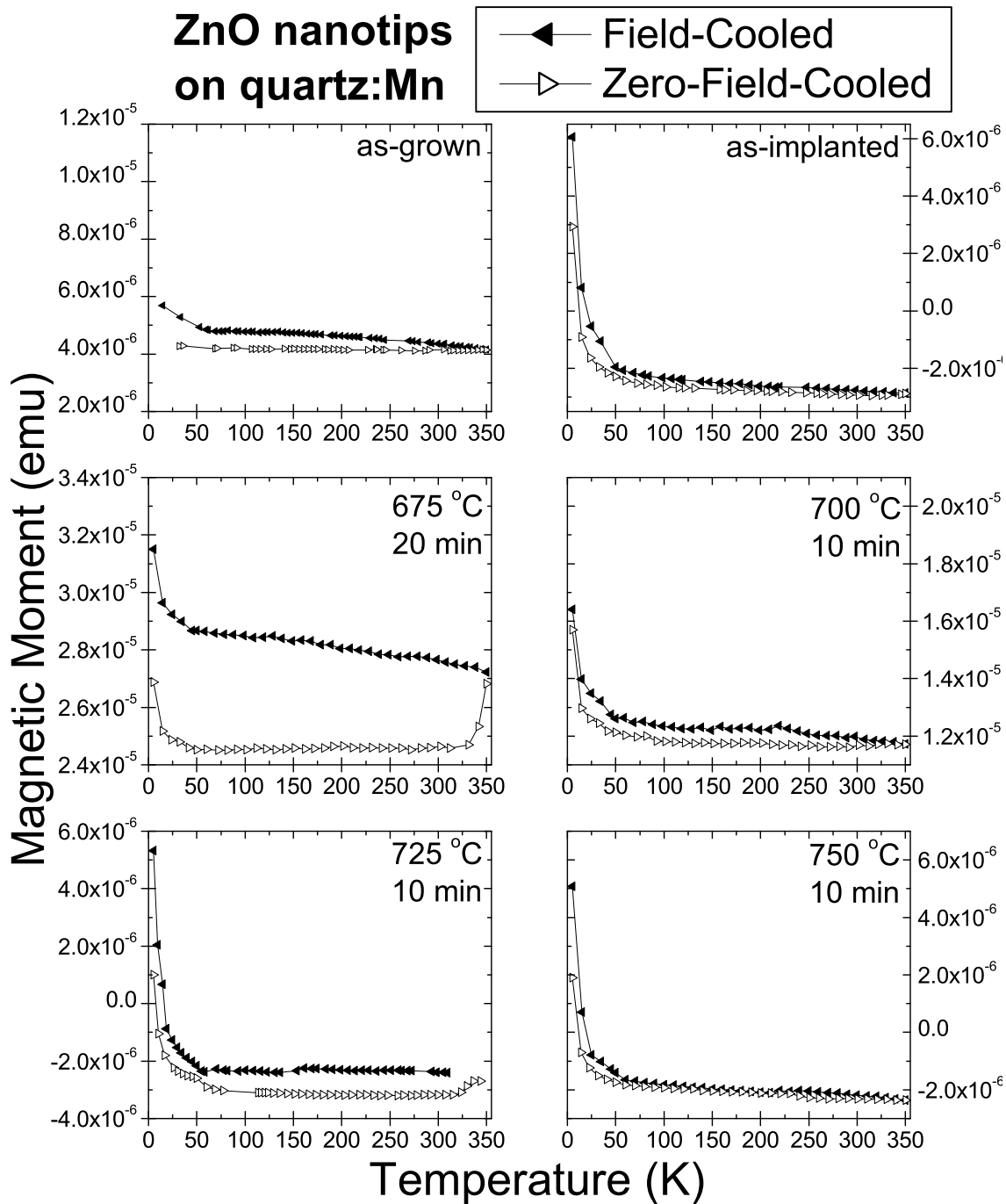


Figure 7.6 Temperature-dependent magnetization for ZnO nanotips implanted with Mn and annealed as indicated in the figure in O₂ flowing at 25 sccm. Note that the y axis spans the same range of magnetic moment despite the fact that background offset causes a difference in absolute values.

ments show that annealing at 675 °C for 20 minutes produces the strongest indicators of ferromagnetism. As seen in the Mn-implanted epitaxial ZnO samples reported in section 6.1, there is precedent for maximizing FC–ZFC separation with a 20-minute annealing time.

7.1.1.3 Optical Measurements

PL spectra, shown in figure 7.7, were collected for ZnO nanotips grown on quartz, implanted with Mn, and annealed at various temperatures. The as-grown sample shows features that are inherent to bulk ZnO. This indicates that, as expected, the size of the ZnO nanotips is too large to induce appreciable quantum confinement effects. The primary peak at 3.3663 eV is attributed to a donor-bound A exciton. The secondary peak at 3.3204 eV is attributed to a two-electron satellite (TES) transition of a donor-bound A exciton [122]. The regular ~ 90 -meV spacing of further subordinate peaks identifies them as phonon replicas.

Optically, the best band-edge recovery occurs when the sample is annealed at 675 °C for 20 minutes. This corresponds with the strongest indication of ferromagnetism in temperature-dependent measurements. The coincidence of these indicators suggests that the highest probability for true DMS behavior as a result of Mn incorporation in the ZnO crystal lattice. Ferromagnetism arising from Mn incorporation will also allow interaction between the implanted Mn and the crystal structure of the ZnO nanotips grown on quartz. Therefore, ZnO/(quartz):Mn should be useful as nanostructure DMS.

7.1.2 Iron-Implanted ZnO Nanotips on Quartz

The ZnO nanotips grown on quartz were implanted with Fe at room temperature with an energy of 200 keV to a level of $5 \times 10^{16} \frac{\text{ions}}{\text{cm}^2}$. Annealing this sample produces inconsistent results. Hysteresis is strongest in the samples annealed at 650, 725, and 800 °C, but FC and ZFC magnetization measurements show the strongest signs of ferromagnetism for annealing at 675 and 700 °C. Photoluminescence measure-

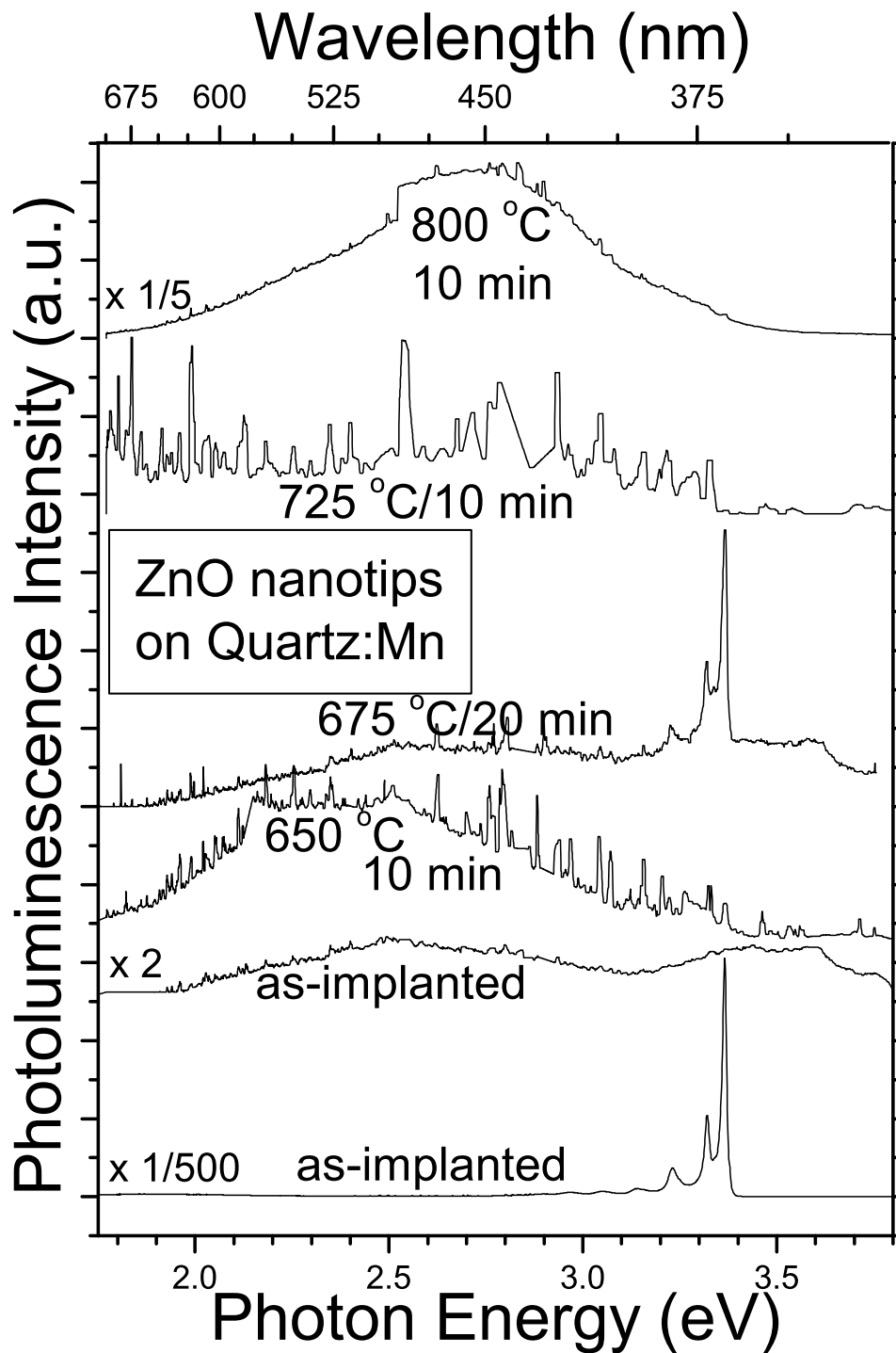


Figure 7.7 Photoluminescence spectra of ZnO implanted with Mn and annealed as indicated in O₂ flowing at 25 sccm. The samples were cooled to ~10 K for these measurements.

ments do not show appreciable recovery of the damage caused by Fe implantation. ZnO/(quartz):Fe does not show convincing signs of ferromagnetism as a result of interaction between the ZnO semiconductor and the implanted Fe.

7.1.2.1 *Magnetic Hysteresis Measurements*

Variable field measurements on ZnO/(quartz):Fe are presented in figure 7.8. From these measurements, magnetic saturation is apparent in every sample, but the saturation magnetization (M_S) is relatively low for this group compared to other materials studied in this research. The Fe-implanted ZnO/(quartz) samples annealed at 650, 700, 725, and 800 °C also show separation between the sides of their hysteresis loops. These signs of ferromagnetism are encouraging, but the fact that they occur in samples annealed at such a wide variety of temperatures calls the true source of this behavior into question. The noise present in measurements performed on the sample annealed at 675 °C for 10 minutes calls into question whether some unknown and uncontrolled factor in the experiment plays a significant role in the magnetic properties of this material. The measurements presented in figure 7.8 for ZnO/(quartz):Fe annealed at 675 °C are accurate (the measurement was performed three times on these pieces of material), but these results may not be repeatable if another Fe-implanted ZnO/(quartz) sample is annealed under the same conditions.

In order to gain more insight into the magnetic behavior of ZnO/(quartz):Fe and to determine values for the coercive field (H_c), the background diamagnetism is removed from the data, which is displayed in figure 7.9. This process entails rotating each data point about the origin by the amount necessary to bring the linear region above saturation parallel to the x axis.

The hysteresis loops with background diamagnetism removed show that the greatest M_S occurs in the sample annealed at 650 °C for 10 minutes. The values of M_S in this sample are 0.18 and 0.16 μ_B per Fe atom at 5 and 300 K, respectively, with a calculated effective magneton for Fe^{2+} of 5.4 [8, Table 31.4]. The previous observation that the samples annealed at 650, 700, 725, and 800 °C are those that show

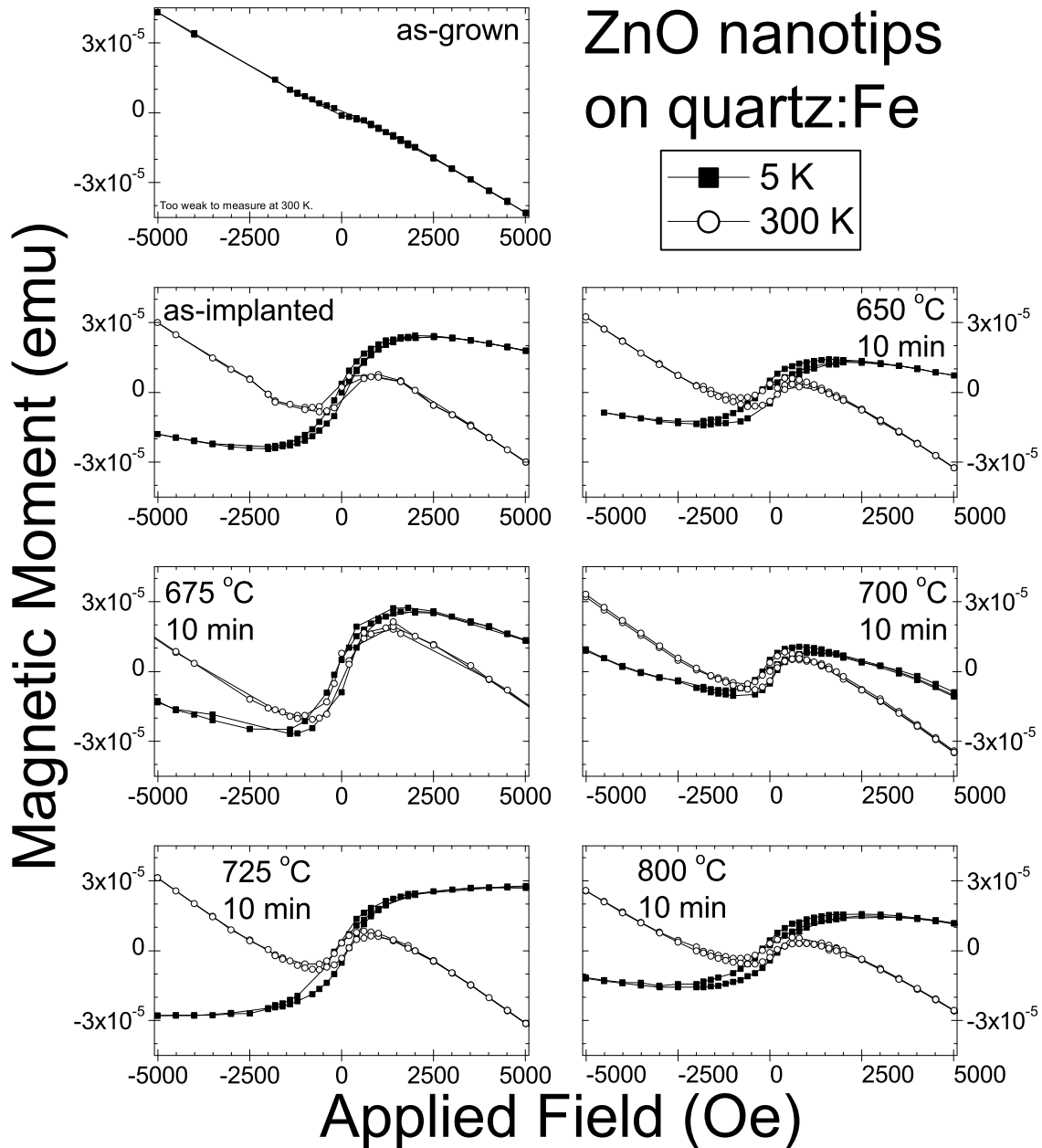


Figure 7.8 Raw data from magnetic hysteresis SQUID measurements of Fe-implanted ZnO nanotips on quartz annealed as indicated in O_2 flowing at 25 sccm. Note that the measurement from the as-grown sample at 300 K is not displayed because the signal was overcome by noise.

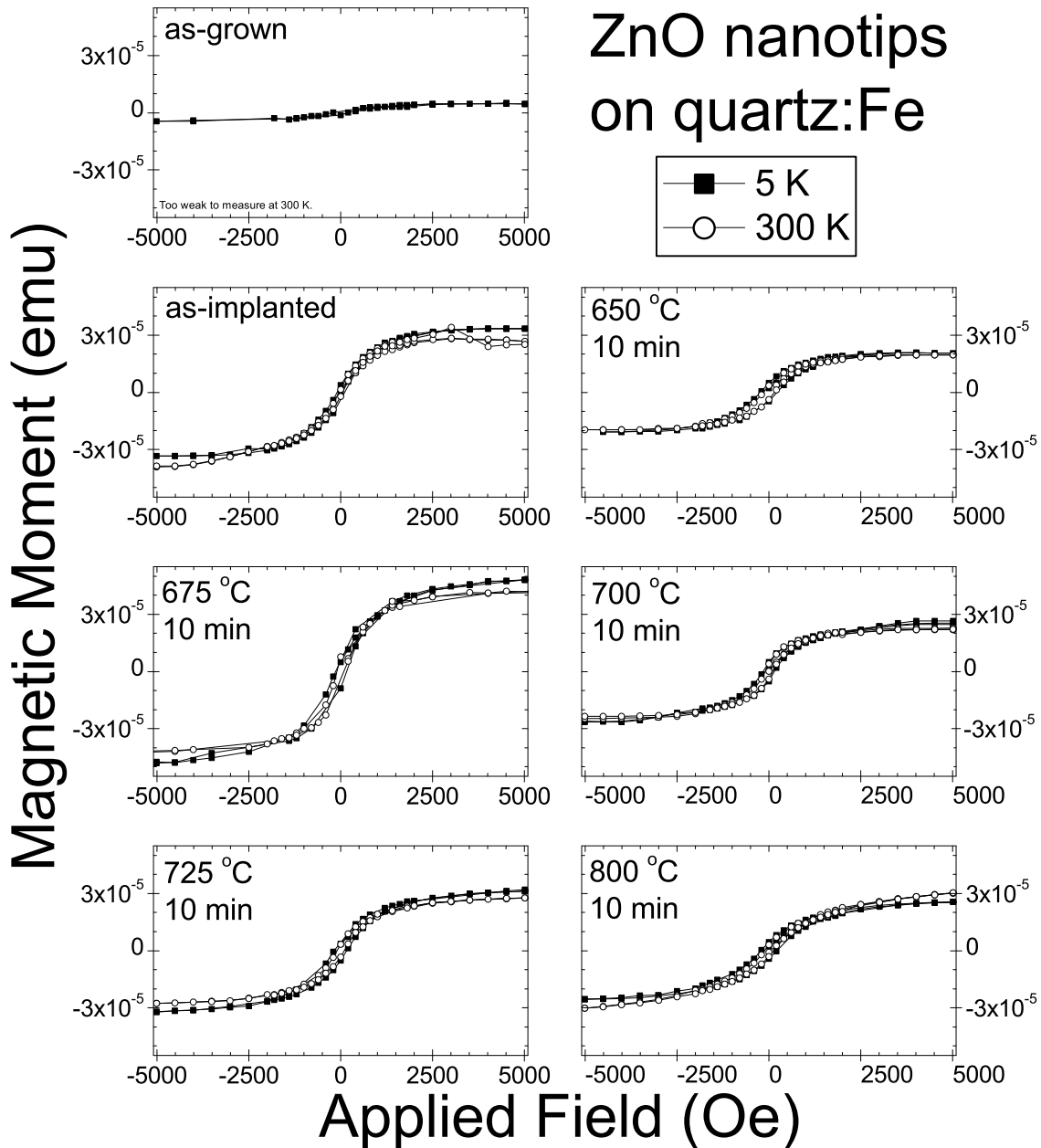


Figure 7.9 Magnetic hysteresis data for ZnO nanotips grown on quartz, implanted with Mn and annealed as indicated in the figure in an atmosphere of O_2 flowing at 25 sccm. Linear diamagnetic influences have been removed from this data. Note that the measurement from the as-grown sample at 300 K is not displayed because the signal was overcome by noise.

noticeable separation between the positive- and negative-going sides of the hysteresis loop is confirmed when the background is subtracted. Note that, in figures 7.8 and 7.9, the room-temperature as-grown measurement is not shown due to the fact that the signal from this sample is overcome by noise at 300 K.

Quantification of the width of magnetic hysteresis is shown in figure 7.10. Of the samples with a clean magnetization signal, the greatest coercive field strength occurs in the one annealed at 650 °C for 10 minutes. H_c for this sample, however, is not appreciably stronger than for the sample annealed at 800 °C. This again calls the quality of the ZnO/(quartz):Fe samples themselves and the repeatability of the process into question. The values from these samples are partially obscured in figure 7.10.

Another measurement of ferromagnetism that can be gleaned from the variable field measurement data with background diamagnetism removed is the remanent

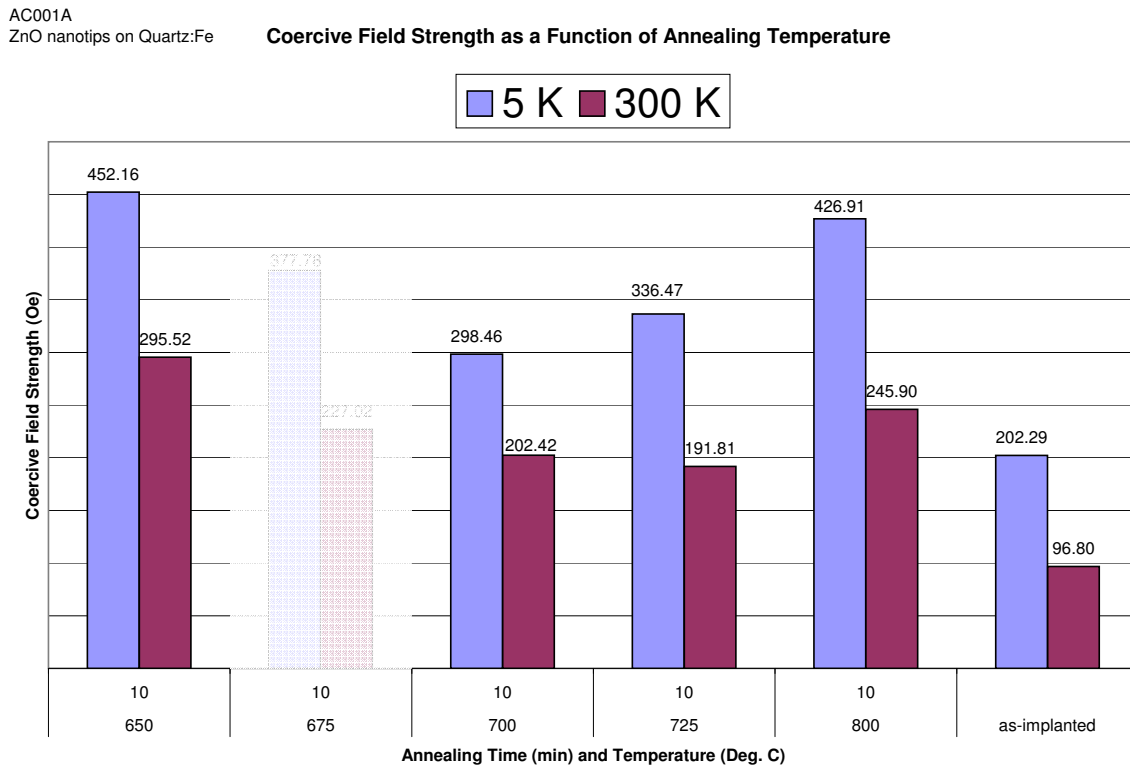


Figure 7.10 Coercive field strengths at 5 and 300 K for various annealing conditions of Mn-implanted ZnO nanotips grown on quartz. Measurements that are suspect due to a noisy signal are partially obscured in the figure.

field (B_R) strength. The results of these determinations are presented in figure 7.11. Clearly, the greatest remanency as a percentage of M_S exists in the sample annealed at 650 °C for 10 minutes.

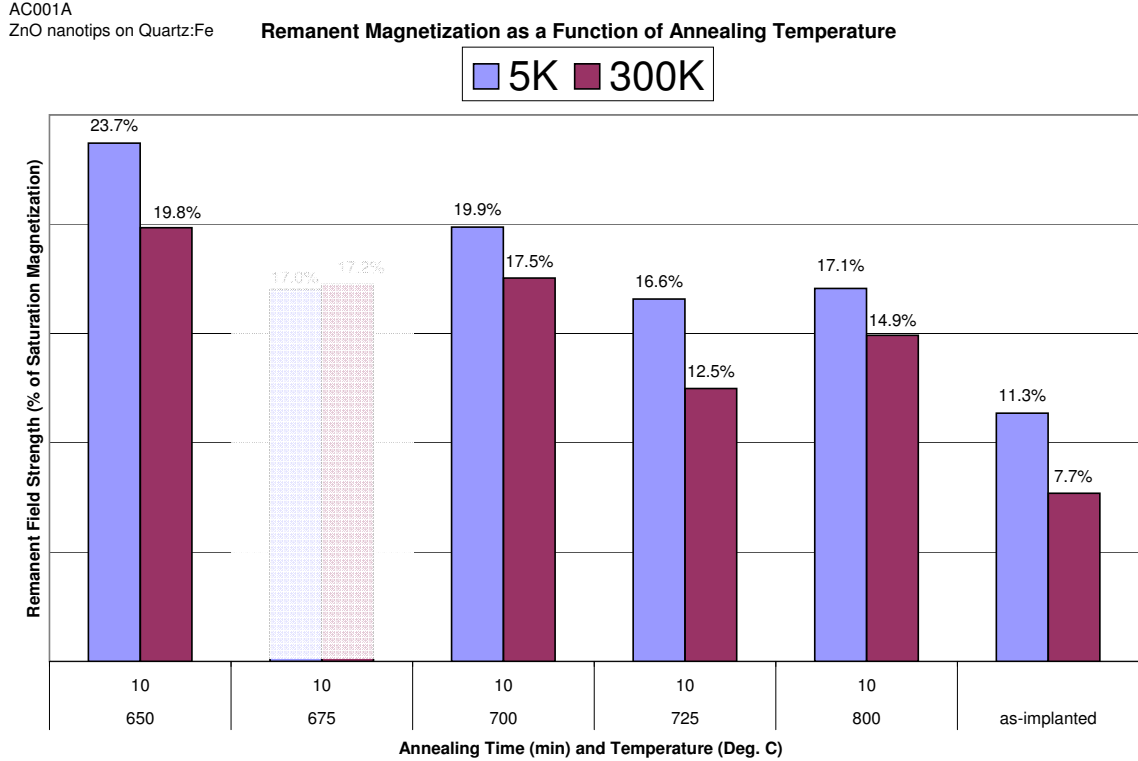


Figure 7.11 Remanent field strengths at 5 and 300 K for various annealing conditions of Mn-implanted ZnO nanotips grown on quartz substrates. Measurements that are suspect due to a noisy signal are partially obscured in the figure.

The magnetic properties of ZnO/(quartz) implanted with Fe as determined by variable field measurements point toward annealing at 650 °C for 10 minutes as the best way to enhance ferromagnetism. However, the similarity of the data collected for other annealing conditions in this sample seem to indicate that ferromagnetism in the sample is not sensitive to annealing conditions, which implies that it does not occur as a result of Fe incorporation into the ZnO crystal structure. Another troubling aspect of these results is the fact that, in ZnO nanotips grown on a glass substrate, samples annealed at 800 °C showed a total melting and fusing of the nanotips. If this is also the case in an 800 °C-annealed sample of ZnO/(quartz):Fe, then the appearance of

ferromagnetic indicators in the likely disordered crystal that would result from such a process seems counterintuitive.

7.1.2.2 *Temperature-Dependent Magnetization*

Magnetization was measured during temperature sweeps between 5 and 350 K for the Fe-implanted ZnO nanotips on quartz. The resulting data is presented in figure 7.12. In most cases, the low-temperature behavior (FC and ZFC measurements rising together) suggests the presence of a ferromagnetic phase in the material. There is no evidence of spin-glass formation, which would be indicated by a peak in the ZFC magnetization. The other indicator of ferromagnetism in variable temperature magnetization measurements is the vertical separation between FC and ZFC magnetization values.

In the measurements shown in figure 7.12, the greatest separation between FC and ZFC measurements occurs when the sample is annealed at 700 °C for 10 minutes. This is problematic because it uncovers yet another annealing temperature for which this material presents a signature of ferromagnetism. There is also noteworthy separation of FC and ZFC magnetization measurements in all of the other samples except for the one annealed at 725 °C. This is another point of contrast with the indications presented by the variable field measurements.

The most feasible explanation for the near-ubiquitous signatures of ferromagnetism in ZnO/(quartz):Fe is that Fe was deposited on the samples. The most probable location for Fe to cluster is between the nanotips themselves. Since Fe and many of its native oxides are ferromagnetic with a high T_C , a sample with Fe clusters or film would present signatures of ferromagnetism. Naturally pure Fe would show more consistent and stronger signals of ferromagnetism in SQUID measurements, but bear in mind that there would be a very small amount of Fe not incorporated into the ZnO/(quartz), it would exist in clusters that are physically separated, and it would be oxidized due to the annealing process where pure O₂ is flowed during heat treatment.

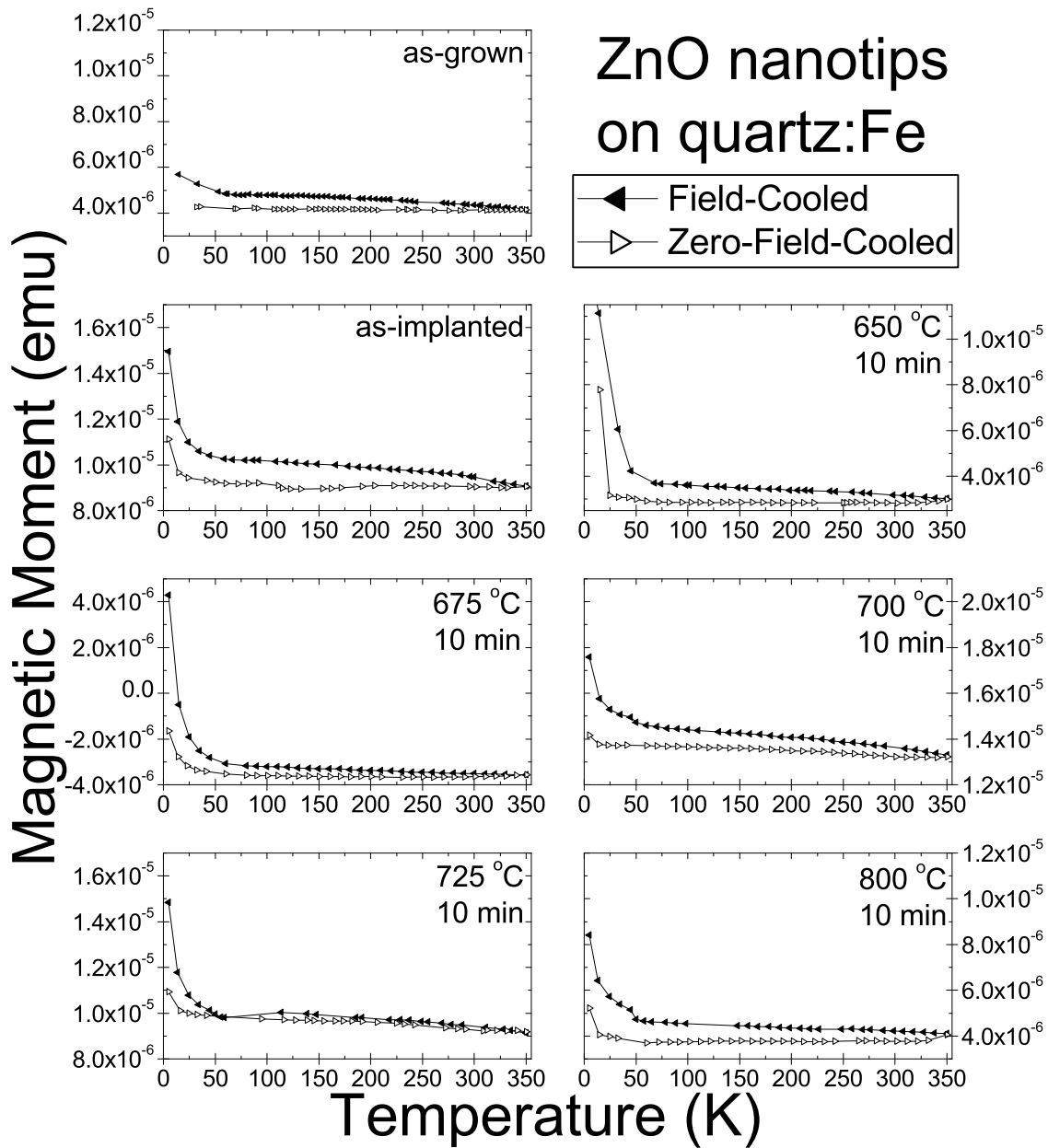


Figure 7.12 Temperature-dependent magnetization for ZnO nanotips implanted with Fe and annealed as indicated in the figure for 10 minutes in O_2 flowing at 25 sccm. Note that the y axis spans the same range of magnetic moment despite the fact that background offset causes a difference in absolute values.

7.1.2.3 Optical Measurements

Spectra collected during PL measurements on Fe-implanted ZnO nanotips grown on quartz are shown in figure 7.13. The as-grown sample shows features that are

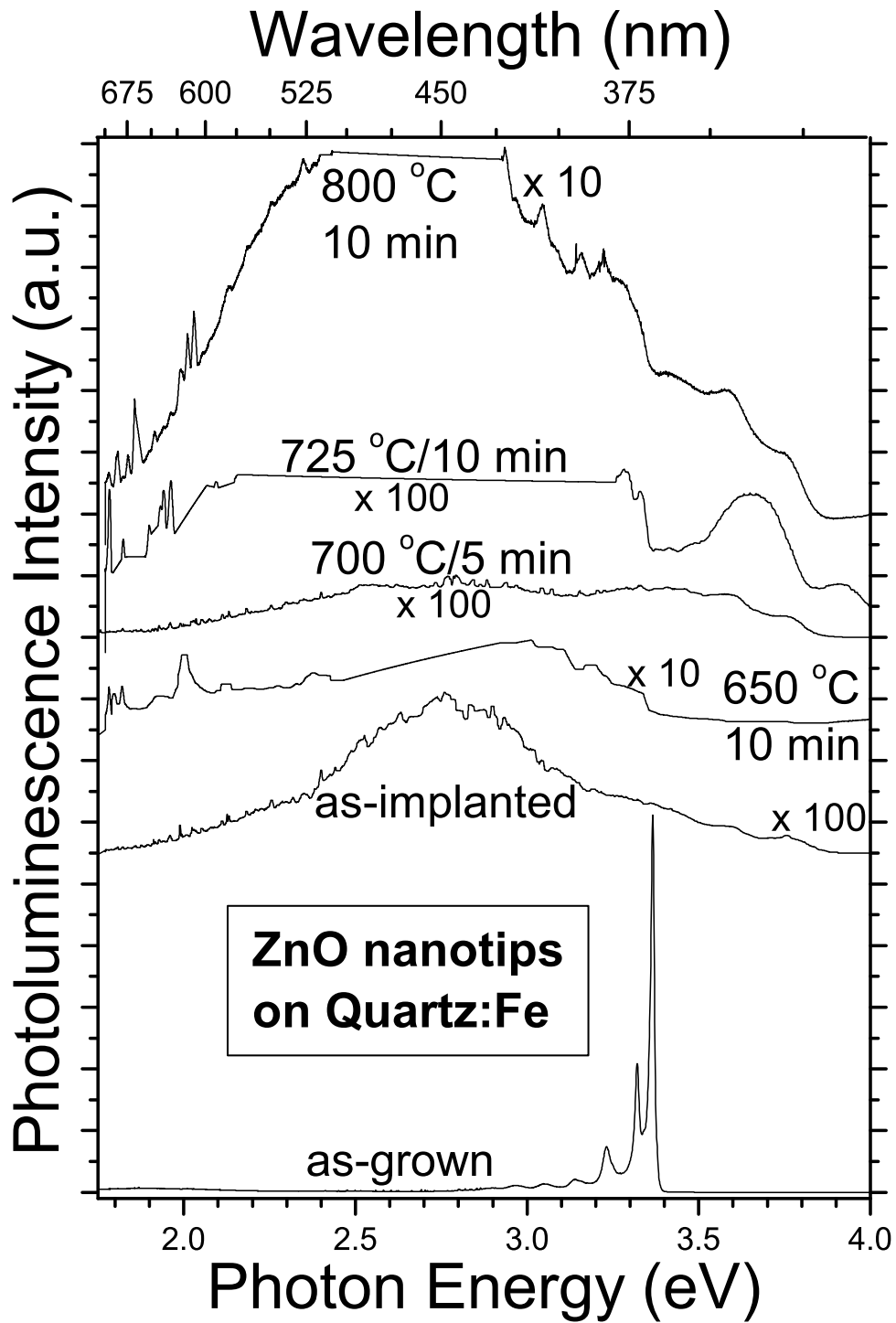


Figure 7.13 Photoluminescence at ~ 10 K of ZnO nanotips on quartz implanted with Fe and annealed as indicated for 10 minutes in O_2 flowing at 25 sccm.

inherent to bulk ZnO. This indicates that, as expected, the size of the ZnO nanotips is too large to induce appreciable quantum confinement effects. The primary peak at 3.3663 eV is attributed to a donor-bound A exciton. The secondary peak at 3.3204 eV is attributed to a two-electron satellite (TES) transition of a donor-bound A exciton [122]. The regular ~ 90 -meV spacing of further subordinate peaks identifies them as phonon replicas.

Implanting Fe into the ZnO/(quartz) causes a major decrease in overall luminescence and the disappearance of PL features. As seen in the figure, there is very little optical damage recovery due to annealing in the Fe-implanted samples. The most prominent feature in any of the implanted samples is a broad blue-violet luminescence around 2.8 eV, which is consistent with implant damage such as Zn interstitials or O vacancies. The above bandgap peak, which is especially prominent in the sample annealed at 725 °C for 10 minutes is attributed to defect complexes in the quartz substrate. The flat tops of the samples annealed at 725 and 800 °C are due to the suppression of plasma lines that dominate the weak PL signal from the samples in this region.

This lack of implant damage recovery indicates that Fe is not incorporated into the ZnO crystal lattice. This indicates that the magnetic properties of the ZnO/(quartz):Mn is not demonstrating true DMS behavior. The most likely explanation for the ferromagnetism observed in these samples is Fe clustering outside the ZnO nanotips.

7.2 Zinc Oxide Nanotips on *c*-Plane Sapphire

ZnO nanotips were also grown on *c*-Al₂O₃ by MOCVD. As noted in Chapter VI, epitaxial thin films of ZnO were grown on *r*-Al₂O₃, but a change in substrate crystal orientation relative to the direction of growth causes ZnO to form nanotips rather than a thin film. A scanning electron microscope (SEM) image of the resulting ZnO structures is shown in figure 7.14.

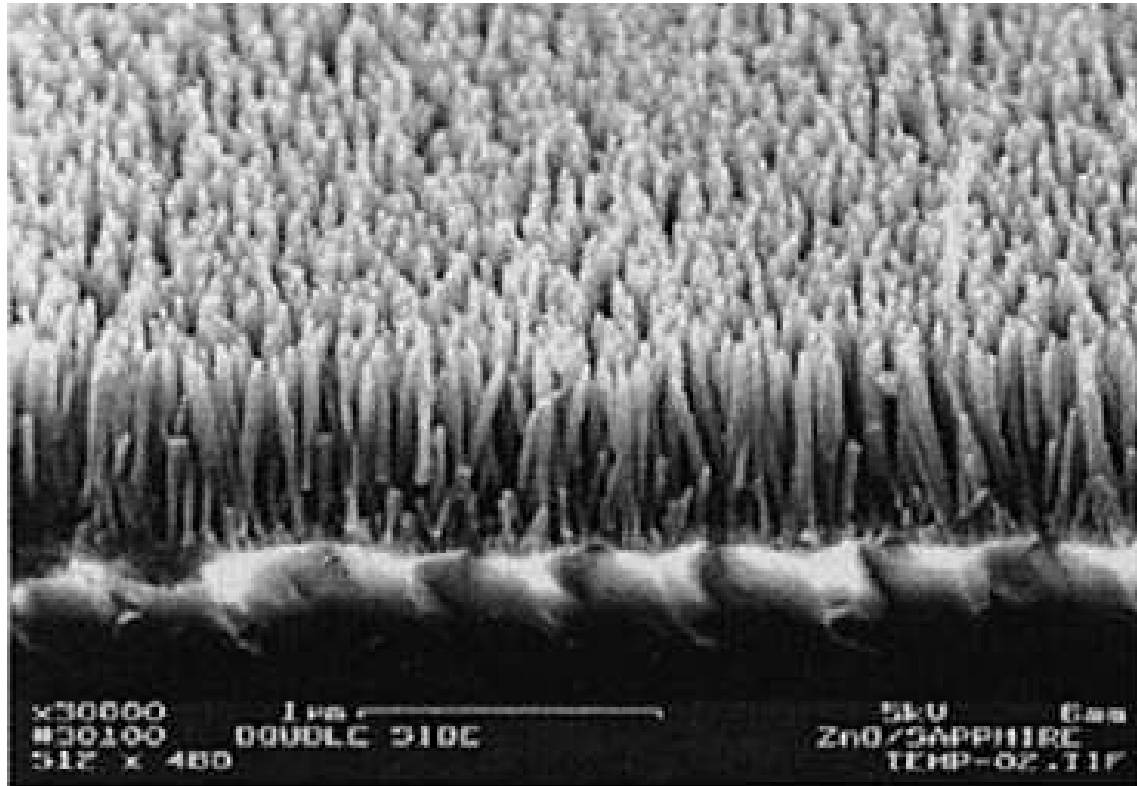


Figure 7.14 A scanning electron microscope image of ZnO nanotips grown on a $c\text{-Al}_2\text{O}_3$ substrate [74].

7.2.1 Manganese-Implanted ZnO Nanotips on $c\text{-Al}_2\text{O}_3$

ZnO nanotips grown on a sapphire were implanted with Mn to a level of $5 \times 10^{16} \frac{\text{ions}}{\text{cm}^2}$ at room temperature with an implantation energy of 200 keV. The magnetic properties of ZnO/($c\text{-Al}_2\text{O}_3$):Mn are plagued by inconsistency. Hysteresis measurements, particularly at room temperature, show that the material is superparamagnetic. This assessment is echoed by the lack of separation between FC and ZFC magnetization measurements except in samples annealed at 650 and 750 °C. Finally, photoluminescence measurements show band-edge recovery only in the sample annealed at 700 °C for 10 minutes. Since magnetic measurements on the sample annealed at 700 °C do not strongly indicate ferromagnetism, it is possible that even fully incorporating Mn into ZnO nanotips grown on $c\text{-Al}_2\text{O}_3$ does not produce DMS material.

7.2.1.1 Magnetic Hysteresis Measurements

Variable field measurements of ZnO/(*c*-Al₂O₃):Mn show that the largest room temperature saturation magnetization (M_S) occurs when the sample is annealed at 650 °C for 10 minutes. The M_S values observed in this sample are 0.32 and 0.28 μ_B per Mn atom at 5 and 300 K, respectively. The calculated maximum magneton for Mn²⁺ is 5.9 μ_B per atom [8, Table 31.4]. Given the lack of separation between upward and downward sweeps of the applied magnetic field, M_S is the only indicator of possible ferromagnetism visible in figure 7.15.

The other prominent feature of the data presented in figure 7.15 is presence of background diamagnetism. This is an expected phenomenon in samples grown on a sapphire substrate. The unexpected phenomenon in this material is the appearance of paramagnetism in the room-temperature measurement of the as-implanted sample and the 5-K measurements of the samples annealed at 700 and 725 °C. The temperature dependence of paramagnetism in this sample indicates that it is Curie-type paramagnetism [127], which means that there is a sparse distribution of Mn atoms in the material either as interstitials in the ZnO lattice or outside of the nanotips. If the Mn were clustered either inside or outside of the ZnO nanotips, it would display an antiferromagnetic characteristic [75].

Although coercive field (H_c) values are small for Mn-implanted ZnO/(*c*-Al₂O₃), they will become more apparent and can be accurately determined by removing the dia- or para-magnetic background from the measurements. Background subtraction is accomplished by rotating each data point around the origin by the amount necessary to make the linear magnetization region above saturation parallel to the x axis. The drawback to this method of background subtraction is that it can yield erroneously high values of H_c in samples where the magnetic saturation transition is not sharp because the sides of the hysteresis loop cross the zero-magnetization line at an angle. As seen in figure 7.16, this effect is a factor in the sample annealed at 700 °C and the room temperature measurement on the the sample annealed at 750 °C for 10 minutes.

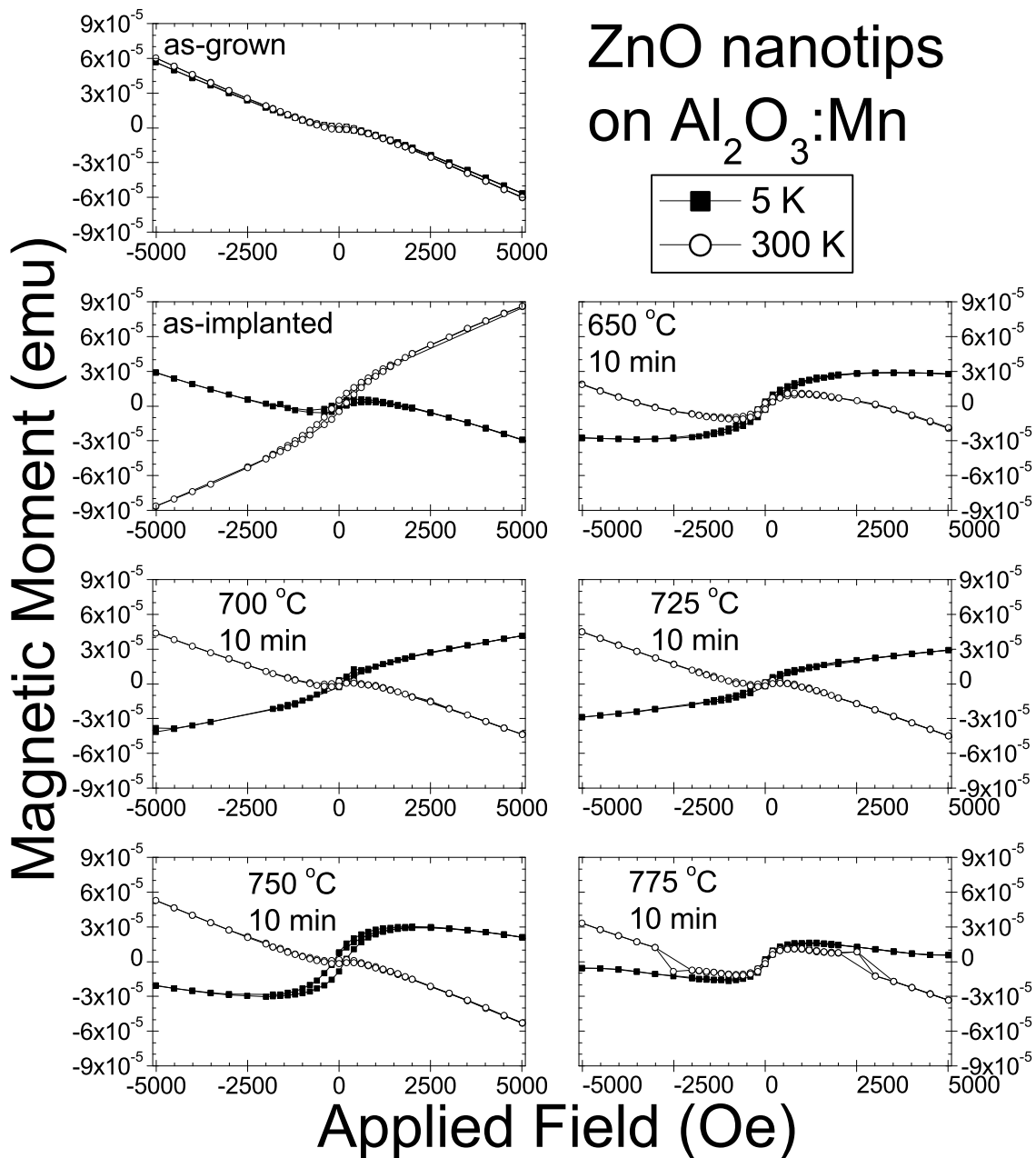


Figure 7.15 Raw data from magnetic hysteresis SQUID measurements of Mn-implanted ZnO nanotips grown on $c\text{-Al}_2\text{O}_3$ and annealed as indicated in O_2 flowing at 25 sccm.

The data with linear magnetic influences (para- and dia-magnetism) removed is presented in figure 7.16. This data confirms that, among the annealed samples, the highest room-temperature M_S occurs in the sample annealed at 650 °C. The presence

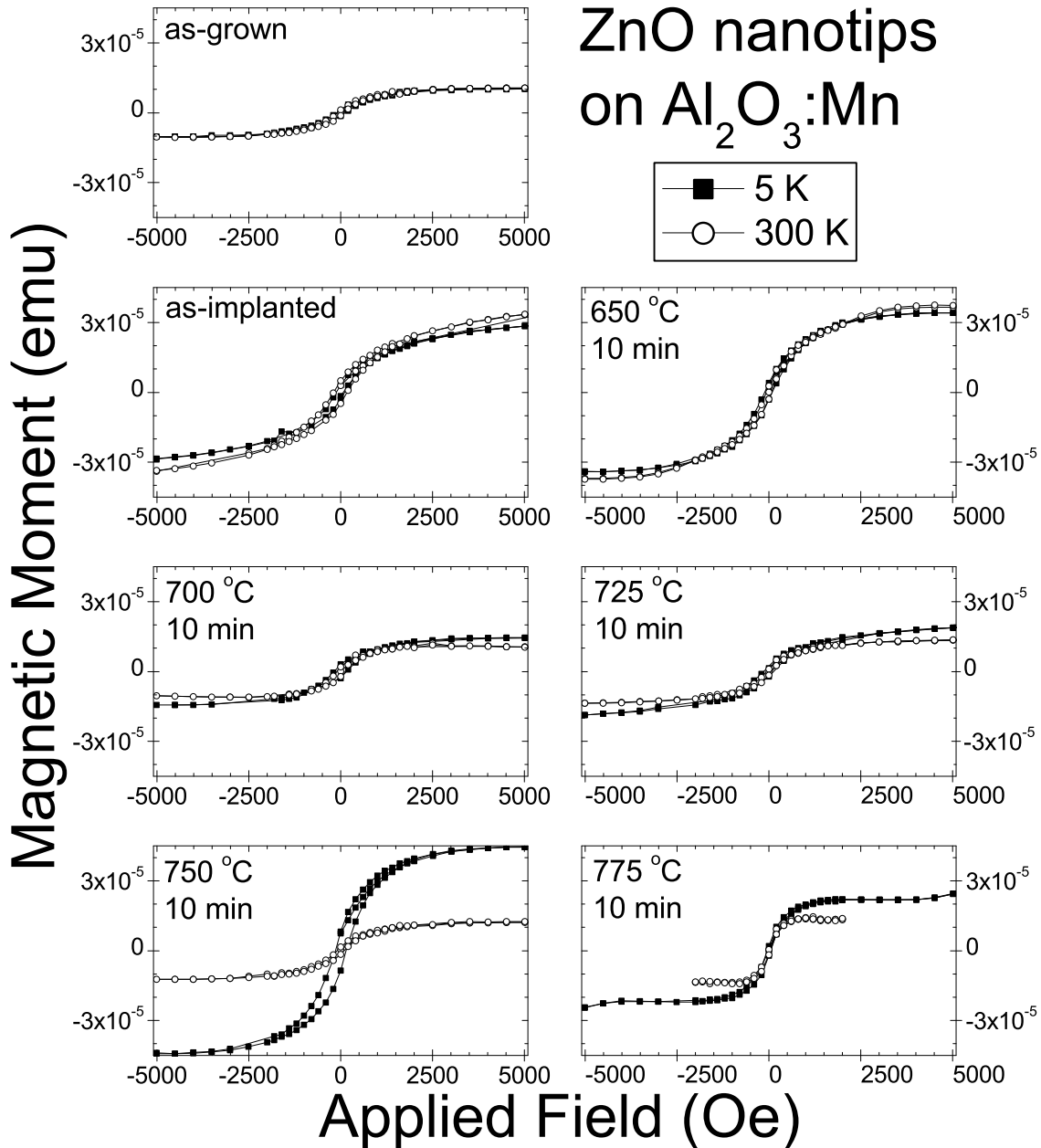


Figure 7.16 Magnetic hysteresis data for ZnO nanotips grown on $c\text{-Al}_2\text{O}_3$, implanted with Mn and annealed as indicated for 10 minutes in O_2 flowing at 25 sccm. Linear magnetic influences have been removed from this data.

of magnetic hysteresis in the 300-K measurement of the sample annealed at 750 °C for 10 minutes is also apparent in figure 7.16.

As mentioned above, the removal of linear background magnetic influences allows a more accurate determination of H_c and M_S . A summary of the coercive field

strengths observed during variable field measurements of the Mn-implanted ZnO nanotips on $c\text{-Al}_2\text{O}_3$ with respect to annealing temperature is presented in figure 7.17. This summary of the H_c data shows that the strongest fields occur in the as-implanted sample. The data that is deemed inaccurate by inspection of the hysteresis loops with background magnetism subtracted are partially obscured, but even these values do not exceed those determined for the as-implanted sample. While as-implanted samples can display anomalously strong indications of ferromagnetism due to a sparse scattering of Mn atoms, the fact that no other field strengths exceed these is a sign that ZnO/($c\text{-Al}_2\text{O}_3$):Mn is not a promising DMS candidate.

AC003B
ZnO nanotips on Sapphire:Mn **Coercive Field Strength as a Function of Annealing Temperature**

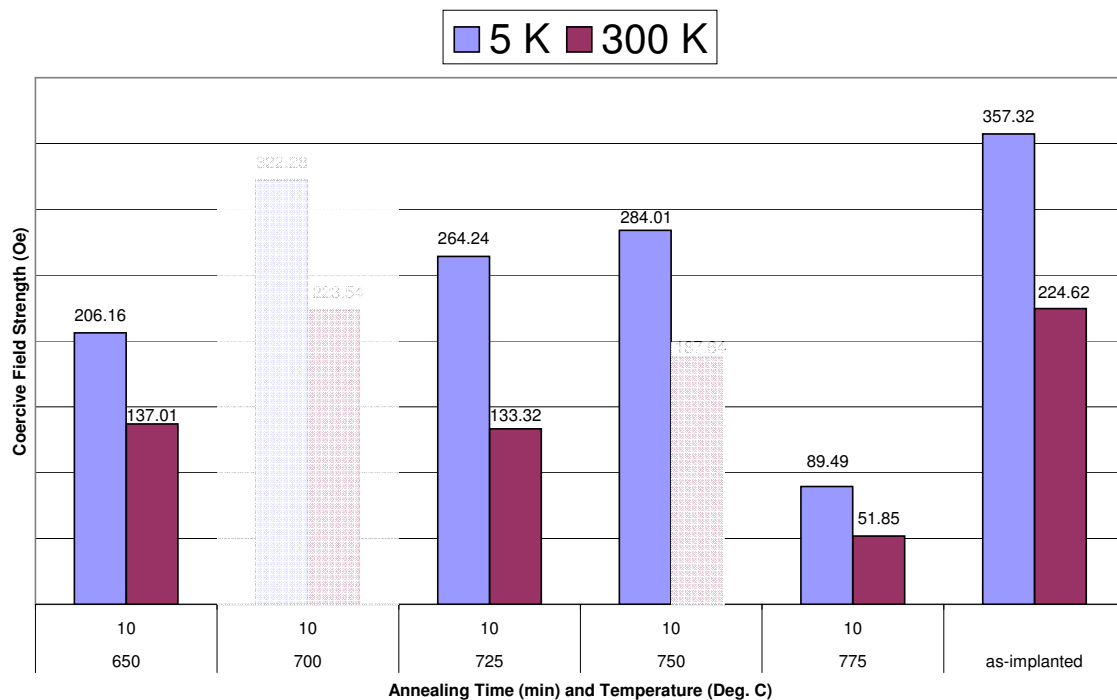


Figure 7.17 Coercive field strengths at 5 and 300 K for various annealing conditions of Mn-implanted ZnO nanotips grown on sapphire.

Numerical data is presented for remanent field (B_R) strengths in figure 7.18. There is a definite peak in the room-temperature value with annealing at 700 °C for 10 minutes. There is, however, no trending in the B_R data for ZnO/($c\text{-Al}_2\text{O}_3$):Mn, which calls into question whether this value occurs as a result of sensitivity to annealing

temperature. There are also increased B_R values for the sample annealed at 750 °C. The lack of trending in the B_R data is yet another indicator that ZnO/(*c*-Al₂O₃):Mn does not lend itself to useful ferromagnetic behavior under the annealing conditions used in this experiment.

There is an interesting feature in the as-implanted remanent field data presented in figure 7.18. The fact that the room-temperature remanency is greater than the 5-K value has been confirmed by multiple measurements on two separate pieces of Mn-implanted ZnO nanotips grown on *c*-Al₂O₃. This behavior is explained by the presence of an antiferromagnetic phase with an ordering temperature between 5 and 300 K, which would compete with the ferro- and para-magnetic properties of the material that persist to higher temperatures. Possible compositions of this AFM phase are presented in Appendix B, and the effect on the temperature dependence of magnetization in this sample are discussed in section 7.2.1.2.

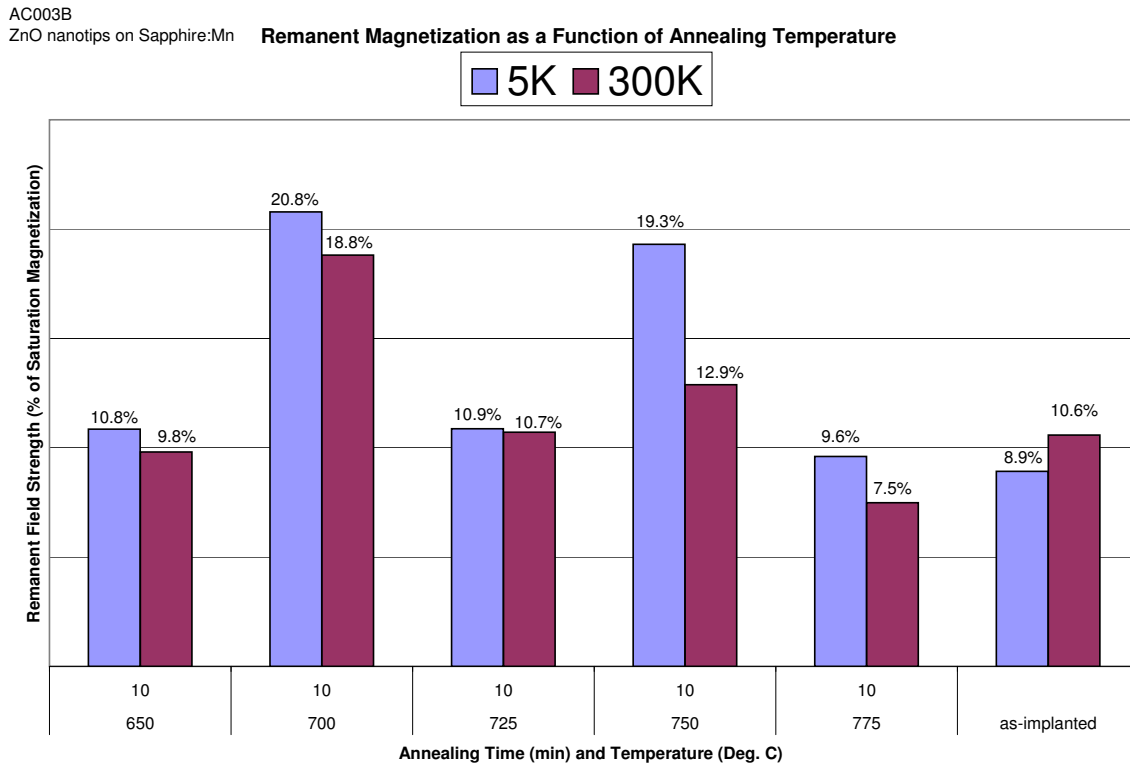


Figure 7.18 Remanent field strengths at 5 and 300 K for various annealing conditions of Mn-implanted ZnO nanotips grown on sapphire substrates.

7.2.1.2 Temperature-Dependent Magnetization

FC and ZFC SQUID measurements of the Mn-implanted ZnO nanotips on *c*-Al₂O₃ are displayed in figure 7.19. For all conditions tested, the low temperature behavior of the temperature-dependent measurements (FC and ZFC tracking higher

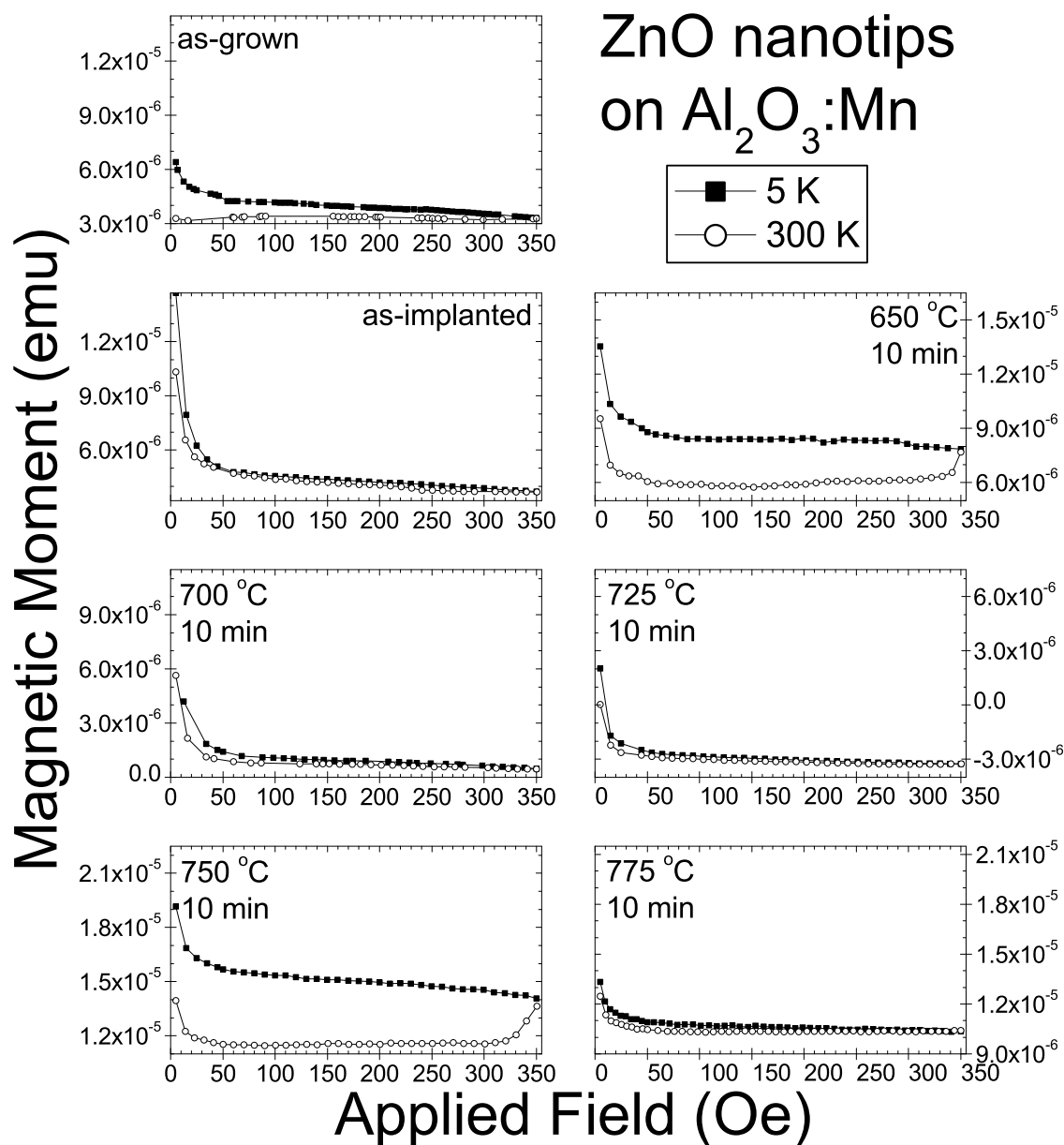


Figure 7.19 Temperature-dependent magnetization for ZnO nanotips grown on *c*-Al₂O₃ implanted with Mn. Samples are annealed as indicated in O₂ flowing at 25 sccm for 10 minutes. Note that the *y* axis spans the same range of magnetic moment despite the fact that background offset causes a difference in absolute values.

together) indicate that a ferro- or para-magnetic phase is dominant in these samples. The lack of separation between FC and ZFC measurements for all samples except those annealed at 650 and 750 °C for 10 minutes indicates that the samples lacking separation are not dominated by ferromagnetism. The fact that such disparate annealing temperatures are the only ones that cause separation in the FC and ZFC magnetization curves suggests again that indications of ferromagnetism in this material are not arising from incorporation of Mn into the ZnO/(*c*-Al₂O₃) nanotips.

7.2.1.3 Optical Measurements

PL measurements of the Mn-implanted ZnO nanotips grown on *c*-Al₂O₃ are shown in figure 7.20. The as-grown sample shows features that are inherent to bulk ZnO. This indicates that, as expected, the size of the ZnO nanotips is too large to induce appreciable quantum confinement effects. The primary peak at 3.3691 eV is attributed to an ionized donor-bound A exciton [14]. The secondary peak at 3.32 eV is attributed to a two-electron satellite (TES) transition of a donor-bound A exciton [122]. The regular ~90-meV spacing of further subordinate peaks identifies them as phonon replicas.

These measurements show that the best implant damage recovery, from an optical standpoint, occurs when the sample is annealed at 700 °C for 10 minutes. In fact, this is the only annealing condition in which the A exciton and TES luminescence peaks observed in the as-grown sample are clearly recovered. There are peaks at these locations in the sample annealed at 750 °C, but they are not more intense than the noise present in this measurement.

In the sample annealed at 725 °C, there is a broad PL feature at 2.9 eV. This luminescence is attributed to band-to-band or excitonic emission in other reports of ZnO nanocolumns [11]. The subordinate peaks in this measurement at 3.20 and 3.11 eV follow the same regular ~90-meV spacing that is attributed to phonon replicas in the as-grown samples.

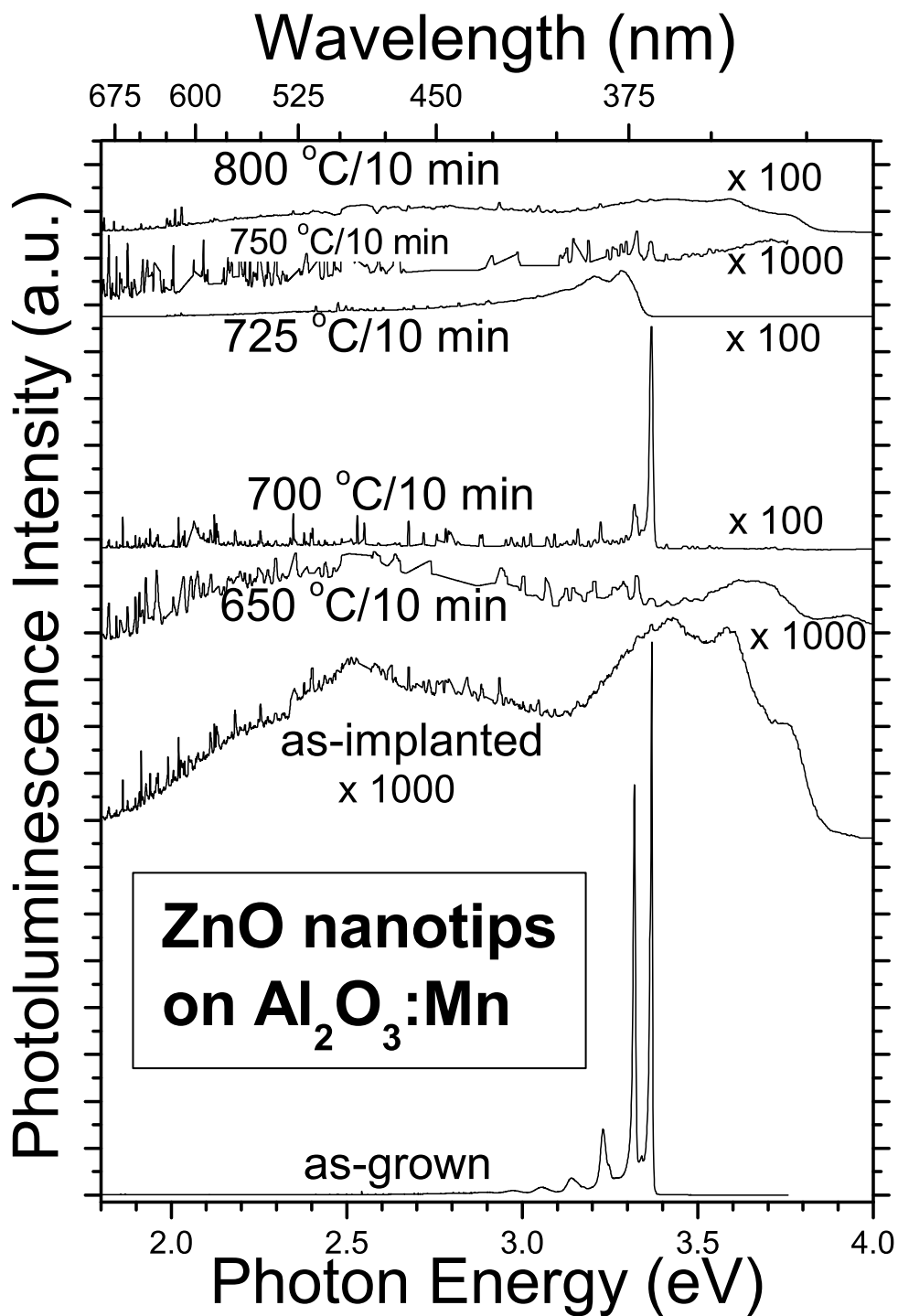


Figure 7.20 Photoluminescence spectra of ZnO nanotips grown on $c\text{-Al}_2\text{O}_3$, implanted with Mn and annealed as indicated for 10 minutes in a 25 sccm O_2 flow. PL measurements were taken at approximately 10 K.

Overall, the PL measurements on the ZnO nanotips grown on $c\text{-Al}_2\text{O}_3$ and implanted with Mn show that there is an optimal annealing condition (700 °C for 10 minutes) for recovery of crystal lattice damage induced by Mn implantation. This implies that the best incorporation of Mn into the ZnO lattice occurs when the sample is annealed at 700 °C. This lattice damage recovery, however, coincides only with a sporadic peak in B_R and not with maxima in H_c and M_S and FC–ZFC separation as well. This suggests that, while there is some magnetic activity present in the sample, it has not been proven useful as a DMS material. Based on previous results with nanotips, new ZnO/($c\text{-Al}_2\text{O}_3$):Mn samples should be annealed across the same range of temperatures discussed above for a period of 20 minutes. This may allow fuller recovery of the damage caused by ion implantation, but it may cause more annealing related harm, such as oxygen loss, because of the relatively large surface area of the ZnO nanotips.

7.2.2 Iron-Implanted ZnO Nanotips on $c\text{-Al}_2\text{O}_3$

ZnO nanotips grown on $c\text{-Al}_2\text{O}_3$ were also implanted with an energy of 200 keV at room temperature with Fe ions to a dose of $5 \times 10^{16} \frac{\text{ions}}{\text{cm}^2}$. The resulting material shows consistent ferromagnetic behavior in the sample annealed at 700 °C for 20 minutes. Other annealing conditions, including the same temperature for a shorter time, show only weak superparamagnetism. Photoluminescence confirms that the ZnO crystal is best recovered when annealed at 700 °C for 20 minutes. The experiment using ZnO/($c\text{-Al}_2\text{O}_3$):Fe shows that annealing time is a factor in fabricating DMS material.

7.2.2.1 Magnetic Hysteresis Measurements

The results of variable field measurements taken on ZnO/($c\text{-Al}_2\text{O}_3$) implanted with Fe are shown in figure 7.21. The data presented show an obvious sensitivity to both annealing time and annealing temperature. There is also an obvious diamagnetic background.

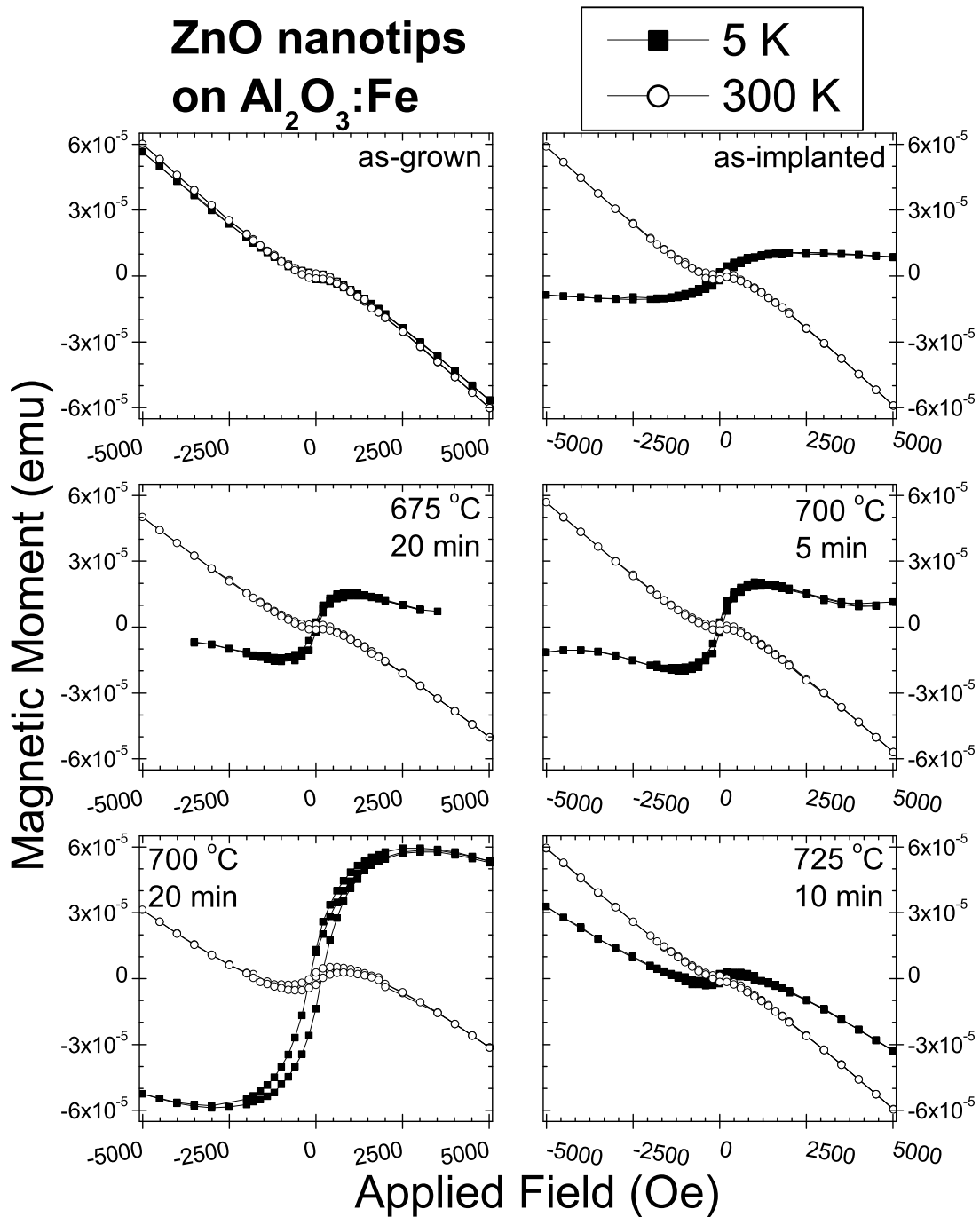


Figure 7.21 Raw data from magnetic hysteresis SQUID measurements of Fe-implanted ZnO nanotips grown on sapphire annealed as indicated in O_2 flowing at 25 sccm.

The sample annealed at 700 °C for 20 minutes shows the strongest signatures of ferromagnetism in terms of hysteretic separation and strong saturation magnetization (M_S). The ZnO/(*c*-Al₂O₃):Fe annealed under other conditions is best characterized as superparamagnetic at 5 K and diamagnetic at room temperature.

In order to accurately determine a numerical value for the coercive field (H_c) in the samples, the data need to be rotated about the origin such that the magnetization values in the linear region are as nearly equal as possible. This process also allows measurement of M_S without the interference of the background diamagnetism.

The variable field measurement data with linear diamagnetic influences removed is shown in figure 7.22. Displaying the data in this fashion makes it even more clear that the only annealing condition (among those tested) that produces ferromagnetism in ZnO/(*c*-Al₂O₃):Fe is 700 °C for 20 minutes. The samples annealed under other conditions show almost no separation between positive- and negative-going legs of the hysteresis loop (small H_c) and none have M_S values rivaling that of the sample annealed at 700 °C for 20 minutes. In terms of Bohr magneton, the M_S values for sample are 0.56 and 0.18 μ_B per Fe atom when measured at 5 and 300 K, respectively. The calculated value of the effective magneton number for Fe²⁺ is 5.4 [8, Table 31.4].

The rotation to remove background diamagnetism serves not only to provide a clearer view of what is happening, but also to allow more accurate measurement of H_c values. There is an artifact of the background subtraction that causes larger values of H_c to be calculated from the corrected data because the legs of the hysteresis loop are tilted relative to the zero-magnetization line. In this set of samples, however, the tilt is roughly equivalent among the various annealing conditions, so the relative strength of H_c can be determined with respect to the other annealing conditions used. The error does, however, manifest itself in that the 300-K measurements are more stretched out upon rotation and hence show higher H_c values than do the 5-K measurements.

Figure 7.23 shows the values of H_c determined for ZnO/(*c*-Al₂O₃):Fe. The numerical results bear out the data gleaned from inspection of the variable field

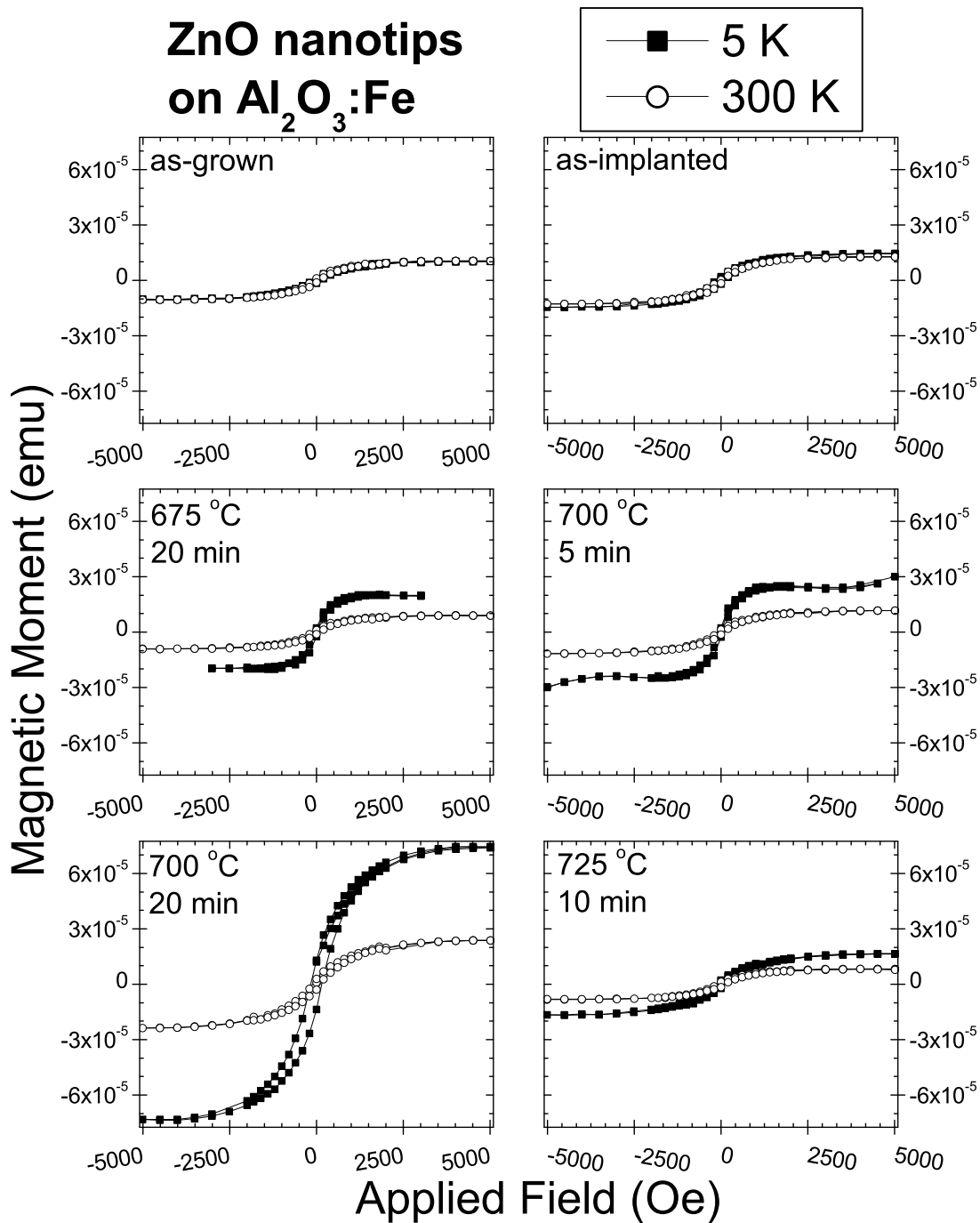


Figure 7.22 Magnetic hysteresis data for ZnO nanotips grown on *c*- Al_2O_3 implanted with Fe and annealed as indicated in the figure in a 25 sccm flow of O_2 . Linear diamagnetic influences have been removed from this data.

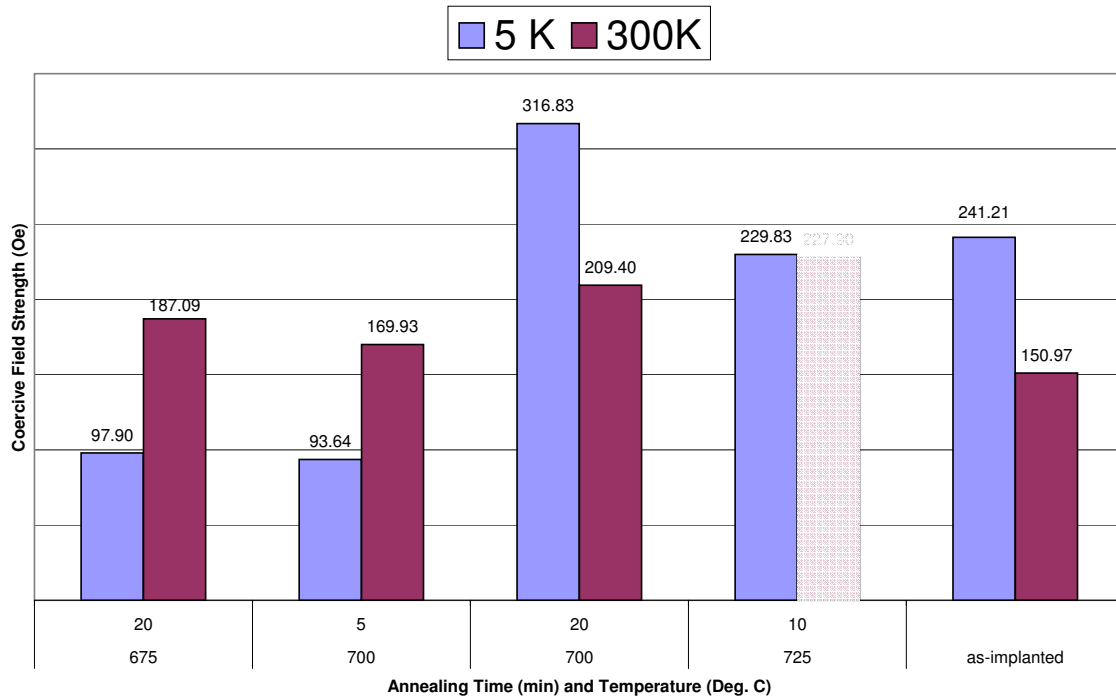


Figure 7.23 Coercive field strengths at 5 and 300 K for various annealing conditions of Fe-implanted ZnO nanotips grown on sapphire. Data that is suspect due to a virtually non-magnetic characteristic in hysteresis is partially obscured.

measurement data: the strongest H_c occurs in the sample annealed at 700 °C for 20 minutes. The values, especially from the 300-K measurement, from the sample annealed at 725 °C are anomalous due to the almost non-magnetic character of the corrected measurements. The fact that the hysteresis loop lies almost flat along the x axis means that a measurement along the zero magnetization line will have a long distance inside the hysteresis loop. This data is partially obscured in figure 7.23.

Remanent field (B_R) values are also determined from the variable field measurements on ZnO/(c -Al₂O₃):Fe. These numbers are presented graphically in figure 7.24. Fortunately, B_R values are far less sensitive to errors induced from background subtraction, but M_S is still affected, so the B_R data is not presented as a percentage of M_S . By far, the strongest remanent fields are obtained when the sample is annealed at 700 °C for 20 minutes.

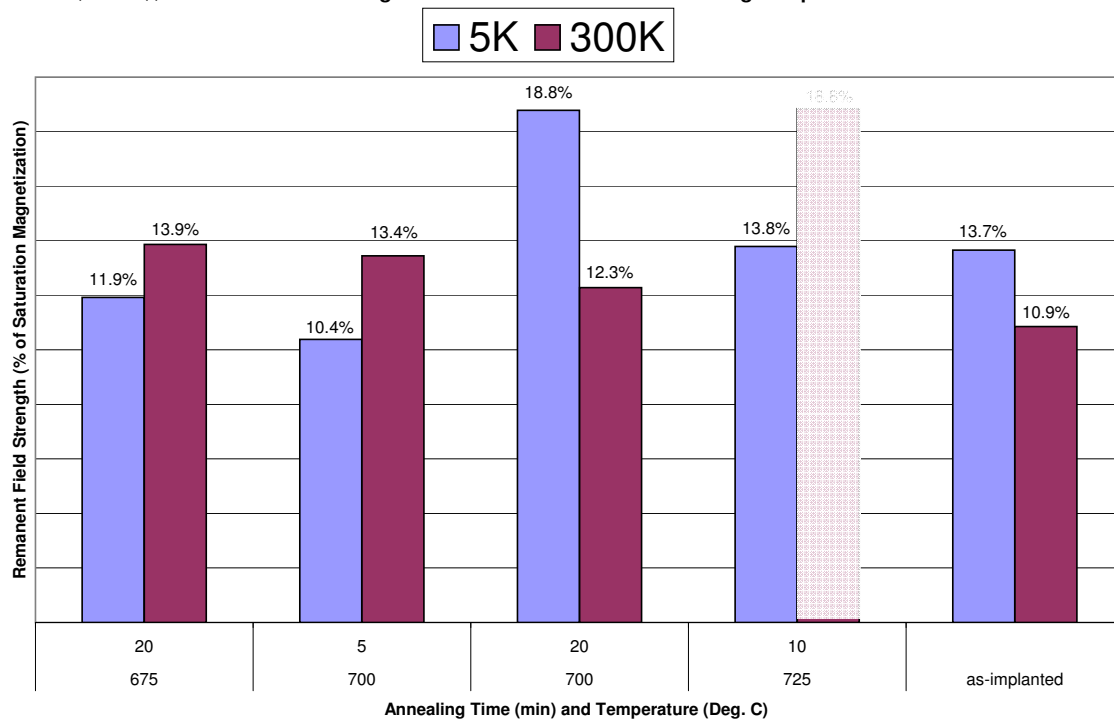


Figure 7.24 Remanent field strengths at 5 and 300 K for various annealing conditions of Fe-implanted ZnO nanotips grown on sapphire substrates. Data that is suspect due to a virtually non-magnetic characteristic in hysteresis is partially obscured.

All of the evidence from variable field measurements points to annealing at 700 °C for 20 minutes as the best annealing condition. The fact that this sample alone demonstrates magnetic properties favorable for DMS fabrication suggests that a longer annealing time may be necessary to activate Fe implanted into ZnO nanotips on $c\text{-Al}_2\text{O}_3$.

7.2.2.2 Temperature-Dependent Magnetization

Temperature-dependent measurements of Fe-implanted ZnO nanotips grown on $c\text{-Al}_2\text{O}_3$ were taken, and the results are shown in figure 7.25. For every annealing condition, the low temperature FC and ZFC magnetization track upward together, which is generally an indicator of ferromagnetism. However, the strength of ferromagnetism is generally indicated by the magnitude of the difference between FC and

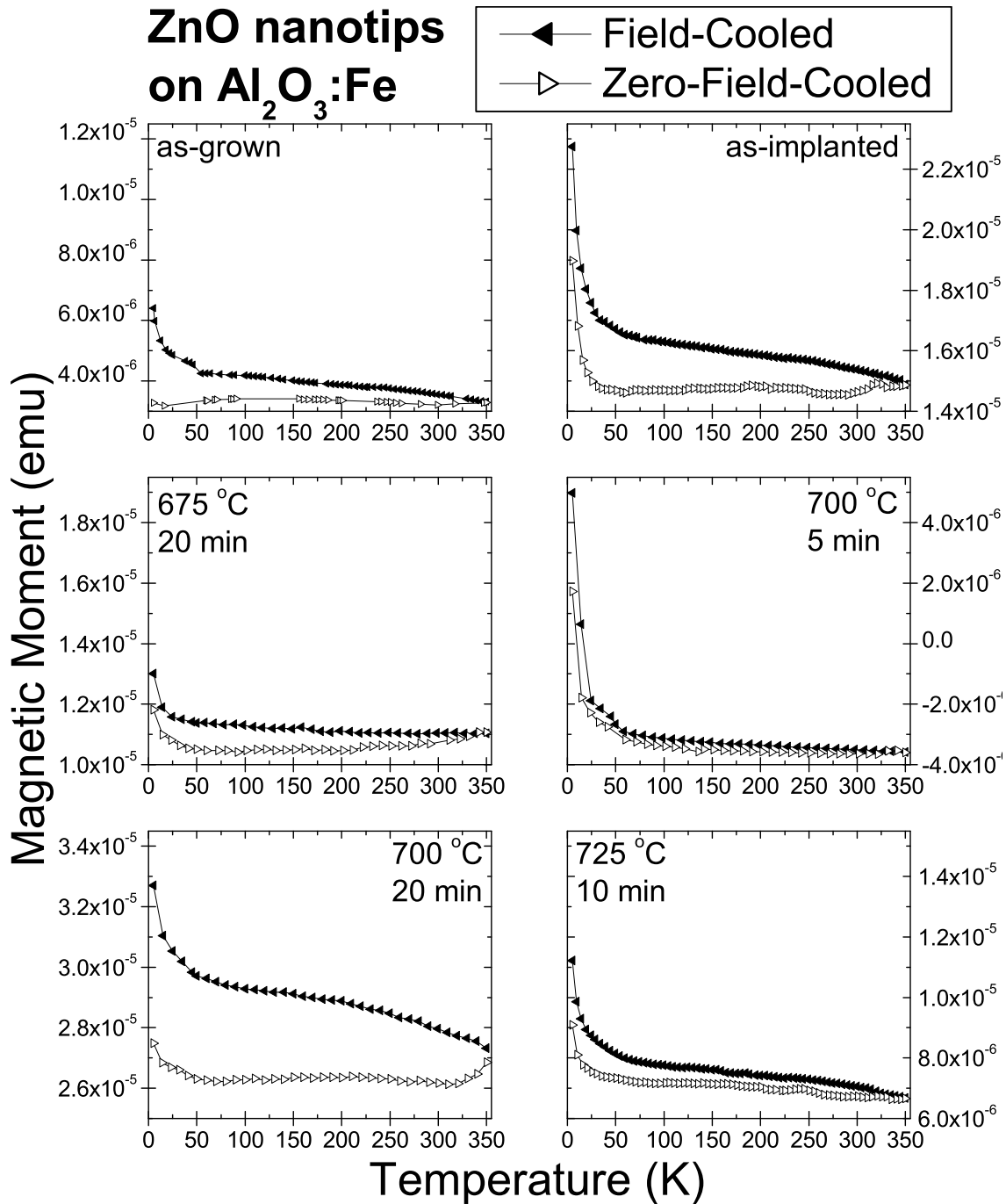


Figure 7.25 Temperature-dependent magnetization for ZnO nanotips on $c\text{-Al}_2\text{O}_3$ implanted with Fe. Samples are annealed as indicated in a 25 sccm flow of O_2 . Note that the y axis spans the same range of magnetic moment despite the fact that background offset causes a difference in absolute values.

ZFC magnetization. By this indication, the strongest ferromagnetism is present in the sample annealed at 700 °C for 20 minutes. Because of the small (less than for the as-implanted sample) FC–ZFC difference, the samples annealed at 675 °C for 20 minutes, 700 °C for 5 minutes, and 725 °C for 10 minutes are basically indicating that they are paramagnetic. The temperature-dependent magnetization measurements show that the indications of ferromagnetism in ZnO/(*c*-Al₂O₃):Fe annealed at 700 °C for 20 minutes seen in hysteresis measurements truly are the product of ferromagnetic ordering in the material.

7.2.2.3 *Optical Measurements*

PL measurements on the as-grown ZnO/(*c*-Al₂O₃) sample shows features that are inherent to bulk ZnO. This indicates that, as expected, the size of the ZnO nanotips is too large to induce appreciable quantum confinement effects. The primary peak at 3.3691 eV is attributed to an ionized donor-bound A exciton [14]. The secondary peak at 3.32 eV is attributed to a two-electron satellite (TES) transition of a donor-bound A exciton [122]. The regular ~90-meV spacing of further subordinate peaks identifies them as phonon replicas. These PL spectra are shown in figure 7.26.

Implanting Fe into ZnO nanotips grown on *c*-Al₂O₃ causes an almost total suppression of photoluminescence. PL emission is not recovered in the samples annealed at 675 °C for 20 minutes or 700 °C for 5 minutes.

Not surprisingly, the near band-edge luminescence is recovered, albeit at much lower intensity, in the sample annealed at 700 °C for 20 minutes. This recovery indicates that Fe is being incorporated into the ZnO lattice, which will allow interaction with the band structure and hence true DMS behavior in this material. PL of ZnO/(*c*-Al₂O₃):Fe annealed at 700 °C for 20 minutes also reveals a broad green luminescence centered around 2.4 eV. This feature is attributable to oxygen vacancies [11], which would be more prevalent in a longer anneal such as the one under discussion.

There is also a stronger, broad, blue luminescence in ZnO/(*c*-Al₂O₃):Fe annealed at 725 °C for 10 minutes. This PL feature can be attributed to Zn vacancies in much

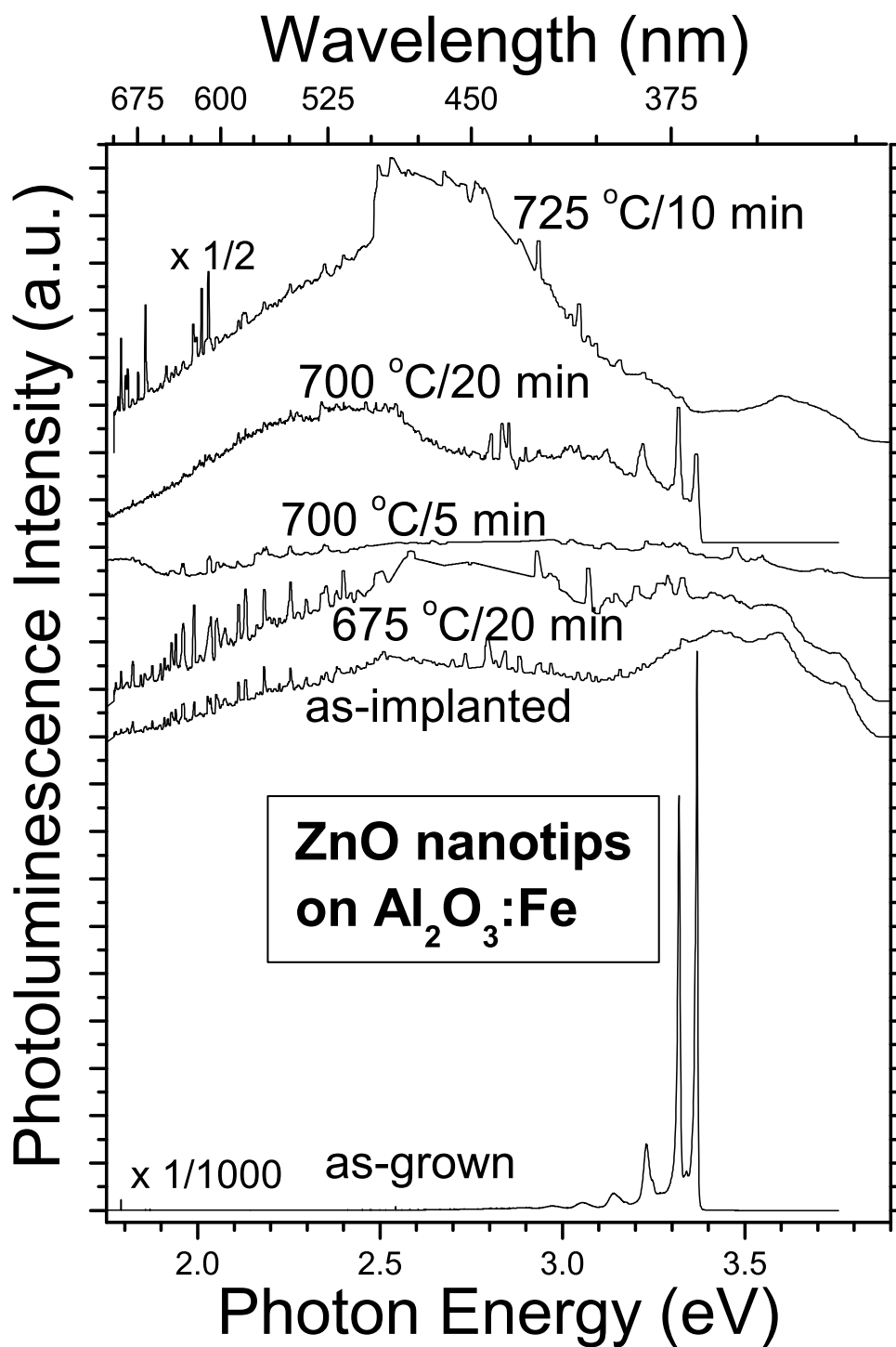


Figure 7.26 Photoluminescence spectra taken at ~ 10 K from ZnO nanotips grown on *c*-Al₂O₃, implanted with Fe and annealed as indicated in the figure in O₂ flowing at 25 sccm.

the same manner that yellow luminescence in GaN is attributed to Ga vacancies [57]. Note that the discontinuity on the low-energy side of this broad peak is due to insertion of a low-pass filter in the optical path to prevent replication of shorter wavelength features from the diffraction grating in the spectrometer.

The photoluminescence measurements taken on Fe-implanted ZnO nanotips grown on *c*-Al₂O₃ substrates show that the best crystal lattice damage recovery occurs when the sample is annealed at 700 °C for 20 minutes. This fact, along with the variable field and temperature measurements, shows that ferromagnetism is present in ZnO/(*c*-Al₂O₃):Fe, but only under specific annealing conditions. The exclusivity of magnetic properties to these annealing conditions, in addition to indications from other ZnO nanotip samples, suggests that further study of this material should involve annealing conditions that span a range of temperatures and use a 20-minute annealing time.

7.3 *Iron-Implanted Zinc Oxide Nanotips on Glass*

ZnO nanotips were grown on a glass substrate and implanted with iron to a level of $5 \times 10^{16} \frac{\text{ions}}{\text{cm}^2}$ with an implantation energy of 200 keV at room temperature. Mn-implantation was also attempted, but a communication error between the crystal growers and Implant Sciences caused the manganese to be implanted directly into the glass substrate rather than into the ZnO nanotips. While interesting from a magnetic coordination standpoint, the Mn-doped glass is decidedly not a DMS. An image of these particular ZnO nanotips is shown in figure 7.27.

The Fe-implanted ZnO nanotips grown on glass show paramagnetism at 5 K and slight diamagnetism at room temperature. While subtracting these backgrounds does make magnetic saturation visible in ZnO/(glass):Fe, the saturation magnetization is so slight that the material should be considered basically non-magnetic. Temperature-dependent measurements confirm the essentially non-magnetic character of the material. Photoluminescence spectra reveal no strong band-edge recovery, which indicates no significant implant damage reversal, so it may be that annealing conditions exist

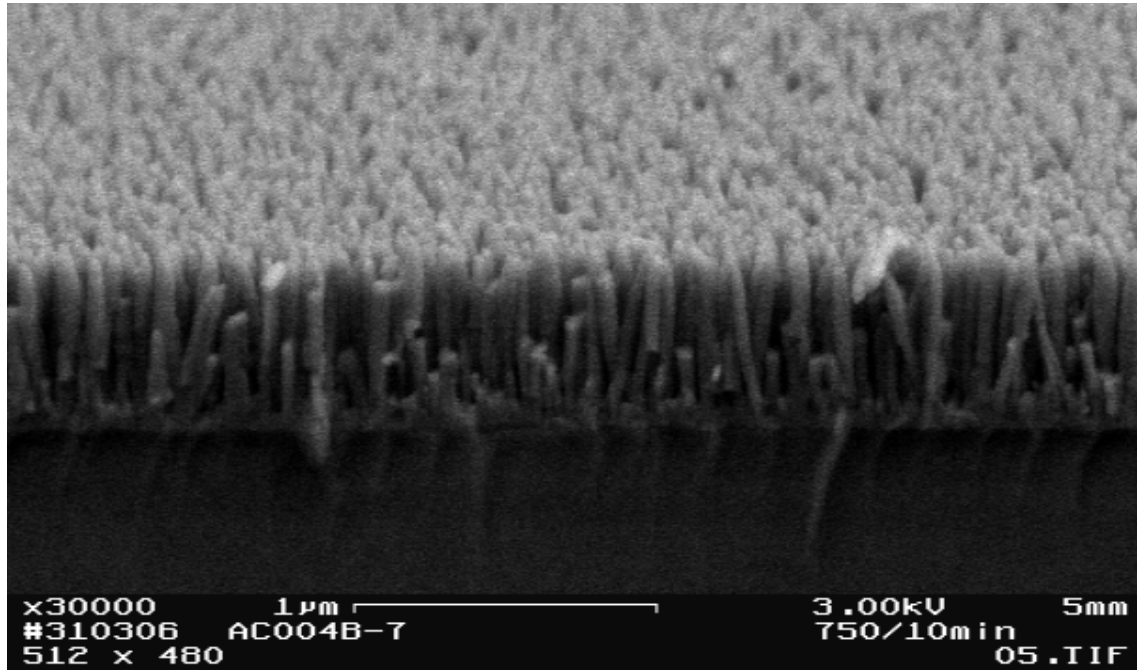


Figure 7.27 An SEM image of ZnO nanotips as-grown on a glass substrate.

outside of those used in this experiment which will render Fe-implanted ZnO/(glass) ferromagnetic. As tested in this work, though, this material shows no utility as a DMS.

7.3.1 Magnetic Hysteresis Measurements

Variable field measurements of ZnO/(glass):Fe are presented in figure 7.28. In this case, the samples had strong paramagnetic backgrounds at 5 K and mild diamagnetic influences at 300 K. The dominance of these background contributions, most likely arising from the glass substrate, is apparent in figure 7.28.

The coercive fields (H_c) for Fe-implanted ZnO nanotips grown on glass are relatively weak. This is clearly seen by the lack of hysteretic behavior in the variable field measurements, which indicates that the ferromagnetic properties of this material are very weak. There is also a lack magnetic saturation visible in the hysteresis loops. These observations point to the conclusion that ZnO/(glass):Fe is a non-magnetic material under the annealing conditions used in this experiment.

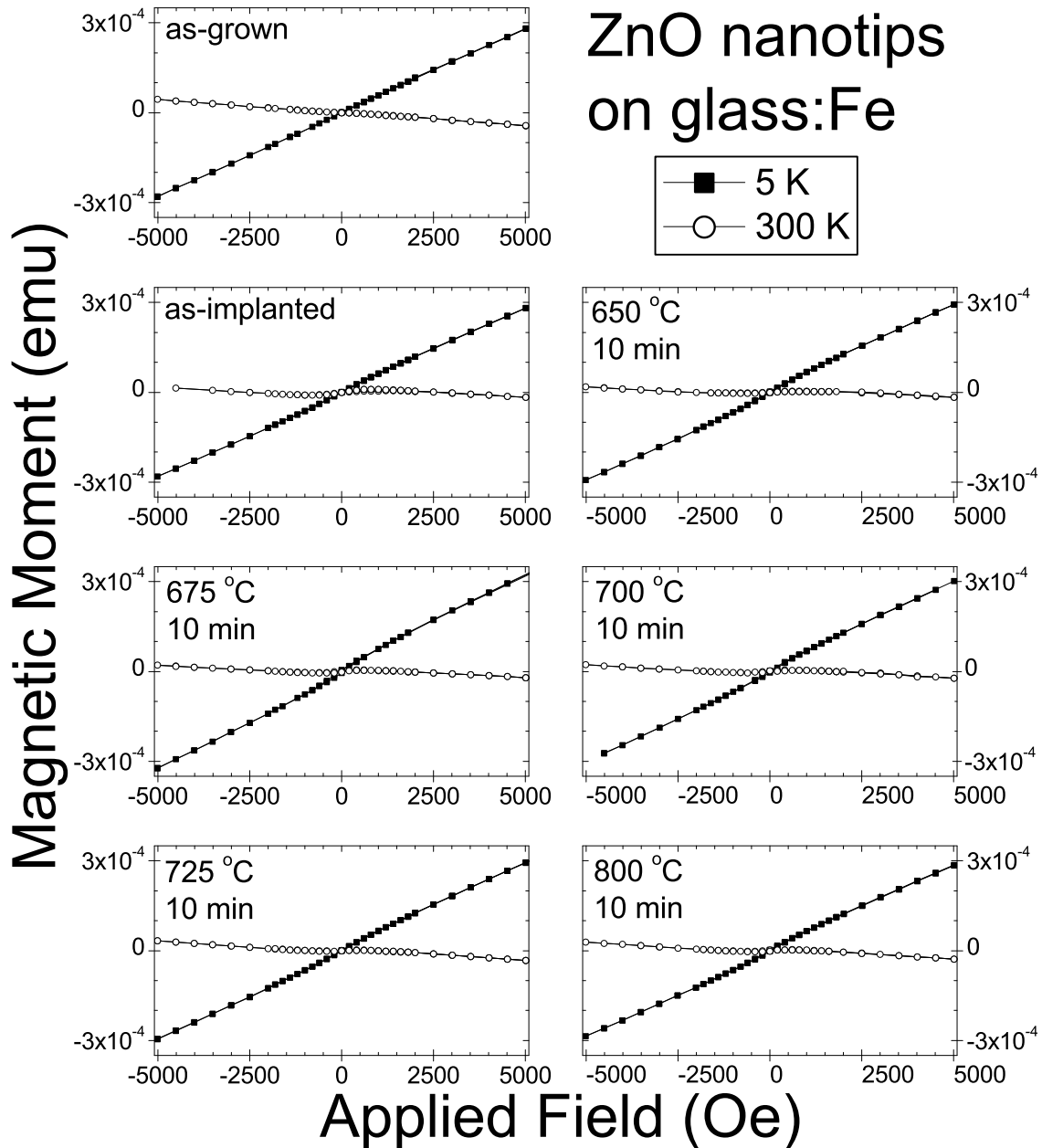


Figure 7.28 Raw data from magnetic hysteresis SQUID measurements of Fe-implanted ZnO nanotips grown on glass and annealed as indicated for 10 minutes in O_2 flowing at 25 sccm.

Even though the dominant characteristic of the measurements presented in figure 7.28 is paramagnetism at 5 K and diamagnetism at 300 K, it is still worthwhile to remove these linear magnetic influences in an attempt to deconvolve the factors contributing to the material's magnetic characteristics. Background subtraction is

accomplished by making the linear portion of magnetization curve above saturation parallel with the x axis.

In figure 7.29, the data gathered during the variable field measurements are shown with linear magnetic influences removed. This allows the presence of saturation and separation of the legs of the hysteresis loop to be observed if they are at all present. It also allows the data to be viewed on a much smaller scale: note the vertical (magnetization) scale in figure 7.28 is five times larger than that for the background-subtracted data in figure 7.29.

Without the linear magnetic backgrounds, the ZnO/(glass):Fe samples show saturation, but still fail to demonstrate any appreciable separation between positive- and negative-going legs of the hysteresis loop. Of course, this indicates a lack of ferromagnetism in the material. The only way to categorize these samples is superparamagnetic for most of them since there is clear magnetic saturation. The samples annealed at 675 and 725 °C do not show a clear linear magnetic saturation region when measurements are taken at 5 K at up to 10-kOe applied magnetic field, so these samples are classified as mostly paramagnetic in nature at low temperatures. The sharper appearance of saturation onset in the 300-K measurements for the samples annealed at 675 and 725 °C is a scaling issue. It occurs due to the fact that a maximum applied magnetic field of 10 kOe was used to test saturation behavior in the 5-K measurement and a maximum applied magnetic field of 5 kOe was used in the other measurements.

The background subtraction process normally facilitates more accurate measurement of H_c , but in this case, the values determined will be erroneously large for all samples because the low saturation magnetization (M_S) values and high background para- or dia-magnetism cause an effective stretching of the hysteretic separation. Since this effect is anticipated to be similar for all of the ZnO/(glass):Fe samples, H_c values are still determined and presented in figure 7.30 for comparison purposes among the annealing conditions used for this sample set.

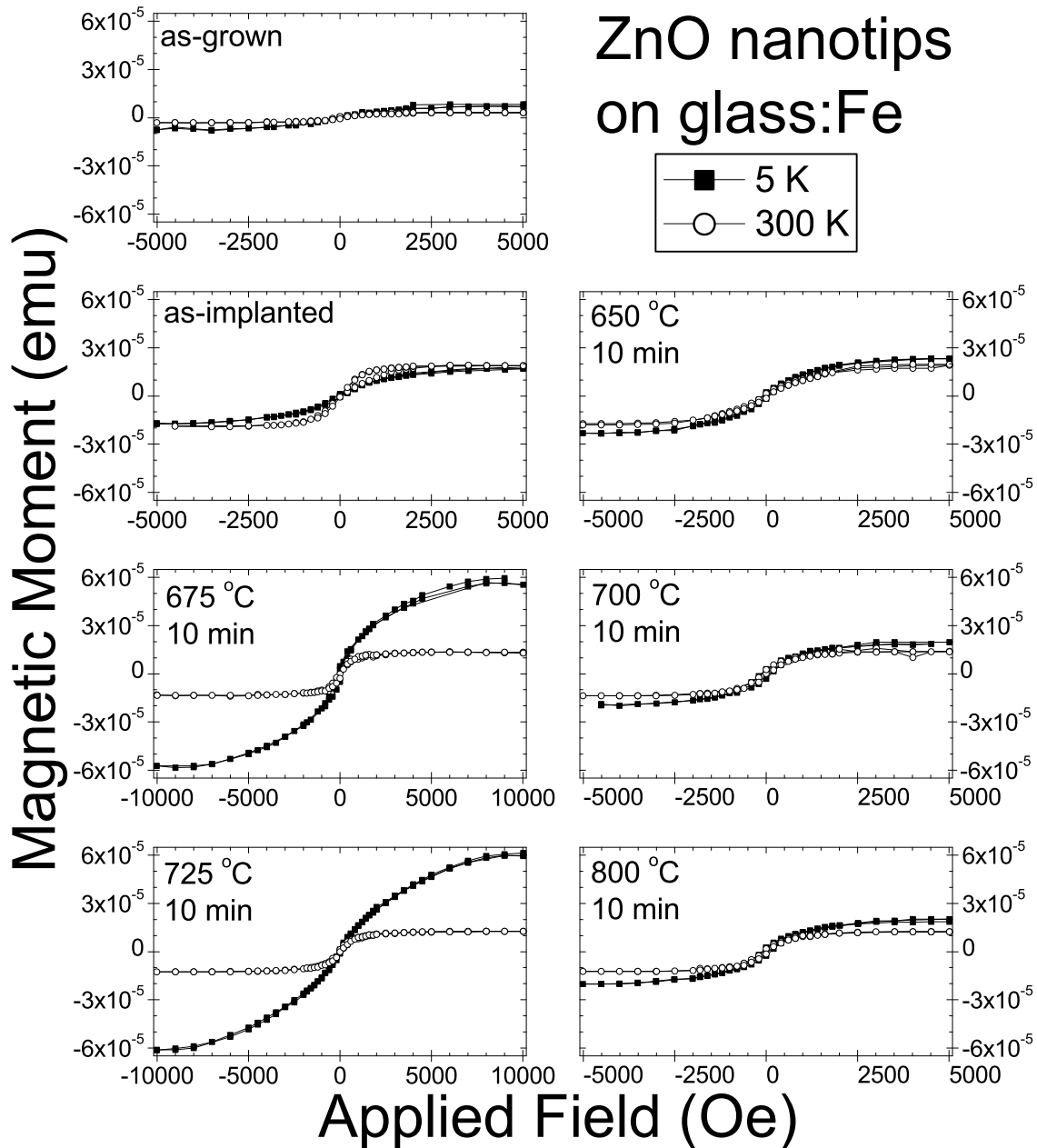


Figure 7.29 Magnetic hysteresis data for ZnO nanotips grown on glass, implanted with Fe and annealed as indicated in O_2 flowing at 25 sccm for 10 minutes. Linear dia- and para-magnetic influences have been removed from this data. Note that the samples annealed at 675 and 725 °C were subjected to a maximum applied magnetic field of 10 kOe in an attempt to find magnetic saturation in them, which affects the scaling and appearance of these measurements relative to the others in the figure.

Coercive Field Strength as a Function of Annealing Temperature

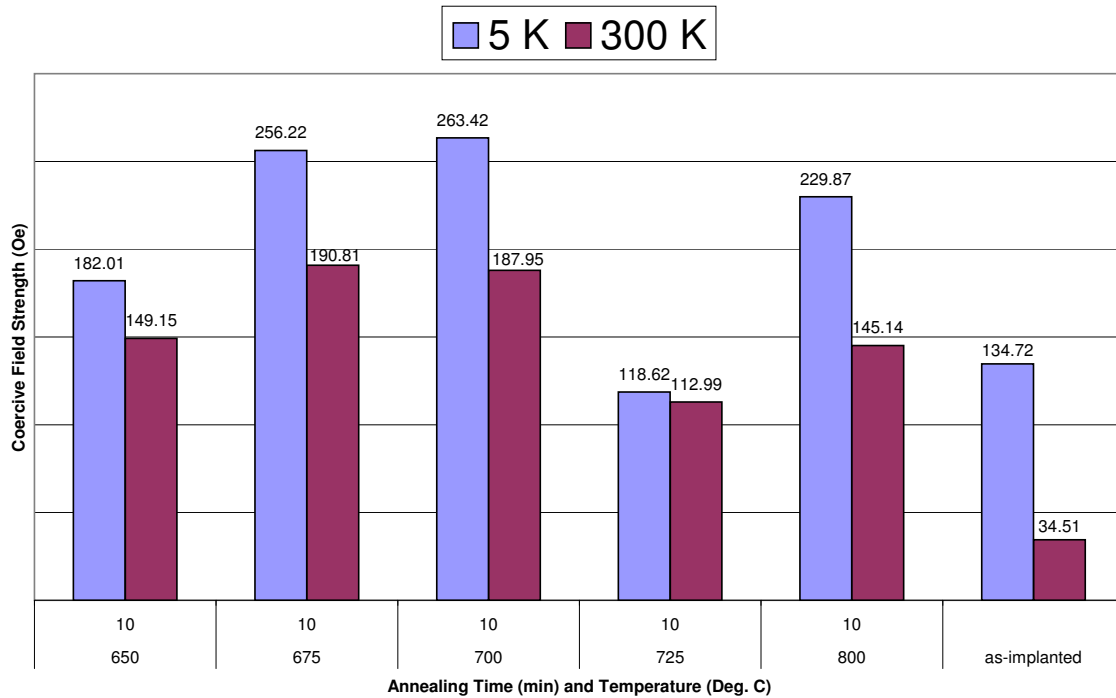


Figure 7.30 Coercive field strengths at 5 and 300 K for various annealing conditions of Fe-implanted ZnO nanotips grown on glass.

H_c is comparable for samples annealed at 675 and 700 °C for 10 minutes. This holds true at 5 K and room temperature. The fact that these two annealing temperatures produce similar magnetic properties suggests that the annealing temperature that will maximize what little coercivity may exist lies between 675 and 700 °C. There may be some true ferromagnetism as a source for these H_c values since they are stronger than those for the as-implanted sample, but despite the numbers determined, these coercive fields are not as great as those found in other samples.

The remanent fields (B_R) measured from the ZnO nanotips implanted with Fe are shown in figure 7.31 as a percentage of saturation magnetization. B_R values are far less sensitive to the background subtraction algorithm than H_c values because the large difference in scales between the x and y axes means that the values near zero applied magnetic field translate far less along the y axis with rotation than the values near zero magnetization move along the x axis with the same rotation. Since the

Remanent Magnetization as a Function of Annealing Temperature

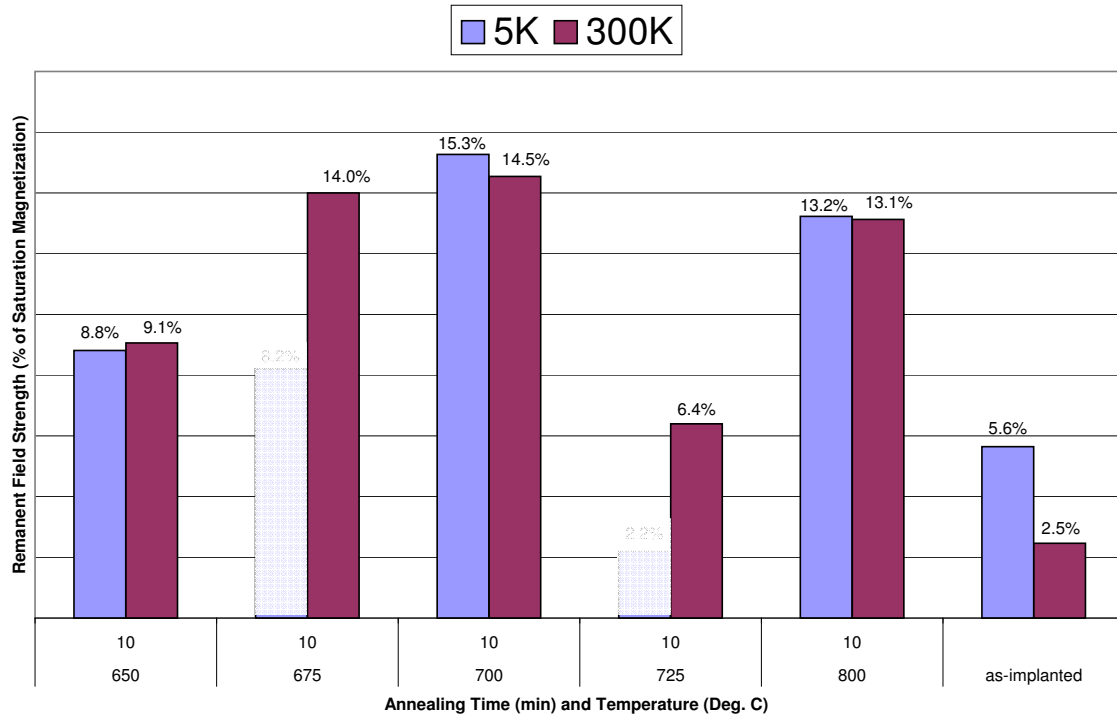


Figure 7.31 Remanent field strengths as a percentage of saturation magnetization at 5 and 300 K for various annealing conditions of Fe-implanted ZnO nanotips grown on glass. Values that are erroneously small due to large M_S values are partially obscured in the figure.

data presented in figure 7.31 are shown as a percentage of M_S , the values presented are sensitive to the determination of M_S . For this reason, the 5-K measurements of samples annealed at 675 and 725 °C for 10 minutes will show erroneously small values since M_S was unclear and a large value was chosen for it. The data that is affected in this way is partially obscured in figure 7.31.

It is clear from figure 7.31 that the annealing conditions that produced maximum H_c are also those that produce the greatest B_R in these samples: 675 to 700 °C for 10 minutes. While consistent, the ferromagnetic signatures in this material are extremely weak. The strength of ferromagnetism necessary for DMS-based devices is still under investigation, but if a weak signal indicates a lack of interaction between the implanted Fe and the ZnO band structure, then ZnO/(glass):Fe will not be a useful DMS.

7.3.2 Temperature-Dependent Magnetization

The data gathered for FC and ZFC conditions during temperature-dependent magnetization measurements on ZnO/(glass):Fe are shown in figure 7.32. Even though FC and ZFC magnetization measurements track together at low temperature, there

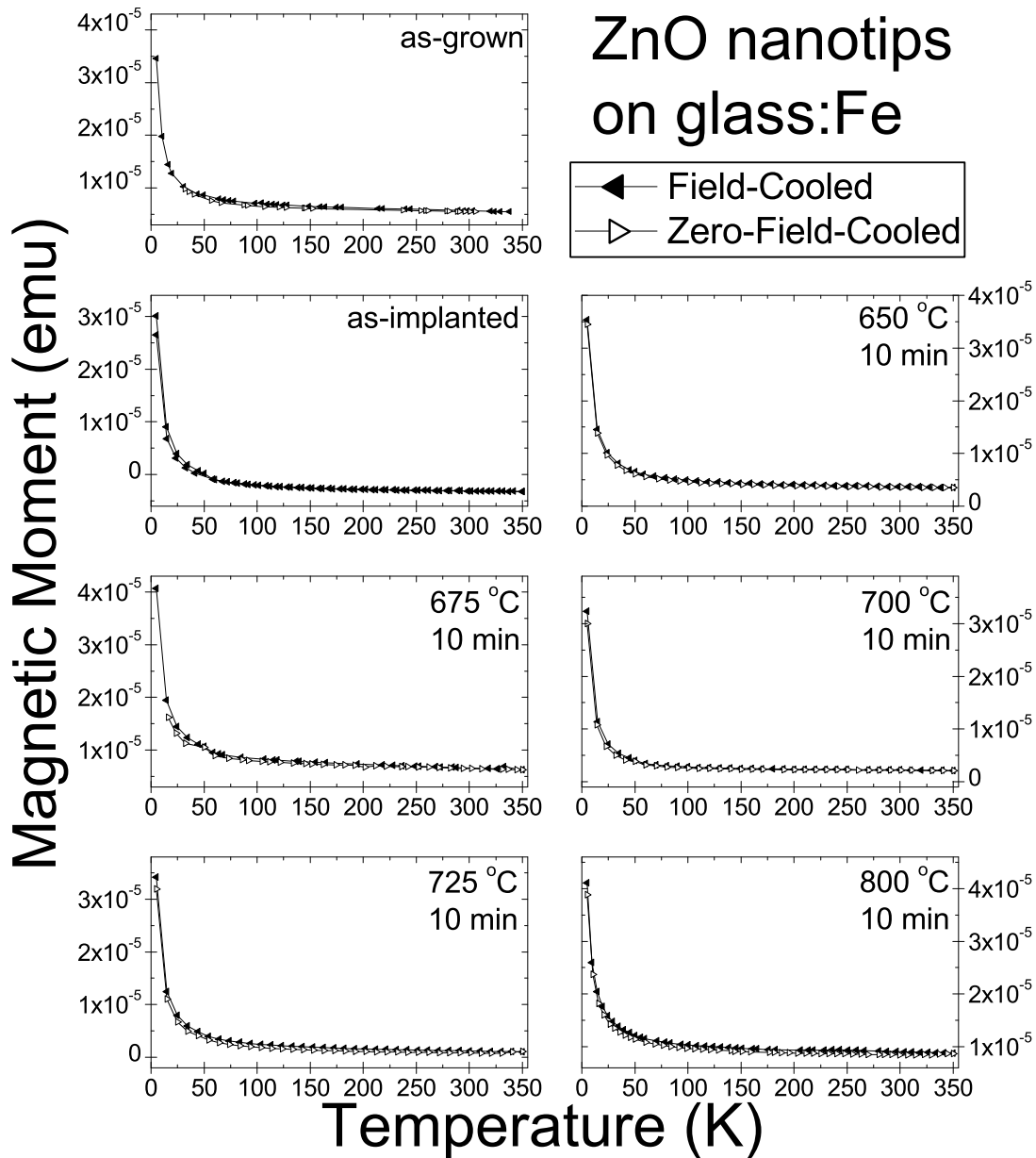


Figure 7.32 Temperature-dependent magnetization for ZnO nanotips grown on glass and implanted with Fe. Samples are annealed as indicated in a 25 sccm flow of O₂ for 10 minutes. Note that the y axis spans the same range of magnetic moment despite the fact that background offset causes a difference in absolute values.

is very little separation between the two across the whole range of the temperature sweep. This is another indication that the sample is dominated by paramagnetism. The separation between FC and ZFC measurements is also used as a metric of ferromagnetic properties because it inherently subtracts background magnetism [44]. Therefore, the lack of FC–ZFC separation in these samples indicates that the magnetic properties in them are arising from the background and not necessarily from the ZnO nanotips. The data shown in figure 7.32 is the best example presented in this work of the temperature-dependent magnetic qualities of a non-ferromagnetic material.

7.3.3 Optical Measurements

PL spectra taken from the ZnO nanotips grown on glass, implanted with Fe, and annealed under various conditions are shown in figure 7.33. The as-grown sample shows features that are inherent to bulk ZnO. This indicates that, as expected, the size of the ZnO nanotips is too large to induce appreciable quantum confinement effects. The primary peak at 3.3663 eV is attributed to a donor-bound A exciton. The secondary peak at 3.3204 eV is attributed to a two-electron satellite (TES) transition of a donor-bound A exciton [122]. The regular ~ 90 -meV spacing of further subordinate peaks identifies them as phonon replicas of the TES transition. The as-grown ZnO/(glass) also shows a small, broad luminescence centered around 1.9 eV. The red luminescence is attributed to oxygen vacancies in the ZnO [64].

Implanting Fe into the ZnO/(glass) causes suppression of PL intensity across the spectrum. The as-implanted sample shows a remnant of the band-edge luminescence, but it is weak and broad, which is expected due to ion implantation damage. The shoulder at 2.5 eV in the as-implanted sample is attributed to singly ionized oxygen vacancies [132]. A broad green luminescence centered around 2.7 eV arises in the sample annealed at 650 °C for 10 minutes. The 2.7-eV (blue-violet) peak shifts in energy closer to 2.8 eV when Fe-implanted ZnO/(glass) is annealed at 725 and 800 °C. This feature is attributed to a transition from neutral oxygen vacancies [146].

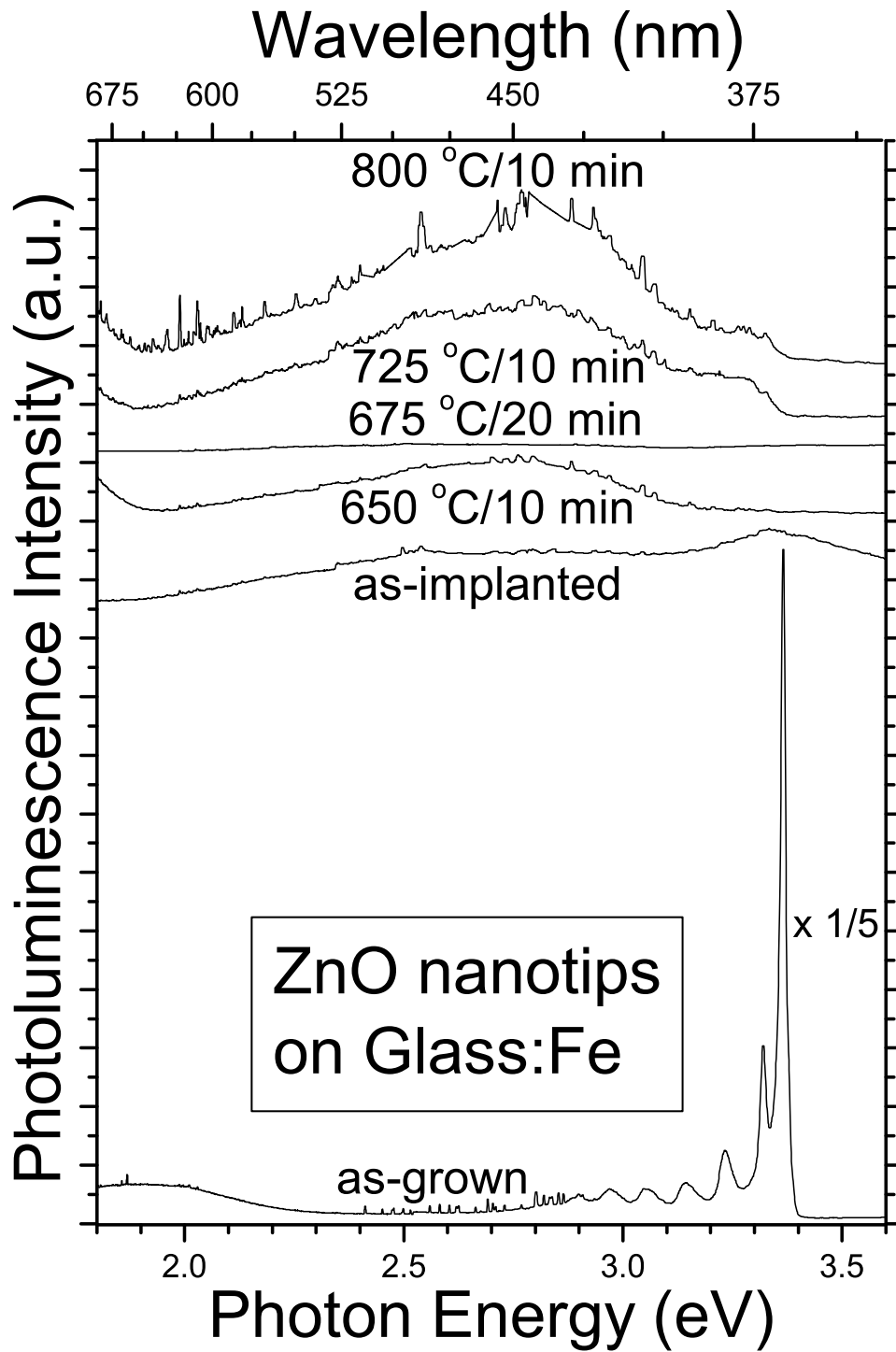


Figure 7.33 Photoluminescence spectra, collected at ~ 10 K, of ZnO nanotips grown on glass, implanted with Fe, and annealed as indicated in the figure in O_2 flowing at 25 sccm.

The near-band-edge luminescence in ZnO/(glass) is not recovered by any of the annealing conditions used in this experiment. From the sample annealed at 675 °C for 20 minutes, it is apparent that even longer annealing time does not necessarily improve implant damage recovery. The fact that there were no annealing conditions for which implantation damage was recovered suggests that Fe was not well-incorporated into the ZnO nanotips. The lack of Fe incorporation along with the SQUID measurements discussed above leads to the conclusion that the magnetic properties of this material are a result of background properties and do not arise from interaction of the implanted Fe with the host semiconductor.

7.4 *Conclusions*

7.4.1 *General Conclusions*

As a group, ZnO nanotips perform worse than their thin-film counterparts. There are several reasons why this may occur discussed below, but only one of them rules out the use of ZnO nanotips as a DMS material.

One reason for the generally poorer performance of ZnO nanotips may be their increased sensitivity to annealing conditions. In ZnO nanotip samples, where the ratio of surface area to crystal volume is very high, annealing conditions will play a larger role. The additional surface area can allow oxygen to escape the crystal lattice. It could also allow repair of native or ion-implantation-induced oxygen vacancies in the lattice when annealing takes place in a pure oxygen environment (as is the case in this work). Further research into which mechanism is dominant would allow the design of an experiment that limits damage or maximizes enhancement of crystal quality using annealing conditions.

Second may be the more extreme dilution, perhaps below some critical level, of the implanted transition metal (TM). Because TMs implanted into ZnO nanotips end up well distributed across the entire volume of the semiconductor material [45], the concentration is far less than the peak concentration just below the surface of

TM-implanted thin films. If there is a minimum concentration of the TM that must be present in order to make the semiconductor exhibit magnetic coordination, then the TM concentration in ZnO nanotips may be too low for ferromagnetic behavior. An experiment involving a higher implantation dose would reveal whether TM concentration is a limiting factor in this material.

Third could be the lack of coordination between implanted TMs to allow for magnetic ordering. The physical separation of ZnO nanotips will not allow coordination between the TMs implanted to cause ferromagnetism in the samples. If magnetic ordering is necessary over a longer range than ~ 50 nm, then ZnO nanotips will not facilitate DMS behavior. It is doubtful that this is the case because of the short range of most magnetic effects in semiconductors and the bulk-like behavior observed in PL characterizations.

7.4.2 Specific Findings

One of the most promising materials found in this research is ZnO nanotips grown on *c*-Al₂O₃, doped with Fe, and annealed at 700 °C for 20 minutes. This material showed a coercive field width (H_c) of 317 Oe at 5 K and 209 Oe at 300 K. The remanent fields (B_{RS}) in this material are 19 and 12% of saturation magnetization (M_S) for measurements made at 5 and 300 K, respectively. Annealing at 700 °C for 20 minutes also produces the greatest separation and low-temperature tracking in temperature-dependent measurements on Fe-implanted ZnO nanotips grown on *c*-Al₂O₃.

The ZnO nanotips grown on quartz and implanted with Fe or Mn show signs of ferromagnetism, but neither are consistent. In Fe-implanted ZnO/(quartz), H_c values of 452 and 396 Oe for 5- and 300-K measurements, respectively, occur when the sample is annealed at 650 °C for 10 minutes. This annealing condition also produces B_{RS} of 24 and 20% at 5 and 300 K, respectively. The inconsistency alluded to occurs because similar values are obtained from the sample annealed at 800 °C for 10 minutes, but lower values are obtained for the samples annealed at temperatures between 650 and

800 °C. The Mn-implanted ZnO/(quartz) show signs of ferromagnetism in variable field measurements with H_{cS} of 344 Oe (5 K) and 267 Oe (300 K) and B_{RS} of $\sim 27\%$ of M_S at both 5 and 300 K. Unfortunately, in both Fe- and Mn-implanted ZnO/(quartz), the temperature-dependent magnetization measurements do not confirm the findings of the variable field measurements.

The ZnO nanotips also produced two of the least useful materials, from a DMS device perspective, seen in this work. The ZnO nanotips grown on *c*-Al₂O₃ and implanted with Mn showed superparamagnetism (clear saturation, but little hysteretic separation) resulting from the dominance of a spin-glass phase across the range of annealing conditions. The Fe-implanted ZnO nanotips grown on glass were the most purely paramagnetic (at 5 K) and diamagnetic (at 300 K) samples seen in this work.

Nanotips will continue to play a role in DMS research. The reasons for this include their ease of growth, uniformity of implanted dopant concentration, and potential application in devices where electrical isolation is desired in a DMS. Further work with this material should involve a more comprehensive search for optimal implantation and annealing conditions.

VIII. Conclusions

8.1 Summary of Results

The goal of this research is to fabricate dilute magnetic semiconductor (DMS) material by implanting a variety of transition metals into wide bandgap semiconductors. The wide bandgap semiconductors used were p -GaN, $\text{Al}_{0.35}\text{Ga}_{0.65}\text{N}$, ZnO thin films and ZnO nanotips grown on quartz, sapphire, and glass, and the transition metals implanted were Mn, Cr, Ni, and Fe. Through magnetic hysteresis measurements using superconducting quantum interference device (SQUID) magnetometry, it has been found that some of the material combinations clearly showed strong ferromagnetism, others showed marginal evidence of ferromagnetism, and several did not demonstrate ferromagnetism at all, rather they were superparamagnetic or diamagnetic. The experiments accomplished in connection with this research show that there are a variety of options available for implantation-based fabrication of DMS material with ferromagnetism persisting to room temperature. Among the various measured samples, the most promising materials for creating spintronic devices using ion implantation are Mn-implanted p -GaN, Cr-implanted $\text{Al}_{0.35}\text{Ga}_{0.65}\text{N}$, and Fe-implanted ZnO nanotips grown on sapphire. In these three cases, the implantation of a transition metal and subsequent annealing produce signatures of above room temperature ferromagnetism that far outstrip any signs seen in the as-grown samples. The optimum anneal temperatures found in these samples were also confirmed by photoluminescence (PL) or cathodoluminescence (CL) measurements.

The specific findings from this work are as follows.

1. In Mn-implanted p -GaN, a coercive field width (H_c) as high as 468 Oe and a remanent field (B_R) over 20% of the saturation magnetization (M_S) of 1.75×10^{-5} emu were achieved at 5 K for the sample implanted at 200 keV with a dose of $5 \times 10^{16} \frac{\text{ions}}{\text{cm}^2}$ and annealed at an optimum annealing temperature of 725 °C for 5 minutes in flowing nitrogen gas (N_2). The ferromagnetism of this sample persisted with H_c and B_R values of 186 Oe and 11% of the M_S of 3.2×10^{-5} emu,

- respectively, at room temperature, and the the Curie temperature (T_C) is estimated to be above 350 K. The ferromagnetic dilute mangetic semiconductor behavior has been confirmed by the temperature-dependent field-cooled (FC) and zero-field-cooled (ZFC) magnetization measurements made on this sample.
2. For Cr-implanted $\text{Al}_{0.35}\text{Ga}_{0.65}\text{N}$, coercive fields of 414 and 249 Oe were obtained through magnetic hysteresis measurements at 5 and 300 K, respectively, on a sample implanted with $5 \times 10^{16} \frac{\text{ions}}{\text{cm}^2}$ at 200 keV and annealed at an optimal anneal temperature of 775 °C for 5 minutes in flowing N_2 . The remanent field also remained greater than 20% of the M_S of 10^{-4} and 6×10^{-5} emu at 5 and 300 K, respectively, and T_C for this sample is estimated at or just above 350 K for this sample. FC and ZFC magnetization measurements of this sample also confirm the presence of DMS-based ferromagnetism persisting to room temperature.
 3. Fe-implanted ZnO nanotips grown on $c\text{-Al}_2\text{O}_3$ showed coercive field widths of 317 Oe at 5 K and 209 Oe at 300 K for the sample implanted at 200 keV to a dose of $5 \times 10^{16} \frac{\text{ions}}{\text{cm}^2}$ and annealed under optimal annealing conditions of 700 °C for 20 minutes in flowing oxygen gas (O_2). The remanent fields in this material are 19 and 12% of M_S (7.1 and 2.3×10^{-5} emu) for measurements made at 5 and 300 K, respectively. Temperature-dependent magnetization measurements confirm that this material demonstrates ferromagnetism consistent with that expected from a dilute magnetic semiconductor of good quality. T_C for this material is believed to be above 350 K.
 4. Mn-implanted $\text{Al}_{0.35}\text{Ga}_{0.65}\text{N}$ showed H_c of 409 and 199 Oe at measurement temperatures of 5 and 300 K, respectively, when implanted at 200 keV to a dose of $5 \times 10^{16} \frac{\text{ions}}{\text{cm}^2}$ and annealed at 775 °C in flowing nitrogen. B_R values at 5 and 300 K were 14×10^{-6} and 7×10^{-6} emu, respectively, for this sample. Although the temperature-dependent magnetization measurements show signs of ferromagnetism, they also indicate that there may be a weak spin-glass phase present in the material. Therefore, further study is necessary to determine the nature and usefulness of this material from a spintronic perspective.

5. Several other cases show signs of ferromagnetism and in fact demonstrate increased ferromagnetism over the as-grown and as-implanted samples, but they are not as convincing as the most promising samples. They do not demonstrate a clear trend of coercive or remanent field strength as a function of annealing temperature, and thus show no optimum annealing temperature. However, these materials have potential for use in DMS-based devices. They include

- (a) Cr-implanted *p*-GaN: This has maxima in H_c at each end of the range of annealing temperatures (650 – 775 °C) and B_R maxima occur at different anneal temperatures of 750 and 700 °C for 5 and 300 K measurements, respectively.
- (b) Fe-implanted ZnO nanotips grown on quartz: The highest coercive and remanent fields occur at both ends of the annealing temperature range of 650 to 800 °C with lower values at temperatures between these. The temperature-dependent magnetization also shows variable separation between FC and ZFC magnetization that does not seem to be sensitive to annealing conditions.
- (c) Mn-implanted ZnO nanotips grown on quartz: They show coercive and remanent field maxima at both 5 K and room temperature when the sample is annealed at 750 °C for 10 minutes. Unfortunately, this sample shows little FC–ZFC separation, indicating that the observed ferromagnetism may be due to background effects rather than arising from the ZnO nanotips.

A more detailed description of magnetization behavior in the materials discussed above is provided in Appendix C.

6. The following samples show signs of ferromagnetism, but slow onset of saturation or low M_S values prevent meaningful determination and comparison of the strength of ferromagnetism among samples annealed at various temperatures. These samples can be characterized as ferromagnetic, but engineering DMS-

based devices with these materials will be impeded by the lack of useable H_c and B_R values and the variability in M_S .

- (a) $\text{Al}_{0.35}\text{Ga}_{0.65}\text{N}$ implanted with Ni at 200 keV to a dose of $3 \times 10^{16} \frac{\text{ions}}{\text{cm}^2}$: This material shows hysteretic behavior, but accurate coercive and remanent fields cannot be determined due to low magnetic saturation values in the 725 to 750 °C annealing temperature range.
- (b) The second epitaxial ZnO wafer implanted with Mn: This material shows hysteresis and FC–ZFC magnetization separation that exceed those seen in the as-grown sample, but these phenomena do not occur at the same annealing temperature.
- (c) The ZnO thin film implanted with Cr: Background diamagnetism distorts the hysteresis loop of the samples annealed at 675 and 700 °C so that accurate H_c and B_R values cannot be determined.

More detailed magnetization information concerning these samples is available in Appendix C.

7. The following samples showed signs of ferromagnetism that were not consistent across the different indicators of ferromagnetism in that an annealing condition that produces a strong coercive field is the same condition that gives the weakest remanent field or FC–ZFC divergence. This is a signal that these materials are not useful for DMS device fabrication under the conditions used in this work.
 - (a) Ni-implanted p -GaN: Annealing this material at 725 °C produces a strong coercive field and wide FC–ZFC separation, but there is also divergence at low temperature between FC and ZFC magnetization, which indicates the possible presence of a spin-glass phase.
 - (b) ZnO from the first epitaxial growth implanted with Mn: In this material, the sample annealed at 675 °C for 20 minutes is the only one with significant FC–ZFC separation, but it shows the weakest coercive and remanent fields.

- (c) ZnO implanted with Ni to a dose of $3 \times 10^{16} \frac{\text{ions}}{\text{cm}^2}$: This material, while some annealing conditions produce respectable coercive and remanent field values, does not show any trending of these numbers as a function of annealing temperature, which suggests that the ferromagnetism present may arise from something other than incorporation of the implanted Ni into the ZnO crystal lattice.

Appendix C provides further detail concerning the magnetization data gathered for these samples.

8. The following samples did not show indications of magnetic ordering. One showed only linear magnetic properties (diamagnetism and paramagnetism) and two others showed superparamagnetism (saturation without hysteretic separation), which most likely results from the presence of a spin-glass phase where magnetic ordering is “frozen” in a non-equilibrium configuration at low temperatures. These materials do not have properties that are useful for fabricating a room-temperature DMS-based device.

- (a) ZnO nanotips grown on sapphire and implanted with Mn to a level of $5 \times 10^{16} \frac{\text{ions}}{\text{cm}^2}$ show mostly spin-glass behavior, and only the sample annealed at 750 °C for 10 minutes shows hysteretic separation at low temperature.
- (b) The epitaxial ZnO from the first growth that is implanted with Fe to a level of $5 \times 10^{16} \frac{\text{ions}}{\text{cm}^2}$ shows divergence of FC and ZFC magnetization curves at low temperature confirming that this material contains a spin-glass magnetic phase which dominates any ferromagnetism that might be present.
- (c) The sample in which ferromagnetism is most glaringly absent is the ZnO nanotips grown on glass and implanted with Fe to level of $5 \times 10^{16} \frac{\text{ions}}{\text{cm}^2}$. Because the paramagnetic background is so dominant at low temperatures, values of H_c and B_R for these samples are meaningless. Temperature-dependent magnetization measurements confirm that this sample does not

demonstrate magnetic ordering by the lack of separation between FC and ZFC magnetization for all annealing conditions.

More detailed information concerning the magnetic behavior of these samples is provided in Appendix C.

All the results described above lead to the conclusion that DMS-type ferromagnetism is possible in TM-implanted wide-bandgap semiconductors. Although there are certain pitfalls and some materials that show a lack of ordering, based on the results of this research, materials can be fabricated with reasonable effort that will allow spintronic devices to be realized.

For those attempting to find a workable theory of magnetic ordering in dilute magnetic semiconductors, one of the most germane discoveries in this work involves the sensitivity of ferromagnetism to the quality of the semiconductor crystal. While intuitively obvious and long expected to be a factor in DMS fabrication, the dependence of ferromagnetism on crystal quality is scarcely reported in the sort of head-to-head test conducted in this research. The comparative experiment involves Mn being implanted at the same dose ($5 \times 10^{16} \frac{\text{ions}}{\text{cm}^2}$) into ZnO thin films grown by the same method in the same growth chamber at different times. The higher quality crystal (grown later, which lends the advantages of a less contaminated growth chamber and a more experienced crystal grower) shows more consistency across annealing conditions and behavior commensurate with the presence of ferromagnetic ordering.

Another unexpected finding is the enhanced dependence of ferromagnetism on annealing time found in ZnO nanotips. The sensitivity is explained by the increased surface area of the ZnO nanotips, and hence the increased exposure to the O₂ gas environment in the annealing furnace.

Notwithstanding certain inconsistencies and unexpected results, the preponderance of this work shows that ion implantation of transition metals into wide-bandgap semiconductors is a viable process for fabricating DMS material. Although scattered reports of successful DMS fabrication by transition metal implantation have been

made, this work shows the broad effectiveness of this method for creating DMS material. As progress is made toward realizing practical spintronic devices, the work reported in this document will be useful for determining material combinations and implantation conditions that will yield the needed materials.

8.2 Future Work

8.2.1 Devices

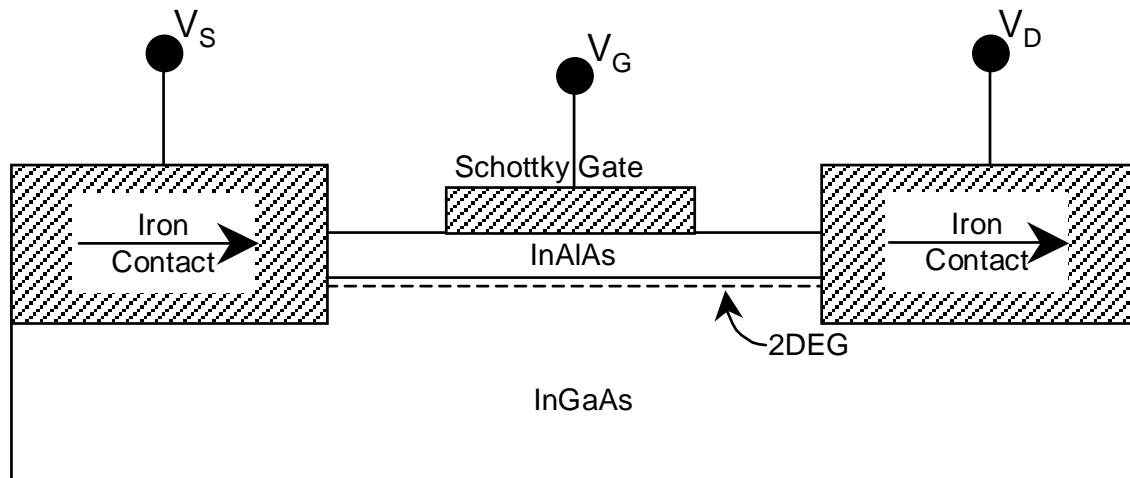
8.2.1.1 Spin-LED

Transition metal (TM) ions implanted at 200 keV have a peak concentration in ZnO and GaN approximately 100 nm below the surface of the host semiconductor. A p - n junction formed by doping during crystal growth and placed 175–200 μm below the surface of the semiconductor would allow radiative recombination of carriers injected through the magnetically active layer formed by TM implantation and subsequent annealing. This would result in a device similar to those discussed in section 2.2.1 and depicted in figure 2.4. If sp - d hybridization is present in the TM-doped region, electroluminescence from such a device could be analyzed for preferential circular polarization, which would indicate injection of spin polarized carriers. This is similar to the magneto-optical experiment described in section 8.2.2.1, and analysis of the resultant radiation would be identical. Spin-LEDs provide another method of testing for sp - d hybridization in DMS materials. Additionally, these devices could be used as integrated polarized light emitters and detectors with low power consumption.

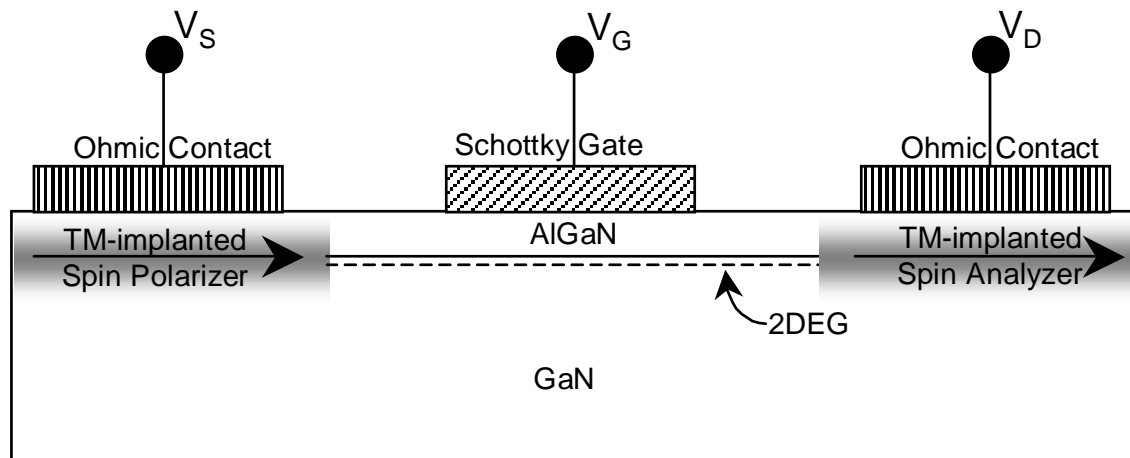
8.2.1.2 Spin-Transistor

The ability to modulate a spin-polarized current is essential to using spintronic devices for computing. The seminal theoretical work in spin-based transistors was contributed by Datta and Das [23]. The structure of their proposed device, which utilizes a narrow-bandgap semiconductor and Fe contacts, is illustrated in figure 8.1(a).

A similar device could be constructed using the DMS materials reported in this research. The device could consist of a GaN/AlGaIn heterojunction where portions



(a)



(b)

Figure 8.1 Schematics of a proposed structures for utilizing electron spin to modulate current output. (a) The device proposed by Datta and Das [23]. (b) A similar device using wide-bandgap semiconductors and fabricated using ion implantation.

of the material are doped with transition metals and made ferromagnetic so that they are able “to preferentially inject and detect specific spin orientations” [23]. The proposed structure for such a device is shown in figure 8.1(b).

The device structure depicted in figure 8.1(b) is enabled by ion implantation because of the lateral control available using this technique. A device fabricated as

shown in figure 8.1(b) has several advantages over the type pictured in figure 8.1(a). First, the lack of a metal–semiconductor junction at the point of polarized electron injection allows for a greater degree of spin polarization [104]. Second, the device proposed in figure 8.1(b) can be fabricated without the necessity for etching, which ensures higher quality material as well as easing the deposition of contacts because the surface is kept planar. These advantages warrant an investigation of spintronic transistors fabricated using ion implantation techniques.

8.2.2 Further Characterization

8.2.2.1 Magnetic Circular Dichroism (MCD)

One tool that is available to determine whether the magnetic properties of a given DMS candidate result in meaningful effects on the semiconductor’s electronic structure is MCD. The experiment is similar to photoluminescence (PL), but the sample is subjected to a magnetic field during measurement and the radiation emanating from the sample is analyzed to determine whether it is polarized preferentially toward right- or left-circular polarization. Interaction between the d -shells of the implanted TM and the conduction or valence band should produce an energetically preferred spin state in the DMS. Carrier annihilation from the two spin states cause light to be emitted in the opposite senses of circular polarization. If there is a preferred spin state, then one of the senses of circular polarization will dominate and circular dichroism will be apparent. Preparations for MCD experiments are being made and the materials reported in this work will be characterized in this way.

The MCD experiment involves applying a magnetic field to a sample and then exciting it with above-bandgap radiation. A photoelastic modulator will be used to convert one sense and then the other of circular polarization into linearly polarized light aligned with a linear polarization analyzer. The analyzer output will be processed by a spectrometer to determine the difference in right- and left-hand circular polarization at each step across a range of wavelengths. A difference in the intensity of radiation, particularly near the band edge, indicates that the optically-injected

carriers in the material have a preferential spin polarization. A difference in MCD measurements between transition-metal-doped and as-grown semiconductors will allow the spin polarization to be attributed to the interaction of charge carriers in the material with the d -shells of the implanted transition metal.

8.2.2.2 Carrier-Dependent Magnetization

In order to examine the effects of carrier type and concentration on magnetic ordering in semiconductors, an experiment should be constructed in which magnetization is measured as a function of these parameters. Such an experiment would be conducted by injecting either free electrons or holes into the material and measuring any resulting change in the magnetic moment emanating from the sample.

The best candidate device for testing carrier-dependent magnetization is a metal-insulator-semiconductor (MIS) diode. The MIS diode offers several advantages: there is no current flow, so carrier movement will not cause false magnetic measurements, and the contacts need not be ohmic, so a non-magnetic metal can be used without compromising performance. The device could be fabricated by implanting a lightly p - or n -doped wide bandgap semiconductor with a transition metal and annealing under conditions that will produce magnetic behavior. The magnetic moment present in the sample can then be measured with the free carriers present (zero bias) and with a depletion region enveloping the TM-implanted region. The experiment could also be accomplished over a range of temperatures to determine the effect of carrier freeze out and whether there exists a point of diminishing returns where additional free carriers cease to enhance magnetic ordering. Energy band diagrams of the proposed MIS diodes are presented in figure 8.2 to illustrate the presence of free holes or electrons in the TM-implanted region.

8.2.2.3 Characterize Background Diamagnetism

In order to understand the nature and causes of the background diamagnetism of most of the samples studied in this work, an attempt can be made to remove it by

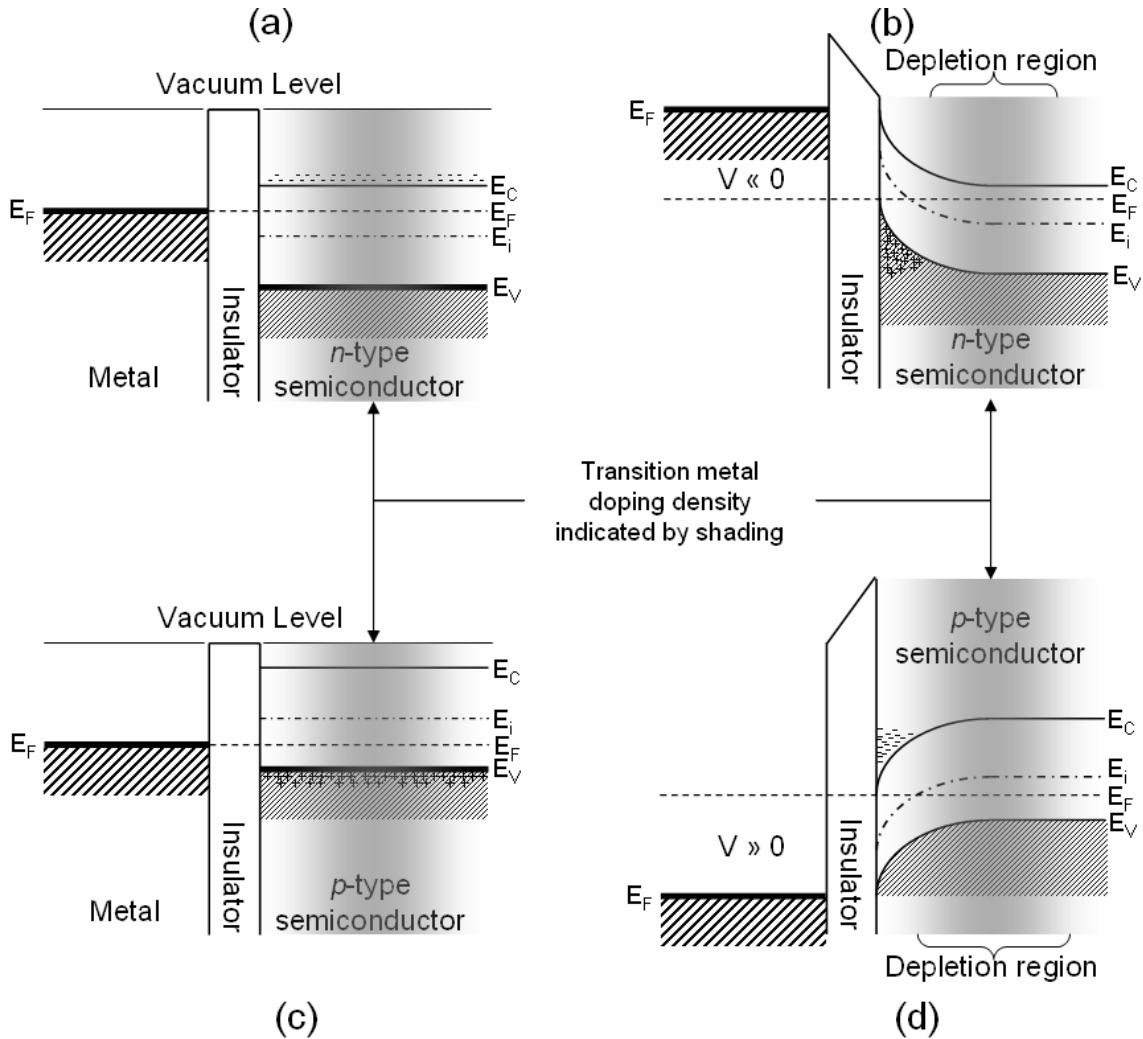


Figure 8.2 Real space energy band diagrams of metal–insulator–semiconductor diodes that could be used to test the carrier dependence of magnetic ordering in transition-metal-implanted semiconductors. Presented are an *n*-type device with (a) no gate bias and (b) a large negative gate bias. A *p*-type device is also illustrated with (c) no gate bias and (d) a large positive gate bias.

annealing prior to TM implantation. To this end, one could anneal *p*-GaN, AlGaN, or ZnO at high temperatures before ion implantation. An initial study should be made in which portions of the as-grown samples of *p*-GaN and $\text{Al}_{0.35}\text{Ga}_{0.65}\text{N}$ used in this work are annealed and then characterized using SQUID magnetometry to find the annealing conditions which remove background diamagnetism most effectively. If annealing conditions are found that effectively remove the diamagnetic background, a wafer of the same material could then be annealed under these conditions after growth

and before ion implantation. Removal of the diamagnetic background will allow better characterization of magnetic properties of the semiconductor after transition metal implantation.

8.2.3 Dopant Distribution Uniformity in Nanotips

Ion implantation of ZnO nanotips leads to uniform distribution of the implanted species throughout the semiconductor [45]. This is advantageous because it avoids variability in composition and concentration gradients of the material. There are two ways in which these advantages can be leveraged.

8.2.3.1 Determine Optimal Dopant Concentration

Nanotips of ZnO (and other materials such as *p*-GaN if desired) can be implanted with TMs at various doses in an attempt to find an optimum doping level for producing ferromagnetism. In TM-implanted thin films, there are a variety of concentrations of the implanted species present, so it is difficult to determine exactly what concentration is optimal. In nanotips, the uniform dopant concentration resulting from ion implantation allows for magnetic measurements of a single concentration in a specific semiconductor. This information will allow persons interested in spintronic device fabrication to choose a TM concentration that will maximize magnetic properties that are desirable for their devices.

8.2.3.2 ZnO Nanotip Recrystallization

The uniform dopant distribution in ZnO nanotips could also be used to produce thin films with a uniform TM distribution. ZnO nanotips tend to melt together and form a film after annealing at temperatures of 800 °C and higher. If this melting and merging can be controlled in a way that will allow a monocrystalline thin film to form, then this technique may prove to be an efficient method of forming DMS material with precisely controlled dopant concentration. The problems surrounding this fabrication method may, however, prove intractable. High-temperature annealing tends to cause clustering of the implanted TM as well as increasing vacancies of the

anions in wide-bandgap semiconductors. The tendency of the melting ZnO nanotips to form a single crystal is another unknown—the conditions required to induce crystal ordering may be impractical, inefficient, or non-existent. Despite these difficulties, the utility of this method may be great enough, especially where DMS-based devices are concerned, to justify at least a preliminary study into its efficacy.

8.2.4 Materials Warranting Further Investigation

Because of the poor crystal quality evident in the epitaxial ZnO wafer into which Fe ions were implanted, determination of the viability of ZnO:Fe as a DMS was not conclusive. The Mn-implanted ZnO proved to be sensitive to crystal quality and showed signs of ferromagnetism when Mn was implanted into a ZnO wafer of higher quality. The same improvement of ferromagnetic properties is likely to be observed if Fe is implanted into a higher-quality ZnO thin film. Based on the results in ZnO nanotips, it will be worthwhile to implant Fe into epitaxial ZnO. It may also be worthwhile to implant Fe ions into GaN or AlGaN.

Mn-implanted $\text{Al}_{0.35}\text{Ga}_{0.65}\text{N}$ showed clear signs of ferromagnetism when annealed at 775 °C for 5 minutes. This material also showed evidence of a spin-glass phase in temperature-dependent magnetization measurements. The ferromagnetic properties of the semiconductor suggest that it will prove useful in spintronic device fabrication, but a determination must be made concerning how well such a device can work in the presence of a competing spin-glass phase. This material provides a good opportunity to make such a determination. Furthermore, future work should address ways to control and limit the formation of the undesired spin-glass phase.

The Cr-implanted *p*-GaN, and the Mn- and Fe-implanted ZnO nanotips grown on quartz show magnetic saturation and hysteresis in variable field measurements that is indicative of ferromagnetism. These samples also show signs of ferromagnetism in temperature-dependent magnetization measurements. However, a clear trend in these properties as a function of annealing temperature is not detected. This suggests that

these materials are capable of producing a ferromagnetic DMS, but that more study is needed to determine the optimal conditions to bring this about with high regularity.

8.3 Finale

Spintronics promise to improve the state of current computation and sensor technology. Whether this improvement is evolutionary in the form of non-volatile memory and faster clock speeds or revolutionary in the form of quantum computing, this technology will be built upon dilute magnetic semiconductors that are useable at room temperature. This work was undertaken to test a cost-effective and precise method for fabricating these materials and has proven that ion implantation is a viable method for producing ferromagnetism in wide-bandgap semiconductors. Ion implantation lends itself especially well to device fabrication and will be key to the practical implementation of spintronic devices in the future. The preponderance of the evidence presented in this document shows that DMS material with magnetism persisting to room temperature can be fabricated by implanting transition metal ions into wide-bandgap semiconductors.

*Appendix A. Prior Experimental and Theoretical Results for GaN
and ZnO Doped with Transition Metals*

Table A.1 shows materials and dopants that have been investigated both theoretically and experimentally as wide-bandgap DMSs. This table is presented to provide the reader a sense of the amount of research performed on each material system. The quality and results of the experimental research cited in table A.1 are discussed in section A.2 and are the basis for the prioritization of materials and dopants for this research. Note that if there is no citation in table A.1 or mention in section A.1 or section A.2, then there is currently no theoretical or experimental report in the literature for that particular combination of material and dopant.

Table A.1 Materials and transition metal dopants reported in literature (as cited in the appropriate block) for useful properties as a DMS.

Dopant	Material	
	<u>ZnO</u>	<u>GaN</u>
Scandium (Sc)	[5]	
Titanium (Ti)	[5] Theoretical [100]	
Vanadium (V)	[5, 99, 120] Theoretical [100, 131]	[62]
Chromium (Cr)	[5, 47, 102, 120, 128] Theoretical [100, 131]	[43, 62, 85, 147]
Manganese (Mn)	[5, 20, 36, 37, 47, 50] [53, 103, 120, 128, 142] Theoretical [28–30, 100, 101, 131]	[4, 59, 63, 83, 94, 95, 111–113, 116] [117, 123, 125, 126, 144, 145] Theoretical [28, 30, 34, 131]
Iron (Fe)	[21, 42, 47, 142] Theoretical [100, 101, 131]	[1, 59, 63, 124, 126] Theoretical [34]
Cobalt (Co)	[5, 21, 47, 54, 61, 97, 120, 128, 142] Theoretical [100, 101, 131]	[62]
Nickel (Ni)	[5, 120, 128, 134] Theoretical [100, 101]	
Copper (Cu)	[5, 42] Theoretical [100]	

A.1 Theoretical Calculations

Calculations have been made to determine the propensity of certain transition metal dopants to cause room-temperature ferromagnetism in ZnO and GaN. The following sections briefly summarize the results of those calculations as well as any notable features or assumptions of the calculations themselves.

A.1.1 Zinc Oxide Theoretical Calculations

Titanium: Sato and Katayama-Yoshida report the results of *ab initio* calculations using the local density approximation. They assumed a transition metal doping of 25 at.% and determined the propensity for ferromagnetism based on which alignment, ferromagnetic (FM) or antiferromagnetic (AFM), between neighboring cells yielded the lowest system energy. According to their calculations, Ti did not show a preference for either state or a magnetic moment, so one would expect paramagnetic behavior [100].

Vanadium: In the case of V, Sato and Katayama-Yoshida report the largest energy preferences for ferromagnetic state of any of the transition metals for which calculations were performed [100].

Uspenskii *et al.* also performed *ab initio* calculations concerning the energy-related preference of a DMS to be ordered either ferromagnetically or antiferromagnetically. They used the tight binding approximation to calculate the local spin density approximation (LSDA) for a 64 atom supercell. These calculations were performed for $\text{Zn}_{1-x}\text{V}_x\text{O}$ ($x = 0.03, 0.06, 0.125, 0.25$), but results were only reported for the $x = 0.125$ case, with no mention of discrepancies for the other cases. In the case of $\text{Zn}_{0.875}\text{V}_{0.125}\text{O}$ ferromagnetic ordering was predicted to be the lowest energy configuration [131].

Chromium: Sato and Katayama-Yoshida also reported an energy preference for ferromagnetic ordering in $\text{Zn}_{1-x}\text{Cr}_x\text{O}$ ($x = 0.25$) [100].

In the case of Cr-doped ZnO, Uspenskii *et al.* found the preferred magnetic ordering to be ferromagnetic. In the case reported, where transition metals comprised 12.5 at. % of the supercell, they calculated the greatest energy preference for ferromagnetism in the Cr-doped case [131].

Manganese: The most detailed calculation reported by Sato and Katayama-Yoshida was for the case of $\text{Zn}_{1-x}\text{Mn}_x\text{O}$. They noted that without any carrier doping or with electron doping (gallium (Ga) substituted on zinc (Zn) sites), the lowest energy state involved antiferromagnetic ordering was preferred. However, they also noted that hole doping (nitrogen (N) substituted on oxygen (O) sites) caused stabilization in the ferromagnetic state [100]. These calculations are confirmed in their later work for $\text{Zn}_{1-x}\text{Mn}_x\text{O}$ ($x = 0.05, 0.10, 0.15, 0.20, 0.25$) by the same calculation methods [101].

Uspenskii *et al.* also reported a ground state preference for antiferromagnetic ordering for the case of $\text{Zn}_{0.875}\text{Mn}_{0.125}\text{O}$ [131].

Dietl *et al.* have performed several calculations concerning Mn-doped ZnO. The first, using the Zener Model, predicts room temperature ferromagnetic ordering for $\text{Zn}_{0.95}\text{Mn}_{0.05}\text{O}$ doped to contain $3.5 \times 10^{20} \frac{\text{holes}}{\text{cm}^3}$ [28]. These calculations are also cited along with predictions of T_C , which only Dietl seems to publish, in other articles [29, 30].

Iron: The *ab initio* calculations of Sato and Katayama-Yoshida also showed an energy preference for ferromagnetic ordering in $\text{Zn}_{1-x}\text{Fe}_x\text{O}$ ($x = 0.25$) [100]. This calculation was later expanded to confirm the results for $\text{Zn}_{1-x}\text{Fe}_x\text{O}$ ($x = 0.05 - 0.25$). This expanded report of their results also showed increasing preference for ferromagnetic ordering as Ga doping was increased up to 25% substitution on Zn lattice sites. Finally, they also showed that a spin-glass state is induced with light hole doping. However, in the $\text{Zn}_{0.95}\text{Fe}_{0.05}\text{O}$ and $\text{Zn}_{0.90}\text{Fe}_{0.10}\text{O}$, the ground state reverts to ferromagnetic ordering with N concentrations above 10% [101].

The LSDA calculations of Uspenskii *et al.* agree that ferromagnetic ordering yields the lowest energy configuration for $\text{Zn}_{0.875}\text{Fe}_{0.125}\text{O}$ [131].

Cobalt: Again, Sato and Katayama-Yoshida find that the ground state of $\text{Zn}_{1-x}\text{Co}_x\text{O}$ ($x = 0.25$) is ordered ferromagnetically [100]. These results are confirmed and expanded for $x = 0.05 - 0.25$ and the energy preference for ferromagnetism increases with electron doping. In the case of $\text{Zn}_{1-x}\text{Co}_x\text{O}$ the spin-glass state is not the lower energy state until a N concentration greater than 5% is reached at all levels of Co doping [101].

Uspenskii *et al.* obtained similar results for $\text{Zn}_{0.875}\text{Co}_{0.125}\text{O}$ finding that ferromagnetic ordering is the lower energy state.

Nickel: According to Sato and Katayama-Yoshida, $\text{Zn}_{1-x}\text{Ni}_x\text{O}$ ($x = 0.25$) was second only to V in its energy preference for ferromagnetic ordering [100]. Their later calculations confirm this result and show that ferromagnetic ordering becomes more preferred with increasing electron concentration up to about 10% Ga substitution on Zn sites in $\text{Zn}_{1-x}\text{Ni}_x\text{O}$ ($x = 0.05 - 0.25$). With increasing hole concentration only $\text{Zn}_{0.95}\text{Ni}_{0.05}\text{O}$ falls into the spin-glass state before hole (N) concentration rises above 5% [101].

Copper: Just as with Ti, Sato and Katayama-Yoshida predicted no preference of ordering for $\text{Zn}_{0.75}\text{Cu}_{0.25}\text{O}$. Again, this implies that one would expect paramagnetic behavior rather than any sort of magnetic ordering [100].

A.1.1.1 Gallium Nitride Theoretical Calculations

Manganese: Uspenskii *et al.* report LSDA calculations using the tight binding approximation for $\text{Ga}_{0.94}\text{Mn}_{0.06}\text{N}$. The results show a strong preference for ferromagnetic ordering in this compound and the energy difference between ferromagnetic and antiferromagnetic ordering that they calculate qualitatively agrees with a reported T_C of 940 K [117]. They also calculated that co-doping GaN with Mn and O to add electrons results in an energy preference for antiferromagnetic ordering in $\text{Ga}_{0.88}\text{Mn}_{0.06}\text{O}_{0.06}\text{N}$ [131].

Dietl *et al.* have used the Zener Model to calculate ordering preference and T_C for $\text{Ga}_{0.95}\text{Mn}_{0.05}\text{N}$ with $3.5 \times 10^{20} \frac{\text{holes}}{\text{cm}^3}$. These calculations showed that p-type $\text{Ga}_{0.95}\text{Mn}_{0.05}\text{N}$ should have a T_C well above room temperature [28, 30].

The linear muffin-tin orbital–tight binding (LMTO-TB) method of calculation was employed by Fong *et al.* to determine whether (Ga,Mn)N would demonstrate magnetic properties. They found that when substituted for Ga atoms, Mn atoms do prefer ferromagnetic alignment [34].

Iron: Fong *et al.* performed the same LMTO-TB calculations for Fe-doped GaN. Their results were similar with the prediction that Fe substituting on Ga sites would cause an even greater magnetic moment than Mn substitution [34].

A.2 Summary of Experimental Results

The transition metals listed below and noted in table A.1 have been used as dopants in ZnO and GaN to attempt to induce magnetic behavior. Each section details the available results along with growth methods and characterization techniques (details concerning these techniques are given in Chapter III).

A.2.1 Zinc Oxide Experimental Results

Scandium and Titanium: Ando *et al.* performed an experiment whereby pulsed laser deposition (PLD) was used to grow $\text{Zn}_{1-x}\text{Sc}_x\text{O}$ ($x = 0.026$) and $\text{Zn}_{1-x}\text{Ti}_x\text{O}$ ($x = 0.016$). The resulting films were characterized by measurements of their spectra of magnetic circular dichroism (MCD). The experiments showed “[n]o enhancement of the MCD amplitude as compared with that of ZnO” for $\text{Zn}_{1-x}\text{Sc}_x\text{O}$ and $\text{Zn}_{1-x}\text{Ti}_x\text{O}$ [5].

Vanadium: Ando *et al.* repeated the experiment detailed above for Sc and Ti using V as the magnetic dopant. Their results were similar: no enhancement of the MCD amplitude for $\text{Zn}_{1-x}\text{V}_x\text{O}$ ($x = 0.016$) [5].

Saeki *et al.* also fabricated $\text{Zn}_{1-x}\text{V}_x\text{O}$ by PLD. They used much higher concentrations of Vanadium ($x = 0.05 - 0.15$) and varied the concentration

to determine the effect of V concentration on magnetic behavior. Magnetic properties were measured using a SQUID magnetometer. The magnetometer revealed positive magnetization signals up to 350 K in the most heavily doped conductive material. Incidentally, the ZnO films were all *n*-type [99]. This research group at Osaka University also produced p-type V-doped ZnO films by growing material in an excited N₂ atmosphere. These films showed similar results: ferromagnetic properties were stronger with increasing V concentration and T_C s above 350 K [120].

Chromium: Ando *et al.* fabricated films of Zn_{1-x}Cr_xO ($x = 0.012$), but again found no increase in the amplitude of the MCD signal [5].

Although their experiments with V showed ferromagnetic behavior, Tabata *et al.* found that the Zn_{1-x}Cr_xO ($x = 0.05 - 0.15$) they grew did not exhibit ferromagnetic behavior [120].

Jin *et al.* grew Zn_{1-x}Cr_xO samples “with different doping concentrations” by combinatorial laser molecular beam epitaxy (CLMBE) [47]. The samples were characterized by magnetic resonance (MR). Positive MR was observed for Cr-doped ZnO, which indicates strong *s-d* exchange coupling causing spin splitting. They concluded, however, that this was not an indication of ferromagnetism [47].

Ueda *et al.* grew Zn_{1-x}Cr_xO ($x = 0.05 - 0.25$) by PLD. The material was made *n*-type by co-doping with aluminum (Al). Magnetic properties were measured by SQUID magnetometry, but Zn_{1-x}Cr_xO failed to exhibit ferromagnetic behavior [128].

Satoh and Kobayashi also grew *n*-type Zn_{1-x}Cr_xO ($x = 0.3$) by PLD. Magnetic measurements were made using a SQUID magnetometer, and showed that magnetization persists to temperatures above 400 K in the more conductive samples [102].

Manganese: In their growth of $\text{Zn}_{1-x}\text{Mn}_x\text{O}$ ($x = 0.010$), Ando *et al.* a sizeable MCD peak near the bandgap energy of ZnO (3.4 eV). This result indicates strong *sp-d* exchange interactions, which means that the material is a DMS. This characteristic was present at 5 K, but data concerning higher temperatures was absent for the Mn-doped sample [5].

The PLD-grown films of Tabata *et al.* did not show ferromagnetic behavior when doped with Mn for $x = 0.05 - 0.25$ [120]. Ueda *et al.* reported a lack of ferromagnetism for a very similar material [128].

Similarly, Jin *et al.* did not observe ferromagnetism in $\text{Zn}_{1-x}\text{Mn}_x\text{O}$ with unspecified doping concentrations despite positive MR readings [47].

Early work by Fukumura *et al.* grew films of $\text{Zn}_{1-x}\text{Mn}_x\text{O}$ ($x < 0.35$) co-doped with Al. The only magnetic measurements made on these films were MR measurements, which revealed “spin splitting enhanced by *s-d* exchange interaction” [37]. The article stopped short of making any claims concerning ferromagnetic ordering in the material. Later work by Fukumura *et al.* used SQUID magnetometry to evaluate a film of $\text{Zn}_{1-x}\text{Mn}_x\text{O}$ ($x = 0.36$). This p-type $\text{Zn}_{1-x}\text{Mn}_x\text{O}$ film did show a strong antiferromagnetic interaction [36].

Yoon *et al.* produced polycrystalline powders of $\text{Zn}_{1-x}\text{Mn}_x\text{O}$ ($x = 0.05, 0.10$) by both solid-state and liquid-phase reactions. Magnetization was measured using a SQUID magnetometer. The result was a demonstration of antiferromagnetic ordering at low temperatures [142].

Cheng and Chien report the growth of $\text{Zn}_{1-x}\text{Mn}_x\text{O}$ ($x = 0.07$) film by radio frequency (RF) magnetron sputtering. They used SQUID magnetometry to determine magnetic characteristics, but found no magnetic ordering—only paramagnetic behavior—even at temperatures as low as 5 K [20].

Sawicki *et al.* report measurements made with their self-constructed SQUID system on films of *n*-type (Al-doped) $\text{Zn}_{1-x}\text{Mn}_x\text{O}$ ($x = 0.07$). The authors conclude that the paramagnetic behavior exhibited is the result of com-

pensating ferromagnetic and antiferromagnetic ordering at temperatures below liquid helium (LHe) [103].

Jung *et al.* report the growth of $\text{Zn}_{1-x}\text{Mn}_x\text{O}$ ($x = 0.1, 0.3$) by laser molecular beam epitaxy (LMBE). The films were not co-doped with acceptors or donors resulting in insulating electrical properties. The magnetic properties of the films were measured by SQUID magnetometry and T_C s of 30 K and 45 K were observed for $\text{Zn}_{1-x}\text{Mn}_x\text{O}$ with $x = 0.1$ and $x = 0.3$, respectively. A pronounced hysteresis curve was also observed at 5 K for both concentrations, although more pronounced for the more heavily Mn-doped sample, which indicates ferromagnetic behavior in this DMS [50].

D. S. Kim *et al.* from Dongguk University recently reported the growth of $\text{Zn}_{1-x}\text{Mn}_x\text{O}$ ($x = 0.04, 0.07$) films by RF magnetron sputtering. Magnetic properties were measured using a SQUID magnetometer. A magnetic hysteresis curve is observed for the $\text{Zn}_{1-x}\text{Mn}_x\text{O}$ ($x = 0.07$) film at 5 K and a T_C of 70 K is observed for this film. The $\text{Zn}_{1-x}\text{Mn}_x\text{O}$ ($x = 0.04$) film showed a lower T_C of 55 K [53].

Iron: Jin *et al.* grew $\text{Zn}_{1-x}\text{Fe}_x\text{O}$ with unspecified doping concentrations. Their MR measurements indicated a negligible *s-d* exchange interaction, and no evidence of ferromagnetism [47].

The polycrystalline $\text{Zn}_{1-x}\text{Fe}_x\text{O}$ ($x = 0.05$) powders of Yoon *et al.* again only showed an antiferromagnetic interaction at low temperatures [142].

Iron/Cobalt Co-Doped: Using reactive magnetron co-sputtering, Cho *et al.* produced films of $\text{Zn}_{1-x}(\text{Co}_{0.5}\text{Fe}_{0.5})_x\text{O}$ ($x = 0.05, 0.10, 0.15$). Rapid thermal annealing (RTA) was also performed under vacuum and found to increase the spontaneous magnetization of the material as well as make the hysteretic behavior more pronounced for the $\text{Zn}_{1-x}(\text{Co}_{0.5}\text{Fe}_{0.5})_x\text{O}$ ($x = 0.15$) material. The magnetization measurements were made with a SQUID magnetometer at a sam-

ple temperature of 300 K, thus confirming room temperature ferromagnetism in this DMS [21].

Iron/Copper Co-Doped: Han *et al.* formed films of $\text{Zn}_{0.95-y}\text{Fe}_{0.05}\text{Cu}_y\text{O}$ by standard ceramic methods in order to study the materials in bulk rather than as thin films. The Cu co-doping, introducing free holes, allowed them to achieve a T_C of 550 K as indicated by a plot of magnetization versus temperature generated by SQUID magnetometry [42].

Cobalt: Ando *et al.* prepared films of $\text{Zn}_{1-x}\text{Co}_x\text{O}$ ($x = 0.012, 0.016$) by PLD. These films showed negative MCD spectral peaks at 5 K which disappeared by 270 K, indicating a strong *sp-d* exchange interaction at low temperatures. Effective values for the Landé splitting factor (g) were obtained of 4 and 9 for $x = 0.012$ and $x = 0.016$, respectively. The authors attribute the small magnitude of these g values to their use of lattice mismatched substrates [5].

Tabata *et al.* also grew $\text{Zn}_{1-x}\text{Co}_x\text{O}$ ($x = 0.05 - 0.25$) films by PLD. They achieved a T_C of 300 K for $\text{Zn}_{1-x}\text{Co}_x\text{O}$ ($x = 0.15$) and a T_C of 280 K for $x = 0.05, 0.25$. They also noticed a hysteresis loop for the $\text{Zn}_{1-x}\text{Co}_x\text{O}$ ($x = 0.05$) sample at 6 K. Unfortunately, their results were not consistent: “reproducibility of the method was poor (less than 10 %)” [120]. The similarly produced and characterized $\text{Zn}_{1-x}\text{Co}_x\text{O}$ ($x = 0.05 - 0.25$) by Ueda *et al.* showed virtually identical results [128].

The CLMBE-grown $\text{Zn}_{1-x}\text{Co}_x\text{O}$ ($x=?$) films of Jin *et al.* showed MR peak fields decreasing with increasing temperature between 2 K and 5 K. This indicates a strong *s-d* exchange coupling, but does not indicate ferromagnetism in this sample [47].

$\text{Zn}_{1-x}\text{Co}_x\text{O}$ ($x = 0.25$) was grown by J. H. Kim *et al.* using PLD. The inhomogeneous films were measured by a vibrating sample magnetometer (VSM), and a well-defined magnetic hysteresis loop was observed at 300 K, but this may have been due to ferromagnetic Co precipitates [54].

The polycrystalline $\text{Zn}_{1-x}\text{Co}_x\text{O}$ ($x = 0.05 - 0.15$) powders synthesized by Yoon *et al.* again failed to show the expected ferromagnetic behaviors. In fact, at low temperature their powders are characterized by SQUID magnetometry as an antiferromagnetic interaction [142].

H.-J. Lee *et al.* formed $\text{Zn}_{1-x}\text{Co}_x\text{O}$ ($0.05 \leq x \leq 0.25$) powders by sol-gel processing. Their measurements taken with a SQUID magnetometer showed magnetization and hysteresis curves for all Co concentrations between 5 and 25% inclusive at temperatures up to 350 K.

Most recently, Rode *et al.* used PLD to produce thin films of $\text{Zn}_{1-x}\text{Co}_x\text{O}$ ($x = 0.25$). The magnetic properties of these films were measured by SQUID magnetometry. A pronounced magnetic hysteresis was apparent at 10 K and magnetization of the sample remained evident up to 300 K [97].

Nickel: Ando *et al.* used PLD to form films of $\text{Zn}_{1-x}\text{Ni}_x\text{O}$ ($x = 0.030$). An enhanced MCD signal was detected for this material, indicating a strong *sp-d* exchange interaction, but again no measurements were made that could confirm ferromagnetic behavior [5].

Tabata *et al.* reported that their PLD-grown, p-type films of $\text{Zn}_{1-x}\text{Ni}_x\text{O}$ ($x = 0.05 - 0.15$) did not show any indications of ferromagnetism [120]. For *n*-type, PLD-grown films of $\text{Zn}_{1-x}\text{Ni}_x\text{O}$ ($x = 0.05 - 0.25$), Ueda *et al.* reported identical results [128].

Wakano *et al.* have also fabricated films of $\text{Zn}_{1-x}\text{Ni}_x\text{O}$ ($x = 0.01, 0.03, 0.05, 0.10, 0.25$) doped *n*-type with Al or lithium (Li) by PLD. SQUID measurements confirmed that $\text{Zn}_{1-x}\text{Ni}_x\text{O}$ ($x = 0.03 - 0.25$) showed ferromagnetism at 2K and maintained superparamagnetism up to 300 K for all films [134].

Copper: The $\text{Zn}_{0.997}\text{Cu}_{0.003}\text{O}$ PLD-grown films of Ando *et al.* also showed a pronounced MCD signal near the bandgap of ZnO. This signal indicates *sp-d* exchange interaction, but magnetic measurements to confirm ferromagnetism were not made [5].

A.2.2 Gallium Nitride Experimental Results

Vanadium: J. S. Lee *et al.* studied the the effect of transition metal ion implantation on magnesium (Mg) doped (p-type) GaN. The implantation doses were $3 \times 10^{16} \text{cm}^{-2}$ and $5 \times 10^{16} \text{cm}^{-2}$ resulting in peak concentrations of 3 and 5 at. %, respectively. Their fabrication process includes a short annealing step to mitigate implantation damage without formation of TM clusters. Magnetization measurements taken using a SQUID magnetometer indicate only paramagnetic behavior for the V-doped material [62].

Chromium: Cr-implanted p-GaN was also fabricated by J. S. Lee *et al.* at the same implant doses and peak concentrations as noted above for V. The magnetization measurements for these samples indicated strong exchange interactions, but did not indicate ferromagnetism in the classical sense because of low carrier concentrations in these samples. The magnetization manifested in (Ga,Cr)N persisted to a temperature of 320 K [62].

Hashimoto *et al.* were the first to report the growth of $\text{Ga}_{1-x}\text{Cr}_x\text{N}$ (unreported Cr concentration) by electron-cyclotron-resonance (ECR) plasma-assisted MBE. The magnetization versus magnetic field (M-H) plots obtained by SQUID magnetometry clearly show hysteresis and saturation at 300 K and the magnetization of the material persists to the temperature limit of the measuring system, 400 K [43].

Park *et al.* report the growth of $\text{Ga}_{0.97}\text{Cr}_{0.03}\text{N}$ single crystals by the flux method. Magnetic measurements were taken using a SQUID system and indicated a T_C of 280 K. Magnetic hysteresis curves were also evident at 150 K and 250 K in this material [85].

$\text{Ga}_{1-x}\text{Cr}_x\text{N}$ with an unreported Cr concentration was grown using ECR plasma-assisted MBE by Zhou *et al.* Magnetic measurements were made using a SQUID system and a T_C greater than 400 K (equipment limit reached) was

reported and magnetic hysteresis and saturation were observed at all temperatures investigated between 10 and 400 K [147].

Manganese: Theodoropoulou *et al.* report the formation of $\text{Ga}_{1-x}\text{Mn}_x\text{N}$ ($x = 0.001 - 0.05$) by ion implantation into p-GaN films and subsequent annealing. SQUID magnetometry showed magnetic hysteresis curves at low temperatures and $T_C < 250$ K for implantation doses resulting in peak concentrations between 3 and 5 at. % [126]. This confirms their earlier work, where ion-implanted p-GaN shows a T_C of about 250 K for Mn concentrations of 3–5 at. % [125].

K. P. Lee *et al.* also doped p-GaN with Mn to about 0.1–5 at. % by ion implantation and annealing. The more heavily doped samples displayed ferromagnetic behavior, as measured by a SQUID magnetometer, below approximately 250 K [63].

Kuwabara *et al.* grew $\text{Ga}_{1-x}\text{Mn}_x\text{N}$ ($x < 0.02$) by RF-plasma-assisted MBE. SQUID magnetometer measurements, however, indicated only paramagnetic behavior for (Ga,Mn)N, probably due to a lack of free carriers [59].

Zajac *et al.* grew films of $\text{Ga}_{1-x}\text{Mn}_x\text{N}$ ($x < 0.1$) by the ammono-thermal technique [31] as well as by reactions of bulk crystals at high temperature in an ammonia atmosphere. Using SQUID magnetometry, they observed paramagnetic behavior from 2–300 K. There was also some AFM ordering noted [145]. Zajac *et al.* report identical results for their earlier production of $\text{Ga}_{1-x}\text{Mn}_x\text{N}$ ($x < 0.005$) by the ammono-thermal method [144].

Reed *et al.* formed films of $\text{Ga}_{1-x}\text{Mn}_x\text{N}$ (concentrations unreported) by diffusion doping. They used VSM and extraordinary Hall effect (EHE) measurements to determine magnetic characteristics. These measurements showed ferromagnetic behavior up to room temperature (~ 275 K) [94]. Later work by Reed, et al used EHE on similarly produced samples to achieve T_C s up to 370 K depending on diffusion conditions [95].

Sonoda *et al.* grew $\text{Ga}_{1-x}\text{Mn}_x\text{N}$ ($x = 0.06, 0.09$) by MBE. SQUID magnetometry was used to determine the magnetic nature of these samples. The $\text{Ga}_{0.94}\text{Mn}_{0.06}\text{N}$ showed ferromagnetic behaviors at 300 K. Ferromagnetism persisted in $\text{Ga}_{0.91}\text{Mn}_{0.09}\text{N}$ up to 750 K, the temperature limit of the measurement equipment, and the estimated $T_C = 940$ K [117]. In later work by Sonoda *et al.* they grew $\text{Ga}_{1-x}\text{Mn}_x\text{N}$ ($x < 0.068$) doped p-type by Ammonia-MBE. They report ferromagnetism, as evidenced by hysteresis curves obtained from SQUID magnetometry, that persists to 400 K in $\text{Ga}_{0.932}\text{Mn}_{0.068}\text{N}$ [116].

$\text{Ga}_{1-x}\text{Mn}_x\text{N}$ ($x = 0.03 - 0.12$) was grown using MBE by Thaler *et al.* SQUID magnetometry revealed ferromagnetic behavior, even clear hysteresis, at temperatures up to 300 K [123].

Shon *et al.* implanted a thin film of GaN with Mn ions to obtain a film of $\text{Ga}_{0.093}\text{Mn}_{0.07}\text{N}$. SQUID magnetometry at 5 K was used to measure the magnetic properties of this film, and showed magnetic hysteresis. The researchers blame this rather weak performance on incomplete decomposition of Mn clusters during implantation [111]. Further implantation/annealing work by Shon *et al.* had a better result with ferromagnetic behavior persisting to ~ 270 K [112]. Further work by Shon *et al.* with similar samples (MOCVD GaN implanted with Mn ions) confirmed this result as well as using photoluminescence (PL) to characterize implantation damage and annealing repair [113].

Ando *et al.* grew $\text{Ga}_{0.932}\text{Mn}_{0.068}\text{N}$ by the AMMONO method [31]. They used low-temperature MCD to determine that there is significant $s,p-d$ exchange interactions. These indications were supported by SQUID measurements that showed ferromagnetic (hysteretic) behavior at 300 K [4].

Overberg *et al.* report on the characteristics of n -type $\text{Ga}_{0.93}\text{Mn}_{0.07}\text{N}$ grown by MBE. SQUID magnetometry revealed hysteretic behavior at 10 K and EHE measurements confirmed ferromagnetic behavior. Although the anomalous Hall effect vanished at 25 K (indicating $10 \text{ K} < T_C < 25 \text{ K}$), this display of

ferromagnetism was significant because it demonstrated that electrons in this n -type material could mediate the exchange interaction [83].

Iron: Films of $\text{Ga}_{1-x}\text{Fe}_x\text{N}$ with Fe concentration $\sim 10^{19}\text{cm}^{-3}$ were grown using ECR MBE by Akinaga *et al.* Magnetic measurements were made using a SQUID magnetometer and showed a ferromagnetic contribution in the most highly doped film at temperatures below 100 K [1].

Theodoropoulou *et al.* implanted films of p-GaN with Fe to peak concentrations of 0.1 to 5 at. % and subsequently annealed them. For the samples doped with 3–5 at. % Fe, SQUID magnetometry again showed a clear hysteresis curve at 10 K and $T_C < 150$ K [126]. Later work by this same group reported $T_C \simeq 250$ K for similarly fabricated $\text{Ga}_{0.97}\text{Fe}_{0.03}\text{N}$ [124].

K. P. Lee *et al.* fabricated films of $\text{Ga}_{1-x}\text{Fe}_x\text{N}$ ($x = 0.001 - 0.05$) by ion implantation into p-GaN and subsequent annealing. SQUID magnetometry revealed ferromagnetic behavior below 200 K with T_C falling with lower Fe concentrations [63].

The MBE-grown $\text{Ga}_{1-x}\text{Fe}_x\text{N}$ ($x < 0.02$) films of Kuwabara *et al.* did show some saturation behavior when subjected to a magnetic field, but only show remanent magnetization at temperatures at or below 10 K. The authors attribute this behavior to superparamagnetic inclusions in the in the doped epitaxial layer [59].

Cobalt: J. S. Lee *et al.* also performed experiments involving the implantation of Co into GaN at 3 and 5 at. %. Much as in their Cr-doped material, SQUID magnetometry of Co-implanted samples revealed ferromagnetic-like behavior up to 270 K, although (Ga,Co)N did show a higher magnetic moment than (Ga,Cr)N at the lowest temperatures explored [62].

*Appendix B. Secondary Phase Concerns in
Transition-Metal-Implanted ZnO, GaN, and AlGaN*

Compound	Type of Magnetism Displayed	Magnetic Transition Temperature (K)	Reference(s)
For ZnO:Mn			
Mn	Antiferromagnetic	100	[75]
MnO	Antiferromagnetic	122	[15, 121]
MnO ₂	Antiferromagnetic	84	[121]
	Antiferromagnetic	17	[39]
	Weakly Ferromagnetic	44	[39]
Mn ₃ O ₄	Ferromagnetic	1443	[136]
	Ferromagnetic	42	[75]
	Ferrimagnetic	46	[39]
ZnMn ₂ O ₄	Ferromagnetic	1298	[136]
Zn _{0.9} Mn _{0.1} O	Ferromagnetic	30	[50]
Zn _{0.7} Mn _{0.3} O	Ferromagnetic	45	[50]
MnZn (15% Mn)	Ferromagnetic	150	[121]
For ZnO:Cr			
Cr	Antiferromagnetic	311	[82]
CrO ₂	Ferromagnetic	387	[141]
ZnCr ₂ O ₄	Antiferromagnetic	14.4	[143]
Cr ₂ O ₃	Antiferromagnetic	308	[110]

Compound	Type of Magnetism Displayed	Magnetic Transition Temperature (K)	Reference(s)
For ZnO:Ni			
Ni	Ferromagnetic	631	[108]
NiO	Antiferromagnetic	525	[76]
Ni ₂ O ₃	Antiferromagnetic	523	[96]
For ZnO:Fe			
Fe	Ferromagnetic	1043	[108]
Fe ₂ O ₃	Ferromagnetic	893	[108]
Fe ₃ O ₄	Ferrimagnetic	848	[7]
Fe _x O	Antiferromagnetic	200	[2]
ZnFe ₂ O ₄	Paramagnetic		[115]
For GaN:Mn or AlGaN:Mn			
Mn	Antiferromagnetic	100	[75]
Mn ₂ Ga	Ferromagnetic	690	[82]
ε-Mn ₃ Ga	Ferromagnetic	743	[82]
ζ-Mn ₅ Ga ₈ (Mn _{0.6} Ga _{0.4})	Ferromagnetic	210	[82]
MnGa	Ferromagnetic	> 300	[82]
Mn ₄ N	Ferromagnetic	745	[82]

Compound	Type of Magnetism Displayed	Magnetic Transition Temperature (K)	Reference(s)
For GaN:Cr or AlGaN:Cr			
Cr	Antiferromagnetic	311	[82]
CrN	Antiferromagnetic	273	[82]
Cr ₂ N	Ferromagnetic(?)	Not Ferromagnetic Between 85 and 500 K	[82]
CrGa	Antiferromagnetic	300–650 Depending on Ga Content	[60]
CrAl	Antiferromagnetic	200–900 Depending on Al Content	[60]
For GaN:Ni or AlGaN:Ni			
Ni	Ferromagnetic	627	[108]
Ni ₃ Al	Ferromagnetic	41	[13]
Ni ₃ Ga	Similar to Ni ₃ Al		[13]

Appendix C. Detailed Summary of Magnetic Behavior

This appendix provides a more detailed numerical results overview of the data summarized in section 8.1, particularly the samples that showed weak or conflicting indications of ferromagnetism (items 5–8 below).

Through magnetic hysteresis measurements, it has been found that some of the material combinations clearly showed strong ferromagnetism, others showed marginal evidence of ferromagnetism, and several did not demonstrate ferromagnetism at all, rather they were superparamagnetic or diamagnetic. The experiments accomplished in connection with this research show that there are a variety of options available for implantation-based fabrication of DMS material with ferromagnetism persisting to room temperature. Among the most promising materials for creating spintronic devices using ion implantation are Mn-implanted p -GaN, Cr-implanted $\text{Al}_{0.35}\text{Ga}_{0.65}\text{N}$, and Fe-implanted ZnO nanotips grown on sapphire. In these three cases, the implantation of a transition metal and subsequent annealing produce signatures of above room temperature ferromagnetism that far outstrip any signs seen in the as-grown samples. The optimum anneal temperatures found in these samples were also confirmed by PL or CL measurements.

The specific findings from this work are as follows.

1. In Mn-implanted p -GaN, a coercive field width (H_c) as high as 468 Oe and a remanent field (B_R) over 20% of the saturation magnetization (M_S) of 1.75×10^{-5} emu were achieved at 5 K for the sample implanted at 200 keV with a dose of $5 \times 10^{16} \frac{\text{ions}}{\text{cm}^2}$ and annealed at an optimum annealing temperature of 725 °C for 5 minutes in flowing nitrogen gas (N_2). The ferromagnetism of this sample persisted with H_c and B_R values of 186 Oe and 11% of the M_S of 3.2×10^{-5} emu, at room temperature, and the the Curie temperature (T_C) is estimated to be above 350 K. The ferromagnetic dilute magnetic semiconductor behavior has been confirmed by the temperature dependent field-cooled (FC) and zero-field-cooled (ZFC) magnetization measurements made on this sample.

2. For Cr-implanted $\text{Al}_{0.35}\text{Ga}_{0.65}\text{N}$, coercive fields of 414 and 249 Oe were obtained through magnetic hysteresis measurements at 5 and 300 K, respectively, on a sample implanted with $5 \times 10^{16} \frac{\text{ions}}{\text{cm}^2}$ at 200 keV and annealed at an optimal anneal temperature of 775 °C for 5 minutes in flowing N_2 . The remanent field also remained greater than 20% of the M_S of 10^{-4} (5 K) and 6×10^{-5} emu (300 K) at both 5 and 300 K, and T_C for this sample is estimated at or just above 350 K for this sample. FC and ZFC magnetization measurements of this sample also confirm the presence of DMS-based ferromagnetism persisting to room temperature.
3. Fe-implanted ZnO nanotips grown on $c\text{-Al}_2\text{O}_3$ showed a coercive field width of 317 Oe at 5 K and 209 Oe at 300 K for the sample implanted at 200 keV to a dose of $5 \times 10^{16} \frac{\text{ions}}{\text{cm}^2}$ and annealed under optimal annealing conditions of 700 °C for 20 minutes in flowing oxygen gas (O_2). The remanent fields in this material are 19 and 12% of M_S (7.1 and 2.3×10^{-5} emu) for measurements made at 5 and 300 K, respectively. Temperature-dependent magnetization measurements confirm that this material demonstrates ferromagnetism consistent with that expected from a dilute magnetic semiconductor of good quality.
4. Mn-implanted $\text{Al}_{0.35}\text{Ga}_{0.65}\text{N}$ showed H_c of 409 and 199 Oe at measurement temperatures of 5 and 300 K when implanted at 200 keV to a dose of $5 \times 10^{16} \frac{\text{ions}}{\text{cm}^2}$ and annealed at 775 °C in flowing nitrogen. B_R values at 5 and 300 K were 14×10^{-6} and 7×10^{-6} emu, respectively, for this sample. Although the temperature-dependent magnetization measurements show signs of ferromagnetism, they also indicate that there may be a weak spin-glass phase present in the material. Therefore further study is necessary to determine the nature and usefulness, from a spintronic perspective, of this material.
5. Several other cases show signs of ferromagnetism and in fact demonstrate increased ferromagnetism over the as-grown and as-implanted samples, but they are not as convincing as the most promising samples. They do not demonstrate a clear trend of coercive or remanent field strength as a function of anneal-

ing temperature, and thus show no optimum annealing temperature. However, these materials have potential for use in DMS-based devices. They include

- (a) Cr-implanted *p*-GaN has maxima in H_c at each end of the range of annealing temperatures (650 °C- 775 degC) and B_R maxima occur at different anneal temperatures of 750 and 700 °C for 5 and 300 K measurements, respectively.
 - (b) For the Fe-implanted ZnO nanotips grown on quartz, the highest coercive and remanent fields occur at both ends of the annealing temperature range of 650 to 800 °C with lower values at temperatures between these. The temperature-dependent magnetization also shows variable separation between FC and ZFC magnetization that does not seem to be sensitive to annealing conditions.
 - (c) Mn-implanted ZnO nanotips grown on quartz: They show coercive and remanent field maxima at both 5 K and room temperature when the sample is annealed at 750 °C for 10 minutes. Unfortunately, this sample shows little FC–ZFC separation, indicating that the observed ferromagnetism may be due to background effects rather than arising from the ZnO nanotips. The sample annealed at 675 °C for 20 minutes shows the greatest difference FC–ZFC magnetization as well as the best indication of implant damage recovery as seen in photoluminescence.
6. The following samples show signs of ferromagnetism, but slow onset of saturation or low M_S values prevent meaningful determination and comparison among among samples annealed at various temperatures of the the strength of ferromagnetism. These samples can be characterized as ferromagnetic, but engineering DMS-based devices with these materials will be impeded by the lack of useable H_c and B_R values and the variability in M_S .
- (a) $Al_{0.35}Ga_{0.65}N$ implanted with Ni at 200 keV to a dose of $3 \times 10^{16} \frac{\text{ions}}{\text{cm}^2}$: This material shows shows clear hysteresis, and maximum coercive field widths

of approximately 350 and 200 in the 725 to 750 °C annealing range for a 5 minute anneal. Unfortunately, this value can only be estimated because M_S is lower in this range than in the rest of the samples, which causes errors when the diamagnetic background is subtracted.

- (b) The second epitaxial ZnO wafer implanted with Mn also shows clear hysteresis when annealed at 700 °C for 10 minutes, but has a maximum M_S when annealed at 650 °C for 10 minutes. The separation between FC and ZFC magnetization was also significantly improved over the as-implanted sample for annealing at 675 °C for 10 minutes.
 - (c) The ZnO thin film implanted with Cr clearly shows magnetic hysteresis when annealed at 725 and 750 °C for 10 minutes. Unfortunately, the strength of the diamagnetic background makes it difficult to determine accurate H_c and B_R values. These samples also fail to demonstrate good separation and low-temperature tracking of FC and ZFC magnetization measurements, although the sample annealed at 725 °C does have the greatest FC–ZFC separation seen in this material. The signs of ferromagnetism in this material are encouraging for DMS device work.
7. The following samples showed signs of ferromagnetism that were not consistent across the different indicators of ferromagnetism in that an annealing condition that produces a strong coercive field is the same condition that gives the weakest remanent field or FC–ZFC divergence. This is a signal that these materials are not useful for DMS device fabrication under the conditions used in this work.
- (a) Ni-implanted *p*-GaN showed coercive field widths of 566 and 339 Oe at 5 and 300 K, respectively when implanted with a dose of $3 \times 10^{16} \frac{\text{ions}}{\text{cm}^2}$ Ni atoms at 200 keV and annealed at 725 °C for 5 minutes. B_R , however, is markedly lower for this sample than for those annealed at 650, 675 and 750 °C for 5 minutes. The widest separation between FC and ZFC magnetization occurs in the sample annealed at 725 °C, but the two magnetization curves

also diverge at low temperature, which contraindicates ferromagnetism. These indications point to competing magnetic phases in this material, which will render it difficult to use in DMS-based devices.

- (b) ZnO from the first epitaxial growth implanted with Mn at a dose of $5 \times 10^{16} \frac{\text{ions}}{\text{cm}^2}$ shows coercive and remanent fields across the range of annealing conditions that do not seem to be sensitive to temperature, with the exception that the sample annealed at 675 °C for 20 minutes is much weaker than the rest in both H_c and B_R . Although it is weakest in variable field measurements, the sample annealed at 675 °C for 20 minutes is the only sample in which FC–ZFC separation appreciably greater than that for the as-implanted sample is achieved. This inconsistency calls into question the true nature of the magnetism observed in this sample.
 - (c) ZnO implanted with Ni to a dose of $3 \times 10^{16} \frac{\text{ions}}{\text{cm}^2}$ yields maximum coercivity when annealed at 725 °C and maximum remanency when annealed at 700 °C for 10 minutes. These coercive and remanent field values do not trend with annealing temperature, even though there is variability of field strengths among the different annealing temperatures. Added to this is the fact that only the as-implanted and annealed at 650 degC samples show FC–ZFC tracking at low temperature and that the damage recovery evident in cathodoluminescence measurements does not trend with annealing temperature. These inconsistencies indicate that ZnO:Ni fabricated as described in this work will not produce reliable DMS material.
8. The following samples did not show indications of magnetic ordering. One showed only linear magnetic properties (diamagnetism and paramagnetism) and two others showed superparamagnetism (saturation without hysteretic separation), which most likely results from the presence of a spin-glass phase where magnetic ordering is “frozen” in a non-equilibrium configuration at low temperatures. These materials do not have properties that are useful for fabricating a room-temperature DMS-based device.

- (a) ZnO nanotips grown on sapphire and implanted with Mn to a level of $5 \times 10^{16} \frac{\text{ions}}{\text{cm}^2}$ show mostly spin-glass behavior, and only the sample annealed at 750 °C for 10 minutes shows hysteretic separation at low temperature. None of the other samples show hysteretic separation, although saturation is clear in all of the annealed samples. The spin-glass behavior is further confirmed by the fact that magnetic hysteresis decays completely at room-temperature.
- (b) The epitaxial ZnO from the first growth that is implanted with Fe to a level of $5 \times 10^{16} \frac{\text{ions}}{\text{cm}^2}$ shows the strongest low-temperature H_c and one of the strongest B_{RS} observed in this work. Unfortunately, the magnetic hysteresis properties do not persist to room temperature and in fact H_c and B_R for this sample are lower than for most of the other samples at room temperature. The divergence of FC and ZFC magnetization curves at low temperature confirming that this material contains a spin-glass magnetic phase which dominates any ferromagnetism that might be present.
- (c) The sample in which ferromagnetism is most glaringly absent is the ZnO nanotips grown on glass and implanted with Fe to level of $5 \times 10^{16} \frac{\text{ions}}{\text{cm}^2}$. Because the paramagnetic background is so dominant at low temperatures, values of H_c and B_R for these samples are meaningless. Temperature-dependent magnetization measurements confirm that this sample does not demonstrate magnetic ordering by the lack of separation between FC and ZFC magnetization for all annealing conditions.

These brief results lead to the conclusion that DMS-type ferromagnetism is possible in TM-implanted wide-bandgap semiconductors. Although there are certain pitfalls and some materials that show a lack of ordering, based on the results of this research, materials can be fabricated with reasonable effort that will allow spintronic devices to be realized.

Bibliography

1. Akinaga, H., S. Németh, J. De Boeck, L. Nistor, H. Bender, G. Borghs, H. Ofuchi, and M. Oshima. “Growth and characterization of low-temperature grown GaN with high Fe doping,” *Applied Physics Letters*, 77(26):4377–4379 (December 2000).
2. Alvarado, S. F., M. Erbudak, and P. Munz. “Final-state effects in the 3d photoelectron spectrum of Fe₃O₄ and comparison with Fe_xO,” *Physical Review B*, 14(7):2740–2745 (October 1976).
3. Ando, K. *Magneto-Optics* (First Edition), chapter 7: Magneto-Optics of Diluted Magnetic Semiconductors: New Materials and Applications, 211–244. Springer Series in Solid-State Sciences, Berlin: Springer, 2000.
4. Ando, K. “Magneto-optical studies of *s,p-d* exchange interactions in GaN:Mn with room-temperature ferromagnetism,” *Applied Physics Letters*, 82(1):100–102 (January 2003).
5. Ando, K., H. Saito, Z. Jin, T. Fukumura, M. Kawasaki, Y. Matsumoto, and H. Koinuma. “Magneto-optical properties of ZnO-based diluted magnetic semiconductors,” *Journal of Applied Physics*, 89(11):7284–7286 (June 2001).
6. Antony, J., S. Pendyala, A. Sharma, D. Meyer, and Y. Qiang. “Ferromagnetism in Ti-Doped ZnO Nanoclusters.” Oral presentation to American Physical Society March meeting: Session P10-7, March 2005.
7. Arrott, A. “Criterion for Ferromagnetism from Observations of Magnetic Isotherms,” *Physical Review*, 108(6):1394–1396 (December 1957).
8. Ashcroft, N. W. and N. D. Mermin. *Solid State Physics* (First Edition). Philadelphia: Saunders College, 1976.
9. Baik, J. M., Y. Shon, T. W. Kang, and J.-L. Lee. “Enhancement of magnetic properties by nitrogen implantation tto Mn-implanted *p*-type GaN,” *Applied Physics Letters*, 84(7):1120–1122 (February 2004).
10. Barabash, R. I. *Defect and Microstructure Analysis by Diffraction* (First Edition), 10. International Union of Crystallography Monographs on Crystallography, chapter 8, 127–140. New York: Oxford University Press, 1999.
11. Baxter, J. B., F. Wu, and E. S. Aydil. “Growth mechanism and characterization of zinc oxide hexagonal columns,” *Applied Physics Letters*, 83(18):3797–3799 (November 2003).
12. Bean, C. P. “Hysteresis Loops of Mixtures of Ferromagnetic Micropowders,” *Journal of Applied Physics*, 26(11):1381–1383 (November 1955).
13. Bernhoeft, N. R., S. M. Hayden, G. G. Lonzarich, D. M. Paul, and E. J. Lindley. “Dispersive Magnetic Density Fluctuations in Ni₃Ga,” *Physical Review Letters*, 62(6):657–660 (February 1989).

14. Boemare, C., T. Monteiro, M. J. Soares, J. G. Guilherme, and E. Alves. "Photoluminescence studies in ZnO samples," *Physica B*, 308-310:985–988 (December 2001).
15. Bradley, F. N. *Materials for Magnetic Functions* (First Edition). New York: Hayden, 1971.
16. Bremser, M. D., W. G. Perry, T. Zheleva, N. V. Edwards, O. H. Nam, N. Parikh, D. E. Aspnes, and R. F. Davis. "Growth, Doping and Characterization of $\text{Al}_x\text{Ga}_{1-x}\text{N}$ Thin Film Alloys on 6H-SiC(0001) Substrates," *Material Research Society Internet Journal of Nitride Semiconductor Research*, 1:8 (September 1996). Available Online at <http://nsr.mij.mrs.org/1/8/manuscript.pdf>.
17. Bube, R. H. *Electrons in Solids: An Introductory Survey* (Third Edition), chapter 11, 242–265. Boston: Academic Press, Inc., 1992.
18. Burkhard, G., H.-A. Engel, and D. Loss. "Spintronics and Quantum Dots for Quantum Computing and Quantum Communication," *Fortschritte der Physik*, 48(Special Issue on Experimental Proposals for Quantum Computing):886–965 (2000). Available at <http://theorie5.physik.unibas.ch/qcomp/qcomp.html>.
19. Chakrabarti, S., D. Ganguli, and S. Chaudhuri. "Photoluminescence of ZnO nanocrystallites confined in sol-gel silica matrix," *Journal of Physics D: Applied Physics*, 36(2):146–151 (January 2003).
20. Cheng, X. M. and C. L. Chien. "Magnetic properties of epitaxial Mn-doped ZnO thin films," *Journal of Applied Physics*, 93(10):7876–7878 (May 2003).
21. Cho, Y. M., W. K. Choo, H. Kim, D. Kim, and Y. Ihm. "Effects of rapid thermal annealing in the ferromagnetic properties of sputtered $\text{Zn}_{1-x}(\text{Co}_{0.5}\text{Fe}_{0.5})_x\text{O}$ thin films," *Applied Physics Letters*, 80(18):3358–3360 (May 2002).
22. Das Sarma, S., J. Fabian, X. Hu, and I. Žutić. "Issues, Concepts, and Challenges in Spintronics." *58th Device Research Conference*. 95–98. Denver, CO: IEEE, June 2000.
23. Datta, S. and B. Das. "Electronic analog of the electro-optic modulator," *Applied Physics Letters*, 56(7):665–667 (February 1990).
24. Daughton, J. "Spin-Dependent Sensors," *Proceedings of the IEEE*, 91(5):681–686 (May 2003).
25. Dhar, S., O. Brandt, A. Trampert, K. J. Friedland, Y. J. Sun, and K. H. Ploog. "Observation of spin-glass behavior in homogeneous (Ga,Mn)N layers grown by reactive molecular-beam epitaxy," *Physical Review B*, 67(16):16205 (April 2003).
26. Dietl, T. "From Magnetic Polarons to Ferromagnetism," *Acta Physica Polonica A*, 94(2):111–123 (1998).

27. Dietl, T., F. Matsukura, and H. Ohno. "Ferromagnetism of magnetic semiconductors: Zhang-Rice limit," *Physical Review B*, 66(3):033203–1–033203–4 (July 2002).
28. Dietl, T., H. Ohno, F. Matsukura, J. Cibert, and D. Ferrand. "Zener Model Description of Ferromagnetism in Zinc-Blende Magnetic Semiconductors," *Science*, 287(5455):1019–1022 (February 2000).
29. Dietl, T., M. Sawicki, L. V. Khoi, J. Jaroszyński, P. Kossacki, J. Cibert, D. Ferrand, S. Tatarenko, and A. Wasiela. "Ferromagnetism in II-VI Compounds," *Physica Status Solidi B*, 229(2):665–672 (January 2002).
30. Dietl, T. "Ferromagnetic semiconductors," *Semiconductor Science and Technology*, 17(4):377–392 (April 2002).
31. Dwiliński, R., R. Doradziński, J. Garczyński, L. Sierzputowski, J. M. Baranowski, and M. Kamińska. "AMMONO method of GaN and AlN production," *Diamond and Related Materials*, 7(9):1348–1350 (September 1998).
32. Ferrand, D., A. Wasiela, S. Tatarenko, J. Cibert, G. Richter, P. Grabs, G. Schmidt, L. W. Molenkamp, and T. Dietl. "Applications of II-VI diluted magnetic semiconductors for magneto-electronics," *Solid State Communications*, 119(4-5):237–244 (July 2001).
33. Fischer, S., G. Steude, D. M. Hofmann, F. Kurth, F. Anders, M. Topf, B. K. Meyer, F. Bertram, M. Schmidt, J. Christen, L. Eckey, J. Holst, A. Hoffmann, B. Mensching, and B. Rauschenbach. "On the nature of the 3.41 eV luminescence in hexagonal GaN," *Journal of Crystal Growth*, 189/190:556–560 (June 1998).
34. Fong, C. Y., V. A. Gubanov, and C. Boekema. "Iron and Manganese Doped Zinc-Blende GaN," *Journal of Electronic Materials*, 29(9):1067–1073 (September 2000).
35. Frazier, R. M., G. T. Thaler, C. R. Abernathy, S. J. Pearton, M. L. Nakarmi, K. B. Nam, J. Y. Lin, H. X. Jiang, J. Kelly, R. Rairigh, A. F. Hebard, J. M. Zavada, and R. G. Wilson. "Transition metal ion implantation into AlGaIn," *Journal of Applied Physics*, 94(8):4956–4960 (October 2003).
36. Fukumura, T., Z. Jin, M. Kawasaki, T. Shono, T. Hasegawa, S. Koshihara, and H. Koinuma. "Magnetic properties of Mn-doped ZnO," *Applied Physics Letters*, 78(7):958–960 (February 2001).
37. Fukumura, T., Z. Jin, A. Ohtomo, H. Koinuma, and M. Kawasaki. "An oxide-diluted magnetic semiconductor: Mn-doped ZnO," *Applied Physics Letters*, 75(21):3366–3368 (November 1999).
38. Furdyna, J. K. "Diluted magnetic semiconductors," *Journal of Applied Physics*, 64(4):R29–R64 (August 1988).
39. Guo, L. W., H. Makino, H. J. Ko, Y. F. Chen, T. Hanada, D. L. Peng, K. Inaba, and T. Yao. "Structural characteristic and magnetic properties of Mn oxide films

- grown by plasma-assisted MBE,” *Journal of Crystal Growth*, 227-228:955–959 (July 2001).
40. Ham, M.-H., S. Yoon, Y. Park, and J.-M. Myoung. “A comparative study on magnetic and magnetotransport properties in (Ga,Mn)N epitaxial films grown on undoped and n-type GaN by PEMBE,” *Journal of Physics: Condensed Matter*, 16(34):6139–6145 (September 2004).
 41. Hammond, C. *The Basics of Crystallography and Diffraction* (Second Edition), 5. International Union of Crystallography Texts on Crystallography. New York: Oxford University Press, 2001.
 42. Han, S.-J., J. W. Song, C.-H. Yang, S. H. Park, J.-H. Park, Y. H. Jeong, and K. W. Rhie. “A key to room-temperature ferromagnetism in Fe-doped ZnO:Cu,” *Applied Physics Letters*, 81(22):4212–4214 (November 2002).
 43. Hashimoto, M., Y.-K. Zhou, M. Kanamura, and H. Asahi. “High temperature (>400 K) ferromagnetism in III–V-based diluted magnetic semiconductor GaCrN grown by ECR molecular-beam epitaxy,” *Solid State Communications*, 122(1-2):37–39 (April 2002).
 44. Heo, Y. W., M. P. Ivill, K. Ip, D. P. Norton, S. J. Pearton, J. G. Kelly, R. Rairigh, A. F. Hebard, and T. Steiner. “Effects of high-dose Mn implantation into ZnO grown on sapphire,” *Applied Physics Letters*, 84(13):2292–2294 (March 2004).
 45. Hill, D., R. A. Bartynski, L. Wielunski, P. Wu, Y. Lu, V. Poltavets, and M. Greenblatt. “Characterization of transition metal doped CVD-grown ZnO films and nanostructures.” Oral presentation to American Physical Society March meeting: Session P10-5, March 2005.
 46. Ip, K., R. M. Frazier, Y. W. Heo, D. P. Norton, C. R. Abernathy, S. J. Pearton, J. Kelly, R. Rairigh, A. F. Hebard, J. M. Zavada, and R. G. Wilson. “Ferromagnetism in Mn- and Co-implanted ZnO nanorods,” *Journal of Vacuum Science and Technology B*, 21(4):1476–1481 (July/August 2003).
 47. Jin, Z., T. Fukumura, M. Kawasaki, K. Ando, H. Saito, T. Sekiguchi, Y. Z. Yoo, M. Murakami, Y. Matsumoto, T. Hasegawa, and H. Koinuma. “High throughput fabrication of transition-metal-doped epitaxial ZnO thin films: A series of oxide-diluted magnetic semiconductors and their properties,” *Applied Physics Letters*, 78(24):3824–3826 (June 2001).
 48. Jonker, B. T. “Progress Toward Electrical Injection of Spin-Polarized Electrons Into Semiconductors,” *Proceedings of the IEEE*, 91(5):727–740 (May 2003).
 49. Josephson, B. D. “Possible New Effects in Superconductive Tunnelling,” *Physics Letters*, 1(7):251–253 (July 1962).
 50. Jung, S. W., S. J. An, G.-C. Yi, C. U. Jung, S.-I. Lee, and S. Cho. “Ferromagnetic properties of $Zn_{1-x}Mn_xO$ epitaxial thin films,” *Applied Physics Letters*, 80(24):4561–4563 (June 2002).

51. Kikkawa, J. M. and D. D. Awschalom. “Resonant Spin Amplification in n -Type GaAs,” *Physical Review Letters*, 80(19):4313–4316 (May 1998).
52. Kikkawa, J. M. and D. D. Awschalom. “Lateral drag of spin coherence in gallium arsenide,” *Nature*, 397(6715):139–141 (January 1999).
53. Kim, D. S., H.-M. Kim, S. U. Yuldashev, S. J. Lee, T. W. Kang, and D. Y. Kim. “Characteristics of $Zn_{1-x}Mn_xO$ Thin Films Prepared by RF Magnetron Sputtering,” *Journal of the Korean Physical Society*, 42(Supplemental Issue 2):S333–S335 (February 2003).
54. Kim, J. H., J. B. Lee, H. Kim, D. Kim, Y. E. Ihm, and W. K. Choo. “Characteristics of Cobalt-Doped Zinc Oxide Thin Films Prepared by Pulsed Laser Deposition,” *IEEE Transactions on Magnetism*, 38(5):2880–2882 (September 2002).
55. Kittel, C. *Introduction to Solid State Physics* (Sixth Edition), chapter 14-16, 395–492. New York: John Wiley & Sons, Inc., 1986.
56. Klug, H. P. and L. E. Alexander. *X-Ray Diffraction Procedures* (Third Edition). New York: John Wiley & Sons, Inc., July 1962.
57. Kohan, A. F., G. Ceder, D. Morgan, and C. G. Van de Walle. “First-principles study of native point defects in ZnO,” *Physical Review B*, 61(22):15019–15027 (June 2000).
58. Krenn, H., K. Kaltenecker, T. Dietl, J. S. Eck, and G. Bauer. “Photoinduced magnetization in dilute magnetic (semimagnetic) semiconductors,” *Physical Review B*, 39(15):10918–10934 (May 1989).
59. Kuwabara, S., T. Kondo, T. Chikyow, P. Ahmet, and H. Munekata. “Molecular Beam Epitaxy of Wurtzite GaN-Based Magnetic Alloy Semiconductors,” *Japanese Journal of Applied Physics, Part 2*, 40(7B):L724–L727 (July 2001).
60. Lee, C.-G., K.-T. Youn, and K. Fukamichi. “Antiferromagnetic CrGa Layers with a High Néel Temperature for Biasing Spin Valves,” *IEEE Transactions on Magnetism*, 36(5):2902–2904 (September 2000).
61. Lee, H.-J., S.-Y. Jeong, C. R. Cho, and C. H. Park. “Study of diluted magnetic semiconductor: Co-doped ZnO,” *Applied Physics Letters*, 81(21):4020–4022 (November 2002).
62. Lee, J. S., J. D. Lim, Z. G. Khim, Y. D. Park, S. J. Pearton, and S. N. G. Chu. “Magnetic and structural properties of Co, Cr, V ion-implanted GaN,” *Journal of Applied Physics*, 93(8):4512–4516 (April 2003).
63. Lee, K. P., S. J. Pearton, M. E. Overberg, C. R. Abernathy, R. G. Wilson, S. N. G. Chu, N. Theodoropoulou, A. F. Hebard, and J. M. Zavada. “Magnetic Effects of Direct Ion Implantation of Mn and Fe into p-GaN,” *Journal of Electronic Materials*, 31(5):411–415 (May 2002).

64. Lima, S. A. M., F. A. Sigoli, M. Jafelicci, Jr., and M. R. Davolos. "Luminescent properties and lattice defects correlation on zinc oxide," *International Journal of Inorganic Materials*, 3(7):749–754 (November 2001).
65. Lin, B., Z. Fu, and Y. Jia. "Green luminescent center in undoped zinc oxide films deposited on silicon substrates," *Applied Physics Letters*, 79(7):943–945 (August 2001).
66. Liu, K. T., Y. K. Su, S. J. Chang, K. Onomitsu, and Y. Horikoshi. "Photoluminescence and Raman scattering in Mg and P co-implanted GaN epitaxial layers," *Physica Status Solidi (b)*, 241(12):2693–2697 (August 2004).
67. Look, D. C., J. W. Hemsky, and J. R. Sizelove. "Residual Native Shallow Donor in ZnO," *Physical Review Letters*, 82(12):2552–2555 (March 1999).
68. Mauger, A. "Magnetic polaron: Theory and experiment," *Physical Review B*, 27(4):2308–2324 (February 1983).
69. McCluskey, M. D., N. M. Johnson, C. G. Van de Walle, D. P. Bour, M. Kneissl, and W. Walukiewicz. "Metastability of Oxygen Donors in AlGa_N," *Physical Review Letters*, 80(18):4008–4011 (May 1998).
70. McElfresh, M. "Fundamentals of Magnetism and Magnetic Measurements Featuring Quantum Design's Magnetic Property Measurement System,". Distributed with Magnetic Property Measurement System Purchase; Available Online at <http://www.qdusa.com/resources/techdocs.html>, Purdue University, 1994.
71. McKelvey, J. P. *Solid State Physics for Engineering and Materials Science* (First Edition). Malabar, Florida: Krieger, 1993.
72. Meyer, B. K., H. Alves, D. M. Hofmann, W. Kriegseis, D. Forster, F. Bertram, J. Christen, A. Hoffmann, M. S. Burg, M. Dworzak, U. Haboeck, and A. V. Rodina. "Bound exciton and donor-acceptor pair recombinations in ZnO," *Physica Status Solidi, B*, 241(2):231–260 (February 2004).
73. Meyer, B. K., G. Steude, A. Göldner, A. Hoffman, H. Amano, and I. Akasaki. "Photoluminescence Investigations of AlGa_N on GaN Epitaxial Films," *Physica Status Solidi (b)*, 216(1):187–191 (November 1999).
74. Muthukumar, S., H. Sheng, J. Zhong, Z. Zhang, N. W. Emanetoglu, and Y. Lu. "Selective MOCVD Growth of ZnO Nanotips," *IEEE Transactions on Nanotechnology*, 2(1):50–54 (March 2003).
75. Norton, D. P., S. J. Pearton, A. F. Hebard, N. Theodoropoulou, L. A. Boatner, and R. G. Wilson. "Ferromagnetism in Mn-implanted ZnO:Sn single crystals," *Applied Physics Letters*, 82(2):239–241 (January 2003).
76. Ohldag, H., N. B. Weber, C. Bethke, and F. U. Hillebrecht. "Surface antiferromagnetism of NiO studied by photoemission microscopy," *Journal of Electron Spectroscopy and Related Phenomena*, 114-116:765–770 (March 2001).

77. Ohno, H., D. Chiba, F. Masukura, T. Omiya, E. Abe, T. Dietl, Y. Ohno, and K. Ohtani. "Electric-field control of ferromagnetism," *Nature*, 408(6815):944–946 (December 2000).
78. Ohno, H. "Magnetotransport and Magnetic Properties of (Ga,Mn)As and Its Heterostructures," *Acta Physica Polonica A*, 94(2):155–164 (August 1998).
79. Ohno, Y., D. K. Young, B. Beschoten, F. Matsukura, H. Ohno, and D. D. Awschalom. "Electrical spin injection in a ferromagnetic semiconductor heterostructure," *Nature*, 402(6763):790–792 (December 1999).
80. O'Reilly, E. P. *Quantum Theory of Solids* (First Edition), chapter 6-7, 128–171. London: Taylor & Francis, 2002.
81. Oseroff, S. and P. H. Keesom. *Semiconductors and Semimetals* (First Edition), 25: *Diluted Magnetic Semiconductors*, chapter 1, 1–34. Boston: Academic Press, Inc., 1988.
82. Overberg, M. E., G. T. Thaler, C. R. Abernathy, N. A. Theodoropoulou, K. T. McCarthy, S. B. Arnason, J. S. Lee, J. D. Lim, S. B. Shim, K. S. Suh, Z. G. Khim, Y. D. Park, S. J. Pearton, and A. F. Hebard. "Growth of the Dilute Magnetic Semiconductor GaMnN by Molecular-Beam Epitaxy," *Journal of Electronic Materials*, 32(5):298–306 (May 2003).
83. Overberg, M. E., C. R. Abernathy, S. J. Pearton, N. A. Theodoropoulou, K. T. McCarthy, and A. F. Hebard. "Indication of ferromagnetism in molecular-beam-epitaxy-derived N-type GaMnN," *Applied Physics Letters*, 79(9):1312–1314 (August 2001).
84. Pankove, J. I., J. E. Berkeyheiser, H. P. Maruska, and J. Wittke. "Luminescent properties of GaN," *Solid State Communications*, 8(13):1051–1053 (July 1970).
85. Park, S. E., H.-J. Lee, Y. C. Cho, S.-Y. Jeong, C. R. Cho, and S. Cho. "Room-temperature ferromagnetism in Cr-doped GaN single crystals," *Applied Physics Letters*, 80(22):4187–4189 (June 2002).
86. Parkin, S., X. Jiang, C. Kaiser, A. Panchula, K. Roche, and M. Samant. "Magnetically Engineered Spintronic Sensors and Memory," *Proceedings of the IEEE*, 91(5):661–680 (May 2003).
87. Pearton, S. J., C. R. Abernathy, M. E. Overberg, G. T. Thaler, D. P. Norton, N. Theodoropoulou, A. F. Hebard, Y. D. Park, F. Ren, J. Kim, and L. A. Boatner. "Wide band gap ferromagnetic semiconductors and oxides," *Journal of Applied Physics*, 93(1):1–13 (January 2003).
88. Pearton, S. J., C. R. Abernathy, M. E. Overberg, G. T. Thaler, A. H. Onstine, B. P. Gila, F. Ren, B. Lou, and J. Kim. "New applications for gallium nitride," *Materials Today*, 5(6):24–31 (June 2002).
89. Pearton, S. J., C. R. Abernathy, G. T. Thaler, R. M. Frazier, D. P. Norton, F. Ren, Y. D. Park, J. M. Zavada, I. A. Buyanova, W. M. Chen, and A. F.

- Hebard. "Wide bandgap GaN-based semiconductors for spintronics," *Journal of Physics: Condensed Matter*, 16(7):R209–R245 (February 2004).
90. Pearton, S. J., M. E. Overberg, G. Thaler, C. R. Abernathy, N. Theodoropoulou, A. F. Hebard, S. N. G. Chu, R. G. Wilson, J. M. Zavada, A. Y. Polyakov, A. V. Osinsky, P. E. Norris, P. P. Chow, A. M. Wowchack, J. M. V. Hove], and Y. D. Park. "Characterization of High Dose Mn, Fe, and Ni implantation into *p*-GaN," *Journal of Vacuum Science and Technology, A*, 20(3):721–724 (May/June 2002).
 91. Polyakov, A. Y., N. B. Smirnov, A. V. Govorkov, R. M. Frazier, G. T. Thaler, C. R. Abernathy, S. J. Pearton, J. M. Zavada, and R. G. Wilson. "Optical and Electrical Properties of AlGaN Films Implanted with Mn, Co, or Cr," *Journal of Electronic Materials*, 33(5):384–388 (May 2004).
 92. Prinz, G. A. "Magnetoelectronics," *Science*, 282(5394):1660–1663 (November 1998).
 93. Radovanovic, P. V. and D. R. Gamelin. "High-Temperature Ferromagnetism in Ni²⁺-Doped ZnO Aggregates Prepared from Colloidal Diluted Magnetic Semiconductor Quantum Dots," *Physical Review Letters*, 91(15):157202 (October 2003).
 94. Reed, M. L., M. K. Ritums, H. H. Stadelmaier, M. J. Reed, C. A. Parker, S. M. Bedair, and N. A. El-Masry. "Room temperature magnetic (Ga,Mn)N: a new material for spin electronic devices," *Materials Letters*, 51(6):500–503 (December 2001).
 95. Reed, M., N. A. El-Masry, H. H. Stadelmaier, M. K. Ritums, M. J. Reed, C. A. Parker, J. C. Roberts, and S. M. Bedair. "Room temperature ferromagnetic properties of (Ga,Mn)N," *Applied Physics Letters*, 79(21):3473–3475 (November 2001).
 96. Richardson, J. T. and W. O. Milligan. "Magnetic Properties of Colloidal Nickelous Oxide," *Physical Review*, 102(5):1289–1294 (June 1956).
 97. Rode, K., A. Anane, R. Mattana, J.-P. Contour, O. Durand, and R. LeBourgeois. "Magnetic semiconductors based on cobalt substituted ZnO," *Journal of Applied Physics*, 93(10):7676–7678 (May 2003).
 98. Ryu, M.-Y., E. A. Chitwood, E. N. Claunch, Y. K. Yeo, R. L. Hengehold, J. A. Fellows, and T. Steiner. "Annealing studies of Si-implanted Al_{0.25}Ga_{0.75}N," *Physica Status Solidi C*, 0(7):2593–2596 (December 2003).
 99. Saeki, H., H. Tabata, and T. Kawai. "Magnetic and electric properties of vanadium doped ZnO films," *Solid State Communications*, 120(11):439–443 (November 2001).
 100. Sato, K. and H. Katayama-Yoshida. "Material Design for Transparent Ferromagnets with ZnO-Based Magnetic Semiconductors," *Japanese Journal of Applied Physics, Part 2*, 39(6B):L555–L558 (June 2000).

101. Sato, K. and H. Katayama-Yoshida. "Stabilization of Ferromagnetic States by Electron Doping in Fe-, Co- or Ni-Doped ZnO," *Japanese Journal of Applied Physics, Part 2*, 40(4A):L334–L336 (April 2001).
102. Satoh, I. and T. Kobayashi. "Magnetic and optical properties of novel magnetic semiconductor Cr-doped ZnO and its application to all oxide p-i-n diode," *Applied Surface Science*, 216(1-4):603–606 (June 2003).
103. Sawicki, M., L. van Khoi, F. Matsukura, T. Dietl, T. Fukumura, Z. Jin, H. Koinuma, and M. Kawasaki. "Experimental Investigation of Ferromagnetism in II-VI Disordered Semiconducting Compounds," *Journal of Superconductivity: Incorporating Novel Magnetism*, 16(1):147–150 (February 2003).
104. Schmidt, G., R. Fiederling, M. Keim, G. Reuscher, T. Gruber, W. Ossau, A. Waag, and L. W. Molenkamp. "Demonstration of electrical spin injection into a semiconductor using a semimagnetic spin aligner," *Superlattices and Microstructures*, 27(5/6):297–300 (May 2000).
105. Schwartz, D. A., K. R. Kittilstved, and D. R. Gamelin. "Above-room-temperature ferromagnetic Ni²⁺-doped ZnO thin films prepared from colloidal diluted magnetic semiconductor quantum dots," *Applied Physics Letters*, 85(8):1395–1397 (August 2004).
106. Selwood, P. W. *Adsorption and Collective Paramagnetism*, chapter 3, 35–50. London: Academic Press, 1962.
107. Semond, F., B. Damilano, S. Vézian, N. Grandjean, M. Leroux, and J. Massies. "GaN on Si(111): From Growth Optimization to Optical Properties of Quantum Well Structures," *Physica Status Solidi (b)*, 216(1):101–106 (November 1999).
108. Serway, R. A. *Physics for Scientists & Engineers (Third Edition)*, vol. II. Saunders Golden Sunburst Series, chapter 30, 860. Philadelphia: Saunders College Publishing, 1990.
109. Shan, W., A. J. Fischer, S. J. Hwang, B. D. Little, R. J. Hauenstein, X. C. Xie, J. J. Song, D. S. Kim, B. Goldenberg, R. Horning, S. Krishnankutty, W. G. Perry, M. D. Bremser, and R. F. Davis. "Intrinsic exciton transitions in GaN," *Journal of Applied Physics*, 83(1):455–461 (January 1998).
110. Shapira, Y. "Ultrasonic Behavior near the Spin-Flop Transition of Cr₂O₃," *Physical Review*, 187(2):734–736 (November 1969).
111. Shon, Y., Y. H. Kwon, D. Y. Kim, X. Fan, D. Fu, and T. W. Kang. "Magnetic Characteristic of Mn⁺ Ion Implanted GaN Epilayer," *Japanese Journal of Applied Physics, Part 1*, 40(9A):5304–5305 (September 2001).
112. Shon, Y., Y. H. Kwon, S. U. Yuldashev, J. H. Leem, C. S. Park, D. J. Fu, H. J. Kim, T. W. Kang, and X. J. Fan. "Optical and magnetic measurements of p-type GaN epilayers implanted with Mn⁺ ions," *Applied Physics Letters*, 81(10):1845–1847 (September 2002).

113. Shon, Y., Y. H. Kwon, S. U. Yuldashev, Y. S. Park, D. J. Fu, D. Y. Kim, H. S. Kim, and T. W. Kang. "Diluted magnetic semiconductor of p -type GaN epilayers implanted with Mn^+ ions," *Journal of Applied Physics*, *93*(3):1546–1549 (February 2003).
114. Sih, V. A., E. Johnston-Halperin, and D. D. Awschalom. "Optical and Electronic Manipulation of Spin Coherence in Semiconductors," *Proceedings of the IEEE*, *91*(5):752–760 (May 2003).
115. Smit, J. and H. P. J. Wijn. *Ferrites: Physical Properties of Ferrimagnetic Oxides in Relation to Their Technical Applications* (First Edition). Wiley Series on the Science and Technology of Materials, Eindhoven: John Wiley & Sons, 1959.
116. Sonoda, S., H. Hori, Y. Yamamoto, T. Sasaki, M. Sato, S. Shimizu, K. Suga, and K. Kindo. "Properties of Ferromagnetic $Ga_{1-x}Mn_xN$ Films Grown by Ammonia-MBE," *IEEE Transactions on Magnetics*, *38*(5):2859–2862 (September 2002).
117. Sonoda, S., S. Shimizu, T. Sasaki, Y. Yamamoto, and H. Hori. "Molecular Beam Epitaxy of Wurtzite (Ga,Mn)N Films on Sapphire(0001) Showing the Ferromagnetic Behaviour at Room Temperature," *Condensed Matter*, *0108*:159 (August 2001). Available at <http://www.arxiv.org/ftp/cond-mat/papers/0108/0108159.pdf>.
118. Sun, X. L., S. H. Goss, L. J. Brillson, D. C. Look, and R. J. Molnar. "Depth-dependent investigation of defects and impurity doping in GaN/sapphire using scanning electron microscopy and cathodoluminescence spectroscopy," *Journal of Applied Physics*, *91*(10):6729–6738 (May 2002).
119. Sze, S. M. *Semiconductor Devices: Physics and Technology* (First Edition), chapter 10, 381–427. New York: John Wiley & Sons, 1985.
120. Tabata, H., M. Saeki, S. L. Guo, J. H. Choi, and T. Kawai. "Control of the electric and magnetic properties of ZnO films," *Physica B*, *308-310*:993–998 (December 2001).
121. Tebble, R. S. and D. J. Craik. *Magnetic Materials* (First Edition). London: John Wiley & Sons, 1969.
122. Teke, A., Ü. Özgür, S. Doğan, X. Gu, H. Morkoç, B. Nemeth, J. Nause, and H. O. Everitt. "Excitonic fine structure and recombination dynamics in single-crystalline ZnO," *Physical Review B*, *70*(19):195207 (November 2004).
123. Thaler, G. T., M. E. Overberg, B. Gila, R. Frazier, C. R. Abernathy, S. J. Pearton, J. S. Lee, S. Y. Lee, Y. D. Park, Z. G. Khim, J. Kim, and F. Ren. "Magnetic properties of n -GaMnN thin films," *Applied Physics Letters*, *80*(21):3964–3966 (May 2002).
124. Theodoropoulou, N., A. F. Hebard, S. N. G. Chu, M. E. Overberg, C. R. Abernathy, S. J. Pearton, R. G. Wilson, and J. M. Zavada. "Characterization of high

- dose Fe implantation into *p*-GaN,” *Applied Physics Letters*, 79(21):3452–3454 (November 2001).
125. Theodoropoulou, N., A. F. Hebard, M. E. Overberg, C. R. Abernathy, S. J. Pearton, S. N. G. Chu, and R. G. Wilson. “Magnetic and structural properties of Mn-implanted GaN,” *Applied Physics Letters*, 78(22):3475–3477 (May 2001).
 126. Theodoropoulou, N., M. E. Overberg, S. N. G. Chu, A. F. Hebard, C. R. Abernathy, R. G. Wilson, J. M. Zavada, K. P. Lee, and S. J. Pearton. “Magnetic Properties of Mn and Fe-Implanted *p*-GaN,” *Physica Status Solidi B*, 228(1):337–340 (November 2001).
 127. Turton, R. *The Physics of Solids* (First Edition), chapter 8-9, 211–278. Oxford: Oxford University Press, 2000.
 128. Ueda, K., H. Tabata, and T. Kawai. “Magnetic and electric properties of transition-metal-doped ZnO films,” *Applied Physics Letters*, 79(7):988–990 (August 2001).
 129. United States Air Force, Maxwell AFB, AL. *Air Force Basic Doctrine*, 1997. Available at <http://www.e-publishing.af.mil/pubfiles/af/dd/afdd1/afdd1.pdf>.
 130. United States Department of Defense, Washington. *Joint Vision 2020*, June 2000. Available at <http://www.dtic.mil/jointvision/jvpub2.htm>.
 131. Uspenskii, Y., E. Kulatov, H. Mariette, H. Nakayama, and H. Ohta. “Ab initio study of the magnetism in GaAs, GaN, ZnO, and ZnTe-based diluted magnetic semiconductors,” *Journal of Magnetism and Magnetic Materials*, 258-259:248–250 (March 2003). Second Moscow International Symposium on Magnetism.
 132. Vanheusden, K., W. L. Warren, C. H. Seager, D. R. Tallant, J. A. Voigt, and B. E. Gnade. “Mechanisms behind green photoluminescence in ZnO phosphor powders,” *Journal of Applied Physics*, 79(10):7983–7990 (May 1996).
 133. von Molnár, S. and D. Read. “New Materials for Semiconductor Spin-Electronics,” *Proceedings of the IEEE*, 91(5):715–726 (May 2003).
 134. Wakano, T., N. Fujimura, Y. Morinaga, N. Abe, A. Ashida, and T. Ito. “Magnetic and magneto-transport properties of ZnO:Ni films,” *Physica E*, 10(1-3):260–264 (May 2001).
 135. Wetzal, C., S. Fischer, J. Krüger, E. E. Haller, R. J. Molnar, T. D. Moustakas, E. N. Mokhov, and P. G. Baranov. “Strongly localized excitons in gallium nitride,” *Applied Physics Letters*, 68(18):2556–2558 (April 1996).
 136. Wohlfarth, E. P., editor. *Ferromagnetic Materials: A Handbook on the Properties of Magnetically Ordered Substances, Vol. 3*. Amsterdam: North-Holland Physics, 1982.
 137. Wolf, S. A., D. D. Awschalom, R. A. Buhrman, J. M. Daughton, S. von Molnár, M. L. Roukes, A. Y. Chtchelkanova, and D. M. Treger. “Spintronics: A

- Spin-Based Electronics Vision for the Future,” *Science*, 294(5546):1488–1495 (November 2001).
138. Wolf, S. A. and D. Treger. “Spintronics: A New Paradigm for Electronics for the New Millennium,” *IEEE Transactions on Magnetism*, 36(5):2748–2751 (September 2000).
 139. Wu, X. L., G. G. Siu, C. L. Fu, and H. C. Ong. “Photoluminescence and cathodoluminescence studies of stoichiometric and oxygen-deficient ZnO films,” *Applied Physics Letters*, 78(16):2285–2287 (April 2001).
 140. Yamamoto, A., K. Miyajima, T. Goto, H. J. Ko, and T. Yao. “Biexciton luminescence in high-quality ZnO epitaxial thin films,” *Journal of Applied Physics*, 90(10):4973–4976 (November 2001).
 141. Yang, F., C. L. Chien, X. W. Li, G. Xiao, and A. Gupta. “Critical behavior of epitaxial half-metallic ferromagnetic CrO₂ films,” *Physical Review B*, 63(9):092403 (March 2001).
 142. Yoon, S. W., S.-B. Cho, S. C. We, S. Yoon, B. J. Suh, H. K. Song, and Y. J. Shin. “Magnetic properties of ZnO-based diluted magnetic semiconductors,” *Journal of Applied Physics*, 93(10):7879–7881 (May 2003).
 143. Yoon, S. J., S. H. Lee, K. H. Kim, and K. S. Ahn. “Electrical and magnetic properties of spinel ZnCr_{2-x}Fe_xO₄ ($0 \leq x \leq 1.0$),” *Materials Chemistry and Physics*, 73:330–334 (2002).
 144. Zając, M., R. Doradziński, J. Gosk, J. Szczytko, M. Lefeld-Sosnowska, M. Kamińska, A. Twardowski, M. Palczewska, E. Grzanka, and W. Gębicki. “Magnetic and optical properties of GaMnN magnetic semiconductor,” *Applied Physics Letters*, 78(9):1276–1278 (February 2001).
 145. Zając, M., J. Gosk, M. Kamińska, A. Twardowski, T. Szyszko, and S. Podsiadło. “Paramagnetism and antiferromagnetic $d-d$ coupling in GaMnN magnetic semiconductor,” *Applied Physics Letters*, 79(15):2432–2434 (October 2001).
 146. Zhang, D. H., Z. Y. Xue, and Q. P. Wang. “The mechanisms of blue emission from ZnO films deposited on glass substrate by r.f. magnetron sputtering,” *Journal of Physics D: Applied Physics*, 35(21):2837–2840 (November 2002).
 147. Zhou, Y.-K., M. Hashimoto, M. Kanamura, and H. Asahi. “Room Temperature Ferromagnetism in III–V-Based Diluted Magnetic Semiconductor GaCrN grown by ECR Molecular-Beam Epitaxy,” *Journal of Superconductivity: Incorporating Novel Magnetism*, 16(1):37–40 (February 2003).

Vita

Captain Jeremy A. Raley graduated from Astronaut High School in Titusville, Florida. His undergraduate studies began soon thereafter at the United States Air Force Academy where he earned a Bachelor of Science degree in Electrical Engineering as well as a commission in the United States Air Force.

His service to the Air Force began as a communications officer at the 738th Engineering Installation Squadron at Keesler Air Force Base, Mississippi. Upon completion of this assignment he was selected to attend the Air Force Institute of Technology where he earned a Master of Science degree in Electrical Engineering. The Master's degree was followed immediately at AFIT by pursuit of the Doctor of Philosophy degree in Electrical Engineering. Upon graduation, Captain Raley will be assigned to the Sensors Directorate of the Air Force Research Laboratory.

REPORT DOCUMENTATION PAGE

Form Approved
OMB No. 0704-0188

The public reporting burden for this collection of information is estimated to average 1 hour per response, including the time for reviewing instructions, searching existing data sources, gathering and maintaining the data needed, and completing and reviewing the collection of information. Send comments regarding this burden estimate or any other aspect of this collection of information, including suggestions for reducing this burden to Department of Defense, Washington Headquarters Services, Directorate for Information Operations and Reports (0704-0188), 1215 Jefferson Davis Highway, Suite 1204, Arlington, VA 22202-4302. Respondents should be aware that notwithstanding any other provision of law, no person shall be subject to any penalty for failing to comply with a collection of information if it does not display a currently valid OMB control number. **PLEASE DO NOT RETURN YOUR FORM TO THE ABOVE ADDRESS.**

1. REPORT DATE (<i>DD-MM-YYYY</i>) July 2005		2. REPORT TYPE Doctoral Dissertation		3. DATES COVERED (<i>From — To</i>) Jul 2003 — Jun 2005		
4. TITLE AND SUBTITLE High-Temperature Ferromagnetism in Transition Metal Implanted Wide-Bandgap Semiconductors				5a. CONTRACT NUMBER		
				5b. GRANT NUMBER		
				5c. PROGRAM ELEMENT NUMBER		
				5d. PROJECT NUMBER		
				5e. TASK NUMBER		
6. AUTHOR(S) Raley, Jeremy A., Captain, USAF				5f. WORK UNIT NUMBER		
7. PERFORMING ORGANIZATION NAME(S) AND ADDRESS(ES) Air Force Institute of Technology Graduate School of Engineering and Management (AFIT/EN) 2950 Hobson Way WPAFB OH 45433-7765				8. PERFORMING ORGANIZATION REPORT NUMBER AFIT/DS/ENP/05-04		
9. SPONSORING / MONITORING AGENCY NAME(S) AND ADDRESS(ES) Todd Steiner AFOSR/NE 4015 Wilson Blvd Arlington VA 22203				10. SPONSOR/MONITOR'S ACRONYM(S) 11. SPONSOR/MONITOR'S REPORT NUMBER(S)		
12. DISTRIBUTION / AVAILABILITY STATEMENT APPROVED FOR PUBLIC RELEASE; DISTRIBUTION UNLIMITED						
13. SUPPLEMENTARY NOTES						
14. ABSTRACT The field of spin transport electronics (spintronics) is a viable candidate for advancing computing and communication technologies. Material with both semiconductor and magnetic properties, which is commonly called a dilute magnetic semiconductor (DMS), will prove most useful in the fabrication of spintronic devices. In order to produce a DMS at above room temperature, transition metals (TMs) were implanted into host semiconductors of <i>p</i> -GaN, Al _{0.35} Ga _{0.65} N, or ZnO. Magnetic hysteresis measurements using a superconducting quantum interference device (SQUID) magnetometer show that some of the material combinations clearly exhibit ferromagnetism above room temperature. The most promising materials for creating spintronic devices using ion implantation are <i>p</i> -GaN:Mn, Al _{0.35} Ga _{0.65} N:Cr, and Fe-implanted ZnO nanotips on Al ₂ O ₃ . Temperature-dependent magnetization measurements confirm that indications of ferromagnetism are due to DMS behavior. Photo- and cathodoluminescence measurements show that implantation damage is recovered and the implanted TMs are incorporated into the semiconductor. As progress is made toward realizing practical spintronic devices, the work reported here will be useful for determining material combinations and implantation conditions that will yield the needed materials.						
15. SUBJECT TERMS Dilute Magnetic Semiconductor, DMS, Semiconductor Ferromagnetism, Wide Gap Semiconductors, Gallium Nitrides, GaN, Aluminum Gallium Nitrides, AlGaN, Zinc Oxides, ZnO, Transition Metals, Ion Implantation, Magnetometry, Superconducting Quantum Interference Device, SQUID, Photoluminescence, PL, Cathodoluminescence, CL						
16. SECURITY CLASSIFICATION OF:			17. LIMITATION OF ABSTRACT UU	18. NUMBER OF PAGES 269	19a. NAME OF RESPONSIBLE PERSON Yung Kee Yeo (ENP)	
a. REPORT U	b. ABSTRACT U	c. THIS PAGE U			19b. TELEPHONE NUMBER (<i>include area code</i>) (937) 255-3636, ext 4532; Yung.Yeo@afit.edu	